# INVESTIGATION OF InP AND SiGe NANOMATERIALS VIA MOLECULAR DYNAMICS SIMULATIONS

A THESIS SUBMITTED TO
THE GRADUATE SCHOOL OF NATURAL AND APPLIED SCIENCES
OF
MIDDLE EAST TECHNICAL UNIVERSITY

BY

NADİRE NAYİR

IN PARTIAL FULFILLMENT OF THE REQUIREMENTS
FOR
THE DEGREE OF DOCTOR OF PHILOSOPHY
IN
PHYSICS

JUNE 27 2018

Approval of the thesis:

**INVESTIGATION OF InP AND SiGe NANOMATERIALS VIA MOLECULAR DYNAMICS SIMULATIONS**

submitted by **NADİRE NAYİR** in partial fulfillment of the requirements for the degree of **Doctor of Philosophy in Physics Department, Middle East Technical University** by,

Prof. Dr. Halil Kalıpçılar
Dean, Graduate School of **Natural and Applied Sciences** _____

Prof. Dr. Altuğ Özpineci
Head of Department, **Physics** _____

Prof. Dr. Şakir Erkoç
Supervisor, **Physics Department, METU** _____

Assoc. Prof. Dr. Emre Taşcı
Co-supervisor, **Physics Engineering Department, Hacettepe University** _____

**Examining Committee Members:**

Prof. Dr. Oğuz Gülseren
Physics Department, Bilkent University _____

Prof. Dr. Şakir Erkoç
Physics Department, METU _____

Prof. Dr. Bilal Güneş
Physics Education Department, Gazi University _____

Prof. Dr. Hatice Kökten
Physics Department, METU _____

Assist. Prof. Dr. Selçuk Yerci
MNT, METU _____

**Date:** _____

**I hereby declare that all information in this document has been obtained and presented in accordance with academic rules and ethical conduct. I also declare that, as required by these rules and conduct, I have fully cited and referenced all material and results that are not original to this work.**

Name, Last Name: NADİRE NAYİR

Signature :

# ABSTRACT

## INVESTIGATION OF InP AND SiGe NANOMATERIALS VIA MOLECULAR DYNAMICS SIMULATIONS

NAYİR, NADİRE
Ph.D., Department of Physics
Supervisor : Prof. Dr. Şakir Erkoç
Co-Supervisor : Assoc. Prof. Dr. Emre Taşcı

June 27 2018, 174 pages

In this dissertation, InP and Si/Ge nanomaterials were investigated via classical molecular dynamics simulations. Structural and dynamical properties of InP nanorods and nanoparticles were examined under different conditions such as heating, cooling, strain etc. In the second part of this dissertation, a ReaxFF reactive force field development has been targeted to provide a more generalized description for the simulation of the crystallization process of amorphous Ge on Si substrate. For this aim, the ReaxFF reactive force developed by Fogarty et al. was re-parametrized for O-interstitial point defect formation in $Si/SiO_2$ interface. Additionally, the ReaxFF reactive force field initially parametrized by Zheng et al. was re-optimized for O-related point defect and its migration in Ge, and the heat treatment of $Ge/GeO_2$ interface. To establish the force field reliability, both force fields were subjected to the validation process further based on MD simulations.

Keywords: Molecular Dynamics simulations, InP, SiGe,nanomaterials, ReaxFF, force field development, Tersoff potential, nanorod, nanoparticle, LPE growth.

# ÖZ

## InP VE SiGe NANOMALZEMELERİNİN MOLEKÜLER DİNAMİĞİ BENZETİŞİMLERİ METODU İLE ARAŞTIRILMASI

NAYİR, NADİRE

Doktora, Fizik Bölümü

Tez Yöneticisi : Prof. Dr. Şakir Erkoç

Ortak Tez Yöneticisi : Doç. Dr. Emre Taşcı

Haziran 27 2018 , 174 sayfa

Bu çalışmada InP ve Si/Ge olmak üzere iki farklı nanomalzeme klasik molekül dinamiği benzetişimleri ile incelenmiştir. InP nanoçubuk ve nanoparçacıkların yapısal ve dinamik özellikleri sıcaklık, basınç, soğutma gibi çeşitli çevresel şartlar altında araştırılmıştır. Tezin ikinci kısmında ise, amorf germanyumun Si alttaşı üzerinde kristalleşme sürecini tanımlayabilecek ReaxFF reaktif kuvvet alanı geliştirilmesi hedeflenmiştir. Bunun için ilk önce $Si/SiO_2$ arayüzündeki oksijen ile ilişkili noktasal bozukluk ve onların arayüz boyunca difuzyonlarını tanımlamak için Fogarty ve çalışma arkadaşları tarafında geliştirilen RexFF reaftif kuvvet alanının yeniden parametrizasyonu gerçekleştirilmiştir. Ayrıca Ge içerisindeki oksijenden kaynaklı noktasal bozukluk ve onun Ge içinde difuzyonunun, ve $Ge/GeO_2$ arayüzünün farklı sıcaklıklar altındaki benzetişimlerini gerçekleştirebilmesi için Zheng ve çalışma arkadaşlarının parametrizasyonunu yaptığı ReaxFF reaktif kuvvet alanının bu çalışmada yeniden optimizasyonu yapılmıştır. Geliştirilen her iki kuvvet alanının geçerliliği moleküler dinamik benzetişim metodu ile test edilmiştir ve her iki kuvvet alanı da geçerlilik testini başarıyla geçmiştir.

Anahtar Kelimeler: Moleküler Dinamik benzetişimleri, InP, SiGe, nanomalzemeler, ReaxFF, kuvvet alanı geliştirilmesi, Tersoff potensiyeli, nanoçubuk, nanoparçacık, sıvı faz epitaksiyel büyüme.

***This thesis is dedicated to my beloved parents,***

***Saniye Nayir and Hamza Nayir***

*For their endless love, support and encouragement*

## ACKNOWLEDGMENTS

Undertaking this Ph.D. has been a truly life-changing experience for me. This feat was possible with the unconditional support and guidance of several people. First and foremost, I would like to express my sincere gratitude to my advisor, Prof. Şakir Erkoç. It has been an honor to be your last Ph.D. student. I am extremely grateful to you for allowing me to grow as a research scientist by supporting me academically and emotionally through the rough road to finish this thesis. During my Ph.D. research, you've treated me more like my father than being my supervisor. I appreciate all your continuous motivation, consistent encouragement, and immense knowledge. I also would like to thank my co-advisor, Assoc. Prof. Emre Taşcı for training that I have received during my dissertation research. He generously provided me his own computer resources/accounts including Ulakbim, EHU/UPV (Mecano and Husniya) and even his personal computers (Manu and Mois) beside your personal wiki. I also gained programming skills thanks to his help.

My special thank also goes to Assist. Prof. Selçuk Yerci being one of my thesis committee member. Thank you for investing your time, providing interesting and valuable feedback during my dissertation and that you gave me friendly advice and wise words about my academic-carrier. I also want to take a moment to thank my other committee members, Prof. Oğuz Gülseren, Prof. Bilal Güneş, Prof. Hatice Kökten. I felt proud and honored that you have accepted to be on my committee.

My sincere gratitude also goes to Prof. Adri van Duin. Thank you for giving me an opportunity to be part of your research group at PennState University. To accomplish my thesis was possible with your guidance, valuable support and kindness you have shown me. Thanks to you, I learned new techniques such as force field development, ReaxFF/ADF simulations, so that I improved my professional skills. I also gratefully acknowledge support from the Scientific and Technological Research Council of Turkey (TUBITAK) 2214-A Program, Grant No. 1059B141600161 for my research at PennState University.

I would like to thank Dr. Yun Kyung Shin for tutoring me during learning ReaxFF force field optimization process. I also wish to thank Margaret Kowalik and Mert Yiğit Şengül for helping me out to solve problems that I encountered in ReaxFF/ADF simulations. My thanks also go to Huseyin Oymak for Gaussian, Hande Toffoli for Quantum espresso and Barış Malcıoğlu for Lammps softwares. I would also like to thank Dr. Paulo S. Branicio for kindly providing us the MD program code with optimized parameters for the InP system. I also thank TUBITAK ULAKBIM High

Performance and Grid Computing Center, and The Institute for CyberScience Advanced CyberInfrastructure (ICS-ACI) for providing the computational resources.

To all my friends, thank you so much for your understanding and encouragement. Your friendship makes my life a wonderful experience. I especially thank Emel Altaş-Kiracı and Ali Kiracı for your precious friendships and always welcoming me at your home. Esin Kenar, Dilek Kızılören, Fatma Acar, Merve Demirtaş, Hilal Mutlu, Mert Şengül, Ümmügül Erözbek, Betül Deliktaş, Dorcas Kawaase, Hong-en Chen, Yun Shin and my all other friends that I did not name here deserve my wholehearted thanks for being always with me with their warm friendships. This story would not have been possible without your inspiration and excellent support.

Last but not least, I have to thank my beloved parents. There aren't enough words or ways to express how grateful I am for all of the sacrifices that they've made on my behalf. Their endless and unconditional support, warm love and continued patience were what gave me the strength to continue, and their prayer for me was what sustained me thus far. My twin sister and best friend, Selda, my elder brother, Hakan Rifat, my elder sister and my brother-in-law, Sema and Ahmet, deserve my wholehearted thanks, as well. They always stood by my side and encouraged me even my worst days that I'm feeling low and sad. I also thank my lovely and beautiful nieces, Sedanur, Vildan, Buğlem and Elif Zeren who are the most beautiful things in my life.

My thanks and appreciation to all of you for being part of this journey and making this thesis possible.

## TABLE OF CONTENTS

ABSTRACT . . . . . v

ÖZ . . . . . vi

ACKNOWLEDGMENTS . . . . . viii

TABLE OF CONTENTS . . . . . x

LIST OF TABLES . . . . . xv

LIST OF FIGURES . . . . . xviii

CHAPTERS

1 INTRODUCTION . . . . . 1

2 SIMULATION METHODS . . . . . 3

2.1 Molecular Mechanic Energy minimization . . . . . 3

2.1.1 Polak Ribiere Conjugate Gradient and Steepest Descent methods . . . . . 4

2.2 Molecular Dynamics . . . . . 6

2.2.1 Integrating Scheme . . . . . 8

2.2.1.1 Verlet algorithm . . . . . 8

2.2.1.2 Velocity-Verlet algorithm . . . . . 9

2.2.2 Ensemble Theory . . . . . 11

2.2.2.1 Canonical Ensemble (NVT): . . . . . 11

2.2.2.2 Isobaric-Isothermal Ensemble (NPT): . . . . . 13

2.2.3 Periodic Boundary Conditions . . . . . 14

2.3 Force Fields and Potential Energy functions . . . . . 15

2.3.1 Branicio Potential . . . . . 15

2.3.2 Reactive Force fields . . . . . 18

2.3.2.1 The Tersoff Potential . . . . . 19

2.3.2.2 The ReaxFF Reactive Force Field . . . 21

2.3.2.3 The ReaxFF Force Field Parametrization Process . . . . . 22

3 SIMULATIONS OF INDIUM PHOSPHIDE NANOMATERIALS . . 23

3.1 Introduction . . . . . 23

3.2 InP Nanorods . . . . . 25

3.2.1 Method & Procedures & Results . . . . . 25

3.2.1.1 Zinc Blende Nanorods . . . . . 28

3.2.1.2 Wurtzite Nanorods . . . . . 33

3.3 InP Nanoparticles . . . . . 46

3.3.1 Method, Procedures and Results . . . . . 46

3.3.1.1 Equilibrium and Non-equilibrated Simulations . . . . . 47

3.4 Concluding remarks . . . . . 55

4 LIQUID PHASE EPITAXIAL GROWTH OF Ge on $SiO_2$ . . . . . 59

4.1 Introduction . . . . . 59

4.1.1 Aims and Goals of the work . . . . . 60

4.2 The ReaxFF force field development for L-LPE system . . . 61

4.2.1 ReaxFF development for Ge/O interactions in L-LPE system . . . . . 62

4.2.1.1 Computational Methods . . . . . 62

4.2.1.2 Force Field Parameterization . . . . . 62

4.2.1.3 Point Defects . . . . . 63

4.2.1.4 MD simulations . . . . . 66

4.2.2 Results and Discussions . . . . . 69

4.2.2.1 Parameterization of the force field . . 69

4.2.2.2 ReaxFF MD simulations . . . . . 71

4.3 ReaxFF development for $Si/SiO_2$ system . . . . . 80

4.3.1 Computational Methods . . . . . 80

4.3.1.1 Force Field Parametrization Process . 80

4.3.1.2 Point Defects . . . . . 81

4.3.1.3 ReaxFF MD simulations . . . . . 85

4.4 Concluding Remarks . . . . . 97

5 CONCLUSIONS AND OUTLOOK . . . . . 101

5.1 Conclusions . . . . . 101

5.2 Outlook . . . . . 102

REFERENCES . . . . . 105

APPENDICES

A STRUCTURAL PROPERTIES OF INDIUM PHOSPHIDE NANORODS:MOLECULAR DYNAMICS SIMULATIONS . . . . . 123

A.1 Zincblende Nanorods . . . . . 124

A.1.1 Gradual Heating . . . . . 124

A.1.2 Stretching at Constant and Increasing Temperatures (5% and 10% Ratio) . . . . . 125

A.1.2.1 Phase Transitions Under Stretching . . 125

A.1.2.2 Breaking Mechanisms with respect to different phases under strain . . . . . 125

A.2 Wurtzite Nanorods . . . . . 137

A.2.1 Gradual Heating and Expansion . . . . . 137

A.2.1.1 Gradual Heating . . . . . 137

A.2.1.2 Expansion . . . . . 138

A.2.2 Annealing, Cooling and Stretching . . . . . 138

A.2.2.1 Annealing . . . . . 138

A.2.2.2 Cooling . . . . . 139

A.2.2.3 Stretching . . . . . 139

A.2.3 Stretching (1% and 5% ; 0.5%@600K: 4x6, 6x9, 8x13; 0.5%@900K: 6x9, 8x13) . . . . . 140

A.2.3.1 Breaking Mechanisms with respect to different phases under streching . . . . 140

A.2.3.2 Phase transition under stretching . . . 140

A.2.4 Compression and Stretching . . . . . 140

A.2.4.1 Stretching after heating . . . . . 153

A.2.4.2 Stretching and Cooling after heating . 153

B THE REAXFF REACTIVE FIELD DEVELOPMENT FOR SI/O AND GE/O SYSTEMS . . . . . 161

B.1 The ReaxFF Reactive force field for Si/O systems . . . . . 161

B.2 The ReaxFF Reactive force field for Ge/O systems . . . . . 167

CURRICULUM VITAE . . . . . 171

## LIST OF TABLES

TABLES

Table 2.1 The parameters of the InP interaction potential. Z, $\alpha$, $\sigma$ are the effective ionic charge, the electronic polarizability and the ionic radius. $\eta$, *w* are the steric repulsion exponent and the van der Waals strength. *B*, $\lambda_1$ and $\lambda_4$ are the three-body strength and the screening lengths for Coulomb and charge–dipole interactions, respectively. . . . . 17

Table 2.2 The parameters of the InP interaction potential. $r_c$, *A*, $r_0$, $\gamma$, $\theta_0$ and *C* are the two-body cutoff radius, the repulsion strength, the three-body range, exponent, bond angle and saturation parameter, respectively. . . . . 17

Table 3.1 Structural data of the analyzed ZB InP NRs shown in Fig. 3.1. . . . 25

Table 3.2 Structural data of the analyzed WZ InP NRs shown in Fig. 3.1. . . . 26

Table 3.3 The transition temperatures and the ZB NRs' thicknesses. The RS phase appeared immediately at 0.7K which is 1st observed transition temperature (1st O.T.T.) as seen in the table, with phase transition temperatures (P.T.T.) indicating the fixed temperature in which the non- deformed nanorod undergoes a complete transition. . . . . 28

Table 3.4 Final length (F.L.) and maximum elongation percentages (M.E.P.) are for the stretched ZB NRs at the constant temperature for the 5% stretching ratio (S.R) by following the equilibrium approach. . . . . 30

Table 3.5 Final length (F.L.) and maximum elongation percentages (M.E.P.) are the for stretched ZB NRs at constant temperature for the 10% stretching ratio (S.R.) by following the equilibrium approach. . . . . 30

Table 3.6 Breaking temperatures (B.T.), maximum elongation percentages (M.E.P.) and final length (F.L.) are the for stretched ZB NRs at constant temperature for the 5% stretching ratio (S.R.) by following the non-equilibriated approach. . . . . 31

Table 3.7 Breaking temperatures (B.T.), maximum elongation percentages (M.E.P.) and final length (F.L.), are for the stretched the ZB NRs at constant temperature for the 10% stretching ratio (S.R.) by following the non-equilibriated approach. . . . . 31

Table 3.8 Phase transition temperatures (P.T.T.) and the WZ NRs' thicknesses. In contrast to the ZB NRs (Table 3.3), it was found that 1st observed transition temperature (1st.O.T.T.) depends also on the NR's thickness. . . 33

Table 3.9 Complete transition temperatures (C.T.T.) in the gradual heated NRs. Comparing this table with Table 3.8, it is observed that gradually heated NRs undergo a phase transition at higher temperatures. . . . . 37

Table 3.10 Final length (F.L.) and maximum elongation percentages (M.E.P.) are for the stretched WZ NRs at the constant temperature for the 1% stretching ratio (S.R) by following the equilibrium approach. . . . . 38

Table 3.11 Final length (F.L.) and maximum elongation percentages (M.E.P.) are for the stretched WZ NRs at constant temperature for the 5% stretching ratio (S.R) by following the equilibrium approach. . . . . 39

Table 3.12 Breaking temperatures (B.T.), maximum elongation percentages (M.E.P.) and final length are for the stretched WZ NRs at increasing temperature for the 1% stretching ratio (S.R.) by following the non-equilibrated approach. . . . . 39

Table 3.13 Breaking temperatures (B.T.), maximum elongation percentages (M.E.P.) and final length are for the stretched WZ NRs at increasing temperature for the 5% stretching ratio (S.R.) by following the non-equilibrated approach. . . . . 40

Table 3.14 Final length, maximum elongation percentages and breaking temperatures are for the stretched WZ NRs at constant temperature for the 0.5% stretching ratio (S.R) by following the equilibrium approach. . . . . 40

Table 3.15 Phase transition temperatures lowered when the WZ NRs were put under strain. Stretch-induced transition temperatures (S.I.T.T.) compared to the phase transition temperatures (P.T.T.) from Table 3.8. . . . . 42

Table 3.16 Heat capacities ($C_v$, in terms of $k_B$) of all the nanoparticles under the equilibrium criterion and their temperature ranges ($\triangle$T) for both before and after transitions. . . . . 48

Table 3.17 Heat capacities ($C_v$, in terms of $k_B$) of all the nanoparticles under the non-equilibrated criterion and their temperature ranges () for both before and after transitions. . . . . 48

Table 3.18 Heat capacities ($C_v(n)$, in terms of $k_B$) of the InP NPs as a function of number of atoms (n) for before (B) and after (A) the phase transitions under both equilibrium and non-equilibriated criteria. . . . . 55

Table 4.1 Formation energies (in kcal/mol) of O-interstitial configurations in bulk diamond Ge reproduced by ReaxFF$_{present}$, DFT [147] and Experiments [155–157]. . . . . 69

Table 4.2 Heats of formation (in kcal/mol) of diamond Ge, GeO and $GeO_2$ predicted by ReaxFF and DFT [146]. . . . . 71

Table 4.3 Activation energy ($E_a$) of O-diffusion in Ge predicted by ReaxFF$_{present}$, Experiment [155–157] and Tersoff. . . . . 75

Table 4.4 Structural properties of the germania prepared by the advanced version of ReaxFF. . . . . 79

Table 4.5 Formation energy (in kcal/mol) of $O$-vacancy in $a-SiO_2$ computed by DFT [180] and $ReaxFF_{present}$. $E_{form,vac}$ is formation energy of $O$-vacancy in $a-SiO_2$. . . . . 82

Table 4.6 Relative total energies for four different $O$-interstitial configurations in bulk $Si$ computed by $ReaxFF_{SiOH(2010)}$, $ReaxFF_{present}$, DFT [147] and experiments [178, 179]. . . . . 83

Table 4.7 Structural properties of the solid and the liquid phases of $Si$ generated by $ReaxFF_{SiOH(2010)}$ and $ReaxFF_{present}$. . . . . 87

Table 4.8 Structural properties of the silica prepared by $ReaxFF_{SiOH(2010)}$ and $ReaxFF_{present}$. . . . . 93

## LIST OF FIGURES

FIGURES

Figure 2.1 Energy minimization process. . . . . 3

Figure 2.2 Comparison of conjugate gradient and steepest descent methods. . . 5

Figure 2.3 Schematic illustration of canonical ensemble where S subsystems with constant N, V are in thermal equilibrium with the external bath at temperature T. . . . . 11

Figure 2.4 Schematic illustration of an isobaric-isothermal canonical ensemble where S subsystems with constant N are in thermal and pressure equilibrium with the external barometer at temperature T and pressure P. . . . 13

Figure 2.5 Two–dimensional work cell and image cells for the use of periodic boundary conditions. . . . . 15

Figure 2.6 Hierarchy of computational methods. . . . . 18

Figure 3.1 The InP NRs in the ZB and WZ structures (Figure is produced by VESTA software package [110, 111]. From now on the figures generated by VESTA will be notified only by VESTA). . . . . 26

Figure 3.2 The difference between expansion (a) and stretching (b) procedures (VESTA). . . . . 28

Figure 3.3 Observed phase transitions in the ZB NRs under strain at constant and increasing temperatures (VESTA). . . . . 32

Figure 3.4 The differences between the breaking mechanisms of the rock salt (RS), zinc blende (ZB) and wurtzite (WZ) nanorods under strain (VESTA). 32

Figure 3.5 Energy versus MD steps graphs for (a) 6x9 subjected to gradual heating and (b) 5x7 at 600K under equilibrium criteria applied stretching. In graph (a), Energy "jump" around $125x10^4$ MD steps is due to complete transition to the RS phase. In graph (b), the first and the second jumps are due to the complete transition to the RS phase and the NR breaking (around $45x10^4$ and $110x10^4$ MD steps), respectively. . . . . 34

Figure 3.6 In the equilibrium case, both reversible and irreversible transitions were observed while only irreversible transition occurs in non-equilibriated case under strain (VESTA). . . . . 41

Figure 3.7 Compressed 5x7 NR for the -0.5% ratio at 0.7K. The times of compression for each the NR in above figure are (a) 1664 ps, (b)6240 ps, (c) 22256 ps, (d) 22364 ps, (e) 39520 ps and (f) 56160 ps (VESTA). . . . . 45

Figure 3.8 Compressed 5x7 NR for 22048 ps with the -0.5% ratio at 0.7K was stretched back at the same temperature with 0.5% ratio. Total elapsed times for each the NR during compression and stretching back processes are (a) 22048 ps, (b) 27248 ps, (c) 37440 ps and (d) 44928 ps (VESTA). . 45

Figure 3.9 Six types of the InP NPs in the ZB structure with different radii (r) and number of atoms (n) (VESTA). . . . . 46

Figure 3.10 E vs T graphs (a and c) and phase transitions (b and d) for 3-b and 4-b NPs under equilibrium criterion (VESTA). . . . . 49

Figure 3.11 E vs T graphs (a and c) and phase transitions (b and d) for 5-b and 6-b NPs under equilibrium criterion (VESTA). . . . . 50

Figure 3.12 E vs T graphs (a and c) and phase transitions (b and d) for 7-b and 8-b NPs under equilibrium criterion (VESTA). . . . . 51

Figure 3.13 E vs T graphs (a and c) and phase transitions (b and d) for 3-b and 4-b NPs under non-equilibrated criterion (VESTA). . . . . 52

Figure 3.14 E vs T graphs (a and c) and phase transitions (b and d) for 5-b and 6-b NPs under non-equilibrated criterion (VESTA). . . . . 53

Figure 3.15 E vs T graphs (a and c) and phase transitions (b and d) for 7-b and 8-b NPs under non-equilibrated criterion (VESTA). . . . . 54

Figure 3.16 Heat capacity (in $k_B$) vs the number of atoms graph for InP NPs under (a) equilibriate and (b) non-equilibrated criterion. . . . . 55

Figure 4.1 The unitcells of Ge and Si in the diamond phase with lattice constants of 5.66 and 5.47 Å, respectively(VESTA). . . . . 61

Figure 4.2 Schematic cross-sections of (a) the initial configuration of L-LPE system where the insulator is defined to be amorphous $SiO_2$ ($a - SiO_2$), and (b) the crystallization process of a-Ge where the growth initiates at the Si seed, propagates along the stripe. During the growth, the dislocations indicated by blue lines are forced to terminate at the oxide walls by trapping them in the seed window. . . . . 61

Figure 4.3 Ball-stick representation of $O$-interstitial configurations in the unit cell of $Ge$ where green, blue and red represents T, H and BC sites, respectively (VESTA). . . . . 65

Figure 4.4 Ball-stick representation of O-interstitial centers in the supercell. (a) Bond-centered, (b) split, (c) tetrahedral and (d) hexagonal O-interstitial sites in bulk diamond Ge (OVITO). . . . . 65

Figure 4.5 Comparison of asymmetric ($a \rightarrow b \rightarrow d$) and symmetric ($a \rightarrow c \rightarrow d$) transition pathways of O- interstitial in the Ge unitcell. O-atom diffuses between two neighboring bond-centered sites (a and d), and goes through the transition state at a saddle point (b and c) where BC, S and $\Theta$ located on (110) plane represent the bond-centered and split sites, and the angle of O atom with respect to the [001] direction, respectively (VESTA). 66

Figure 4.6 Ball-stick representation of minimum energy migration path of O-interstitial in the Ge unit cell on (110) plane in [001] direction where BC and ATS represent the bond-centered site and the asymmetric transition state occurring at the split site, respectively, derived from Ref. [148] as an input data for the force field training set (VESTA). . . . . 67

Figure 4.7 Initial configuration of Ge matrix containing 14 O-interstitial atoms located at BC sites (OVITO). . . . . 67

Figure 4.9 Equations of state of $GeO_2$ and GeO reproduced by ReaxFF and DFT [146]. . . . . 70

Figure 4.8 Energy of O-interstitial diffusing between two neighboring BC sites in the (110) plane in the Ge matrix, estimated by DFT [148] and $\text{ReaxFF}_{present}$. $\Theta_0$ is the angle of O atom with respect to [001] axis . . . . 70

Figure 4.10 Snapshots taken from the final MD steps of the simulations by $ReaxFF_{present}$ ($a_1$, $b_1$ and $c_1$) and Tersoff ($a_2$, $b_2$ and $c_2$) at the temperatures up to 1400 K where white and red spheres are Ge and O atoms, and green line represents the diffusion trajectory of O atom between the numbered Ge atoms. O atom jumps between the neighboring BC sites regardless of the force field (OVITO). . . . . 72

Figure 4.11 Snapshots taken from the final MD steps of the simulations by $ReaxFF_{present}$ ($a_1$ and $a_2$) and Tersoff ($b_1$ and $b_2$) at 1400 K where white and red spheres are Ge and O atoms, red circles around B and H sites in $a_1$ and $b_1$ are the sites that O atom pass through during the diffusion, and green line in $a_2$ and $b_2$ represents the diffusion trajectory of O atom between the numbered Ge atoms. ($a_1$) ReaxFF results that O atom jumps only between the neighboring BC sites ($b_1$) while Tersoff reproduces the O-diffusion along a pathway between B and H sites at 1400 K (OVITO). . 73

Figure 4.12 Snapshots taken from the final MD steps of the simulations by $ReaxFF_{present}$ ($a_1$ and $a_2$) and Tersoff ($b_1$ and $b_2$) at the temperatures over 1400 K where white and red spheres are Ge and O atoms (OVITO). . 73

Figure 4.13 MSD profiles produced by the advanced version of ($a_1$ and $a_2$) ReaxFF and ($b_1$ and $b_2$) Tersoff at given temperatures. . . . . 74

Figure 4.14 Arrhenius plot of the O-interstitial's diffusion coefficient in Ge computed by the advanced version of ReaxFF, Tersoff and experiments (Reference a: [157], Reference b: [156, 157], Reference c: . . . . . 74

Figure 4.15 Snapshots taken from the MD simulations at given temperatures where green and white balls are Ge atoms initially located in $GeO_2$ and Ge slabs, respectively, and red ball is oxygen atom. $a_1$, $b_1$ and $c_1$ show the MD results based on ReaxFF and the figures in $a_2$, $b_2$ and $c_2$ illustrate the results of the Tersoff-based simulations (OVITO). . . . . 76

Figure 4.16 $GeO_2$ and Ge thicknesses in $GeO_2$/Ge(100) depending on the coordination number, oxidation time and temperature. a and b show the MD results based on ReaxFF and the graphs in c and d display the results of the Tersoff-based simula- tions. . . . . 77

Figure 4.17 Amorphous $GeO_2$ relaxed at 300 K in an NPT ensemble for 0.5 ns. 78

Figure 4.18 Structural characterization of the $GeO_2$ glass. (a) Ge-O, Ge-Ge, and O-O partial RDFs (b) O-Ge-O and Ge-O-Ge BADs and (c) analysis for coordination number distribution of the glass relaxed at 300 K in the NPT ensemble for 0.5 ns. . . . . 78

Figure 4.19 Snapshots taken from the MD simulation performed by $ReaxFF_{Fogarty}$ at 1000 K. (a) The initial configuration of the supercell where O atoms are initially positioned at BC sites and (b) the annealed supercell at 1000 K for 2.5 ns where O atoms are positioned at H and T sites inside the units of honeycomb in the lattice (OVITO). . . . . 82

Figure 4.20 Ball-stick representation of minimum energy migration path of $O$-interstitial in the $Si$ unit cell, derived from Refs. [148,181] as an input data for the force field training set where gray background represents (110) plane in [100] direction. $O$ diffuses by jumping from (a) the right BC site to (h) the left BC site or vice versa. During the diffusion, (e) $O$ atom goes through the asymmetric transition state (ATS) at the S site (VESTA). . . . 84

Figure 4.21 Energy of $O$-interstitial diffusing between two neighboring BC sites in the (110) plane in the $Si$ matrix, estimated by QM [181] and $ReaxFF_{present}$. $\Theta_0$ is the angle of $O$ atom with respect to [100] axis shown in Figure 4.5. $ReaxFF_{present}$ produces an asymmetric transition state at $\Theta_0$=17$^o$ with an energy barrier of 64.8 kcal/mol, showing good agreement with DFT [148]. . . . . 84

Figure 4.22 Snapshots taken from the two-phase MD simulations. (a) Coexistence phase including liquid and solid of $Si$ obtained in the NVT (b) solid/liquid interface moving towards to liquid phase (c) solid/liquid interface moving towards to crystal phase (d) crystal phase completely overtaking liquid phase at 2420 K for 3.4 ns (e) liquid phase filling the box at 2421 K for 5 ns (OVITO). . . . . 86

Figure 4.23 Partial RDFs belonging to the liquid and solid phases of $Si$ . $L-Si_{SiOH(2010)}$ and $S-Si_{SiOH(2010)}$ stand for liquid and solid phases, respectively, generated by $ReaxFF_{SiOH(2010)}$. In the same manner, $L-Si_{present}$ and $S-Si_{present}$ are the labels for $ReaxFF_{present}$. . . . . 87

Figure 4.24 Snapshots taken from the final MD steps of the simulations by $ReaxFF_{present}$ at different target temperatures. The top four snapshots represent the initial configuration of the system from different views, and the bottom four images show the diffusion trajectory of O atom for 3.5 ns with a green line. (a) No diffusion was observed at 1400 K, and O atoms at BC sites vibrate around themselves. (b) At 1425 K, O atom residing in the BC site neighboring 1. and 2. Si atoms hops to the next BC site between 2. and 3. Si atoms, and, during the jumping, O atom goes through the transition state at the S site located above 2. Si atom. (c) At 1800 K, O atom initially being at BC site neighboring 1. and 2. atoms, first, jumps to the BC site between 2. and 3. Si atoms, and then hops the next BC site between 3. and 4. Si atoms. (d) At 2400 K, O diffuses by hoping, first, the BC site between 1. and 2. Si atoms following by the BC sites between 2. and 3. Si atoms, and 3. and 4. Si atoms. Finally, it occupies the BC site between 4. and 5. Si atoms (OVITO). . . . . 89

Figure 4.25 (a) Temperature dependence of the diffusion coefficient computed by both versions of the ReaxFF force field and experiment [191], (b) and (c) MSD profiles at given temperatures where the enumeration with roman numbers refers to indicated regions in (a). The observed trajectory types of $O$ atom during diffusion are as following: ($a_1$) confined, ($b_1$) free, ($c_1$) directed and anomalous diffusion types combined of ($d_1$) directed-confined and ($e_1$) directed-free-confined. The main difference between the trajectories in ($d_1$) and ($e_1$) is that $O$ atoms intermittently moves away from their initial locations in ($d_1$) contrary to $O$ atoms moving back towards their initial positions in ($e_1$). . . . . 90

Figure 4.26 (a) The initial bulk configuration of crystalline $\beta - SiO_2$, (b) $a - SiO_2$ quenched from the liquid state to 300 K and (c) the polyhedral model of $a - SiO_2$ (VESTA). . . . . 92

Figure 4.27 Structural characterizations of $glass_{present}$ and $glass_{SiOH(2010)}$ with superscript $a$. (a) $Si - O$, $Si - Si$, and $O - O$ partial radial distribution functions (b) $O - Si - O$ and $Si - O - Si$ BADs and (c) analysis for coordination number distribution of both glasses quenched from the liquid state to 300 K. . . . . 93

Figure 4.28 $a - SiO_2/Si$ system annealed at temperatures ranging between [300-2400 K] for 500 ps by applying $ReaxFF_{present}$ and $ReaxFF_{SiOH(2010)}$. Snapshots shown in ($a_1$), ($b_1$), ($c_1$), ($d_1$) belongs to the results generated by $ReaxFF_{SiOH(2010)}$. ($a_2$), ($b_2$), ($c_2$), ($d_2$) represents the results reproduced by $ReaxFF_{present}$. Also, ($d_1$) and ($d_2$) illustrate the magnified views of the framed regions with black enclosures at 2400 K (OVITO). . . . . 95

Figure 4.29 Temperature dependence of $O$ solubility and depth profiles in the $Si$ substrate based on $ReaxFF_{present}$ and $ReaxFF_{SiOH(2010)}$ under heat treatment where the label of $ReaxFF_{present(Depth)}$ represents the depth profiling of $O$ generated by the new force field, and the labels of $ReaxFF_{present}$ and $ReaxFF_{SiOH(2010)}$ belong to the $O-$concentration plots. . . . . 96

Figure A.1 Gradually heated ZB NRs. When the ZB NRs were subjected to heating, increasing the temperature by 50K, the phase transitions (ZB->RS) and stacking faults were observed except for the 9x9 NR (VESTA). . . . . 124

Figure A.2 Phase transitions observed in the 4x4 ZB NR under strain for the 5% S.R. (VESTA) . . . . . 125

Figure A.3 Phase transitions in the 4x4 ZB NR under strain for the 10% S.R. At this ratio, the WZ phase occurred at a lower temperature (300K) with respect to the the stretching at the 5% S.R. (500K) in Figure A.2 (VESTA). 126

Figure A.4 Phase transitions in the 5x5 ZB NR under strain for the 5% S.R. The WZ phase was observed under strain at 0.7, 300, 600K and increasing temperatures (VESTA). . . . . 126

Figure A.5 Phase transitions in the 5x5 ZB NR under strain for the 10% S.R. The WZ phase occurred in the 5x5 ZB NR at lower temperatures (0.7 and 300K) than the stretching for the 5% S.R. in Figure A.4, in addition to increasing temperature (VESTA). . . . . 127

Figure A.6 Phase transitions in the 6x6 ZB NR under strain for the 5% S.R. The WZ phase in the 6x6 ZB NR occurred at 0.7, 300, 600K (VESTA). . 127

Figure A.7 Phase transitions in the 6x6 ZB NR under strain for the 10% S.R. The WZ phase was observed at the same temperatures (0.7, 300 and 600K) with the stretching for the 5% S.R. in the Figure A.6 but the WZ regions appeared were more dense at 5% than 10% stretching ratio (VESTA). . . . 128

Figure A.8 Phase transitions in the 7x7 ZB NR under strain for the 5% S.R. The WZ regions appeared in the 7x7 ZB NR at 300, 400K and increasing temperature (VESTA). . . . . 128

Figure A.9 Phase transitions in the 7x7 ZB NR under strain for the 10% S.R. At this ratio, the WZ phase was not observed at 400K because of higher stretching ratio while appearing at this temperature for the 5% ratio in Figure A.8 (VESTA). . . . . 128

Figure A.10Phase transitions in the 8x8 ZB NR under strain for the 5% S.R. The WZ phase occurred at 300 and 600K in the 8x8 ZB NR (VESTA). . . 129

Figure A.11Phase transitions in the 8x8 ZB NR under strain for the 10% S.R. The WZ region was observed in the 8x8 ZB NR only at 300K while this phase occurred at 300 and 600K for the 5% S.R. in Figure A.10 (VESTA). 129

Figure A.12Phase transitions in the 9x9 ZB NR under strain for the 5% S.R. The WZ phase appeared at 300K (VESTA). . . . . 130

Figure A.13Phase transitions in the 9x9 ZB NR under strain for the 10% S.R. The WZ phase was not observed in the 9x9 ZB NR for the 10% S.R. because of the thicker NR and higher stretching ratio (VESTA). . . . . 130

Figure A.14Breaking mechanism for the 4x4, 5x5 and 6x6 ZB NRs under strain for the 5% S.R. (VESTA). . . . . 132

Figure A.15Breaking mechanism for the 7x7, 8x8 and 9x9 ZB NRs under strain for the 5% S.R. (VESTA). . . . . 133

Figure A.16Breaking mechanism for the 4x4, 5x5 and 6x6 ZB NRs under strain for the 10% S.R. (VESTA). . . . . 134

Figure A.17Breaking mechanism for the 7x7, 8x8 and 9x9 ZB NRs under strain for the 10% S.R. (VESTA). . . . . 135

Figure A.18Gradually heated WZ NRs. When the WZ NRs were subjected to heating via increasing the temperature by 50K, interestingly, stacking faults first occurred at the kinks. Due to these kinks, the completely transformed systems were segmented as a result of the stacking faults (VESTA). 137

Figure A.19Expansion and heating procedures were applied to the 7x11 WZ NR in consecutive runs as shown in the figure. Elongation percentages (E.P.) are given for the expanded parts of the NR (VESTA). . . . . 138

Figure A.20Heated non-deformed WZ NRs at constant temperatures to investigate the annealing effect. The heating times (ps) are given for each nanorod (VESTA). . . . . 138

Figure A.21The cooled WZ NRs to observe if the transition was reversible. It was found that the phase transition temperatures and the ratio of kinks' region to the over all area have effect on the reversibility (VESTA). . . . . 139

Figure A.22Cooled WZ NRs were stretched for the 0.5% ratio at 0.7K to see if the cooling process was reversible. The calculations on the thin, average and thick NR specimens showed that the cooled NRs below their phase transition temperatures can completely transform back to the WZ phase under strain (VESTA). . . . . 139

Figure A.23Breaking mechanism in the stretched 3x4, 4x6 and 5x7 WZ NRs at constant and increasing temperatures (inc.temp.) for the 1% S.R. (VESTA). 141

Figure A.24The 3x4, 4x6 and 5x7 WZ NRs were put under strain for the 5% S.R. at constant and increasing temperatures (inc.temp.) to investigate the breaking mechanism of the NRs (VESTA). . . . . 142

Figure A.25The 6x9, 7x11 and 8x13 WZ NRs were put under strain for the 1% S.R. at constant and increasing temperatures (inc.temp.) to analyze the breaking mechanism of the NRs (VESTA). . . . . 143

Figure A.26Breaking mechanisms of the put 6x9, 7x11 and 8x13 WZ NRs under strain for the 5% S.R. at constant and increasing temperatures (inc.temp.) (VESTA). . . . . 144

Figure A.27The 6x9 and 8x13 WZ NRs were put under strain for the 0.5% S.R. at constant temperatures of 600 and 900K (VESTA). . . . . 145

Figure A.28Observed transitions in the stretched 3x4 WZ NR for the 1% S.R. The WZ phase again appeared at 200 and 300K while the phase transition temperature is 200K for the 3x4 NR. Also, reversible transition occurred at 0.7, 200 and 300K (VESTA). . . . . 145

Figure A.29Observed transitions in the stretched 3x4 WZ NR for the 5% stretching ratio. Due to increasing of the S.R. (from 1% to 5%), the WZ phase occurred at lower temperatures (0.7 and 200K) than 1% stretching ratio (0.7, 200 and 300K) in Figure A.29 (VESTA). . . . . 146

Figure A.30Observed transitions in the stretched 4x6 WZ NR for the 1% S.R. While the phase transition temperature is 475K for the 4x6 NR, total transition to the RS phase occurred at 400K (lowering effect). Also the reversible transition occurred at 300K (VESTA). . . . . 146

Figure A.31Observed transitions in the stretched 4x6 WZ NR for the 5% S.R. The WZ phase at lower temperatures (0.7, 300 and 400K) than 5% S.R. (0.7, 300, 400 and 500K as it is shown in Figure A.30) appeared. So it was observed that the occurrence of the WZ phase depends on the stretching ratio (VESTA). . . . . 147

Figure A.32Observed transitions in the stretched 5x7 WZ NR for the 1% S.R. Complete transition was observed at 550K which is below the phase transition temperature (590K). Also the reversible transition occurred at 400, 500 and 550K (VESTA). . . . . 147

Figure A.33Observed transitions in the stretched 5x7 WZ NR for the 5% S.R. Comparing the results of the 1% (Figure A.32) and 5% ratios, it was observed that the ratio of the WZ region to the over all area for the 5% ratio is lower while the WZ phase appears at the same temperatures for both ratios. Also, the reversible transition occurred at 400 and 500K (VESTA). 148

Figure A.34Observed transitions in the stretched 6x9 WZ NR for the 1% S.R. The complete transition occurred below the phase transition temperature (780K) and reversible transition was observed at 500K (VESTA). . . . . 148

Figure A.35Observed transitions in the stretched 6x9 WZ NR for the 5% S.R. Reversible phase transition occurred at 500K and the phase transition temperature was reduced from 780K to 700K under strain (VESTA). . . . . 149

Figure A.36Observed transitions in the stretched 7x11 WZ NR for the 1% S.R. The RS region was observed where the breaking occured at 600K which is below the first observed transition temperature (650K) and reversible phase transition appeared at 700K. Also, the phase transition temperature reduced to 700K under strain while it was normally 830K (VESTA). . . . 149

Figure A.37Observed transitions in the stretched 7x11 WZ NR for 5% S.R. The reversible phase transition was observed at 700K and the RS phase in the breaking region appeared at 600K which is below the 1st observed phase transition temperature. Also, the reducing effect on the phase transition temperature was observed for the 5% ratio (VESTA). . . . . 150

Figure A.38Observed transitions in the stretched 8x13 WZ NR for the 1% S.R. The RS phase appeared at heavily deformed regions where breaking occurred at 600 and 700K which are below the 1st observed transition temperature and the reversible transition occurred at 800K. Also, the total transition to the RS phase was observed at 800K which is below the phase transition temperature of 895K (VESTA). . . . . 150

Figure A.39Observed transitions in the stretched 8x13 WZ NR for the 5% S.R. The RS phase appeared at heavily deformed regions where breaking occurred at 600 and 700K which are below the 1st observed transition temperature and the reversible transition occurred at 800K. Also, the total transition to the RS phase was observed at 800K which is below the phase transition temperature of 895K (VESTA). . . . . 151

Figure A.40Observed transitions in the stretched 4x6, 6x9 and 8x13 NRs for the 0.5% S.R. In the 4x6 NR, while the phase transition temperature was 475K, the reversible transition (WZ->RS->WZ) was observed at 600K and the NR in the WZ phase did not evolve back to the RS phase under further stretching. But this effect was not observed for the 8x13 NR at 900K (VESTA). . . . . 152

Figure A.41Gradually heated 8x13 NR until 900K (22. run) was stretched at 900K for the 1% S.R. to investigate if the transition is reversible (VESTA).. 153

Figure A.42Gradually heated NR until 950K (23. run) that was first stretched for the 1% S.R. and then 8x13 NRs in 23., newly achieved 24. and 25. runs at 950K were cooled (VESTA). . . . . 153

Figure A.43Compressed 4x6 NR for the -0.5% S.R. at 0.7K (VESTA). . . . . 154

Figure A.44Compressed 4x6 NR for the -0.5% S.R. was stretched for the 0.5% S.R. at 0.7K (VESTA). . . . . 154

Figure A.45Compressed 5x7 NR for the -0.5% S.R. at 0.7K (VESTA). . . . . 155

Figure A.46Compressed 5x7 NR for the -0.5% S.R. was stretched for the 0.5% S.R. at 0.7K (VESTA). . . . . 155

Figure A.47Compressed 6x9 NR for the -0.5% S.R. at 0.7K (VESTA). . . . . 156

Figure A.48Compressed 6x9 NR for the -0.5% was stretched for the 0.5% S.R. at 0.7K (VESTA). . . . . 156

Figure A.49Compressed 8x13 NR for the -0.5% S.R. at 0.7K (VESTA). . . . . 157

Figure A.50Compressed 8x13 NR for the -0.5% S.R. was stretched for the 0.5% S.R. at 0.7K (VESTA). . . . . 157

Figure A.51Compressed 4x6 NR with -0.5% S.R. at 300K (VESTA). . . . . 158

Figure A.52Compressed 5x7 NR for the -0.5% S.R. at 300K (VESTA). . . . . 159

Figure A.53Compressed 8x13 NR for the -0.5% S.R. at 600K (VESTA). . . . . 159

Figure A.54Compressed 8x13 NR for the -0.5% S.R. at 900K (VESTA). . . . . 160

Figure B.1 Energy curves for equations of states of three phases of silicon predicted by (a) QM and (b) ReaxFF. . . . . 161

Figure B.2 Energy curves for equations of states of two phases of silica predicted by (a) QM and (b) ReaxFF. . . . . 161

# CHAPTER 1

# INTRODUCTION

Semiconductor nanostructures are considered as the critical components in a wide range of nanotechnological applications owing to their unique structural properties under various conditions such as varying temperature, pressure etc. Molecular modeling based on computational methods is a powerful tool to predict the structural and the dynamic behaviors of semiconductors and their amorphous forms. It plays an important complementary role to the experimental studies in providing a deeper insight into the materials on the atomistic level. The focus of my thesis is the investigation of the mechanical properties of Indium Phosphide and Silicon/Germanium being the significant components of the semiconductor technology via Molecular Dynamics (MD) simulations.

In this thesis, Chapter 2 presents the methods that we used throughout the thesis work. We, first, give a brief introduction to the Polak-Ribiere optimization procedure being one of conjugate gradient energy minimization methods where the detail of steepest descent method is also represented to compare it with the conjugate gradient method. Then, the MD method, the integrating scheme to solve Newton's equation of motion, the ensembles together with the thermostat/barostat, and force fields and their functional formalism are given in detail.

Chapter 3 reports the calculations details, results and discussion regarding the InP nanorods and nanoparticles with a detailed introduction to InP nanomaterials. The section end of this chapter is devoted to our concluding remarks regarding InP nanostructures.

Chapter 4 begins with a comprehensive introduction to the seed-induced L-LPE growth of Ge and gives an overview of the experimental studies reported in the literature.

Then, the computational details, results, and the studies of the ReaxFF force field development for Si/O and Ge/O interactions in the L-LPE are presented in detail. The fruitful discussions made for the force field validation based on our MD simulations take their places in Chapter 4. In a similar way with Chapter 3, last section of this chapter is dedicated to the conclusion regarding the ReaxFF force field development.

As a final part of this thesis, Chapter 5 summarises the main contributions of this thesis to the field, also providing discussions for possible future works.

# CHAPTER 2

# SIMULATION METHODS

This chapter contains the details of energy minimization method, Molecular Dynamics (MD) method, integrating schemes containing Verlet and velocity-Verlet algorithm, ensembles, nonreactive and reactive force fields, and their algorithms.

## 2.1 Molecular Mechanic Energy minimization

Energy minimization is a numerical procedure carried out to determine a minimum energy conformation before the MD simulations. With the application of the energy minimization, an initial conformation dominated by bad interactions such as overlapped atoms achieves one of the stable conformers. The idea behind the minimization is expressed as follows: the geometry of the system changes in a step-wise fashion, starting from the initial structure with higher energy until a global or local minimum on the potential energy surface is reached.

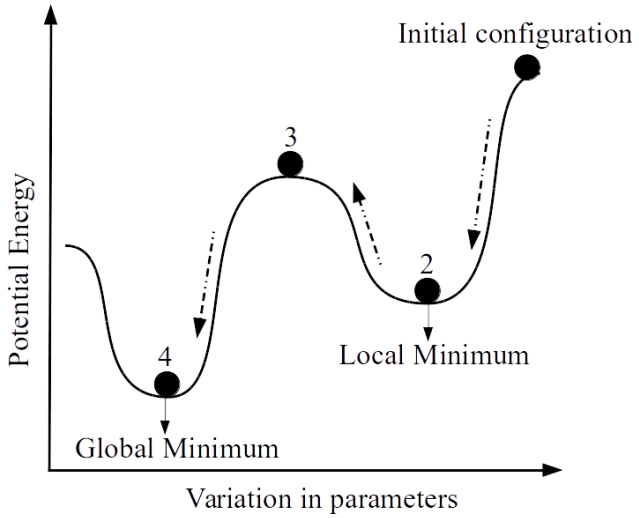


Figure 2.1: Energy minimization process.

As illustrated in Fig. 2.1, during the minimization, initial conformation has higher energy, and its energy reduces until finding its first stable conformer which is the so-called local energy minimum marked by 2 in the figure. Depending on the value of energy minima, the system reaches the nearest stable conformer by overcoming the energy barrier. There are many energy minimization methods facilitating the determination of the stable conformer of the system. The optimization method used in this thesis is Polak-Ribiere CG procedure [1]. This subsection presents the details regarding the algorithm and its implementation. In addition, a brief introduction is given to the Steepest Descent (SD) method [2] to show the superiority of CG method over the SD method.

### 2.1.1 Polak Ribiere Conjugate Gradient and Steepest Descent methods

A common way to find the minimum of a potential function $U(\vec{x})$ is using its derivative or its gradient. Stepeest Descent (SD) and Conjugate Gradient (CG) methods are two line search methods commonly used to minimize $U(\vec{x})$ function. The SD method is a basic line search method, and it is based on the idea that the search direction given by the negative gradient of U(x) function at a given point $\vec{x}$ is the steepest descent direction. In other words, the method repeatedly moves in the steepest direction to the minimum point during the minimization. Consequently, the technique approaches the minimum in a zig-zag manner, where the new search direction is always perpendicular to the previous as is evident from Fig. 2.2. However, its zigzag behavior is usually not the optimal and fastest path towards the minimum. These back-and-forth steps converge very slowly to the minimum, especially, across narrow valleys of the contour as depicted in Fig. 2.2.

The CG method, again, uses the first derivative of the potential function but avoids "undoing" previous works which refer the oscillation back and forth, as it moves toward the minimum. This allows the method to move rapidly to the minimum as illustrated in Fig. 2.2. So that the superiority of the CG method over the SD method comes from the direction chosen in the methods. The CG method uses conjugate search directions for going downhill instead of local minimum search direction used in the SD method. In the CG method, each minimization step is independent of

another, and the direction of each step should be conjugate to each other.

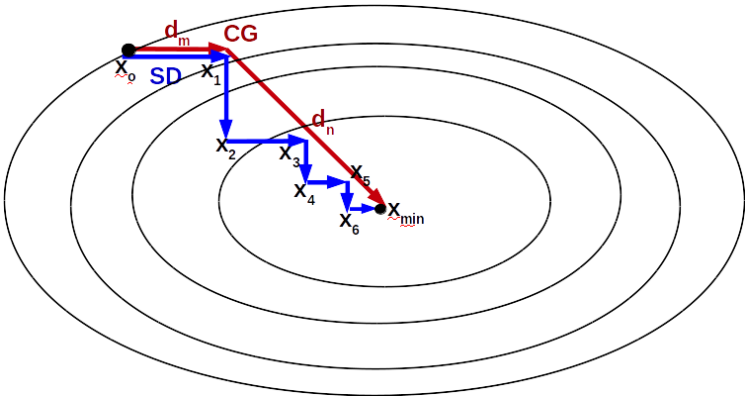


Figure 2.2: Comparison of conjugate gradient and steepest descent methods.

To explain the CG algorithm, let's consider a quadratic scalar field f which goes from $R^n \rightarrow R$;

$$f(x) = c - bx^T + \frac{1}{2}xHx^T \tag{2.1}$$

where $c \in R$, $b \in R^n$ and $H > 0 \in R^{n \times n}$ and $\boldsymbol{H}$ is a $n \times n$ Hessian matrix of the second-order partial derivatives of the scalar field as it is shown in Eqs. 2.3 and 2.4

$$\nabla f(x) = b + Hx \tag{2.2}$$

$$\Delta f(x) = H \tag{2.3}$$

$$Hf(x) = \begin{bmatrix} \triangle_{x_1x_1} f(x) & \triangle_{x_1x_2} f(x) & . & . & \triangle_{x_1x_n} f(x) \\ \triangle_{x_2x_1} f(x) & \triangle_{x_2x_2} f(x) & . & . & \triangle_{x_2x_n} f(x) \\ . & . & . & . & \\ . & . & . & . & \\ \triangle_{x_nx_1} f(x) & \triangle_{x_nx_2} f(x) & . & . & \triangle_{x_nx_n} f(x) \end{bmatrix} \tag{2.4}$$

It is also assumed to be symmetric satisfying $H^T = H$ condition and a positive definite matrix with the positive eigenvalues where the scalar field is a "concave up".

If:

$$\nabla f(x^*) = 0 \Longleftrightarrow \Delta f(x^*) > 0$$

then $x^*$ is a minimizer.

Then we set $f(x^*)$ to 0

$$f(x^*) = 0 Ax^* = b \tag{2.5}$$

$$d_n^T A d_m = 0 (n > m >= 0) \tag{2.6}$$

where each $d_n$ is chosen to be conjugate to all previous search directions with respect to *H* matrix.

The resulting search directions being linearly independent can be obtained from the following algorithm:

$$d_n = g_n + \gamma_n d_{n-1} \tag{2.7}$$

where the coefficient $\gamma$ described by Polak-Ribiere for the CG method as follows:

$$\gamma_n = \frac{(g_n - g_{n-1}) g_n}{g_{n-1} * g_{n-1}} \tag{2.8}$$

As evident from Eqs. 2.7 and 2.8, the gradient search direction, $d_n$ can be determined using only the knowledge of $d_{n-1}$, $g_n$ and $g_{n-1}$. For more details of the CG method's algorithm, the reader is referred to Refs. [1, 3–5]

## 2.2 Molecular Dynamics

MD simulation first conducted by Beni Alder and Tom Wainwright in the late 1950s [6] is a molecular modeling method that explores the real dynamics of a complex system such as condensed phase by computing the trajectory of the individual atoms in the system. The basic idea lying behind the MD method is that of numerically

integrating Newton's equation of motion for a many-particle system. In the elementary classical physics, the dynamics of a single object (in a simplest case, atom) with mass m moving with a constant acceleration is governed by Newton's second law of motion written as the second order differential equation for time-dependent position of the particle, (t):

$$\frac{d^2\vec{r}(t)}{dt^2} = \frac{1}{m}\vec{F}[\vec{r}(t), \frac{d\vec{r}(t)}{dt}, t] \tag{2.9}$$

where r is the position of the particle and F denotes the force acting on the atom during the motion. We can also simplify Eq. 2.9 by rewriting the two-coupled first order equations emanating from Euler's method to demonstrate the relation between the position, velocity, and acceleration of the object.

$$\dot{\vec{v}}(t) = \vec{a}(t) \tag{2.10}$$

$$\dot{\vec{r}}(t) = \vec{v}(t) \tag{2.11}$$

where $\vec{v}(t)$ and $\vec{a}(t)$ represent velocity and acceleration of the atom at time t. MD, being a deterministic method, calculates the position of particle, velocity and acceleration at any instant time of t.

In this work, we were interested in conservative fields depending on the position of the atom. In case that the external forces are absent the total energy of the system is conserved. This leads to obtaining a conservative force exerted on the individual atom. Hence, the change in the potential energy can be associated to the conservative force as follows:

For the motion of N interacting atoms,

$$\vec{F_i} = -\vec{\nabla}_i U(\vec{r}_1, \vec{r}_2, \vec{r}_3, ..., \vec{r}_N) \tag{2.12}$$

where $r_i$ is the position of $i^th$ particle, $U(r_i)$ is the potential energy of the system consisted of N interacting atoms located at the position of $\vec{r}_i$, $\vec{F_i}$ is the total force acting on the $i^th$ particle.

### 2.2.1 Integrating Scheme

The Newton's equations of motion displayed in Eq. 2.9 and 2.10 can be integrated at each time step by means of the integrating scheme enabling to evaluate the trajectory of particles in the system. Several integrating schemes are available for use in MD simulations for this purpose such as Verlet [7, 8], Velocity-Verlet [7], Leap-frog, Beeman algorithm [9], Predictor-corrector [10] etc. Each of the algorithms is based on Taylor's series expansion to extrapolate the position and velocity at any time. Verlet and velocity-Verlet algorithms used in this thesis are detailed as follows:

#### 2.2.1.1 Verlet algorithm

The Verlet algorithm first implemented by Loup Verlet in MD simulation [7, 8] is the most frequently used and cost-effective integrating scheme. It can be derived by writing the Taylor expansion for backward and forward positions in time, $r(t + \Delta t)$ and $r(t - \Delta t)$, respectively, under consideration that a particle propagates by a time step, $\Delta t$ :

The position of particle at a later time $\Delta t$ is written as:

$$r(t + \Delta t) = r(t) + \dot{r}(t)\Delta t + \ddot{r}(t)\frac{\Delta t^2}{2} + \dddot{r}(t)\frac{\Delta t^3}{6} + O(\Delta t^4) \tag{2.13}$$

Substituting Equations 2.10 and 2.11 and replacing the acceleration with the force, the formula becomes in the following form:

$$r(t + \Delta t) = r(t) + v(t)\Delta t + \frac{F(t)}{m}\frac{\Delta t^2}{2} + \dddot{r}(t)\frac{\Delta t^3}{6} + O(\Delta t^4) \tag{2.14}$$

The backward position $r(t - \Delta t)$ is,

$$r(t - \Delta t) = r(t) - v(t)\Delta t + \frac{F(t)}{m}\frac{\Delta t^2}{2} - \dddot{r}(t)\frac{\Delta t^3}{6} + O(\Delta t^4) \tag{2.15}$$

When we sum up 2.14 and 2.15 and move the term of $r(t - \Delta t)$ to the righ hand side

of the formula:

$$r(t + \Delta t) = 2r(t) - r(t - \Delta t) + \frac{F(t)}{m}\Delta t^2 + O(\Delta t^4) \tag{2.16}$$

This equation is a core of the Verlet algorithm. As is evident from 2.16, the Verlet algorithm does not use the velocity of the particle to determine the position at the next time step. The knowledge of velocities are not stored in the time evolution. In addition, the order $O(\Delta t^4)$ is expressed as truncating error and plays a crucial role in the determination of the accuracy of the results. Smaller time step leads to the more accurate approximation to the equation of motion in the MD simulations. However, in the course of the simulation, we need to know the velocity of the particle to compute the kinetic energy of the system, so that the conservation of the total energy can be controlled which is one of the most important tests to verify that a MD simulation is proceeding correctly, and the temperature being a macroscopic property can be computed. It can be derived indirectly from the trajectories belonging to the previous and next runs.

Subtracting 2.14 and 2.15 and dividing both sides by $\Delta t$, the velocity is as follows:

$$v(t) = \frac{r(t + \Delta t) - r(t - \Delta t)}{2\Delta t} + O(\Delta t^2) \tag{2.17}$$

The disadvantage of the Verlet algorithm can be seen from this equation in terms of the memory consumed in the simulation. To determine the velocity of the particle at any time, the system needs to store the knowledge of both previous and current runs in the memory. In addition, we can not achieve the position and velocity, simultaneously, using the Verlet algorithm.

#### 2.2.1.2 Velocity-Verlet algorithm

The velocity-Verlet integrating scheme based on the following two equations, eliminates the disadvantages arising from the Verlet algorithm.

$$r(t + \Delta t) = r(t) + [v(t) + a(t)\frac{\Delta t}{2}]\Delta t \tag{2.18}$$

$$v(t+\Delta t) = v(t) + \frac{a(t)}{2}\Delta t + \frac{a(t+\Delta t)}{2}\Delta t \tag{2.19}$$

where a(t) is equal to $\frac{F(t)}{m}$

This algorithm uses the velocity directly so that it provides the information for positions and velocities, simultaneously. However, it requires to store the accelerations at the current and next runs which is impractical for the memory usage as is evident from Eq. 2.19. To avoid the memory consumption, the velocity-Verlet algorithm can be expressed in terms of the velocity at half time step:

By defining

$$v(t+\frac{\Delta t}{2}) = v(t) + a(t)\frac{\Delta t}{2} \tag{2.20}$$

for notational convenience, Eq. 2.17 and Eq. 2.18 take the following forms:

$$r(t+\Delta t) = r(t) + v(t+\frac{\Delta t}{2})\Delta t \tag{2.21}$$

$$v(t+\Delta t) = v(t+\frac{\Delta t}{2}) + a(t+\Delta t)\frac{\Delta t}{2} \tag{2.22}$$

With the restatement of Eqs. 2.20-2.22, the implementation of this algorithm is as follows:

- Given r(t) and v(t) at one time, compute a(t) as a function of r(t).
- Calculate the velocity at half time step using a(t) and v(t) as in Eq. 2.22
- Update the position to $r(t+\Delta t)$ with r(t) and $v(t+\frac{\Delta t}{2})$ using Eq. 2.21.
- Compute $a(t+\frac{\Delta t}{2})$ as a function of $r(t+\frac{\Delta t}{2})$.
- Update the velocity to $v(t+\Delta t)$ with $a(t+\frac{\Delta t}{2})$ and $v(t+\frac{\Delta t}{2})$ using Eq. 2.22.

This implementation requires less memory, and the algorithm does not need anymore to store the acceleration at two different time steps. If we generalize this implementation to a system including N particles in three dimensions, this algorithm requires

only 9N memory locations for saving 3N positions, 3N velocities and 3N accelerations for the current run. More detailed information regarding the algorithm of the integrators can be found in Refs. [11, 12]

### 2.2.2 Ensemble Theory

MD method can provide the trajectory information including the acceleration, velocity, and position of the particle at any instant time. However, the conversion between the trajectory information and the macroscopic properties such as pressure, energy, temperature, etc. is required to emulate the experimental studies using MD simulations. By using the "ensemble theory" of the statistical mechanics introduced by J. Willard Gibbs [13], a connection between the microscopic dynamics and its counterparts on the macroscopic level can be established by statistically averaging the microsystems to reach the time average of the macrosystem. Ensembles used in this thesis for molecular modeling are detailed below.

#### 2.2.2.1 Canonical Ensemble (NVT):

This ensemble is an assembly of microstates each of which has the same number of particles (N), same volume (V) and are at same temperature (T). In this ensemble, the subsystems are brought to thermal equilibrium with the heat reservoir at temperature T by allowing the energy exchange between the systems as illustrated in Fig. 2.3.

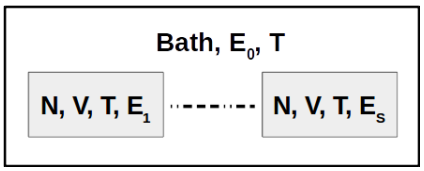


Figure 2.3: Schematic illustration of canonical ensemble where S subsystems with constant N, V are in thermal equilibrium with the external bath at temperature T.

To keep the temperature at the specified value, several methods are used in NVT simulations such as Berendsen thermostat, Nosé-Hoover thermostat, Anderson thermostat, etc. In this thesis, Berendsen [14] and Nosé-Hoover [15–17] thermostats were used to control the system's temperature.

**Berendsen Thermostat:** Using Berendsen thermostat [14], each subsystem is coupled to the external bath with a constant temperature. Rescaling the velocities at each time step also allows altering temperature to the desired value. To compute the instantaneous value of the temperature using the kinetic energy the following equation is used:

$$\sum_{i}^{N} \frac{|p_i|^2}{2m_i} = \frac{k_b T}{2}(3N - N_c) = \frac{k_b T}{2} N_{df} \tag{2.23}$$

where $N_{df}$ is number of degrees of freedom, $N_c$ is number of constraints.

$$T = \sum_{i}^{N} \frac{|p_i|^2}{m_i N_{df} k_b} = \sum_{i}^{N} \frac{m_i {v_i}^2}{N_{df} k_b} \tag{2.24}$$

The following equation gives a relationship between the rate of the temperature change and the temperature difference between the heat reservoir ($T_{bath}$) and the system ($T_{system}$).

$$\frac{dT(t)}{dt} = \frac{1}{\tau}(T_{bath} - T_{system}(t)) \tag{2.25}$$

where $\tau$ is a coupling constant regulating how tightly the subsystems and the reservoir are coupled with each other. If the value of $\tau$ is small, we can say that the both bath and subsystem are strongly coupled. In the large coupling constant, they are called as weakly coupled systems, If the coupling constant is chosen a very high value ($\tau \to \infty$), the systems behave like independent and isolated systems, regardless of the thermostat, as if in an Micro canonical Ensemble (NVE) ensemble instead of an NVT ensemble.

**Nosé-Hoover Thermostat:** Nosé-Hoover thermostat is the extended system method introduced by Nosé [15, 16] and Hoover [17], and treats the heat bath as a part of the system by introducing a fictitious heat reservoir. By using Nosé-Hoover thermostat, an artificial friction term is introduced in the equation of motion to control the energy transfer between the heat bath and the system so that to bring the temperature at the desired value.

The equations of motion in 3D are:

$$\frac{d^2 r_i(t)}{dt^2} = \frac{F_i}{m_i} - \xi \frac{dr_i}{dt} \tag{2.26}$$

$$\frac{d\xi(t)}{dt} = \sum_{i=1}^{N} \frac{1}{Q} \Big[ \frac{{p_i}^2}{2m_i} - \frac{3N+1}{2} k_B T \Big] \tag{2.27}$$

where $\xi$ is the friction coefficient and Q is the mass of the "artificial heat bath"

Small Q values cause unphysical energy fluctuations and equilibration problem during the simulations. For larger Q values, the ensemble approaches to the NVE ensemble by coupling the system very weakly to the heat bath.

#### 2.2.2.2 Isobaric-Isothermal Ensemble (NPT):

Akin to the NVT ensemble, this ensemble, once again, considers the constant number of particle (N) besides constant temperature, but the volume can change so as to bring the system at thermal and pressure equilibriums by driving system's internal pressure towards the external pressure. Fig. 2.4 illustrates the subsystem and a pressure barometer being under thermal and pressure equilibrium.

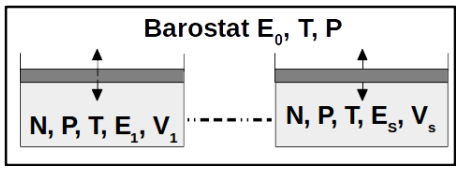


Figure 2.4: Schematic illustration of an isobaric-isothermal canonical ensemble where S subsystems with constant N are in thermal and pressure equilibrium with the external barometer at temperature T and pressure P.

The volume fluctuation can be correlated to the isothermal compressibility by following equation:

$$\kappa = -\frac{1}{V} \Big( \frac{\partial V}{\partial P} \Big)_T \tag{2.28}$$

Similar to the NVT ensemble, there are many barostats facilitating to maintain the pressure at the specified value such as Berendsen, Parrinello-Rahman, Nosé-Hoover etc. The barostats used in this thesis are Berendsen and Nosé-Hoover.

**Berendsen barostat:** In a similar manner with the Berendsen thermostat, the system is coupled to a barostat with constant pressure. The relationship between the rate of the pressure change and the pressure differences between the system and the heat bath is governed by the following equation.

$$\frac{dP(t)}{dt} = \frac{1}{\tau_p}(P_{bar} - P_{system}(t)) \tag{2.29}$$

where $\tau_p$ is a coupling constant used to adjust the strength of the coupling, $P_{bar}$, and $P_{system}$ are the barostat and system pressures, respectively. Weak-coupling scheme can be created by large $\tau_p$ value (or vice versa), which means that the barostat is not a function to control the pressure.

**Nosé-Hoover barostat:** Analogous to Nosé-Hoover thermostat algorithm, the pressure is controlled by a fictitious barostat acting through a "friction" process.

### 2.2.3 Periodic Boundary Conditions

Periodic boundary conditions imposed on the simulated system enable the MD method to provide the mechanic insight into the experiment by duplicating a series of actual system being a primitive cell of an infinite periodic lattice as illustrated in Fig. 2.5. In this approximation, if the particle leaves the box, its image in the neighboring box enters from the opposite side. To increase computational efficiency, a cut-off radius is determined around each particle so that only short-range interactions for the particles within this distance are considered and the energy contributions are truncated beyond the cut-off distance.

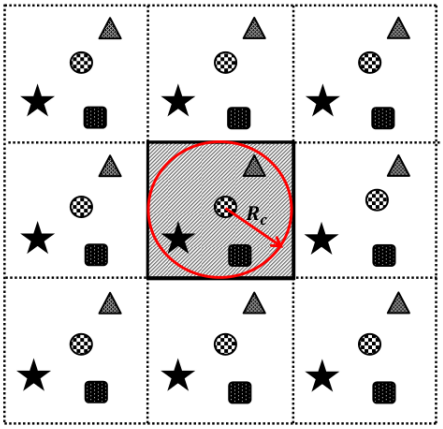


Figure 2.5: Two–dimensional work cell and image cells for the use of periodic boundary conditions.

## 2.3 Force Fields and Potential Energy functions

### 2.3.1 Branicio Potential

The interaction potential based on Vashishta et al.' work on semiconductors and ceramic materials [18] is used for the calculations. The potential parameters (being courtesy of Branicio) were optimized by Branicio et al. [19] against experimental data such as lattice constants, cohesive energy, melting temperature, bulk modulus; as well as theoretical data of energy, volume, bulk modulus obtained via ab-initio calculation. The potential energy function comprises two- and three-body interaction terms:

$$U = \sum_{i<j}^{N} U_{ij}^{(2)}(r_{ij}) + \sum_{i,j<k}^{N} U_{ijk}^{(3)}(\vec{r_{ij}}, \vec{r_{ik}}) \tag{2.30}$$

where $j \neq i, k \neq i$, N is number of atoms, $\vec{r_i}$ is the position of $i_{th}$ atom, $\vec{r_{ij}} = \vec{r_i} - \vec{r_j}$ and $r_{ij}$ is magnitude of vector $\vec{r_{ij}}$.

Two-body term is

$$U_{ij}^{(2)}(r_{ij}) = \frac{H_{ij}}{r^{\eta_{ij}}} + \frac{Z_i Z_j}{r} e^{-\frac{r}{\lambda_1}} + \frac{D_{ij}}{r^4} e^{-\frac{r}{\lambda_4}} - \frac{w_{ij}}{r^6} \tag{2.31}$$

where $H_{ij}$ is a steric repulsion term, $\eta_{ij}$ is the exponent of the steric repulsion term, $Z_i$ and $Z_j$ are the effective charges, $D_{ij}$ is the strength of the charge-dipole attraction,

$w_{ij}$ is the van der Waals interaction strength, $\lambda_1$ and $\lambda_4$ are the screening lengths for the Coulomb and charge dipole terms, respectively.

The strength of the steric repulsion, $H_{ij}$, and the charge-dipole, $D_{ij}$ for the cross-interactions can be computed by applying mixing rule as following:

$$H_{ij} = A(\sigma_i + \sigma_j)^{\eta_{ij}} \tag{2.32}$$

$$D_{ij} = \frac{\alpha_i Z_j^2 + \alpha_j Z_i^2}{2} \tag{2.33}$$

where *A* is the repulsion strength, $\sigma_i$ and $\sigma_j$ are ionic radii, and $\alpha_i$ and $\alpha_j$ are the electronic polarizabilities of $i_{th}$ and $j_{th}$ atoms. For computational efficiency the screening lengths, $\lambda_4$ and $\lambda_1$, were set to 2.75 Åand 4.5 Å, respectively and cut-off distance,$r_c$, was determined to be 6.0 Å. The two-body potential expression is shifted as follows:

$$\mathrm{U}_{ij}^{(2)}(r)_{shifted} = \begin{cases} U_{ij}^{(2)}(r) - U_{ij}^{(2)}(r_c) - (r - r_c)(\frac{dU_{ij}^{(2)}(r)}{dr})_{r=r_c}, & r \leq r_c \\ 0, & r > r_c \end{cases} \tag{2.34}$$

In addition to the two-body term of the potential, the three-body term is also included into the potential expression to describe all the interatomic interactions in InP. The three-body term including the description of the covalent bond bending and stretching is defined by the following equation in terms of spatial and angular dependency:

$$U_{ijk}^{(3)}(\vec{r_{ij}}, \vec{r_{ik}}) = \Gamma(r_{ij}, r_{ik})\Lambda(\theta_{ijk}) \tag{2.35}$$

where

$$\Gamma(r_{ij}, r_{ik}) = B_{jik} exp(\frac{\gamma}{r_{ij} - r_0} + \frac{\gamma}{r_{ik} - r_0})\Theta(r_0 - r_{ij})\Theta(r_0 - r_{ik}) \tag{2.36}$$

and

$$\Lambda(\theta_{jik}) = \frac{(cos\theta_{jik} - cos\theta_0)^2}{1 + C(cos\theta_{jik} - cos\theta_0)^2} \tag{2.37}$$

Here $B_{jik}$, $\theta_{jik}$, $\theta_0$, $C$ and $r_0$ are the strength of the three-body interaction, the angle formed by $r_{ij}$ and $r_{ik}$, the covalent bond angle, the three-body saturation parameter and the three-body range, respectively. $\Theta(r_0 - r_{ij})$ is the step function and expressed as follows:

$$\Theta(x) = \begin{cases} 1, & x \leq 0 \\ 0, & x > 0 \end{cases} \tag{2.38}$$

The potential parameters used in our MD simulations are displayed in Table 2.2

Table 2.1: The parameters of the InP interaction potential. Z, $\alpha$, $\sigma$ are the effective ionic charge, the electronic polarizability and the ionic radius. $\eta$, $w$ are the steric repulsion exponent and the van der Waals strength. $B$, $\lambda_1$ and $\lambda_4$ are the three-body strength and the screening lengths for Coulomb and charge–dipole interactions, respectively.

| | Z(e) | $\alpha(A^3)$ | $\sigma(A)$ |
|---|---|---|---|
| In | 1.21 | 0.0 | 1.1000 |
| P | -1.21 | 2.5 | 1.4412 |

| | $\eta$ | $w(JA^6)$ |
|---|---|---|
| In-In | 7.0 | 0.0 |
| In-P | 9.0 | 43.276x$10^{-18}$ |
| P-P | 7.0 | 0.0 |

| | $B(J)$ |
|---|---|
| In-P-In | $6.969x10^{-19}$ |
| P-In-P | $6.969x10^{-19}$ |

Table 2.2: The parameters of the InP interaction potential. $r_c$, $A$, $r_0$, $\gamma$, $\theta_0$ and $C$ are the two-body cutoff radius, the repulsion strength, the three-body range, exponent, bond angle and saturation parameter, respectively.

| | |
|---|---|
| $\lambda_1(A)$ | 4.5 |
| $\lambda_4(A)$ | 2.75 |
| $r_c(A)$ | 6.0 |
| $A(J)$ | $1.7573x10^{-19}$ |
| $r_0(A)$ | 3.55 |
| $\gamma(A)$ | 1.0 |
| $\theta_0(deg)$ | 109.47 |
| $C$ | 7.0 |

The molecular dynamics program used for investigation of the InP nanostructures is

based on the reversible extended molecular dynamics procedures proposed by Martyna et al. [20].

### 2.3.2 Reactive Force fields

A reactive force field facilitates to simulate the chemical reactions by describing the bond breaking/formation between particles. Unlike non-reactive potentials considering the static bond-assumption in the simulations, they can be utilized to simulate transition states with corresponding energy barrier accurately. Thus, they help to bridge between the non-reactive force fields and quantum methods as illustrated in Fig. 2.6 which gives a neat overview on the multi-scale simulation methods used in the molecular modeling which span several orders of time and length ranging from quantum mechanics to finite element methods at macro scales.

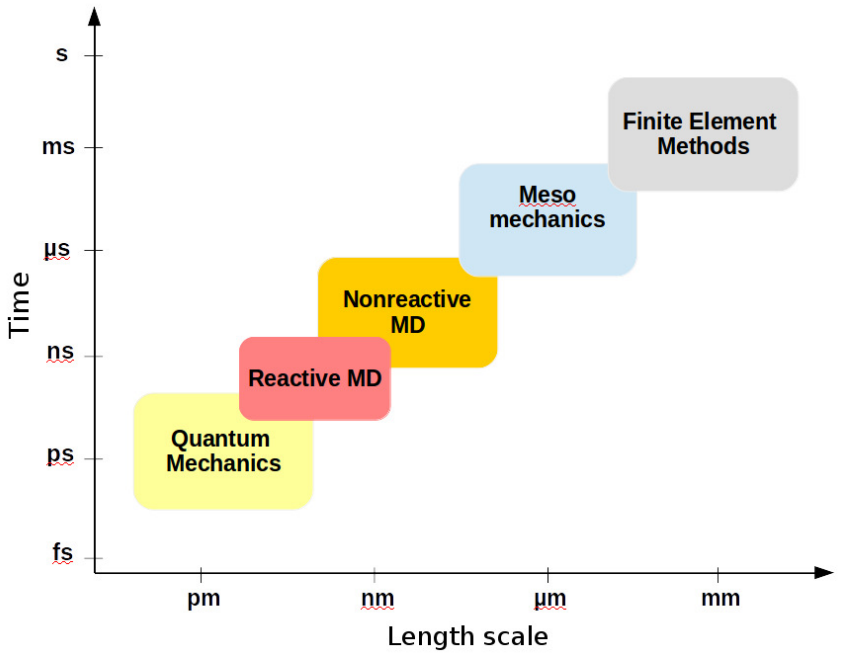


Figure 2.6: Hierarchy of computational methods.

Even though they have more computational cost than non-reactive methods, they provide more realistic and accurate results close to QM calculations due to bond information updated at each iteration. Tersoff potential and the ReaxFF reactive force field applied in this thesis can be shown as commonly used reactive force field in literature, and their details are presented as follows:

#### 2.3.2.1 The Tersoff Potential

Tersoff empirical inter-atomic potential is feasible to calculate the structure and energetics of multicomponent systems and has already been widely used in various applications for Si, Si-Ge, Si-O, Ge and Si-C systems [21–28]. The potential energy computed by using the atomic positions of a system is given by [29]:

$$E = \sum_i E_i = \sum_{i<j} V_{ij} \tag{2.39}$$

Within the Tersoff model, the form of the energy consists of an attractive ($f_A$) and a repulsive ($f_R$) pair potentials.

$$V_{ij} = f_c(r_{ij})[a_{ij} f_R(r_{ij}) + b_{ij} f_A(r_{ij})] \tag{2.40}$$

where $a_{ij}$depends on the local electronic density, $r_{ij}$ is the distance between the atoms *i* and *j* and $f_c$ is

$$f_c(r) = \begin{cases} 1, & r < R \\ \frac{1}{2} + \frac{1}{2}\cos[\pi \frac{(r-R)}{S-R}], & R < r < S \\ 0, & r > S \end{cases} \tag{2.41}$$

a smooth cut-off function. *R* and *S* are used to control the range of interactions. $f_A$ and $f_R$ are defined as:

$$f_R(r_{ij}) = Aexp(-\lambda_1 r) \tag{2.42}$$

$$f_A(r_{ij}) = -Bexp(-\lambda_2 r) \tag{2.43}$$

where *A* and *B* are defined as bond order terms. The $b_{ij}$ term

$$b_{ij} = (1 + \beta^n \zeta_{ij}^n)^{-1/2n} \tag{2.44}$$

denotes that the strength of each bond depends on the local environment, with

$$\zeta_{ij} = \sum_{k(\neq i,j)} f_c(r_{ik}) g(\theta_{ijk}) exp[\lambda_3^3 (r_{ij} - r_{ik})^3] \tag{2.45}$$

$$g(\theta) = 1 + c^2/[d^2 + (h - cos\theta)^2] \tag{2.46}$$

$$n_{ij} = \sum_{k(\neq i,j)} f_c(r_{ik}) exp[\lambda_3^3 (r_{ij} - r_{ik})^3] \tag{2.47}$$

$\theta_{ijk}$ is defined as the angle between the lines connecting atoms *i,j* and *j,k*. The parameters for the interaction between different type of atoms can be calculated using the Tersoff mixing rules [30, 31]:

$$R_{ij} = (R_i R_j)^{1/2} \tag{2.48}$$

$$S_{ij} = (S_i S_j)^{1/2} \tag{2.49}$$

$$\mu_{ij} = (\mu_i + \mu_j)/2 \tag{2.50}$$

$$\lambda_{ij} = (\lambda_i + \lambda_j)/2 \tag{2.51}$$

$$A_{ij} = (A_i A_j)^{1/2} \tag{2.52}$$

$$B_{ij} = \chi_{ij} (B_i B_j)^{1/2} \tag{2.53}$$

The parameters $R_{ij}, S_{ij}, \mu_{ij}, \lambda_{ij}, A_{ij}$ and $B_{ij}$ can be expressed by the fitted parameters for the individual atoms such as $B_i, R_i, \mu_i, A_i$. $\chi_{ij}$ in Eq. 2.53 is used to adjust the strength of heteropolar bonds.

#### 2.3.2.2 The ReaxFF Reactive Force Field

The ReaxFF method is developed by van Duin et al. [32, 33] and it has successfully described the covalent, ceramic and metallic materials and their interfaces. It is based on bond-order dependent concept, as proposed by Abell [34], Tersoff [35, 36] and Brenner [37] to allow for a smooth transition from non-bonded to bonded systems. The potential energy of the system given in Eq. 2.54 is expressed as sum of the partial contributions of bond order dependent and non-bonded energy terms, and basically consists of bond ($E_{bond}$), angle ($E_{angle}$), torsion ($E_{torsion}$) and overcoordination (($E_{over}$)) energies to be bonded terms, and van-der waals ($E_{vdWaals}$) and coulomb interactions ($E_{coulomb}$) to be non-bonded terms. Depending on the simulation, extra term ($E_{extra_term}$) such as conjugate, under coordination, penalty, lone-pair etc is added to the potential energy function.

$$E_{system} = E_{bond} + E_{over} + E_{angle} + E_{tor} + E_{vdWaals} + E_{coulomb} + E_{extra_term} \quad (2.54)$$

where bonded terms depend on bond-order which in turn is determined via interatomic distances from the equation:

$$BO_{ij} = BO_{ij}^{\sigma} + BO_{ij}^{\sigma} + BO_{ij}^{\pi\pi} \quad (2.55)$$

where there are distinct differences between contributions from sigma, pi and double pi bonds,

$$BO_{ij}^{\sigma} = exp\left[P_{bo1}\left(\frac{r_{ij}}{r_o^{\sigma}}\right)^{P_{bo2}}\right] \quad (2.56)$$

$$BO_{ij}^{\pi} = exp\left[P_{bo3}\left(\frac{r_{ij}}{r_o^{\pi}}\right)^{P_{bo4}}\right] \quad (2.57)$$

$$BO_{ij}^{\pi\pi} = exp\left[P_{bo5}\left(\frac{r_{ij}}{r_o^{\pi\pi}}\right)^{P_{bo6}}\right] \quad (2.58)$$

where $BO_{ij}$ and $r_{ij}$ represent the bond order and the interatomic distance between the $i^{th}$ and $j^{th}$ atom respectively. The $r_0$ terms correspond to equilibrium bond

lengths, and $P_{b0}$ terms are fitted bond parameters. The bond-order is continuously updated in order to allow formation and breaking of chemical bonds in the course of dynamics, which is also the main difference between the ReaxFF and other force fields. This feature ensures a continuous energy landscape during the simulations as a consequence of that the energy contributions of the bond-dependent terms disappear upon bond dissociation. Non-bonded interactions including Coulomb ($E_{coulomb}$) and van der Waals ($E_{vdWaals}$) energy terms are calculated for every iteration, regardless of connectivity. For the van der Waals interactions, the ReaxFF uses a distance-corrected Morse-potential to define the short-range interactions accurately. Coulomb energy is calculated by employing the Electronegativity Equalization Method [38] to avoid any excessive short-range nonbonded interactions by the inclusion of a shielding term. For more details of the ReaxFF energy formalism, the reader is referred to Refs. [32, 33, 39, 40].

#### 2.3.2.3 The ReaxFF Force Field Parametrization Process

During the parametrization process, the force field parameters included in the potential terms are optimized against the QM and/or literature values by using a single-parameter search optimization method. With this method, the parameters are determined by minimizing the following sum of the squared error between ReaxFF values and QM data until ReaxFF values and the QM data reach a compromise during the training.

$$Error = \sum_{i=1}^{n} \left[ \frac{(x_{i,QM} - x_{i,ReaxFF})}{\sigma} \right]^2 \tag{2.59}$$

where $x_{QM}$ and $x_{ReaxFF}$ are the Quantum mechanical and the ReaxFF calculated value, respectively. $\sigma$ is the accuracy value determined in the training set.

# CHAPTER 3

# SIMULATIONS OF INDIUM PHOSPHIDE NANOMATERIALS

## 3.1 Introduction

Indium phosphide (InP) nanomaterials have gained increasing attention over the past decades due to their unique properties. In particular, InP nanorods (NRs) and nanoparticles (NPs) have a wide range of application field in the semiconductor technology. Recent experiments prove InP NRs' superiority over the InP planar devices in photocurrent density [41–43] and open circuit voltage [41, 42], in addition to possessing the low surface coverage advantage. Their excellent absorption also enables them to operate even with incident light at very small angles [43,44]. Moreover, their efficient utilization in decreasing the consumption of semiconductor materials, so that, reducing the need for anti-reflective coatings [45], designates them as sought components for highly efficient and cheaper solar cells [46,47]. The charge carriers can be manipulated through the utilization of heterostructures composed of different types of the NRs to manufacture high-performance devices [48, 49]. In this regard, the InP NRs have been used in various devices such as bipolar transistors, modulation-doped high-mobility field effect transistors, multijunction photovoltaic structures [45], quantum dots [50–52] and core-shell structures [53]. The heterostructured InP NRs are also promising candidates for high-speed electron [54], optoelectronic devices [55], photodetectors [56], waveguides [57] and like. The experimental works [45,58–61] report that the lattice mismatches are significantly reduced in heterostructures based on the InP NRs, since the NRs can treat the stress-induced lattice mismatch by relaxing via expansion or contraction mechanisms in contrast to the planar devices. The InP NRs differ from the bulk InP concerning the ground state phase: whereas zincblende (ZB) structure is reported to be the stable phase for the bulk, the most stable form of NRs

is the wurtzite (WZ) phase [62, 63] due to the lower dangling bond ratio of the WZ structure than that of the ZB structure [63]. Experimental studies also report the structural transition from the ZB to WZ phase in the InP NRs under the growth conditions of various temperature and pressure values [64–66].

The InP Nanoparticles (NPs) being another InP derivative discussed in this chapter manifest interesting size-dependent behaviour so that they are effectively used in various fields, such as photovoltaics devices (due to their high photoactivity, excellent absorption, solution processability, possessing the effect of quantum confinement and cheaper fabrication) [67–70], biomedical [71–74] and biological/chemical applications [75, 76], LEDs [77], catalysts [78, 79] and like. Among all II-VI and III-V semiconductors, InP is considered as the best candidate material in manufacturing NPs due to the following reasons: the systems covered with InP NPs are considered as alternatives for industrial hydrogen production since the InP NPs being inexpensive and environmentally benign material reduces the need for organic molecules due to their excellent absorption ability, as in InP NRs. [80]. Moreover, they are widely utilized in solar cells [81], optoelectronic devices [82] and composite thin films [83]. Also, due to efficient carrier multiplication, they are strong candidates for the fabrication of the next generation n/p solar cells [84–86]. Their electronic [84, 85, 87, 88] and optical properties [89], the ability to reduce lattice mismatches with low bandgap materials bring them forward among the other III-V materials [90]. Due to their high-quality electrochemical properties, InP NPs have been considered as the best material for electrochemical devices used in biomedical applications [91]. A lot of theoretical [92–98] and experimental [99–103] methods have been applied to investigate the properties (structural, thermal, electronic, optical, etc.) of the semiconductor NPs. By means of molecular dynamics method, it can be facilitated to obtain deeper information about the NPs when the experimental methods have some difficulties directly observing these nanostructures [95]. Even though there are experimental reports on their synthesis and characterization [91, 104–107] and applications as mentioned above, to the best of our knowledge, no MD study has been performed on the characterization of the InP NPs.

In this chapter, we report the computational details, results and discussion on structural properties of InP NRs in ZB and WZ phases [108] and NPs [109] based on

our molecular-dynamics (MD) simulations. The mechanical behavior of InP NRs were investigated under various external conditions such as compression, expansion, stretching and varying temperatures while InP NPs in ZB phase were subjected to only heat treatment under equilibrium and non-equilibrated conditions. The rest of the chapter is divided into three subsections: (i, ii) Sections 3.2 and 3.3 present the computational details, results, and discussion of InP NRs and InP NPs, respectively. (iii) Section 3.4 is devoted to our concluding remarks.

## 3.2 InP Nanorods

### 3.2.1 Method & Procedures & Results

In this work, MD simulations based on the potential developed by Branicio et al. [19] were conducted using MD program, courtesy of Branicio, in an NVT ensemble. A verlet algorithm was employed to integrate Newton's equation of motion with the time step of 5.2 fs. A Nosé-Hoover thermostat was applied to control the temperature. Considering six different InP NRs, each constructed from ZB and WZ phases, periodic boundary condition was imposed only along the uniaxial c direction to provide the relaxation of the NR along the a and b directions. All the NRs have different sizes (taken as the half-diagonal length) and same length. The labels of NRs were specified as $N_a x N_b$ by taking into account the number of In/P atoms in a and b directions, respectively. In this regard, the ZB NRs were referred as 4x4, 5x5, 6x6, 7x7, 8x8, 9x9, while WZ NRs were labeled as 3x4, 4x6, 5x7, 6x9, 7x11 and 8x13 (Fig. 3.1) throughout the chapter. The structural data of the investigated systems are listed in Tables 3.1-3.2.

Table 3.1: Structural data of the analyzed ZB InP NRs shown in Fig. 3.1.

| ZB NRs (The length of all the ZB NRs=266.22Å) | | | | | | |
|---|---|---|---|---|---|---|
| Type | 4x4 | 5x5 | 6x6 | 7x7 | 8x8 | 9x9 |
| Half-diagonal length (Å) | 12.45 | 16.60 | 20.75 | 24.90 | 29.06 | 33.21 |
| Number of Atoms | 768 | 1200 | 1728 | 2352 | 3072 | 3888 |

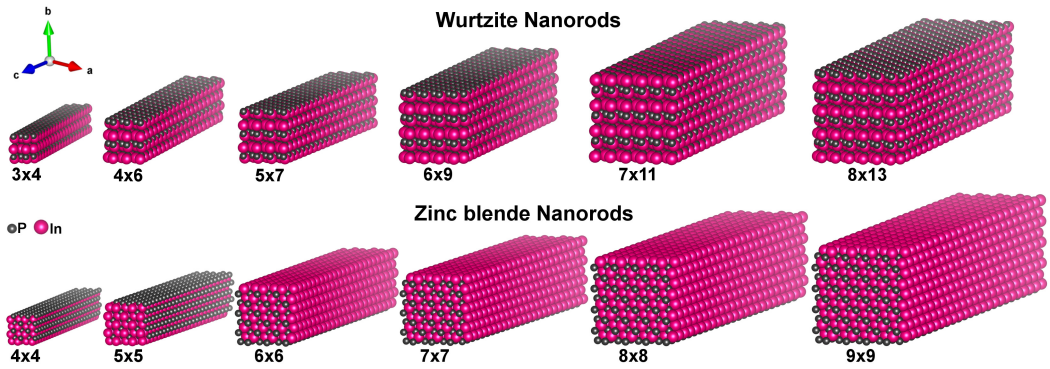


Figure 3.1: The InP NRs in the ZB and WZ structures (Figure is produced by VESTA software package [110, 111]. From now on the figures generated by VESTA will be notified only by VESTA).

Table 3.2: Structural data of the analyzed WZ InP NRs shown in Fig. 3.1.

| WZ NRs (The length of all the WZ NRs=271.65Å) | | | | | | |
|---|---|---|---|---|---|---|
| Type | 3x4 | 4x6 | 5x7 | 6x9 | 7x11 | 8x13 |
| Half-diagonal length (Å) | 9.87 | 15.71 | 18.40 | 23.84 | 29.05 | 34.47 |
| Number of Atoms | 480 | 960 | 1400 | 2160 | 3080 | 4160 |

In the simulations, equilibrium and non-equilibrated approaches were carried out according to the implementation of the convergence criterion by which the energy fluctuations are analyzed. A system is assumed in the equilibrium state if the computed energy difference between the maximum and minimum energies of the last consecutive 10 MD steps is less than the convergence criterion being set in the order $10^{-3}$ eV. In the course of the equilibrium simulations, upon the system's energy reaches to equilibrium state, the system proceeds to the next stage which is a modified temperature for gradual heating/cooling procedures, and a modified length for stretching/compressing applications. Otherwise, it starts a new run with the last state of the structure obtained from the previous run as an initial structure without changing the system temperature. In non-equilibrated simulations, the convergence criterion is ignored, so the system proceeds onto the next stage at the end of each run being composed of 40000 MD steps.

Four different procedures were applied in the simulations as follows: heating, cooling, stretching, and compression. Equilibrium approach was taken into account in all procedures while non-equilibrated criterion was carried out only in stretching proce-

dure.

**Heating/Cooling:** During the procedure, the system is gradually heated/cooled with a temperature gradient of 50 K as the convergence criterion is applied.

**Stretching:** The unit cell dimension along the uniaxial direction is increased while keeping the fractional coordinates of the atoms constant. The stretching ratio (SR) denotes the ratio of the difference between the final and initial lengths of the InP NR to its initial length. In the stretching simulations, the equilibrium and non-equilibrated approaches were employed as follows.

*Equilibrium approach:* The system's length is increased in accordance with the stretching ratio upon bringing the system to equilibrium state by satisfying the convergence criterion. During the simulation, the temperature is kept constant.

*Non-equilibrated approach:* By ignoring the convergence criterion, the temperature of the system is gradually increased by 50 K along with the stretching in accordance with the stretching ratio at the end of each run.

**Compression:** In this procedure, the compression ratio corresponds to the negative stretching ratio. It means that the NR's unit cell dimension in uniaxial direction is decreased in accordance with the compression ratio when the system reaches to the equilibrium state. During the simulations, the system temperature is kept constant.

**Expansion:** Concerning the stretching, the expansion procedure was also applied to implement variable periodic boundary conditions, such that in between the successive runs, the NR's unit cell dimension in the uniaxial direction is increased by keeping the cartesian coordinates of the atoms constant, thus imposing a "vacuum area" in which the NRs fill in through relaxation due to their thermal expansions. The relaxation ratio is determined in a similar way to that of the stretching ratio. There is a critical difference between stretching under equilibrium approach and expansion procedures. In the stretching procedures, stretching is realized when the computed energy difference for each run becomes lower than the convergence criterion, i.e. when the system arrives at equilibrium. However, expansion is implemented when the computed energy difference between the consecutive runs is greater than the convergence criterion i.e. when the system deviates from equilibrium. The difference between the expansion

and stretching procedures are delineated in Fig. 3.2.

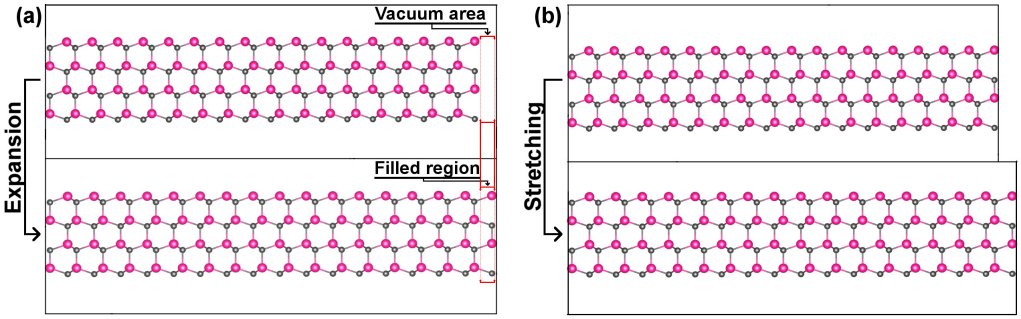


Figure 3.2: The difference between expansion (a) and stretching (b) procedures (VESTA).

#### 3.2.1.1 Zinc Blende Nanorods

**Gradual Heating**

The NRs constructed from the ZB phase were gradually heated starting from 0.7 K by an increment of 50 K as the convergence criterion was applied. Our simulations demonstrate that the partial transition of the ZB NRs to the RS structure occurs at 0.7K, and the complete transition takes place at elevated temperatures except for the 4x4 NR for which the complete transformation occurs at 0.7K.

Table 3.3: The transition temperatures and the ZB NRs' thicknesses. The RS phase appeared immediately at 0.7K which is 1st observed transition temperature (1st O.T.T.) as seen in the table, with phase transition temperatures (P.T.T.) indicating the fixed temperature in which the non- deformed nanorod undergoes a complete transition.

| ZB NRs | 1st O.T.T.(K) | P.T.T.(K) |
|---|---|---|
| 4x4 | 0.7 | 0.7 |
| 5x5 | 0.7 | 125 |
| 6x6 | 0.7 | 345 |
| 7x7 | 0.7 | 480 |
| 8x8 | 0.7 | 637 |
| 9x9 | 0.7 | 705 |

During the simulations, the phase transitions arrised uniformly and stacking faults

were also observed in the completely transformed systems under further heat treatment except for the 9x9 NR (Fig. 1 of Appendix A). Table 3.3 illustrates the dependence of the phase transition temperature on the NR's thickness, where the referred temperatures were determined for the non-deformed nanorods annealed at constant temperatures. Our simulations also prove that the gradually heated NRs completely transform to the RS phase at higher temperatures (Fig. 1 of Appendix A) than their phase transition temperatures displayed in Table 3.3.

**Stretching Under Equilibrium and Non-equilibrated Approaches**

Stretching procedure was performed at constant (0.7, 300, 600 and 900K) temperatures under equilibrium approach and increasing temperatures by 50 K for non-equilibrated approach with 5% and 10% stretching ratios. In both equlibrium and non-equilibrated simulations, the ZB NRs first transformed into the RS phase for all of the cases, and under further stretching, a variety of phases including the ZB, WZ and RS, and their combinations appeared.

Maximum elongation percentages reached before the breaking of the NRs are presented in Tables 3.4 and 3.5 for the equilibrium approach, and Tables 3.6 and 3.7 for the non-equilibrated approach. The frequently encountered maximum elongation ratios for the NRs under the equilibrium approach are 40.71%, 55.13% and 71.03% for the 5% (Table 3.4); and 46.40%, 61.05% and 114.36% for the 10% stretching ratios (Table 3.5). Also, in the non-equilibrated simulations, the NRs usually broke at temperatures of 450K and 200K for the 5% (Table 3.6) and 10% (Table 3.7) stretching ratios, respectively.

Table 3.4: Final length (F.L.) and maximum elongation percentages (M.E.P.) are for the stretched ZB NRs at the constant temperature for the 5% stretching ratio (S.R) by following the equilibrium approach.

| ZB NRs (Initial length of all NRs=266.22Å) | | | | | |
|---|---|---|---|---|---|
| Stretch at Constant Temperature (S.R.=5%) | | | | | |
| Type | | 0.7K | 300K | 600K | 900K |
| 2*4x4 | F.L.(Å) | 389.78 | 413.00 | 901.53 | 640.70 |
| | M.E.P. | 46.41% | 55.13% | 238.64% | 140.66% |
| 2*5x5 | F.L.(Å) | 570.80 | 374.60 | 433.65 | 339.78 |
| | M.E.P. | 114.36% | 40.71% | 62.89% | 27.63% |
| 2*6x6 | F.L.(Å) | 339.78 | 413.00 | 374.60 | 858.60 |
| | M.E.P. | 27.63% | 55.13% | 40.71% | 222.51% |
| 2*7x7 | F.L.(Å) | 413.00 | 455.33 | 455.33 | 455.33 |
| | M.E.P. | 55.13% | 71.03% | 71.03% | 71.03% |
| 2*8x8 | F.L.(Å) | 433.65 | 374.60 | 413.00 | 356.77 |
| | M.E.P. | 62.89% | 40.71% | 55.13% | 34.01% |
| 2*9x9 | F.L.(Å) | 374.60 | 413.00 | 640.70 | 356.77 |
| | M.E.P. | 40.71% | 55.13% | 140.66% | 34.01% |

Table 3.5: Final length (F.L.) and maximum elongation percentages (M.E.P.) are the for stretched ZB NRs at constant temperature for the 10% stretching ratio (S.R.) by following the equilibrium approach.

| ZB NRs (Initial length of all NRs=266.22Å) | | | | | |
|---|---|---|---|---|---|
| Stretch at Constant Temperature (S.R.=10%) | | | | | |
| Type | | 0.7K | 300K | 600K | 900K |
| 2*4x4 | F.L.(Å) | 389.78 | 389.78 | 428.76 | 389.78 |
| | M.E.P. | 46.41% | 46.41% | 61.05% | 46.41% |
| 2*5x5 | F.L.(Å) | 570.68 | 428.76 | 428.76 | 570.68 |
| | M.E.P. | 114.36% | 61.05% | 61.05% | 114.36% |
| 2*6x6 | F.L.(Å) | 518.80 | 570.68 | 389.78 | 389.78 |
| | M.E.P. | 94.87% | 114.36% | 46.41% | 46.41% |
| 2*7x7 | F.L.(Å) | 428.76 | 428.76 | 428.76 | 471.63 |
| | M.E.P. | 61.05% | 61.05% | 61.05% | 77.16% |
| 2*8x8 | F.L.(Å) | 428.76 | 389.78 | 428.76 | 389.78 |
| | M.E.P. | 61.05% | 46.40% | 61.05% | 46.41% |
| 2*9x9 | F.L.(Å) | 428.76 | 428.76 | 389.78 | 389.78 |
| | M.E.P. | 61.05% | 61.05% | 46.41% | 46.41% |

Table 3.6: Breaking temperatures (B.T.), maximum elongation percentages (M.E.P.) and final length (F.L.) are the for stretched ZB NRs at constant temperature for the 5% stretching ratio (S.R.) by following the non-equilibriated approach.

| ZB NRs (Initial length of all NRs=266.22Å) | | | |
|---|---|---|---|
| Stretch at Increasing Temperature (S.R.=5%) | | | |
| Type | B.T.(K) | F.L.(Å) | M.E.P. |
| 4x4 | 350 | 374.60 | 40.71% |
| 5x5 | 500 | 433.65 | 622.89% |
| 6x6 | 450 | 413.00 | 55.13% |
| 7x7 | 450 | 413.00 | 55.13% |
| 8x8 | 550 | 455.33 | 71.03% |
| 9x9 | 650 | 502.00 | 88.56% |

Table 3.7: Breaking temperatures (B.T.), maximum elongation percentages (M.E.P.) and final length (F.L.), are for the stretched the ZB NRs at constant temperature for the 10% stretching ratio (S.R.) by following the non-equilibriated approach.

| ZB NRs (Initial length of all NRs=266.22Å) | | | |
|---|---|---|---|
| Stretch at Increasing Temperature (S.R.=10%) | | | |
| Type | B.T.(K) | F.L.(Å) | M.E.P. |
| 4x4 | 200 | 389.78 | 46.41% |
| 5x5 | 200 | 389.78 | 46.41% |
| 6x6 | 150 | 354.35 | 33.10% |
| 7x7 | 250 | 428.76 | 61.05% |
| 8x8 | 200 | 389.78 | 46.41% |
| 9x9 | 350 | 518.80 | 94.87% |

**General Behaviour of the Zinc Blende Nanorods Under Strain**

In the strain simulations, the ZB NRs underwent a transition into the RS phase at lower temperatures starting from 0.7K, following by WZ phase as shown in Fig. 3.3. At 0.7K, the 4x4 NR completely transformed into the RS phase after the first MD run then proceeded to the WZ phase (Figs. 2 and 3 of Appendix A) while the 5x5 and 6x6 ZB NRs partially converted into the RS and then to the WZ phases (Figs. 4-7 of Appendix A). For the thicker NRs (7x7, 8x8 and 9x9), the partial transitions to the RS phase occurred after the first run and the ZB phase dominated throughout the rest of the simulation at 0.7K (Figs. 8-13 of Appendix A). At high temperatures, 600K for the 4x4 and 5x5 NRs, 900K for the 6x6, 7x7, 8x8 and 9x9 NRs, a complete transformation into the RS phase occurred.

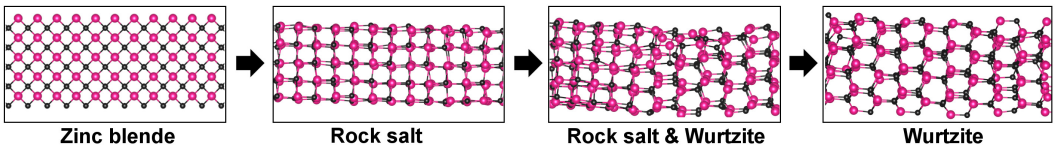


Figure 3.3: Observed phase transitions in the ZB NRs under strain at constant and increasing temperatures (VESTA).

On the basis of our stretching simulations, we can draw the following results: The occurrence of the WZ phase in the ZB NRs depends on the temperature, stretching ratio, and the NR thickness. The WZ region occurs more densely under strain for a 5% stretching ratio in the thinner NRs (4x4, 5x5 and 6x6). The strain application with 10% ratio also results that the transition into the WZ phase occurs at lower temperatures than that of the 5% ratio (Figs. 2-13 of Appendix A). In addition, the breaking mechanism is entirely different depending on the observed phase. If the structure is in the ZB or WZ phases, an elongation and inclination occurred towards to the breaking point as opposed to the situation in the RS phase where any inclination towards breaking point was not observed, as shown in Fig. 3.4. In all of the structures (ZB, WZ and RS), a single atom chain was observed, which forms in the thinning region where the stress was concentrated.

The effect of expansion on the deformation temperature of the NR was also investigated, where the systems were relaxed after each heating run. The simulations demonstrate that the expansion procedure causes the structural deformation of the NR at the lower temperature than the stretching, acting as a destructive factor.

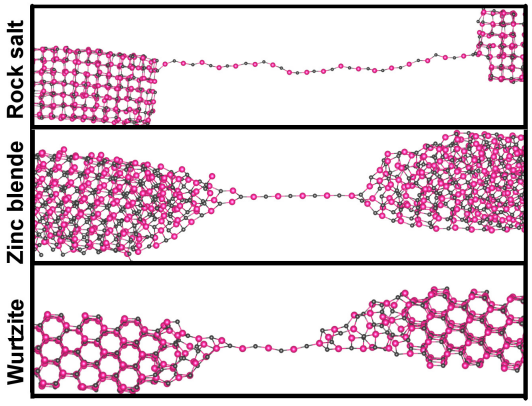


Figure 3.4: The differences between the breaking mechanisms of the rock salt (RS), zinc blende (ZB) and wurtzite (WZ) nanorods under strain (VESTA).

#### 3.2.1.2 Wurtzite Nanorods

**Gradual Heating**

The NRs constructed from WZ phase were gradually heated with a temperature gradient of 50 K while employing the convergence criterion. In the course of the simulations, the RS domains first appeared at the kinks due to the curvature observed in the NRs (except for the 3x4 NR). Eventually, all of the WZ NRs transformed into the RS phase at high temperatures. However, the completely transformed systems were segmented as a result of the stacking faults due to the inhomogeneity caused by the RS domains localized at the kinks (Fig. 18 of Appendix A). As evident from 3.5-a where the transition for the gradually heated 6x9 NR is realized around the $125x10^4$ MD steps, the complete transition to the RS phase is marked by "an energy jump" occurring in the potential energy. Table 3.8 shows the dependence of the phase transition temperature on the NR thickness. In the same manner with ZB NRs, the phase transition temperature was determined by keeping the NRs at fixed temperatures until the non-deformed nanorods completely underwent a phase transition. In the simulations gradually heated, the NRs completely transformed into the RS phase at higher temperatures than their the phase transition temperatures as displayed in Table 3.9, the similar result with the ZB NRs.

Table 3.8: Phase transition temperatures (P.T.T.) and the WZ NRs' thicknesses. In contrast to the ZB NRs (Table 3.3), it was found that 1st observed transition temperature (1st.O.T.T.) depends also on the NR's thickness.

| WZ NRs | 1st.O.T.T. (K) | P.T.T. (K) |
|---|---|---|
| 3x4 | 50 | 200 |
| 4x6 | 150 | 475 |
| 5x7 | 250 | 590 |
| 6x9 | 450 | 780 |
| 7x11 | 650 | 830 |
| 8x13 | 800 | 895 |

To further test the effect of relaxation on the phase transition under heat treatment, the 7x11 NR was gradually heated with an increment of 50 K along with the application of the expansion with a 0.5% ratio (Fig. 19 of Appendix A) as discussed above in Section 3.2.1. We observed that the intermediate expansion runs were successful in the elimination of the RS regions by straightening the bends out and, thus, eliminating the countering of the system against the shearing via the RS regions, but, eventually, the RS phase dominated the system. It was evident that the expansion procedure did not have much effect in the complete evolution of the system, rather, delaying the com-

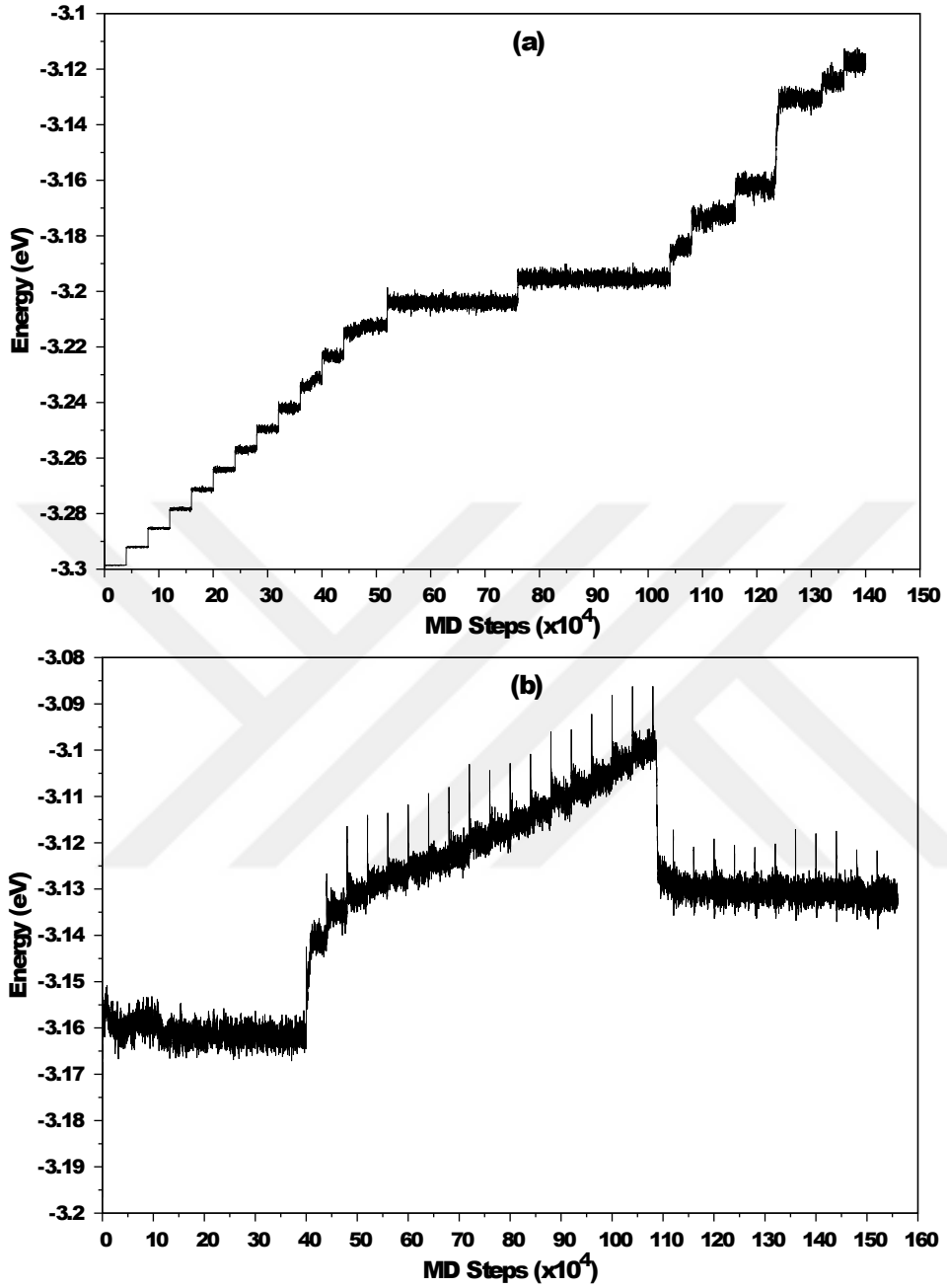


Figure 3.5: Energy versus MD steps graphs for (a) 6x9 subjected to gradual heating and (b) 5x7 at 600K under equilibrium criteria applied stretching. In graph (a), Energy "jump" around $125x10^4$ MD steps is due to complete transition to the RS phase. In graph (b), the first and the second jumps are due to the complete transition to the RS phase and the NR breaking (around $45x10^4$ and $110x10^4$ MD steps), respectively.

plete phase transition. When the 7x11 NR was heated without applying expansion, a transition from the WZ into RS phase was observed at 650K for the first time and the complete transition being at 900K, while the complete transition was observed at 1000K with the expansion procedure. Hence, for the other systems, the expansion process has not been applied.

**Annealing, Cooling and Stretching**

To observe the effect of an annealing procedure, the non-deformed NRs (3x4@50K, 4x6@300K, 5x7@400K and 8x13@850K - nomenclature showing the type of the NR along with the temperature being kept constant during the simulation) were subjected to heating at constant temperatures below their phase transition temperatures as shown in Table 3.8 (Fig. 20 of Appendix A). The crucial results that we observed in the annealing simulations are as follows:

- Reversible phase transition under annealing: When a non-deformed 4x6 NR was treated at 300 K, the RS regions appeared at the kinks after the first run, but, in case that the NR was further kept at the same temperature for 2080 picoseconds, the RS regions evolved back to the WZ phase because the increase in the surface area leads to lower the strain (Fig. 20 of Appendix A).
- Irreversible phase transition depending on the NR's thickness at constant temperature: For the thicker NRs (i.e., 5x7@400K and 8x13@850K), the RS regions grew further and did not transform back to the WZ phase below the phase transition temperatures through the rest of the simulation.
- For the 3x4 NR, the RS phase was dominant at 50K which is lower than the phase transition temperature shown in Table 3.8, meaning that annealing takes over the countering weak WZ expansion due to the low ratio of the surface to all area (Fig. 20 of Appendix A).

Besides annealing of the non-deformed 4x6 NR at 300K, it was also gradually heated from 0.7 to 300K and was kept at this temperature during the simulation. The kinks missing in the annealing appeared and complemented by the RS regions which were persistent and did not convert into the WZ phase as opposed to the annealing procedure.

The gradually heated NRs (Fig. 18 of Appendix A) were then subjected to cooling to see if the transition was reversible by following the same temperature gradient path (3x4 NR was excluded due to its complete transition at 50K as explained above). For each NR, three initial configurations were selected as follows:

- The first system was taken from below the phase transition temperature with respect to Table 3.8,
- The second one is from the run just before the complete transition to the RS phase,
- The final one belongs to the completely transformed system into the RS phase.

After cooling the system, the obtained results are following:

- When the NRs in the first batch were cooled down from the temperature below their phase transitions, 6x9@750K, 7x11@800K and 8x13@900K perfectly returned to their initial structures in the WZ phase (Fig. 21 of Appendix A) while 4x6 being initially at 450 K partially transformed back to the WZ phase although 450K is below the phase transition temperature. In case that 4x6 being initially at 400 K was cooled down, the system completely evolved back into WZ phase. The 5x7 could not completely transform to the WZ phase neither at 500 nor 550K even though these temperatures were below the phase transition temperature (Fig. 21 of Appendix A).
- In the second batch of systems, the WZ phase was partially recovered to WZ phase for 5x7@600K and 8x13@950K NRs while the 4x6@500K, 7x11@900K and 6x9@800K were not evolved back to WZ phase, they completely transformed into the RS phase (Fig. 21 of Appendix A).
- The NRs in the final batch of systems retained their structures except for 4x6@500K NR.

During the cooling processes, an interesting result was also observed for the 4x6, 7x11 and 8x13 NRs taken from the runs of the heating process below and above the phase transition temperatures. Although 7x11@800 and 850K had almost the same

configurations at the beginning of the cooling, the 7x11@800K NR below the transition temperature completely transformed back to the WZ phase while 7x11@850K being above the phase transition temperature only partially recovered to the WZ phase; this situation was also observed for the 4x6 at 400 and 500K and 8x13 at 900 and 950K. So, we can confidently say that the behavior of the NRs having almost the same configuration in terms of evolving back to the WZ phase or completing its transition into the RS phase depends strongly on their formation temperature with respect to the phase transition temperature (Fig. 21 of Appendix A).

Even though a complete recovery of the WZ phase by the cooling process could not be observed for all of the NRs (some of the RS regions being present), upon stretching with a 0.5% ratio at 0.7K after cooling, these residual RS regions were completely removed by transforming back to the WZ phase. Note that the calculations related to the stretching procedure after cooling were done on thin, average and thick NR specimens, namely the 4x6, 5x7 and 8x13 NRs, respectively, as seen in the Fig. 22 of Appendix A. We can say that the transition in the cooling procedure is reversible since the cooled NRs recovered their initial structures via stretching procedure.

Table 3.9: Complete transition temperatures (C.T.T.) in the gradual heated NRs. Comparing this table with Table 3.8, it is observed that gradually heated NRs undergo a phase transition at higher temperatures.

| WZ NRs | 3x4 | 4x6 | 5x7 | 6x9 | 7x11 | 8x13 |
|---|---|---|---|---|---|---|
| C.T.T.(K) | 200 | 500 | 650 | 800 | 900 | 950 |

**Stretching Under Equilibrium and Non-equilibriated Approaches**

Equilibrium and non-equilibriated approaches were employed while the NRs were stretched with 0.5%, 1% and 5% ratios. Depending on the approach, constant and increasing temperatures were set so as to test their endurance. Their critical temperatures and maximum elongation percentages are given in Tables 3.10, 3.11, 3.12, 3.13 and 3.14 for the three stretching ratios. The phase of the system is the decisive factor in the breaking process in a similar manner with ZB NRs: for the RS structured NR, the thinning region occurred where the stress was concentrated, without any inclination towards breaking points, a single atom chain formed in the thinning region. For the WZ systems, an elongation and inclination towards the breaking point was

Table 3.10: Final length (F.L.) and maximum elongation percentages (M.E.P.) are for the stretched WZ NRs at the constant temperature for the 1% stretching ratio (S.R) by following the equilibrium approach.

| WZ NRs (Initial length of all NRs=271.65Å) | | | | | |
|---|---|---|---|---|---|
| Stretch at Constant Temperature(S.R.=1%) | | | | | |
| Type | | 0.7K | 300K | 600K | 900K |
| 2* 3x4 | F.L.(Å) | 425.08 | 1030.57 | 1138.39 | 1138.39 |
| | M.E.P. | 56% | 279% | 319% | 319% |
| 2* 4x6 | F.L.(Å) | 344.93 | 1138.39 | 1138.39 | 961.23 |
| | M.E.P. | 27% | 319% | 319% | 253% |
| 2* 5x7 | F.L.(Å) | 503.43 | 483.78 | 1138.39 | 508.46 |
| | M.E.P. | 85% | 78% | 319% | 87% |
| 2* 6x9 | F.L.(Å) | 366.15 | 803.60 | 1138.39 | 1138.39 |
| | M.E.P. | 35% | 195% | 319% | 319% |
| 2* 7x11 | F.L.(Å) | 377.24 | 534.40 | 1138.39 | 678.55 |
| | M.E.P. | 39% | 97% | 319% | 150% |
| 2* 8x13 | F.L.(Å) | 309.17 | 412.58 | 896.56 | 1138.39 |
| | M.E.P. | 14% | 52% | 230% | 319% |

observed (Fig. 3.4). Still, there were exceptions to this classification as for instance the 8x13@0.7K NR and the 4x6@300K NR also broke into fragments sharply under strain for the 1% stretching ratio (Fig. 25 of the Appendix A).

Table 3.10 illustrates that a dominant pattern for a maximal elongation of 319% has emerged for the 1% stretching ratio before the breaking of the NRs. The endurance of the systems was not dependent on their size, but instead, the stretching ratio played a dominant role as the NRs broke at much lower temperatures for the 5% stretching ratio compared to the high temperatures while the NRs broke at relatively high temperatures for the %1 ratio (Tables 3.12 and 3.13). The breaking manifests itself clearly in the energy graph in Fig. 3.5-b as a steep jump where the breaking occurs around 110x$10^4$ MD steps for the 5x7@600K.

**Wurtzite → Rock Salt → Wurtzite Phase Transition Under Strain**

The bent regions in the WZ NRs undergo a transition into the RS phase (except for the 3x4 NR) to counter the deformation that can result in shearing. These RS regions

Table 3.11: Final length (F.L.) and maximum elongation percentages (M.E.P.) are for the stretched WZ NRs at constant temperature for the 5% stretching ratio (S.R) by following the equilibrium approach.

| WZ NRs (Initial length of all NRs=271.65Å) | | | | | |
|---|---|---|---|---|---|
| Stretch at Constant Temperature(S.R.=5%) | | | | | |
| Type | | 0.7K | 300K | 600K | 900K |
| 2* 3x4 | F.L.(Å) | 442.49 | 965.90 | 1174.06 | 512.24 |
| | M.E.P. | 63% | 255% | 332% | 89% |
| 2* 4x6 | F.L.(Å) | 421.42 | 382.24 | 487.85 | 919.91 |
| | M.E.P | 55% | 41% | 79% | 238% |
| 2* 5x7 | F.L.(Å) | 442.49 | 442.49 | 653.76 | 421.42 |
| | M.E.P | 63% | 63% | 141% | 55% |
| 2* 6x9 | F.L.(Å) | 382.24 | 442.49 | 686.45 | 686.45 |
| | M.E.P | 41% | 63% | 152% | 152% |
| 2* 7x11 | F.L.(Å) | 364.04 | 364.04 | 382.24 | 464.62 |
| | M.E.P | 34% | 34% | 41% | 71% |
| 2* 8x13 | F.L.(Å) | 364.04 | 346.70 | 382.24 | 622.63 |
| | M.E.P | 34% | 28% | 41% | 129% |

Table 3.12: Breaking temperatures (B.T.), maximum elongation percentages (M.E.P.) and final length are for the stretched WZ NRs at increasing temperature for the 1% stretching ratio (S.R.) by following the non-equilibrated approach.

| WZ NRs (Initial length of all NRs=271.65Å) | | | |
|---|---|---|---|
| Stretch at Increasing Temperature(S.R.=1%) | | | |
| Type | B.T.(K) | Final Length(Å) | M.E.P. |
| 3x4 | 1350 | 355.83 | 31% |
| 4x6 | 1400 | 358.93 | 32% |
| 5x7 | 1350 | 355.38 | 31% |
| 6x9 | 1550 | 369.81 | 36% |
| 7x11 | 1250 | 348.38 | 28% |
| 8x13 | 1550 | 369.81 | 36% |

Table 3.13: Breaking temperatures (B.T.), maximum elongation percentages (M.E.P.) and final length are for the stretched WZ NRs at increasing temperature for the 5% stretching ratio (S.R.) by following the non-equilibrated approach.

| WZ NRs (Initial length of all NRs=271.65Å) | | | |
|---|---|---|---|
| Stretch at Increasing Temperature(S.R.=5%) | | | |
| Type | B.T.(K) | Final Length((Å)) | M.E.P. |
| 3x4 | 950 | 686.45 | 152% |
| 4x6 | 550 | 464.62 | 71% |
| 5x7 | 300 | 364.01 | 34% |
| 6x9 | 400 | 401.35 | 48% |
| 7x11 | 300 | 364.01 | 34% |
| 8x13 | 250 | 346.70 | 28% |

Table 3.14: Final length, maximum elongation percentages and breaking temperatures are for the stretched WZ NRs at constant temperature for the 0.5% stretching ratio (S.R) by following the equilibrium approach.

| WZ NRs (Initial length of all NRs=271.65Å) | | | |
|---|---|---|---|
| Stretch at const.Temp(S.R.=0.5%) | | | |
| Type | Temperature(K) | Final Length(Å) | M.E.P. |
| 4x6 | 600 | 618.60 | 128% |
| 2*6x9 | 600 | 1136.77 | 318% |
| | 900 | 423.44 | 55% |
| 2*8x13 | 600 | 603.37 | 122% |
| | 900 | 364.59 | 34% |

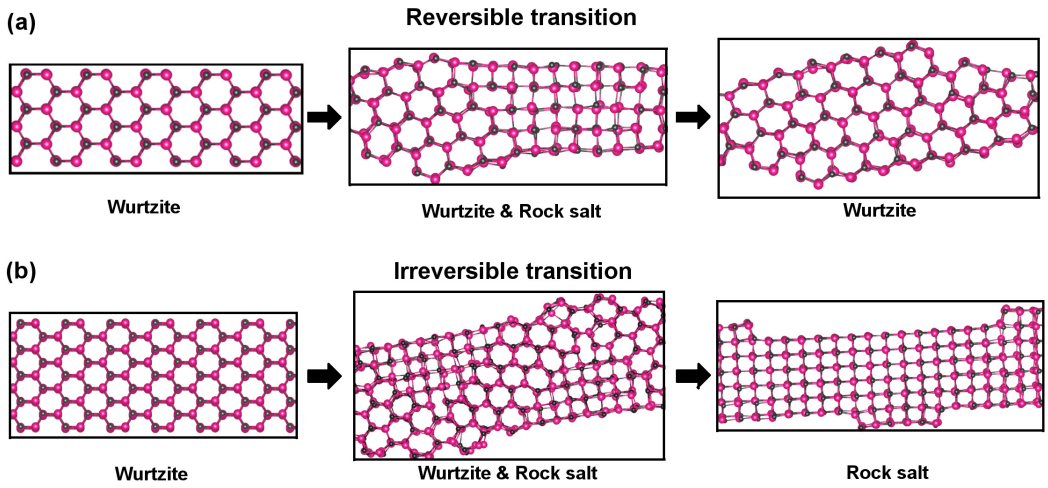


Figure 3.6: In the equilibrium case, both reversible and irreversible transitions were observed while only irreversible transition occurs in non-equilibriated case under strain (VESTA).

can be made to evolve back to the WZ phase via a stretching procedure (Fig. 3.6).

In some of the systems (e.g., 4x6 with 1% stretch at 300K and 0.5% stretch at 600K; to some extent (regionally) 3x4 with 1% at 0.7K and at 300K, 5x7 with 5% stretch at 300K and at 1% stretch at 500K,6x9 with 0.5% and 1% at 600K and %1 stretch at 500K, 7x11 with 1% stretch at 600K) a return to the WZ phase (reversible phase transition) has been achieved by applying stretching at the constant temperature (Figs. 28-40 of Appendix A). Eventually, the WZ NRs underwent a transition into the RS phase at high temperatures. The complete transition to the RS phase causes a "jump" in the energy graph as seen in Fig. 3.5-b where the complete transition occurs around $45x10^4$ MD steps in the given example for the 5x7@600K. Also, during the endurance tests under stretching, a transition into the RS phase was observed in some of the systems (8x13 at 600 and at 700K, 7x11@600K, for both stretching ratios of 1% and 5%) at the heavily deformed (thinned) regions where the breaking occurs, even if the system was below the 1st observed transition temperature as given in Table 3.8 (Fig. 39 of Appendix A). Irreversible phase transition sequence of WZ $\rightarrow$ RS also occurred under stretching at increasing temperatures (Figs. 28-40 of Appendix A).

In summary, stretching procedure was observed to decrease the phase transition temperatures for the 1% and 5% stretching ratios except for the 3x4 NR for which stretching had a delaying effect (see Table 3.15 and compare with Table 3.8 and Figs. 28-40

Table 3.15: Phase transition temperatures lowered when the WZ NRs were put under strain. Stretch-induced transition temperatures (S.I.T.T.) compared to the phase transition temperatures (P.T.T.) from Table 3.8.

| Types | S.I.T.T.(K) | P.T.T.(K) |
|---|---|---|
| 3x4 | 300 | 200 |
| 4x6 | 400 | 475 |
| 5x7 | 500 | 590 |
| 6x9 | 700 | 780 |
| 7x11 | 700 | 830 |
| 8x13 | 800 | 895 |

of Appendix A). Also, when the 4x6 NR was stretched at 600K with 0.5% stretching ratio (the phase transition temperature being 475K), the NR completely transformed to the RS phase. Upon further stretching, the NR evolved back to the WZ phase, and the RS region did not appear through the rest of the simulation (Fig. 40 of Appendix A). This behavior was also observed in the 3x4 at 300K with the 1% ratio (Fig. 28 of Appendix A). However, the reversible transition did not appear in the thicker NRs (5x7, 6x9, 7x11, 8x13). The reason for the 4x6 NR and 3x4 NR regaining their initial phases under stretching may be due to being relatively thin NRs and also smaller stretching ratios.

Phase interchanges were also observed depending on the approach applied during the stretching simulations: while the irreversible phase transition from the WZ into the RS phase was observed during the gradual heating under the non-equilibrated approach, the reversible transitions between the phases occurred for treatments at constant temperatures under the equilibrium approach.

**The Effects of the Stretching and Temperature on the Reversibility**

To investigate the effects of stretching and temperature on the reversibility of the "stretch-induced" transitions, 1% stretching ratio was applied to two specimens of 8x13 NR, one taken just before the complete transition into the RS formation 950K, the other from 900K. Even though the systems are very much alike due to the fact that 8x13@950K having evolved from 8x13@900K, 8x13@900K was able to fully recover to its original WZ phase, while 8x13@950K still underwent the complete transition into the RS phase (Figs. 41-42 of Appendix A) under strain. Further

stretching of 8x13@900K led to a forced transition to the RS at 900K (Fig. 42 of Appendix A).

To further test if stretching had any delaying or lowering effect on the complete transition, the 8x13 @950K (23rd run) NR was heated without stretching applied, for which the complete phase transition occurred at the 24th run at 950K (Fig. 18 of Appendix A). Starting from the 23rd run, with a 1% stretching factor to see if the WZ phase could be recovered, it was found that the procedure has a slight delaying effect, not lowering the transition temperature but shifting its occurrence to the 25th run (Fig. 42 of Appendix A). Starting from the newly "obtained" 24th and 25th runs, we cooled down these systems (without stretching) to see if a reverse transition would occur. The wurtzite phase was partially recovered for the process originating from the 24th run as the temperature was gradually cooled down to 0.7K, but the RS phase was preserved during the process originating from the 25th run where a complete transition had taken place (Fig. 42 of Appendix A). With this in mind, this type of effect will be discussed in the conclusion section as a blocking factor in terms of heterogeneity due to kinks as a result of the stacking faults.

**Compression**

To test the strength of the NRs under compression, we applied a uniform press manifested as a "negative stretch" (i.e., with the atoms being repositioned within a shortened unit cell in the uniaxial direction) with a -0.5% stretching ratio. These calculations were done for the 4x6, 5x7,6x9 and 8x13 NRs.

Similar to the previous observations concerning the heating, the regions at the kinks were observed to be undergoing phase transitions to cope with the shear (Fig. 18 of Appendix A). As the compressions were further applied at temperatures above 0.7K (6x9 and 8x13 already possessing the kinks at 0.7K), the kink volumes became the dominant factor in bending due to the fact that for sufficiently high volumes, the atoms switching to the RS phase prevented further bending and thus, leading to a deformation (Figs. 47,49 and 51-54 of Appendix A). Being relatively free of these kink regions, the 4x6 and 5x7 NRs at 0.7K reacted very elastically to the compression (Fig. 3.7 shows compressed 5x7 NR at 0.7K). Both of the 4x6 and 5x7 NRs retained their WZ structures as the compression was going on and ZB phase was observed

only in 4x6 at 0.7K before the disintegration took place (Figs. 43, 45 of Appendix A).

However, when the same procedure was applied to the 4x6 NR at 300K, in accordance with the phase transition being first occurring at 150K, there was sufficient energy for the kinks to transform into the RS phase. We interestingly observed that the interchange of the phases in these regions occurred as the compression went on. The WZ dominates the NR once the stress decreases, and then the RS formation return with the formation of new bends (Fig. 51 of Appendix A).

When the 5x7 NR was subjected to compression at 300K (above the first observed phase transition temperature of 250K), the RS regions were observed in the bended areas of the NR. As the compressing continued, complete transition back to the WZ phase occurred once again and the NR retained this phase until deformation/fragmentation (Fig. 52 of Appendix A).

For the thicker system of 8x13 NR, the system was compressed with -0.5% stretching ratio at 600K (phase transition initiation temperature being 800K) (Table 3.8). Even though the RS formation was not expected below at this temperature, the kink regions transformed to the RS phase and led to regional expansions via transitions back to the WZ (Fig. 53 of Appendix A). When the same system was subjected to compression at 900K (phase transition temperature being 890K) (Table 3.8), an early complete transition occurred, eventually falling back to the WZ phase and then to RS once again and then to the WZ phase as the compression continued (Fig. 54 of Appendix A). Also, when the 6x9 and 8x13 NRs were compressed at 0.7K, and these NRs reacted inelastically to the compression in contrast to the thinner NRs (5x7@0.7K and 4x6@0.7K) (Figs. 47 and 49 of Appendix A).

The compressed NRs were then stretched back with the same stretching ratio of 0.5% corresponding to that of compression in magnitude at 0.7K to test if the compression process was reversible. The reason for limiting the investigation to low temperature lies in the fact that, once the RS phase forms, they deform the NR rapidly as is evident from the compression calculations for the 4x6@300K, 8x13@600K, 5x7@300K and 8x13@900K NRs (Figs. 51-54 of Appendix A). The 4x6 and 5x7 NRs showed complete success in reverting to their initial configurations (it is shown in Fig. 3.8 for the

5x7 NR) while for the thicker NRs of 6x9 and 8x13, partial recovery was observed at 0.7K (Figs. 44, 46, 48 and 50 of Appendix A).

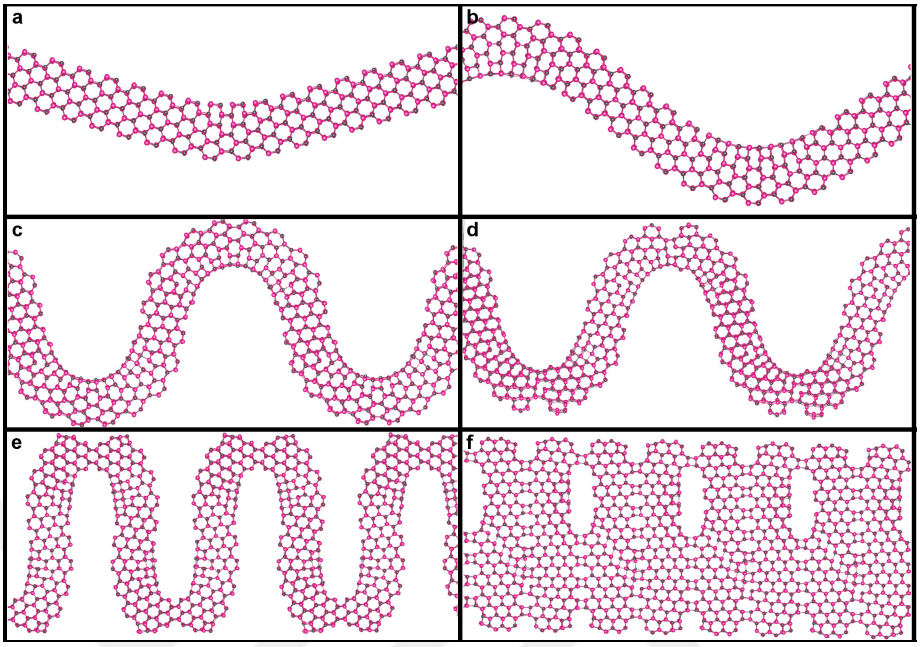


Figure 3.7: Compressed 5x7 NR for the -0.5% ratio at 0.7K. The times of compression for each the NR in above figure are (a) 1664 ps, (b)6240 ps, (c) 22256 ps, (d) 22364 ps, (e) 39520 ps and (f) 56160 ps (VESTA).

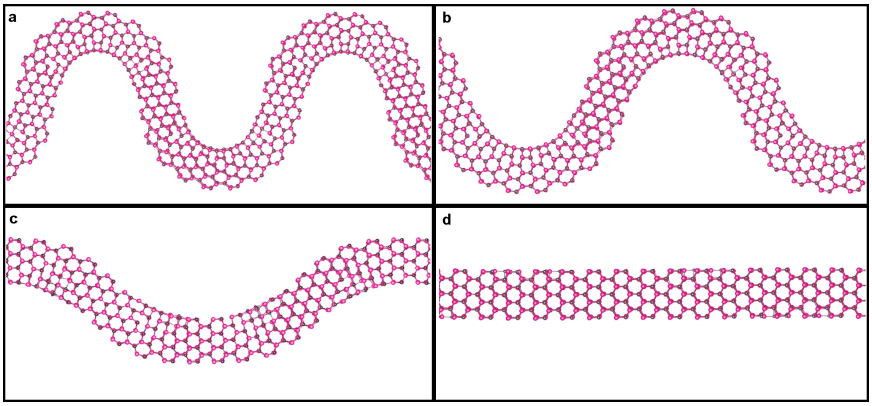


Figure 3.8: Compressed 5x7 NR for 22048 ps with the -0.5% ratio at 0.7K was stretched back at the same temperature with 0.5% ratio. Total elapsed times for each the NR during compression and stretching back processes are (a) 22048 ps, (b) 27248 ps, (c) 37440 ps and (d) 44928 ps (VESTA).

## 3.3 InP Nanoparticles

### 3.3.1 Method, Procedures and Results

Based on the same potential used in the MD simulations of InP NRs, the temperature was maintained by choosing a Nosé-Hoover thermostat and an NVT ensemble was used to heat and/or equilibrate the system with the temperature being evaluated at every 50 steps during the simulation. The equations of motion was solved by employing MD techniques based on the Verlet algorithm. The six types of spherical NPs were produced from the ZB bulk by applying a filter as a function of various bond lengths as the radius of the NP, excluding the remaining atoms outside this sphere. The samples are labelled as n-b and their radii are determined as $r = n \cdot b$, where $b$ and $n$ (3 to 8) represent the nearest-neighbor bond length and number of the bond lengths with respect to the origin. The bond distance between In and P atoms is equal to 2.54 Å. The generated models are displayed in Fig. 3.9.

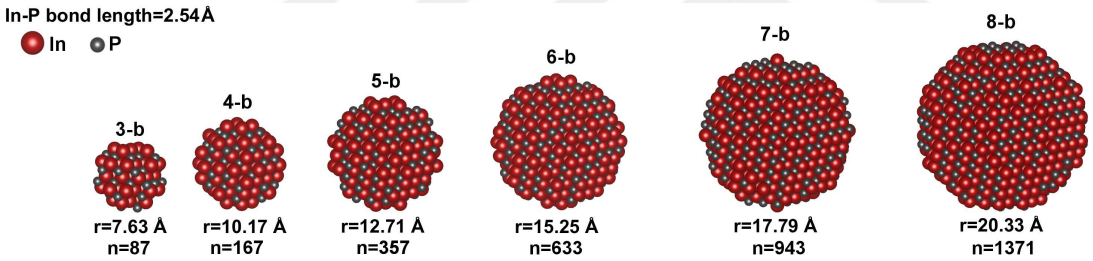


Figure 3.9: Six types of the InP NPs in the ZB structure with different radii (r) and number of atoms (n) (VESTA).

In the computations, the heating procedure was applied with a temperature gradient of 50 K. During this procedure, two different approaches, equilibrium and non-equilibrated, are employed. As indicated in Section 3.2 presenting InP NRs results, there is a considerable difference between the non-equilibrated and equilibrium approach applied simulations in terms of the implementation of the convergence criterion which is a parameter used to analyze energy fluctuations. This analysis is done by comparing the convergence criterion with respect to the energy difference between the maximum and minimum energies in the last consecutive 10 MD steps for each run. In all the simulations, each run is composed of 40000 MD steps except for 3-b

for which 20000 MD steps. Also, by using the convergence criterion, the temperature of the system can be controlled. To keep the temperature constant, the convergence criterion's value is set to a very small value in the order of $10^{-5}$ eV. In this manner, the computed energy difference for each run is always greater than the convergence criterion and, thus, the increasing of the temperature of the system is prevented, otherwise, the system's temperature is gradually increased by 50K. In the simulations, by switching the convergence criterion on or off, equilibrium and non-equilibrated approaches were incorporated. In the equilibrium simulations, the convergence criterion value is chosen as small as possible (in order of $10^{-5}$ eV), and this value is kept constant until the system arrives at the equilibrium state. Once the equilibrium with respect to the energy fluctuations is ensured, the value of the convergence criterion increases to increase the system temperature by 50K. As the system's temperature reaches the new temperature, the convergence criterion decreases to a smaller value once again to obtain equilibrium for the system's new temperature. This process is repeated at every increment of the temperature by 50K. However, in the non-equilibrated simulations, the convergence criterion is switched off (i.e., it is set to a high value, and thus the system's temperature is allowed to gradually increase by 50K with a heating rate of 0.25 K/ps (0.50 K/ps for 3-b NP) without waiting for the system to reach the equilibrium state).

In this work, the relationship between phase transition and temperature for each NP was examined, and the dependence of the heat capacity on the size of NPs was also demonstrated for both equilibrium and non-equilibrated approaches.

#### 3.3.1.1 Equilibrium and Non-equilibrated Simulations

Under both equilibrium and non-equilibrated approaches, all the NPs transform from the ZB to rock salt (RS) phase at high temperatures as presented in the Figs. 3.10, 3.11, 3.12, 3.13, 3.14 and 3.15.

During the phase transition, the shape of the NPs perfectly evolve from the sphere to the cubic structure (Figs. 3.10, 3.11, 3.12, 3.13, 3.14 and 3.15) except for 4-d under non-equilibrated criterion (Fig. 3.13). For all the NPs under both equilibrium and non-equilibrated criteria, the heat capacities were calculated from the slope of

energy E vs T graphs obtained by fitting the data points using the least squares method (Tables 3.16-3.17).

Since two different tendencies were observed regarding the phase transition under both equilibrium and non-equilibrated criteria as seen in Figs. 3.10-a, 3.11-c, 3.12-a, 3.13-c, 3.14-a and 3.15-c, the heat capacity was obtained for two different temperature ranges for each NP, meaning that the phase of the structure has a direct effect on the heat capacity. In addition, it is interesting to note that the heat capacity and the size have a linear relationship after the transition, whereas the heat capacity is nearly constant before the transition under both equilibrium and non-equilibrated criteria (Fig. 3.16).

Table 3.16: Heat capacities ($C_v$, in terms of $k_B$) of all the nanoparticles under the equilibrium criterion and their temperature ranges ($\triangle$T) for both before and after transitions.

| 2*NP | Before Transition | | After transition | |
|---|---|---|---|---|
| | $C_v$ | $\triangle$T (K) | $C_v$ | $\triangle$T (K) |
| 3-b | 1.55 | 0-450 | 1.73 | 500-600 |
| 4-b | 1.45 | 50-400 | 1.96 | 450-650 |
| 5-b | 1.21 | 50-500 | 1.80 | 550-900 |
| 6-b | 1.18 | 50-350 | 2.20 | 400-1000 |
| 7-b | 1.10 | 150-600 | 2.76 | 650-1050 |
| 8-b | 1.45 | 50-900 | 3.97 | 950-1100 |

Table 3.17: Heat capacities ($C_v$, in terms of $k_B$) of all the nanoparticles under the non-equilibrated criterion and their temperature ranges () for both before and after transitions.

| 2*NP | Before Transition | | After transition | |
|---|---|---|---|---|
| | $C_v$ | $\triangle$T (K) | $C_v$ | $\triangle$T (K) |
| 3-b | 1.72 | 50-600 | 2.31 | 650-1100 |
| 4-b | 1.52 | 200-450 | 2.49 | 500-800 |
| 5-b | 1.53 | 150-450 | 2.24 | 500-900 |
| 6-b | 1.40 | 50-550 | 2.41 | 600-1200 |
| 7-b | 1.38 | 50-800 | 3.63 | 850-1150 |
| 8-b | 1.73 | 50-950 | 5.02 | 1000-1150 |

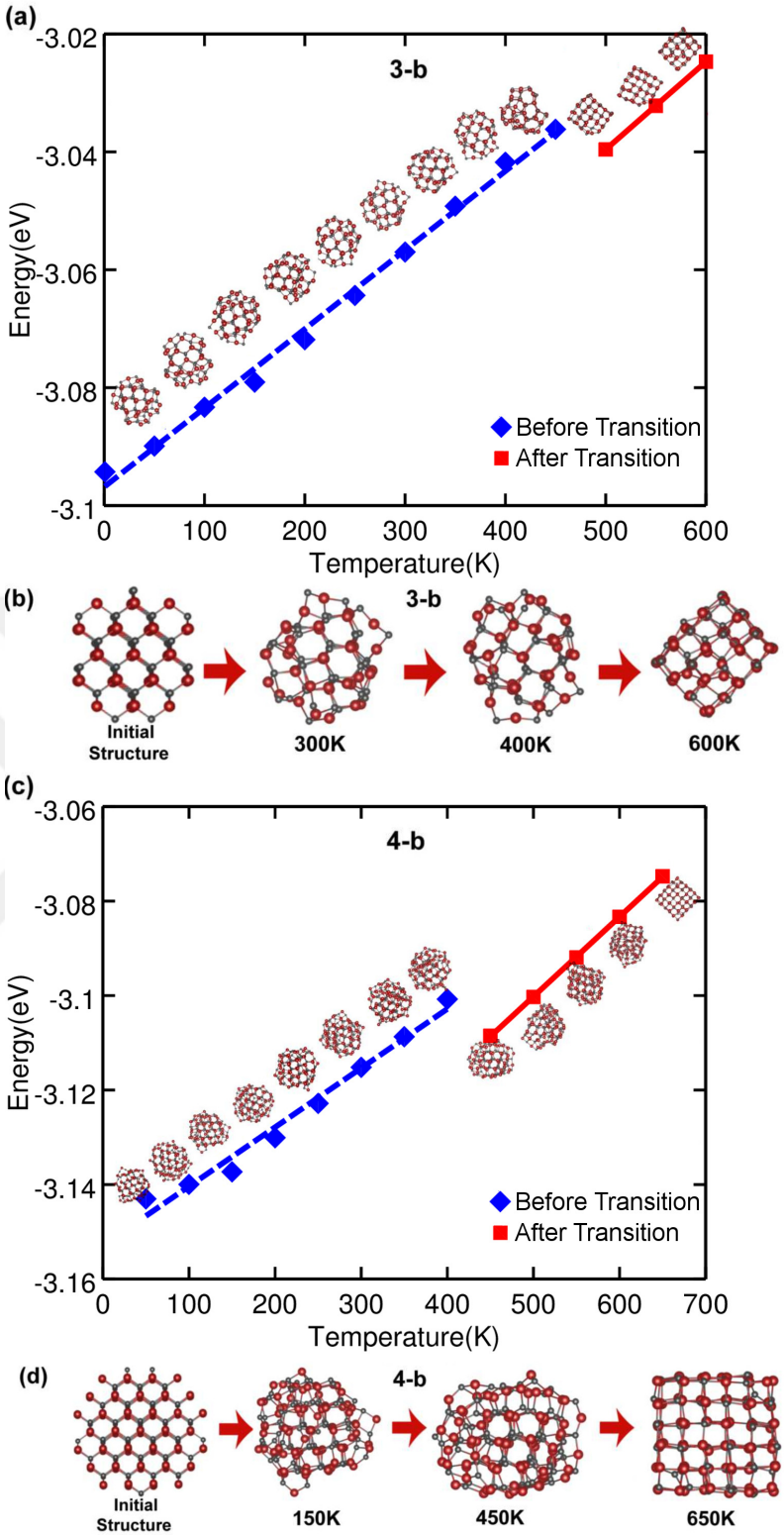


Figure 3.10: E vs T graphs (a and c) and phase transitions (b and d) for 3-b and 4-b NPs under equilibrium criterion (VESTA).

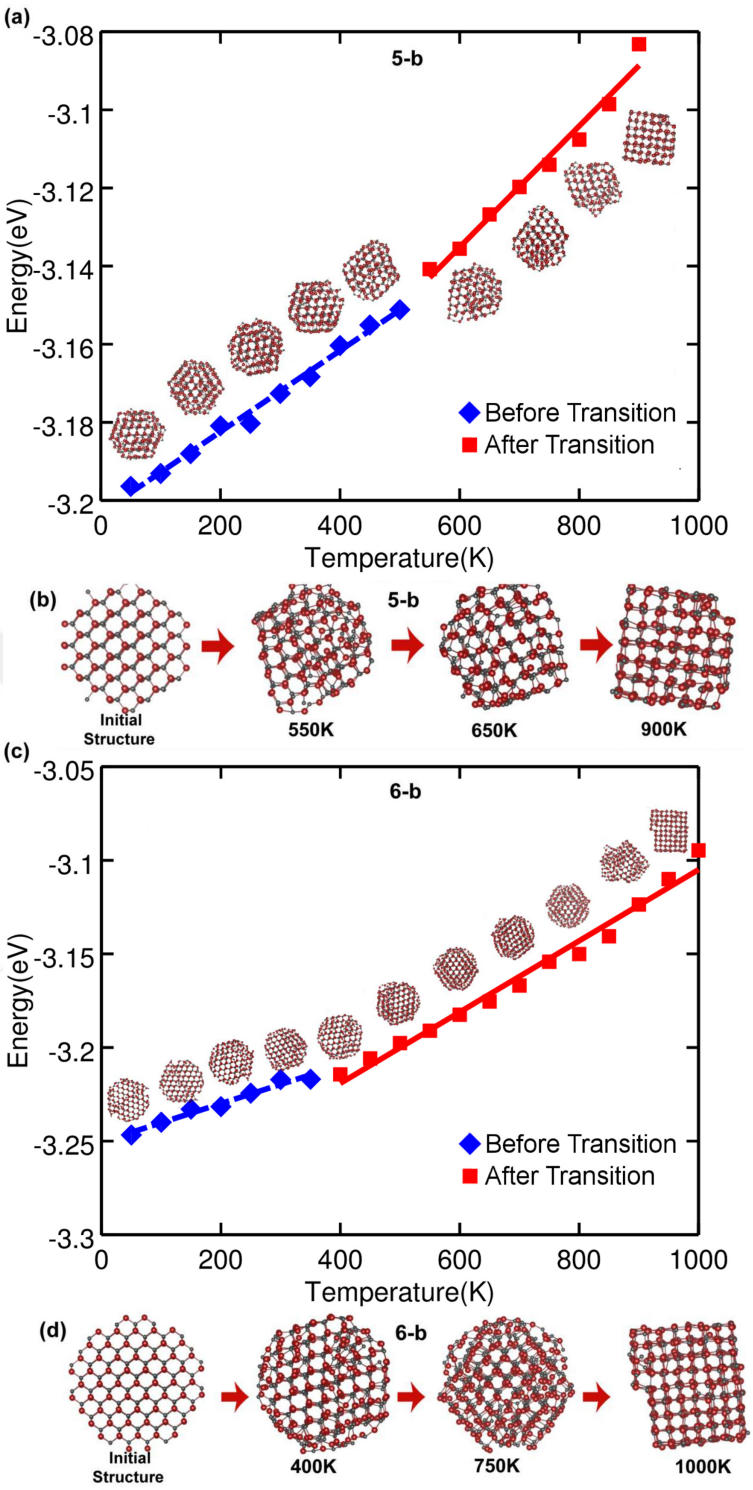


Figure 3.11: E vs T graphs (a and c) and phase transitions (b and d) for 5-b and 6-b NPs under equilibrium criterion (VESTA).

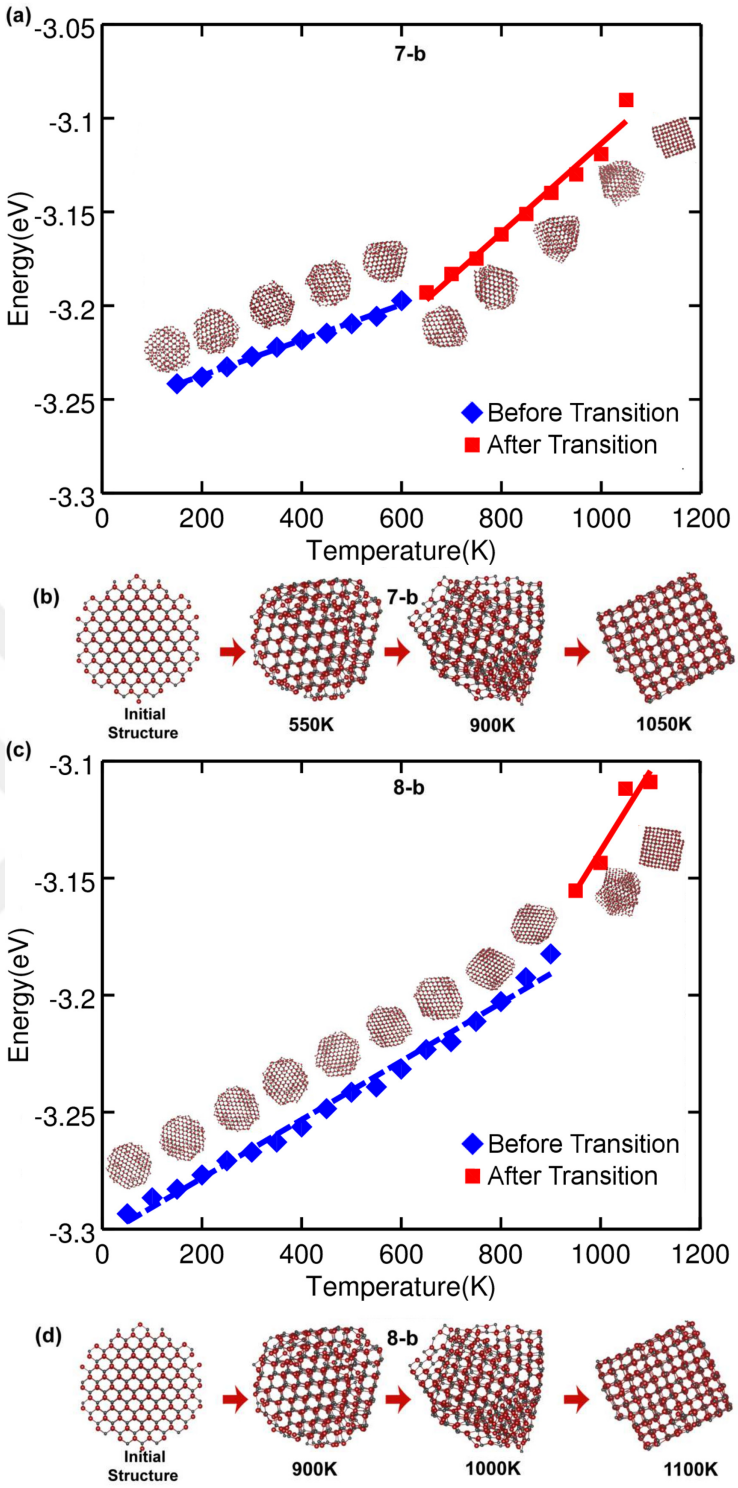


Figure 3.12: E vs T graphs (a and c) and phase transitions (b and d) for 7-b and 8-b NPs under equilibrium criterion (VESTA).

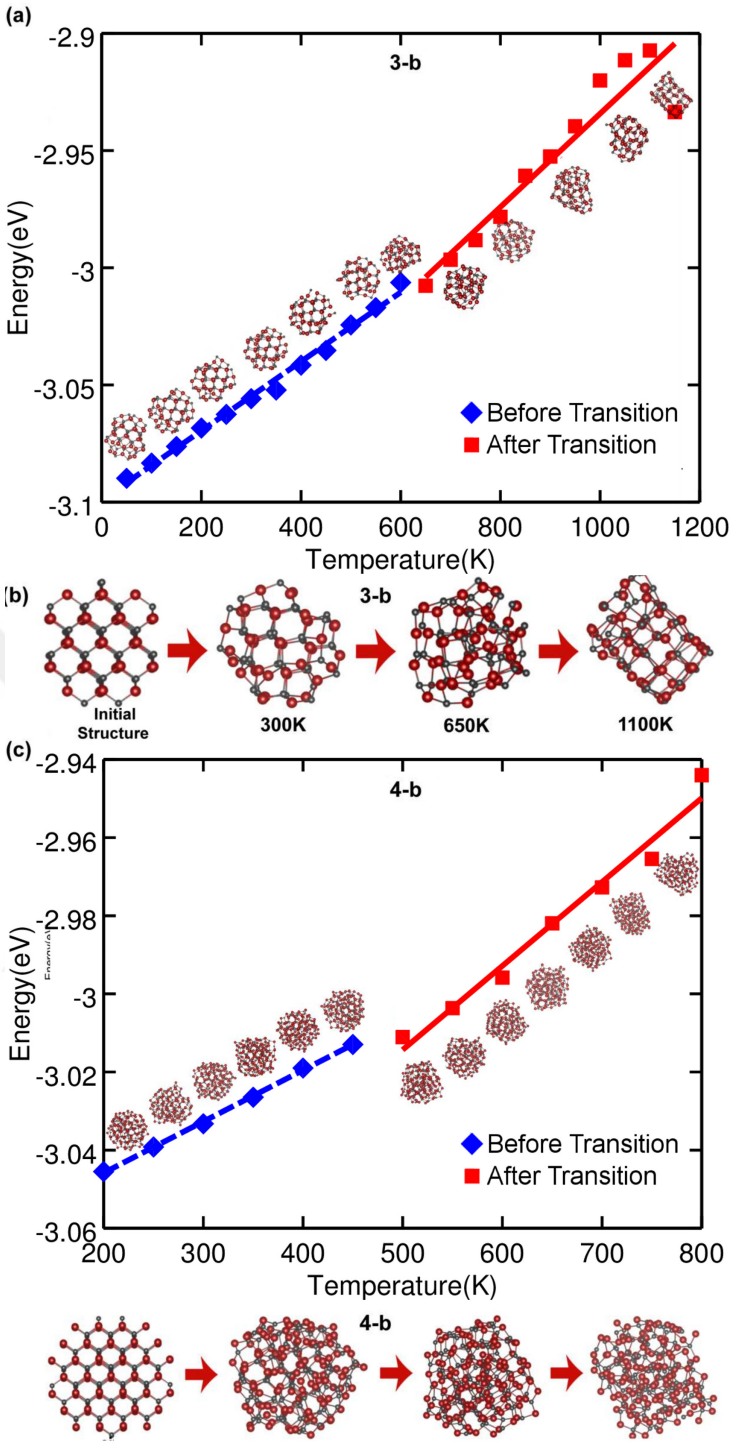


Figure 3.13: E vs T graphs (a and c) and phase transitions (b and d) for 3-b and 4-b NPs under non-equilibrated criterion (VESTA).

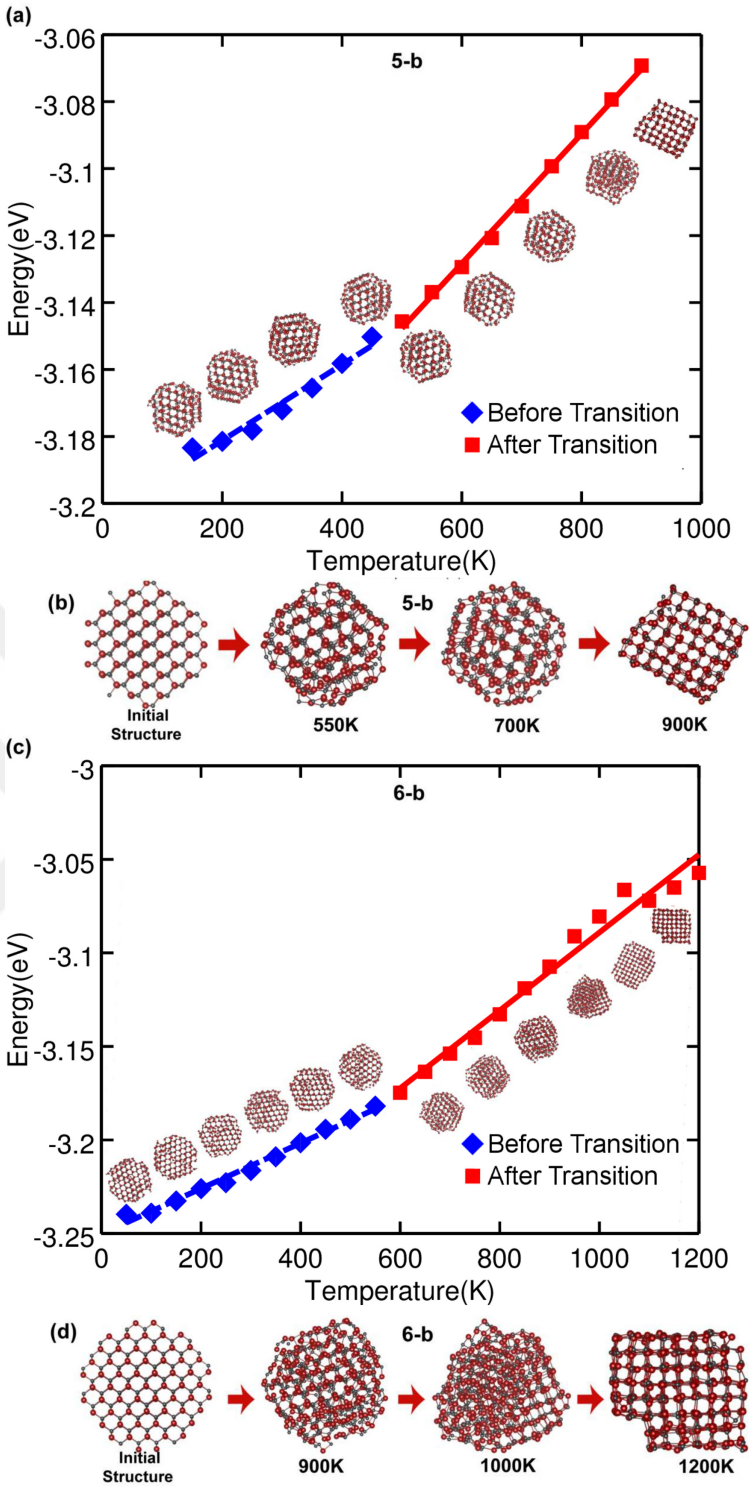


Figure 3.14: E vs T graphs (a and c) and phase transitions (b and d) for 5-b and 6-b NPs under non-equilibrated criterion (VESTA).

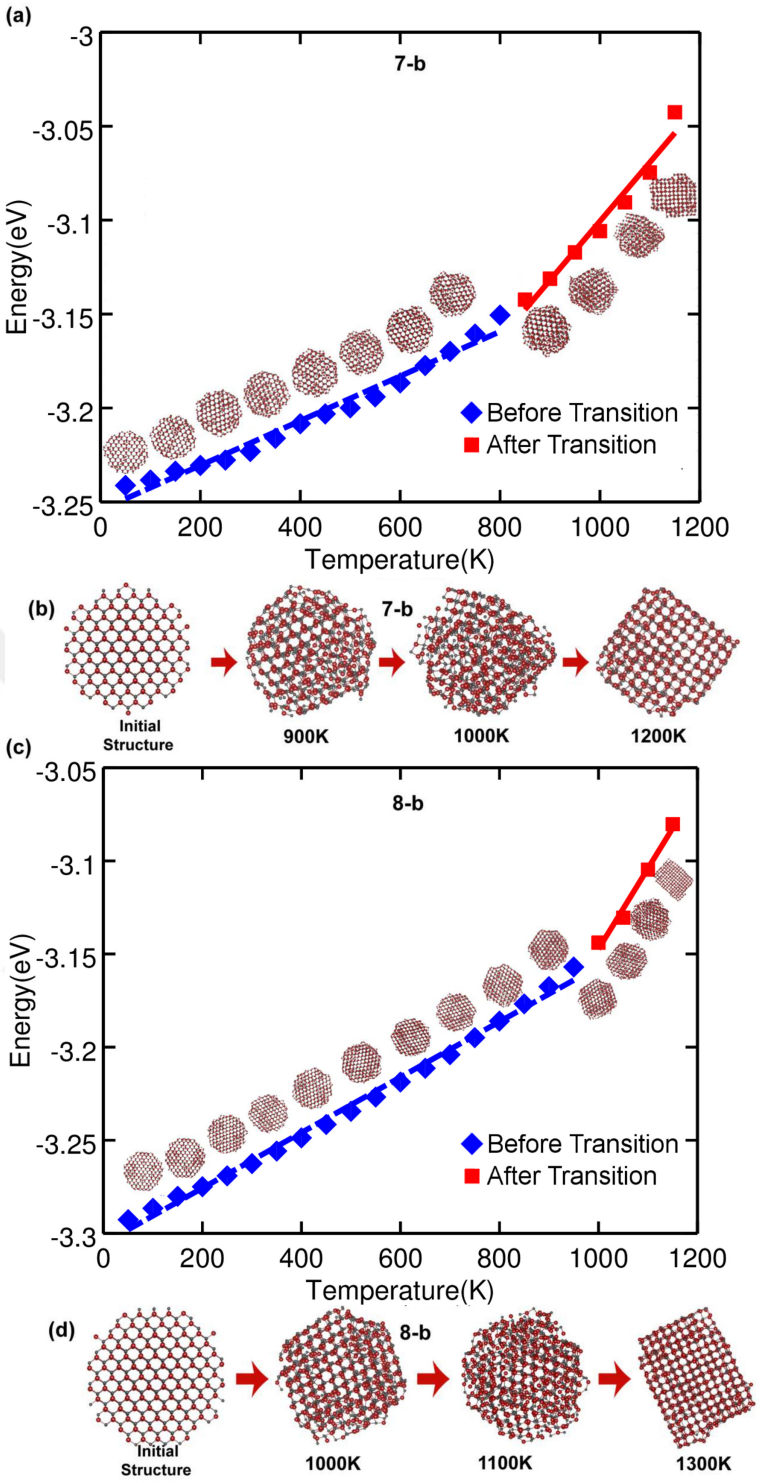


Figure 3.15: E vs T graphs (a and c) and phase transitions (b and d) for 7-b and 8-b NPs under non-equilibrated criterion (VESTA).

We suggest a function for the heat capacity with respect to the size (number of atoms, n) for both before and after transitions under equilibrium and non-equilibrated criteria

separately, as given in Table 3.18.

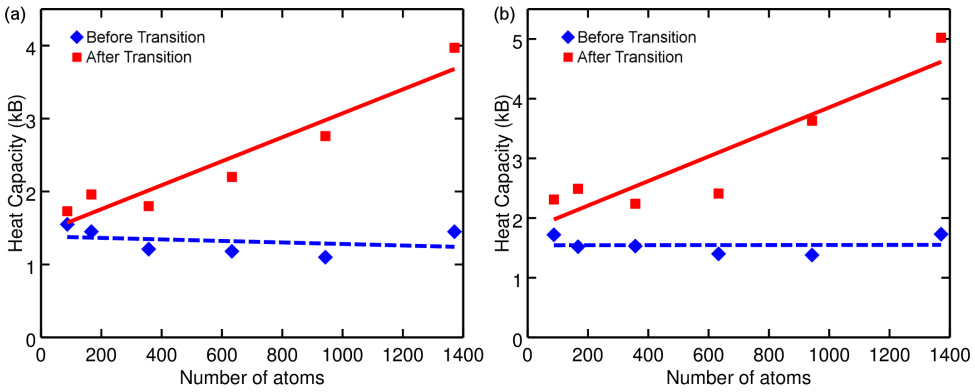


Figure 3.16: Heat capacity (in $k_B$) vs the number of atoms graph for InP NPs under (a) equilibriate and (b) non-equilibrated criterion.

Table 3.18: Heat capacities ($C_v(n)$, in terms of $k_B$) of the InP NPs as a function of number of atoms (n) for before (B) and after (A) the phase transitions under both equilibrium and non-equilibriated criteria.

| InP NPs | Equilibrium | Non-equilibrium |
|---|---|---|
| B | $C_v = -0.000104{*}n + 1.39$ | $C_v = 0.000005{*}n + 1.54$ |
| A | $C_v = 0.001642{*}n + 1.43$ | $C_v = 0.002056{*}n + 1.80$ |

## 3.4 Concluding remarks

The structural properties of the InP NRs and NPs are investigated via MD simulations using the potential developed by Branicio et al. for In-P systems [19]. The computations were realized under the equilibrium and non-equilibrated criteria for both nanostructures. By the results throughout this chapter, we can draw the following conclusions: The ZB phase was the unstable phase for the InP NRs because the RS phase appeared immediately after the first run in all of the simulations. So it was determined that the WZ phase was more favourable than the ZB phase for the NRs as in DFT calculations [63]. For both types of the NRs in ZB and WZ forms, the phase transition temperatures increase with increasing of the NRs' thicknesses. Heating the WZ and the ZB NRs without stretching resulted in the complete transition to the RS phase at higher temperatures. In the WZ NRs, the regions at the kinks al-

ways undergo the RS transition to counter the shear. When the systems completely transformed, the segmented formation of the WZ NRs was observed due to stacking faults. In the thicker WZ NRs, stacking faults prevent the reversibility. To remove the stacking faults and thus, to restore the reversibility of the NRs, cooling, expansion and stretching processes were successfully applied. In contrast to the ZB NR structures keeping rigid under stretching, the WZ NRs countered the strain on the kink regions by transforming into the RS phase. Various phases have also been observed under specific conditions: when the ZB NRs were put under strain, the phase sequence was usually observed to be as ZB $\rightarrow$ RS $\rightarrow$ WZ. The occurrence of the WZ phase in the ZB NRs depends on the stretching ratio, the NR's thickness and the temperature. The WZ NRs undergo irreversible WZ $\rightarrow$ RS phase transition under stretching at increasing temperatures with the non-equilibrated approach while both reversible and irreversible phase transitions are observed when the equilibrium criterion is applied at the constant temperature. The phase of the system was the decisive factor in the breaking process: For the RS phase, a single atom chain occurs in the thinning region without any inclination due to stretching while an elongation and inclination towards the breaking point were observed for the WZ and ZB phases. In addition, the strain is a procedure being a direct factor in lowering the transition temperature for the WZ NRs. Upon cooling the WZ NRs that were treated to gradual heating before, some of the NRs that had partially transformed to the RS phase recovered their WZ structure depending on their initial temperatures and RS regions at the beginning of the cooling, while the NRs which had been fully transformed to RS phase kept their configuration, they manifest irreversible phase transition. We can conclude that the phase transition temperature and the regions in the RS structured have a direct effect on the direction of the transition. As the compression procedure was performed on the WZ NRs with different thickness, crucial results were observed: only thinner NRs which were initially non-deformed exhibited elastic behavior at low temperatures under compression. When these compressed NRs were stretched back at the same temperature, the thinner NRs perfectly recovered their non-deformed states. In addition, both the thinner and thicker NRs at high (constant) temperatures exhibited cyclic phase transitions between the WZ and RS phases until the deformation and/or fragmentation of the NRs take place during the compression procedure. Also, the ZB phase was observed just before the disintegration only in NRs with small cross

section area. Elastic behavior of the thinner WZ NRs at low temperatures under compression and the observed reversible phase transitions in the WZ NRs under various processes (cooling, stretching, expansion and compression) are significant properties for the memory and mechanical energy storage applications. So, due to the excellent mechanical properties, InP NRs are promising candidates for many such applications and they demand further theoretical and experimental investigations.

As for InP NPs, we further investigated the relationship between the size and the heat capacity for the InP spherical NPs via molecular dynamics. The computations were realized under both equilibrium and non-equilibrated criteria as in InP NRs. During the simulations executed in various degrees of temperature ranging from 0.7 K to 1300 K, phase transition from the ZB structure to the RS structure was observed. Therefore for each the NP, two different heat capacities were calculated for both before and after the transition; thus it was found that the phase of the structure plays a direct role in the heat capacity. Moreover, the relationship between the size and the heat capacity for the InP spherical NPs was constructed. There is linear dependence between the heat capacity and the size after transition under both equilibrium and non-equilibrated criteria. However, the heat capacity looks nearly constant before transition under both two criteria.

# CHAPTER 4

# LIQUID PHASE EPITAXIAL GROWTH OF Ge on $SiO_2$

## 4.1 Introduction

Silicon ($Si$)-based CMOS (commercial Complementary Metal Oxide Semiconductor) technology has reached its geometrical scaling limits, which led to exploring novel materials in the industry. For decades, germanium (Ge) being the chemical analogue of Si had not been preferred in the semiconductor technology due to the instability and low quality of its native oxides [112]. Nonetheless, the key development in high-k dielectric technology which solves the issues related to oxides of Ge encountered in the manufacturing technology has reopened the door to Ge [113–116]. Thus, Ge has reemerged as a promising candidate for CMOS technology because of its larger charge carrier mobility and smaller band gap compared to $Si$, and its favorable strain induced optical properties such as indirect-to-direct band gap transition [117–126]. To establish high-mobility Ge-based CMOS, the formation of high-quality Ge MOS interfaces is of great interest in the technology. In particular, Ge/oxides interfaces such as Ge/$SiO_2$ etc. have received considerable attention for the growth of single crystal Ge. In this regard, Ge on insulator (GOI) on the silicon wafers has been proposed as a suitable device enabling the fabrication of the single crystal Ge in a cost-effective way by reducing the demand of the Ge films [127]. Ge condensation [128, 129], layer transfer [129], lateral solid phase epitaxial (L-SPE) growth [130–132] and lateral liquid phase epitaxial (L-LPE) growth [133–139] are commonly used for the fabrication of GOI devices. Among these approaches, the L-LPE technique takes the advantages of other methods since it enables to fabricate a high-quality single $c - Ge$ by eliminating the crystal defects originated from the thermal and lattice mismatching between Ge and Si (Fig. 4.1) [133, 135–139].

In the L-LPE method illustrated in Fig. 4.2, amorphous $SiO_2$ (a-$SiO_2$) is deposited on a Si substrate, into which a seed window is opened and filled with amorphous Ge (*a*-Ge) thin film, forming a contact surface with Si and Ge. After the deposition, a stripe region is also filled with *a*-Ge film, and the sample is coated with the a-$SiO_2$. Upon subjecting the system to rapid thermal annealing above the melting temperature of $Ge$ and then cooling down naturally to the room temperature, amorphous $Ge$ ($a-Ge$) encapsulated in the insulator is first vertically grown through the seed window by taking up the crystal orientation of the $Si$ seed and propagates laterally along the stripe. Fig. 4.2-b shows the reason why this method is chosen in the fabrication of the $c-Ge$. In this figure, threading dislocations arising from the lattice-mismatching between $Si$ and $Ge$ are trapped in the seed window and forced to terminate at $Ge$/a-$SiO_2$ interface. Thus, the single $c-Ge$ films without the defects such as dislocations [135, 140–142] are successfully achieved in the stripes.

In the experiments, nearly defect-free single $c-Ge$ film has been experimentally fabricated in the system coated with $a-SiO_2$ insulator by this technique [133, 135, 137]. However, $c-Ge$ films with widths greater than $5\mu m$ could not be attained due to the agglomeration and random crystal nucleation of $c-Ge$ atoms [133].

### 4.1.1 Aims and Goals of the work

To understand the growth mechanism of $Ge$ in the L-LPE on the atomistic level is of great importance for the experimental studies to fabricate the large area ($> 5\mu m$) single crystal Ge. However, even though several experimental works have been conducted on the growth of $Ge$ in L-LPE system in many aspects, there has been no theoretical study reported so far. In this thesis, we developed two different ReaxFF force fields for Si/O and Ge/O against to Density Functional Theory (DFT) and experimental data to provide a more generalized description for the configuration of L-LPE coated with the insulator of $a-SiO_2$, and to investigate the growth dynamics of $Ge$ on the atomistic level.

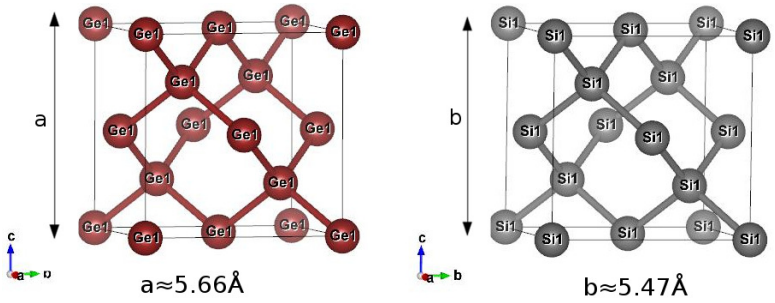


Figure 4.1: The unitcells of Ge and Si in the diamond phase with lattice constants of 5.66 and 5.47 Å, respectively(VESTA).

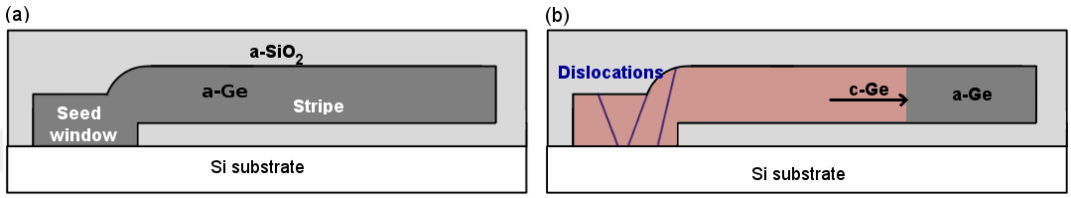


Figure 4.2: Schematic cross-sections of (a) the initial configuration of L-LPE system where the insulator is defined to be amorphous $SiO_2$ ($a - SiO_2$), and (b) the crystallization process of a-Ge where the growth initiates at the Si seed, propagates along the stripe. During the growth, the dislocations indicated by blue lines are forced to terminate at the oxide walls by trapping them in the seed window.

The rest of chapter is mainly divided into two sections: (i) In Section 4.2, we report the computational details of our the ReaxFF force field parametrization for Ge/O [143] and Si/O [144]. We further discussed the ability of the advanced versions of two different ReaxFF force fields on the basis of our MD simulations. (ii) The final section of this chapter is dedicated to our concluding remarks.

## 4.2 The ReaxFF force field development for L-LPE system

The L-LPE system composed of Si/O/Ge interatomic interactions requires a force field describing the Si/Ge, Ge/O, Si/O and Si/O/Ge interactions besides Si, Ge, and O atomic contributions. Psofogiannakis et al. [145] developed the force field for Si-Ge alloys parameters. In this thesis, we also improved the force fields for Si/O and Ge/O cross-interactions in the L-LPE system and validated them with MD simulations.

### 4.2.1 ReaxFF development for Ge/O interactions in L-LPE system

This subsection reports the improvement of the force field description developed by Zheng et al. [146] with a particular focus on O-interstitial diffusion in Ge. In a manner conforming to DFT reports [147, 148], O-interstitial configurations and minimum energy migration pathway in the asymmetric configuration were included in the original training set taken from Ref. [146]. To establish the force field reliability, MD simulations were performed to investigate the diffusion mechanism under different temperatures. Furthermore, we simulated $GeO_2$/Ge(100) interface and compared the ReaxFF with Tersoff potential in terms of their ability to describe the theoretical diffusion mechanism at the temperatures ranging between [800-2000 K]. We also generated an amorphous $GeO_2$ and evaluated its structural properties for further validation of the new ReaxFF model.

#### 4.2.1.1 Computational Methods

#### 4.2.1.2 Force Field Parameterization

The ReaxFF force field previously reported by Zheng et al. [146] ($ReaxFF_{GeOH2017}$) enabled simulation of GeO and $GeO_2$ crystal structures besides surface chemistry of Trimethylamine and $H_2O$ chemisorption on Ge and $GeO_2$/Ge surfaces. We also expanded the force field description to the simulations of the O-diffusion in diamond Ge under varying temperatures. For the force field parametrization, the volume/energy equation of state is essential data to obtain a realistic description of the bulk properties of the condensed phase in MD simulations. The heat of formation ($\Delta H_f$) is another crucial parameter required for the training set to describe the formation and stability of condensed phases in the force field. It provides information about the amount of the energy absorbed or released of the heat during the formation of a compound from its components under the same temperature and pressure conditions. The original training set taken from Ref. [146] includes a set of equations of state which is established by calculating the total energy of a primitive unit cell under expansion and compression of the lattice volume, and heats of formation of GeO and $GeO_2$ condensed phases as well as the molecular data containing dissociation energies for single and double

bonds of Ge and angle distortion of O-Ge-O. Additionally, we included the formation energies of the different interstitial configurations [147] and the minimum energy migration pathway of O in diamond Ge in line with DFT results [148]. On the basis of the augmented training set, we re-parametrized the $ReaxFF_{GeOH2017}$ force field parameter values by using a single-parameter search optimization method. During the optimization, only Ge-O bond and off-diagonal, and Ge-O related valence angle parameter values were modified by minimizing the sum of the squared error between ReaxFF values and Quantum Mechanic (QM) data until ReaxFF approaches the values of QM methods. The following sections give the details of QM data including the training set and the results of the newly developed ReaxFF.

#### 4.2.1.3 Point Defects

Point defects play a profound role in the kinetics of diffusion and oxidation reactions observed in solid phases. Diffusion of the light impurity atoms (or their vacancies) such as O, occurs through local point defects in the structure. Typically, the migration of an impurity atom in the condensed phase happens by a jump between two neighboring unoccupied interstitial centers. During the jump, the atom goes through the transition state at a saddle point. In that regard, it is critical to describe the interstitial configurations involved in migration pathway based on the relative stability of different interstitial centers in Ge during the force field training.

**Interstitial Oxygen in Diamond Ge**

Interstitial atoms residing in highly symmetric sites in diamond Ge (and Si) have been commonly reported as: bond-centered (BC) between two neighboring host Ge atoms, hexagonal (H), tetrahedral (T) and split (S) in the literature [147, 149–151]. The point group of T site in Hermann-Mauguin notation is $4-3m$, that of BC and H is $-3m$, and point group of S site switches between $-42m$ and $3m$ depending on the atom [151]. Figure 4.3 illustrates the first three interstitial configurations in diamond Ge unit cell. The last one, S site, is illustrated in the next section. In this study, to achieve the force field correctly describing the relative stability order of the interstitial configurations as in DFT, four 3x3x3 supercells containing 216 atoms were built from the diamond Ge unit cell with a dimension of 5.76 Å. A single point defect was introduced in each

supercell through an additional O atom individually positioned at the BC, S, T and H sites in the matrices. For the BC configuration, one of the Ge-Ge covalent bonds lying on (110) plane was broken and an O atom was situated at the position making an angle of 44.8 with respect to [001] direction, between adjacent two Ge atoms by forming Ge-O bond length of 1.77 Å [148]. The S site is at a position making an angle of 20.6 with respect to [001] direction, where the distances between the O atom and its left, center and right Ge neighbors are 1.83, 1.85 and 2.35 Å, respectively, as in DFT [148] (Fig. 4.4-b). T and H interstitials reside in the positions of (1/4, 3/4, 3/4) and (3/8, 5/8, 5/8) in terms of the fractional coordinates, respectively (Fig. 4.4-c and d).

The following energy formula was introduced in the training set for the calculation of the interstitial formation energy:

$$E_{form,ins} = E_{(Ge+O)} - (E_{Ge} + 1/2E_{O_2}) \tag{4.1}$$

where $E_{(Ge+O)}$ is the total energy of the system consisting of bulk Ge with an additional O atom, and $E_{Ge}$ and $E_{O_2}$ are the reference energies of the bulk Ge and $O_2$ molecule.

Furthermore, to derive the QM energies and the structures of the interstitials, the force field was augmented with an additional bond-restraint force which was applied only to the Ge-O bond distances while keeping relaxed the remaining internal coordinates for the intermediate points, except for the H configuration. For the BC (Fig. 4.4-a and c) and S (Fig. 4.4-b) configurations, the bond restraint was also applied to the Ge-Ge bond distances between the center and right, and the center and left Ge atoms surrounding O atom. During the calculations, the restraint energy is computed by considering the following equation:

$$E_{restraint} = k_1 * [1.0 - e^{k_2 * (r_{ij} - R_{restraint})^2}]$$

where $k_1$ and $k_2$ are the constants with units of kcal/mol and $Å^{-2}$, $R_{restraint}$ is a QM distance between two atoms of interest, and it is gradually shifted by $r_{ij}$ at every iteration. In this study, bond restraint constants were set at the values of 200 kcal/mol

and 1 $Å^{-2}$ for the BC and S sites. For the T site, the values of $k_1$ and $k_2$ are 400 kcal/mol and 2 $Å^{-2}$, respectively. During the calculations, $r_{ij}$ value was set to 0.0 to keep the distances at value of $R_{restraint}$.

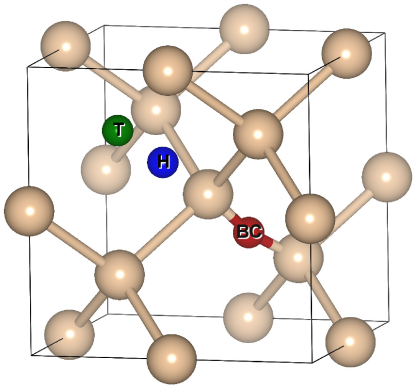


Figure 4.3: Ball-stick representation of $O$-interstitial configurations in the unit cell of $Ge$ where green, blue and red represents T, H and BC sites, respectively (VESTA).

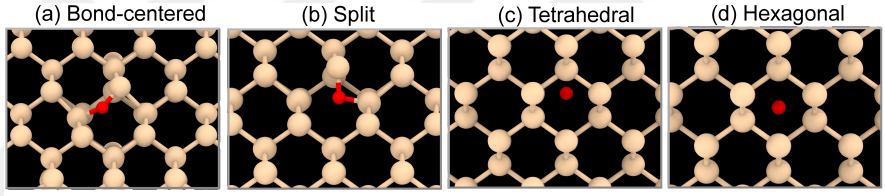


Figure 4.4: Ball-stick representation of O-interstitial centers in the supercell. (a) Bond-centered, (b) split, (c) tetrahedral and (d) hexagonal O-interstitial sites in bulk diamond Ge (OVITO).

### Migration pathway of O atom in diamond Ge

As reported by DFT works [147, 148], the O atom, first, resides in the bond-center position by breaking a covalent bond between two host Ge atoms, and diffuses between two neighboring bond-centered sites by going through the transition state. It was broadly accepted that the transition state for O-diffusion in Ge (and Si) has a saddle point configuration lying midway between two neighboring bond-centered sites, called as symmetric transition state [152–154]. However, a recent DFT study [148] proved the contrary that an asymmetric configuration of the diffusion mechanism (Fig. 4.5-b) brings the theoretical energy barrier in much closer agreement with experiment [155–157] rather than the symmetric consideration (Fig. 4.5-c).

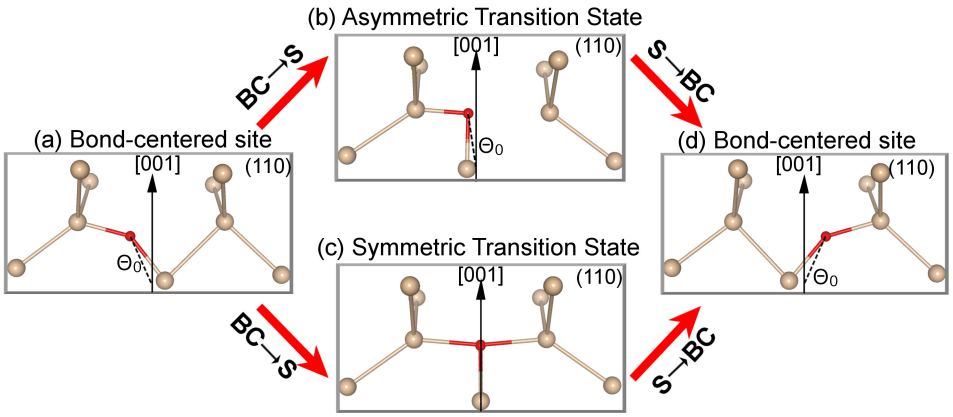


Figure 4.5: Comparison of asymmetric ($a \rightarrow b \rightarrow d$) and symmetric ($a \rightarrow c \rightarrow d$) transition pathways of O- interstitial in the Ge unitcell. O-atom diffuses between two neighboring bond-centered sites (a and d), and goes through the transition state at a saddle point (b and c) where BC, S and Θ located on (110) plane represent the bond-centered and split sites, and the angle of O atom with respect to the [001] direction, respectively (VESTA).

In this study, the minimum energy pathway of interstitial O in Ge was derived in a manner described in previous DFT work [148]. Nine interstitial configurations involving two adjacent BC and S sites were determined along the migration pathway as illustrated in Fig. 4.6. In the same fashion with the BC and S configurations mentioned in the previous section, additional six 3x3x3 supercells were constructed from the Ge unit cell, and an O atom was individually positioned at each specified site along the pathway of $BC \rightarrow S \rightarrow BC$ in the supercells. In each network, O atom and three surrounding Ge atoms to O were located on (110) plane along the [001] axis as represented in Figure 4.6. Note that the presence of O atom neighboring two host Ge atoms causes to slight distortions of the Ge atoms from their ideal sites because of the formations of Ge-O bond and Ge-O-Ge angle between them.

#### 4.2.1.4 MD simulations

**Temperature dependence of O-interstitial diffusion**

To reveal the temperature dependence of the O-diffusion, a series of simulation were also performed under various temperatures based on both versions of ReaxFF and

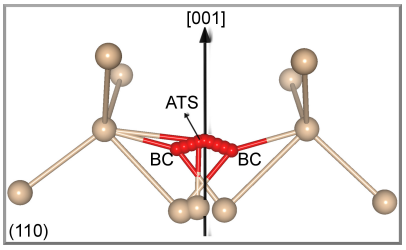


Figure 4.6: Ball-stick representation of minimum energy migration path of O-interstitial in the Ge unit cell on (110) plane in [001] direction where BC and ATS represent the bond-centered site and the asymmetric transition state occurring at the split site, respectively, derived from Ref. [148] as an input data for the force field training set (VESTA).

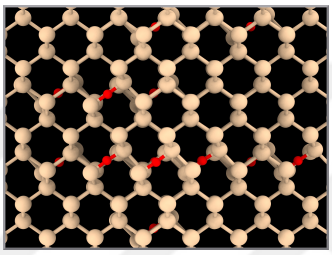

Figure 4.7: Initial configuration of Ge matrix containing 14 O-interstitial atoms located at BC sites (OVITO).

Tersoff. For this aim, a 4x4x4 supercell containing 512 Ge atoms was constructed from the diamond Ge unit cell, and 14 O atoms were randomly incorporated as the interstitial defect at the BC sites in the system as illustrated in Fig. 4.7.

Periodic boundary conditions were imposed in all simulations and a velocity-Verlet algorithm was employed to integrate Newton's equation of motion. An unwrap function for the calculation of a not-back translated trajectory [158] was also implemented in the program with an additional keyword in ReaxFF control file in order to remedy the effect of the periodic boundary conditions on the trajectory. Whereupon minimizing the total energy of the system to remove the overlaps, the system was subjected to two consecutive steps at the target temperature ranging from 800 to 2000 K in an NVT ensemble, regardless of the force field. In the first simulation stage we applyed a Berendsen thermostat with a coupling constant of 100 fs, thus hearing up the matrix to the target temperature with a temperature gradient of 0.01 K/step, and equilibrated for 1 ns. This step is required to reduce the memory effects regarding the possible crystal defects in the initial structure on the system. After achieving the equilibrium

position, in the second stage the computational box was maintained at a constant temperature for 3.5 ns with a relatively larger coupling constant of 1000 fs to achieve weakly-coupled system to the bath. In this step, the unwrapped trajectories were collected at every 100 MD frames for the calculation of interstitial-mediated diffusion coefficient. At each temperature, the diffusion coefficient averaged over all O atoms in Ge was calculated using Einstein relation [159] as shown in Eq. 4.2. The activation energy, $E_a$, and diffusion pre-factor, $D_0$, were obtained by plotting the logarithm of the diffusion coefficient against the reciprocal of the temperature within the target temperature range as described in Eq. 4.3:

$$D(t) = \frac{1}{2d} \lim_{t \to \text{inf}} \frac{d}{dt} < (r_i(t) - r(0))^2 > \tag{4.2}$$

$$D = D_o e^{-\frac{Ea}{RT}} \tag{4.3}$$

$$In(D) = In(D_o) - \frac{E_a}{RT} \tag{4.4}$$

where $r_i(t)$ is the position of O atoms $i^{th}$ at the time t, d is the dimension and $< (r(t) - r(0))^2 >$ is the mean square displacement (MSD) with respect to the reference particle. The activation energy, $E_a$, required to achieve the transition state during the diffusion was computed by an Arrhenius-type expression.

In this study, MD simulations based on ReaxFF and Tersoff were performed using ADF/ReaxFF [160–162] and LAMMPS [163], respectively.

**$GeO_2$/Ge interface**

We also performed MD simulations of the quartz-$GeO_2$/Ge(100) systems for further validation of our force field parametrization. To model quartz-$GeO_2$/Ge(100) interface, a Ge substrate containing 3700 atoms in the dimensions of 47.5x49.5x35.5 $Å^3$ was generated from the diamond unit cell with a lattice constant of 5.76 Å. A quartz-$GeO_2$ slab was deposited on the diamond Ge matrix normal to z-axis by leaving a gap of 2 Å. The total system comprising 8577 atoms was established in a periodic 47.5X49.5X35.5 $Å^3$ computational box. By applying Berendsen thermostat with a

damping constant of 100 fs in an NVT ensemble, the system was heated up to the different temperatures ranging between 900 and 1800 K with a temperature gradient of 0.01 K/step and equilibrated for 0.5 ns based on ReaxFF and Tersoff. Velocity-Verlet algorithm was used to integrate Newton's equation of motion.

**Amorphous $GeO_2$**

A $SiO_2$ glass with a density of 2.21 g/cm$^3$, whose preparation detail is presented in Sec. 4.4.1.3, was taken as a reference and Ge atoms were replaced with Ge atoms. A structural relaxation of the atomic positions was performed at 300 K in an NPT ensemble for 0.5 ns in order to obtain a $GeO_2$ glass.

### 4.2.2 Results and Discussions

#### 4.2.2.1 Parameterization of the force field

Table 4.1 shows the formation energies of the interstitial configurations predicted by ReaxFF$_{present}$, DFT and experiment where the energy of BC site is taken as a reference energy.

Table 4.1: Formation energies (in kcal/mol) of O-interstitial configurations in bulk diamond Ge reproduced by ReaxFF$_{present}$, DFT [147] and Experiments [155–157].

| | BC | S | T | H |
|---|---|---|---|---|
| $ReaxFF_{present}$ | 0 | 51.4 | 55.5 | 56.6 |
| DFT [147] | 0 | 48.0 | 56.0 | 57.0 |
| Exps. [155–157] | - | 47.2 | - | - |

After the optimization of the reactive force field against to the QM-based augmented training set, the ReaxFF$_{present}$ reproduces the stability of the interstitials in a correct energy ordering from most stable to least stable site to be $BC \rightarrow S \rightarrow T \rightarrow H$ as displayed in Table 4.1. Furthermore, it correctly predicts the energies of S, T, and H interstitials as 51.4, 55.5 and 56.6 kcal/mol with a acceptable difference from DFT by 2.6, 0.5 and 0.4 kcal/mol, respectively.

The graph displayed in Fig. 4.8 gives additional support to Table 4.1. As evident from the graph, our reparametrized version of Ge/O ReaxFF is in qualitative agreement with theory and the corresponding experimental result by predicting the energy barrier

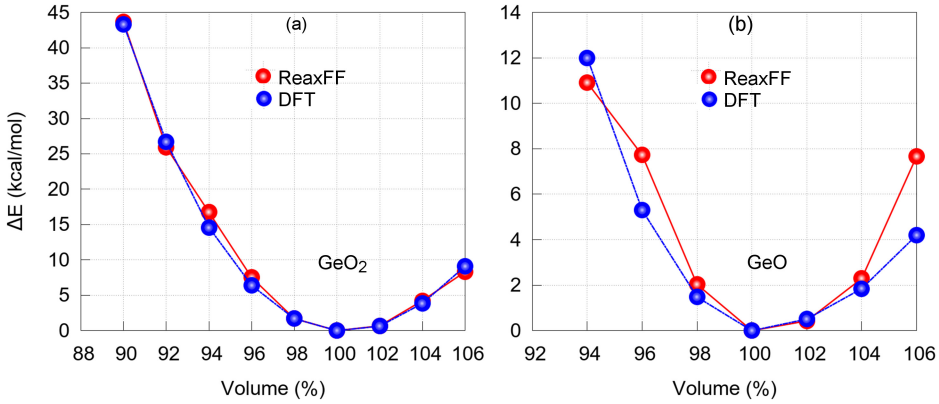


Figure 4.9: Equations of state of $GeO_2$ and GeO reproduced by ReaxFF and DFT [146].

to be 51.4 kcal/mol with a slight shift from DFT and experiment by 2.6 and 4.2 kcal/mol, respectively. Note that the difference between the energies of the S and BC in Table 4.1 simply corresponds to the energy barrier. Furthermore, $\text{ReaxFF}_{present}$ successfully describes the transition state in an asymmetric geometry as identified in the DFT work [148].

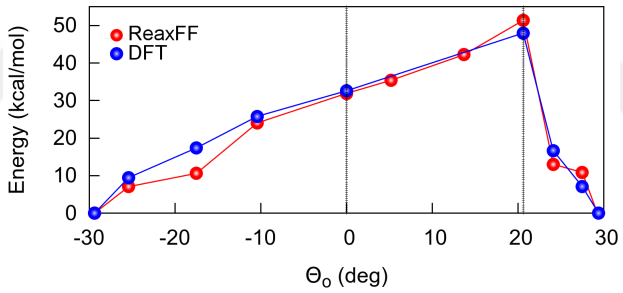


Figure 4.8: Energy of O-interstitial diffusing between two neighboring BC sites in the (110) plane in the Ge matrix, estimated by DFT [148] and $\text{ReaxFF}_{present}$. $\Theta_0$ is the angle of O atom with respect to [001] axis

**Equations of state and Heats of formation for Ge/O condensed phases**

Fig. 4.8 shows the ReaxFF and QM energy/volume curves calculated for the equations of state of GeO and $GeO_2$. According to the graphs, ReaxFF and QM exhibit a very good agreement for the equations of state of the supercells. The expansion/compression energies of $GeO_2$ perfectly fit to QM. Within a 6% volume variation from the equilibrium state, the maximum energy differences calculated by QM and ReaxFF for GeO are less than 4 kcal/mol.

Table 4.2: Heats of formation (in kcal/mol) of diamond Ge, GeO and $GeO_2$ predicted by ReaxFF and DFT [146].

| $\Delta H_f$ | ReaxFF | DFT [146] |
|---|---|---|
| Ge | -86.78 | -85.95 |
| GeO | -50.32 | -50.57 |
| $GeO_2$ | -108.51 | -107.91 |

Tab. 4.2 represents ReaxFF and QM heats of formation of diamond Ge and Ge oxides. Three crystal phases are successfully reproduced by ReaxFF with a difference of less than 1 kcal/mol from DFT [146].

$ReaxFF_{present}$ force field parameters developed in this work are supplied in Appendix B.

#### 4.2.2.2 ReaxFF MD simulations

**Temperature dependence of O-diffusion in Ge**

To further assess the quality of the re-parametrized ReaxFF description, the diffusion of O-interstitial in Ge was studied under different temperatures ranging from 800 K to 2000 K, as mentioned the computational details in Sec. 4.2.1.4. The results were compared with those of Tersoff potential as depicted in Fig. 4.10, Fig. 4.11 and Fig. 4.12. On the basis of our results, O-diffusion commences in our simulation time scales at temperatures over 1076 K and 1126 K in ReaxFF and Tersoff-based simulations, respectively. Regardless of the force field, up to that temperatures, O atoms occupying BC sites on place, they can not hop to the other BC sites because of not having required energy to reach the transition state. At 1200 K, O atoms jump to the next BC sites being a most energetically favorable site by both ReaxFF and Tersoff. However, the diffusing atoms still do not have enough energy for a second jump, they are likely trapped by the adjacent Ge atoms. When the temperature reaches 1300 K, the atoms begin to further diffuse between the neighboring BC sites.

However, at 1400 K, the diffusion behavior of O atom shows discrepancy depending on the force field. ReaxFF still follows the theoretical O-diffusion mechanism [147, 148]. Furthermore, even at high temperatures such as 1700 and 2000 K, ReaxFF has

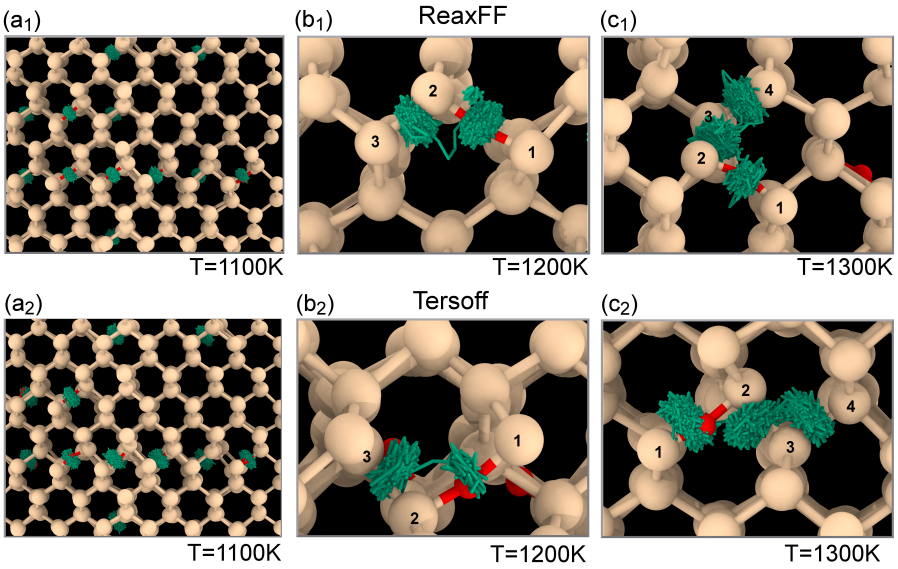


Figure 4.10: Snapshots taken from the final MD steps of the simulations by $ReaxFF_{present}$ ($a_1$, $b_1$ and $c_1$) and Tersoff ($a_2$, $b_2$ and $c_2$) at the temperatures up to 1400 K where white and red spheres are Ge and O atoms, and green line represents the diffusion trajectory of O atom between the numbered Ge atoms. O atom jumps between the neighboring BC sites regardless of the force field (OVITO).

the ability to mimic the diffusion mechanism reported in DFT [147, 148] regardless of the temperature. However, at the temperatures over 1400 K, the Tersoff potential begins to produce a diffusion along a pathway involving BC, H and T sites. As evident from Fig. 4.11-$b_1$ and $b_2$, O atoms hop from BC site to H or T site, then to BC site. We can infer from the results that Tersoff potential is unable to correctly describe the diffusion mechanism in the way indicated by literature [148]. We may ascribe the reason of the inconsistent diffusion pathway by Tersoff with literature to an incorrect relative stability ordering of the interstitial configurations.

Figure 4.8 also shows the temperature dependence of diffusion coefficient computed by using the slopes of MSD plots produced by ReaxFF and Tersoff (Fig. 4.13).

The calculations reveal that both the Tersoff ReaxFF and the ReaxFF potentials produce a relationship between temperature and diffusion coefficients that is supported by experiments [155–157]. The ability of ReaxFF to mimic the O interstitial diffusion in Ge was further proved with the diffusion barrier derived from the arrhenius equation 4.3. ReaxFF predicts an energy barrier within the temperature range of

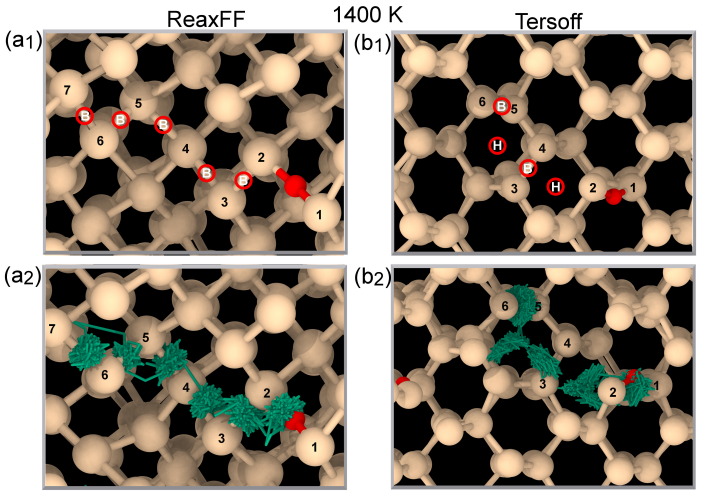


Figure 4.11: Snapshots taken from the final MD steps of the simulations by $ReaxFF_{present}$ ($a_1$ and $a_2$) and Tersoff ($b_1$ and $b_2$) at 1400 K where white and red spheres are Ge and O atoms, red circles around B and H sites in $a_1$ and $b_1$ are the sites that O atom pass through during the diffusion, and green line in $a_2$ and $b_2$ represents the diffusion trajectory of O atom between the numbered Ge atoms. ($a_1$) ReaxFF results that O atom jumps only between the neighboring BC sites ($b_1$) while Tersoff reproduces the O-diffusion along a pathway between B and H sites at 1400 K (OVITO).

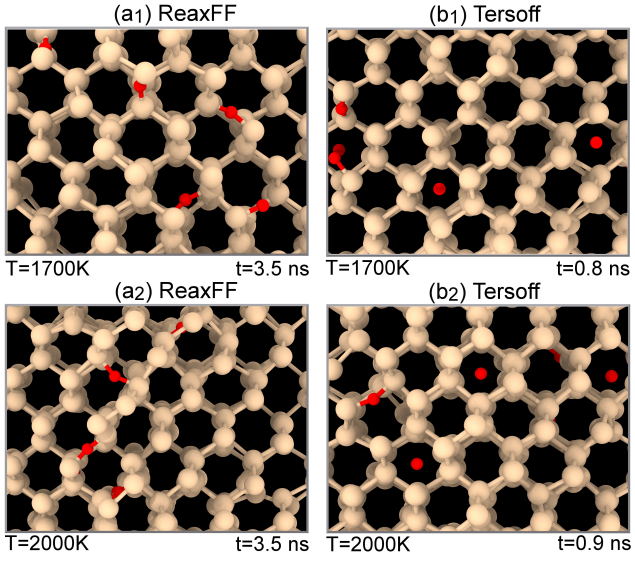


Figure 4.12: Snapshots taken from the final MD steps of the simulations by $ReaxFF_{present}$ ($a_1$ and $a_2$) and Tersoff ($b_1$ and $b_2$) at the temperatures over 1400 K where white and red spheres are Ge and O atoms (OVITO).

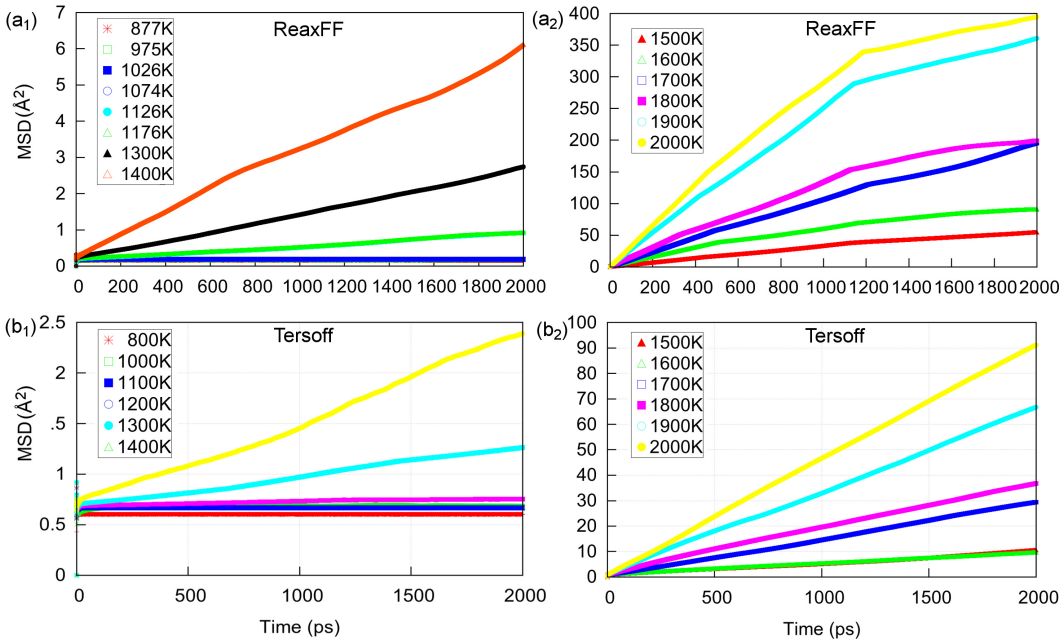


Figure 4.13: MSD profiles produced by the advanced version of ($a_1$ and $a_2$) ReaxFF and ($b_1$ and $b_2$) Tersoff at given temperatures.

[800-2000 K] to be 50 kcal/mol with a modest deviation of 3 kcal/mol from the experiments [155–157] while Tersoff potential predicts an energy barrier of 42 kcal/mol which differs from the experiment by around 5 kcal/mol (Tab. 4.3).

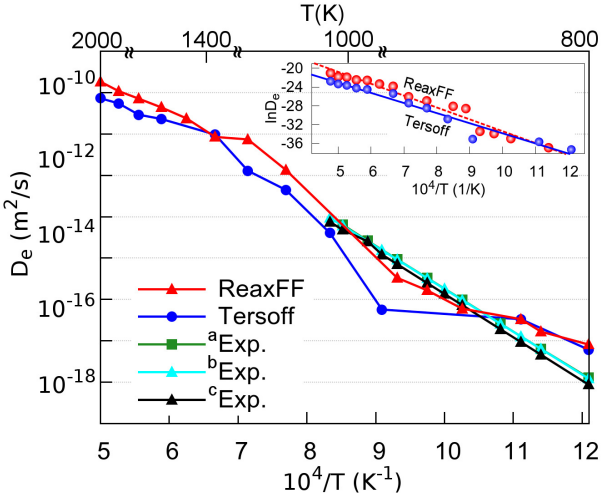


[155–157].

Figure 4.14: Arrhenius plot of the O-interstitial's diffusion coefficient in Ge computed by the advanced version of ReaxFF, Tersoff and experiments (Reference a: [157], Reference b: [156, 157], Reference c:

Table 4.3: Activation energy ($E_a$) of O-diffusion in Ge predicted by ReaxFF$_{present}$, Experiment [155–157] and Tersoff.

| | ReaxFF | Exp. [155–157] | Tersoff |
|---|---|---|---|
| $E_a$ (kcal/mol) | 50 | 47.2 | 42 |

The O-interstitial diffusion coefficient computed by ReaxFF within the given temperature range is determined as

$$D_e = 2.4\, exp[\frac{-50.02}{RT}]x10^{-2} \quad m^2/s$$

**Ge/GeO$_2$ interface**

According to the experimental studies [164, 165], even though $GeO_2$ is a chemical analogue of SiO$_2$, the reactions occurring at $GeO_2/Ge$ and $SiO_2/Si$ interfaces are different:

For the $GeO_2/Ge$ interface, the following reaction occurs:

$$Ge + GeO_2 \rightarrow 2GeO_2 + 2V_o \tag{4.5}$$

where $V_o$ represents an oxygen vacancy.

While for the $SiO_2/Si$ interface the following reaction is dominant:

$$Si + SiO_2 \rightarrow 2SiO \tag{4.6}$$

As evident from Eq. 4.5, the reaction triggers the formation of $GeO_2$ at the interface, so that causes the reduction of Ge mass, showing a discrepancy from the chemical reaction (Eq. 4.6) that happens at the Si/SiO$_2$ interface.

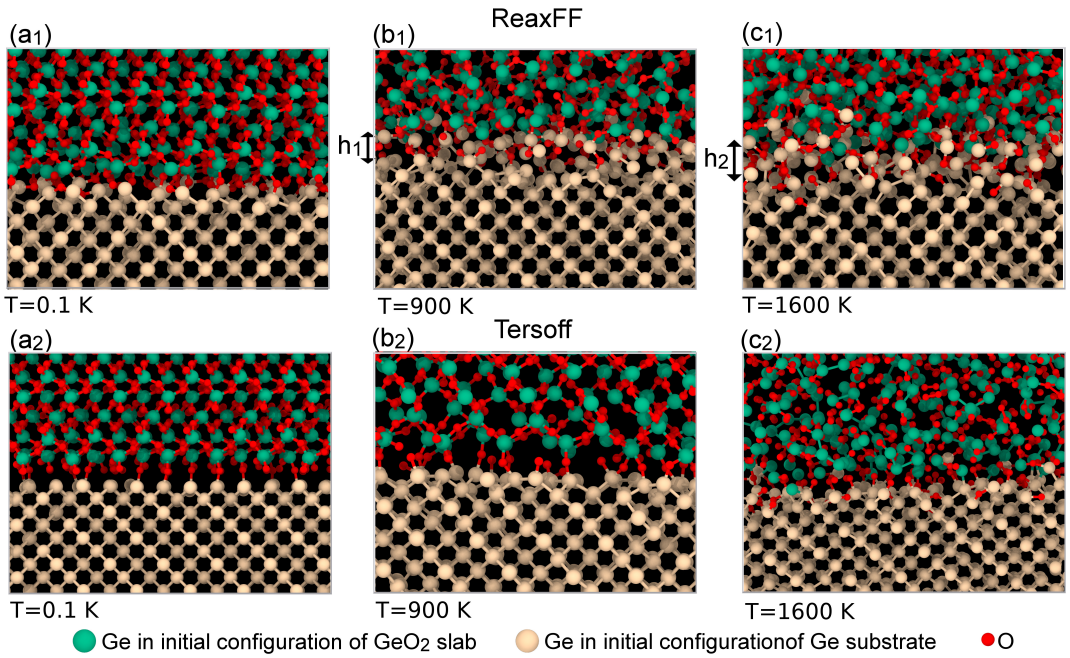


Figure 4.15: Snapshots taken from the MD simulations at given temperatures where green and white balls are Ge atoms initially located in $GeO_2$ and Ge slabs, respectively, and red ball is oxygen atom. $a_1$, $b_1$ and $c_1$ show the MD results based on ReaxFF and the figures in $a_2$, $b_2$ and $c_2$ illustrate the results of the Tersoff-based simulations (OVITO).

Fig. 4.15 shows the initial configurations and the results observed from the MD simulations of $GeO_2/Ge$ system based on ReaxFF and Tersoff potential under different temperatures. The ReaxFF results show that the Ge substrate is consumed depending on the annealing time and temperature while the thickness of $GeO_2$ increases which agrees very well with the experiments [166, 167]. However, during the Tersoff-based simulations, we observed a sharp interface between Ge and $GeO_2$, and the thickness of each slab does not change regardless of the temperature and the oxidation time. Fig. 4.15 also supports our findings that we observed in the ReaxFF and Tersoff simulations where $h_1$ and $h_2$ are the thickness of $GeO_2$ formation occurring at the interface, prompting a decrease in the thickness of the Ge substrate as a consequence of oxidation of Ge atoms coming from the substrate in the vicinity of the interface according to Eq. 4.5. However, Tersoff results for the Ge/$GeO_2$ interface shows similar behavior with Si/$SiO_2$ interface which contradicts the experiments [166, 167]. As illustrated in Fig. 4.15-$b_2$ and $c_2$, there are no Ge atoms that originates from the sub-

strate in the $GeO_2$ slab. This shows that $GeO_2$ and GeO formation does not occur even at the high temperature such 1600 K, instead, O atoms diffuse into Ge substrate without causing a consumption of the substrate.

The graphs displayed in Fig. 4.16 also gives an additional support to the results illustrated in Fig. 4.15. As seen from Fig. 4.16-a and b, ReaxFF reproduces the experimental result [166] an increase of the thickness of the $GeO_2$ slab with temperature and time while our Tersoff- based simulations find that the thicknesses of both Ge and $GeO_2$ slab stay the same during the simulations (Fig. 4.16-c and d).

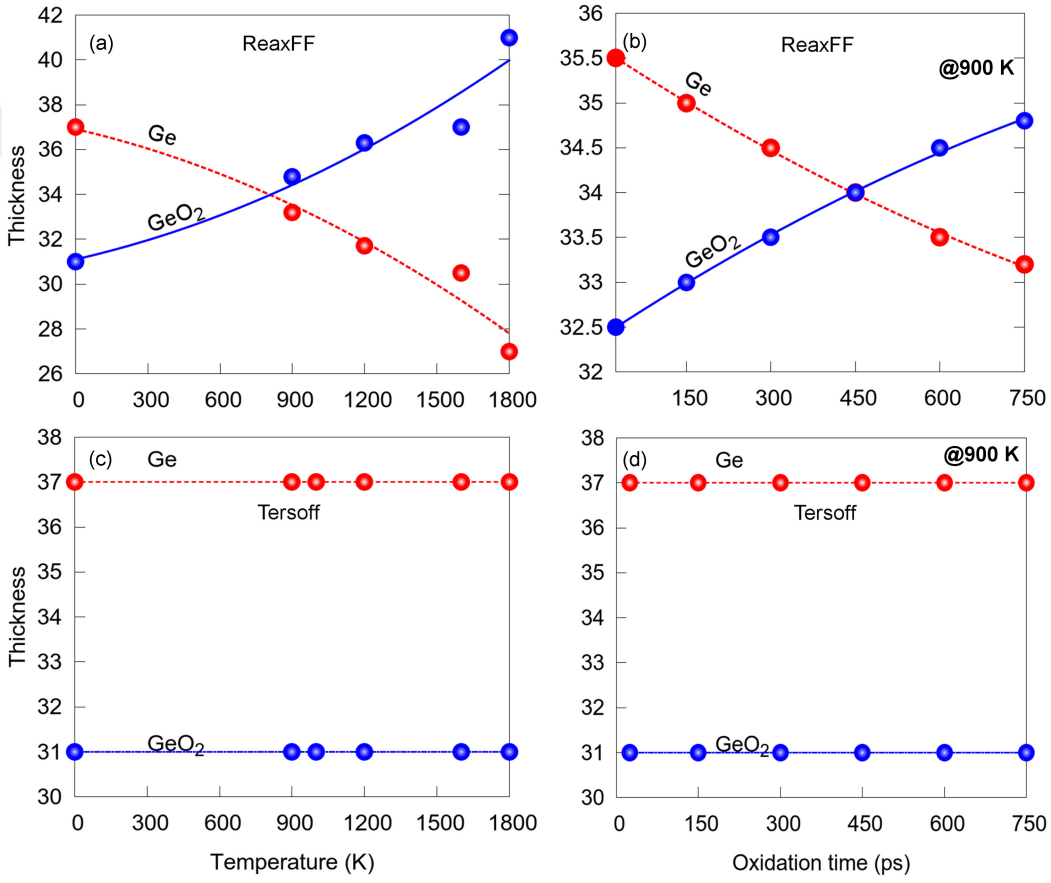


Figure 4.16: $GeO_2$ and Ge thicknesses in $GeO_2$/Ge(100) depending on the coordination number, oxidation time and temperature. a and b show the MD results based on ReaxFF and the graphs in c and d display the results of the Tersoff-based simulations.

### Amorphous $GeO_2$

The structural properties of vitreous germania illustrated in Fig. 4.17 are inferred by means of the mass density, partial radial distributions functions (RDF), coordination number and bond angle distribution (BAD). The mass density of the glass is predicted by $ReaxFF_{present}$ to be 3.68 $gr/cm^3$, which agrees well with the experimental density of 3.66 $gr/cm^3$ [168] as shown in Tab. 4.4.

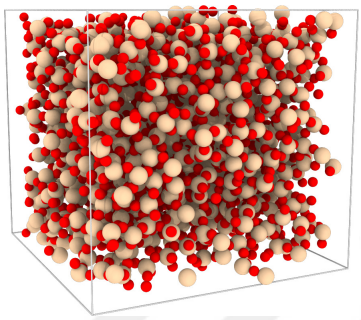

Figure 4.17: Amorphous $GeO_2$ relaxed at 300 K in an NPT ensemble for 0.5 ns.

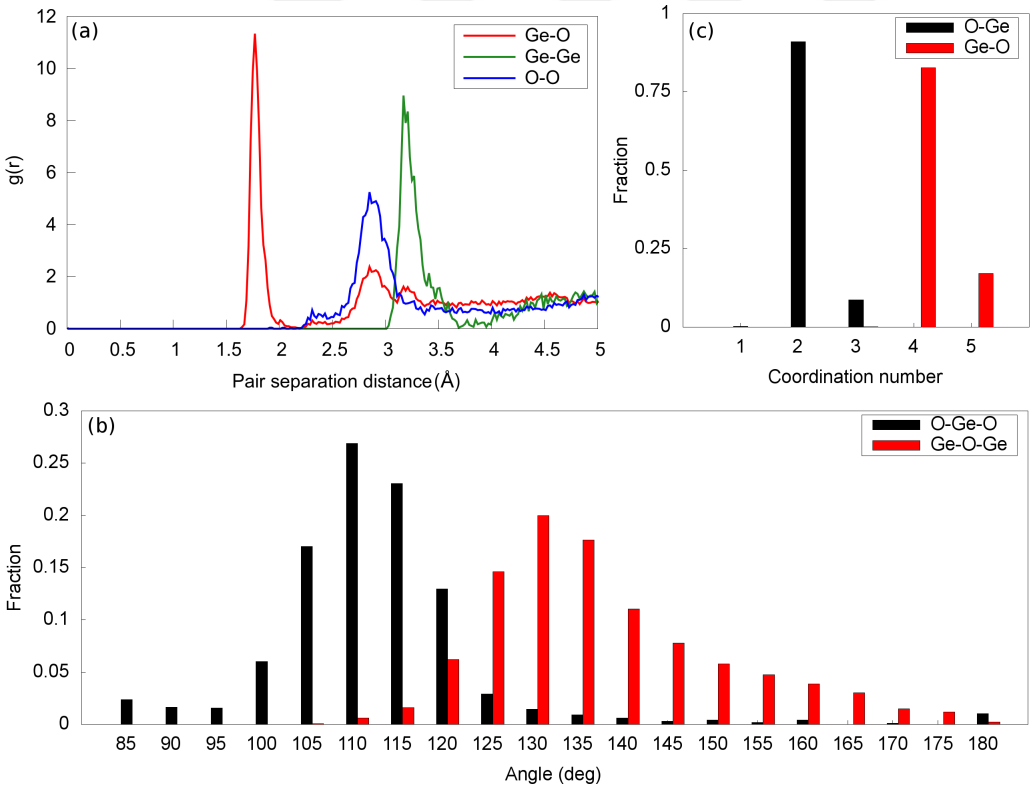


Figure 4.18: Structural characterization of the $GeO_2$ glass. (a) Ge-O, Ge-Ge, and O-O partial RDFs (b) O-Ge-O and Ge-O-Ge BADs and (c) analysis for coordination number distribution of the glass relaxed at 300 K in the NPT ensemble for 0.5 ns.

Table 4.4: Structural properties of the germania prepared by the advanced version of ReaxFF.

| | ReaxFF | MD | Experiment |
|---|---|---|---|
| Density ($gr/cm^3$) | 3.68 | 3.70[a] | 3.66[b], 3.70$\pm$0.1[c,d] |
| $d_{Ge-O}$ (Å) | 1.75 | 1.72[a], 1.75[e], 1.78[f] | 1.73[g], 1.733 0.001[h],1.74[h] 1.744 0.05[j], 1.75[j] |
| $d_{Ge-Ge}$ (Å) | 3.17 | 3.32[a], 3.25[f] | 3.26[e], 3.16[g], 3.17[h], 3.18[h], 3.16 0.03[h] 3.155 0.01[h], 3.18 0.05[h] |
| $d_{O-O}$ (Å) | 2.84 | 2.81[a], 2.84[e], 2.88[f] | 2.83[g], 2.822 0.002[h], 2.84 0.01[h] 2.84 0.02[h], 2.83 0.05[h], 2.82[h] |
| Ge-O-Ge (deg) | 130 | 159[a], 130[e], 135[f] | 132[g], 132 5[h], 133 8.3[h] 130.1[h], 133[h] |
| O-Ge-O (deg) | 110 | 108[a], 108.7[e], 109[f] | 109[g] |
| $n_{Ge-O}$ | 4.17 | 4.1[a], 4.0[e], 4.01[f] | 3.99 0.1[h], 4.0 0.2[h] |
| $n_{O-Ge}$ | 2.09 | 2.0[e] | |

Reference a: [172],Reference b: [168], Reference c: [173], Reference d: [174], Reference e: [175], Reference f: [176], Reference g: [169], Reference h: [170]

As depicted in Figure 4.18-a and Table 4.4, the Ge-O, Ge-Ge, and O-O bond distances obtained from the first peak in RDF, are in good agreement with experimental values [169, 170]. From the data presented in Table 4.4 and the graph in Figure 4.18-b, the new force field framework correctly generates $Ge-O-Ge$ and $O-Ge-O$ angle distributions having peaks at $130^\circ$ and $110^\circ$, respectively, being consistent with the experiments. The glass has a broad $Ge-O-Ge$ and $O-Ge-O$ angular distributions contrary to that of the crystalline phase, which is a fundamental way of distinguishing the crystalline and the amorphous phases [171].

Further analysis of the glass performed in terms of the coordination number distribution is illustrated in Figure 4.18-c. The glass contains mostly four-coordinate $Ge$ and two-coordinate $O$ atoms. Moreover, as evident from the graph displayed in Figure 4.18-c, there is no $O-O$ radical remained in the glass. Around 96% of Ge atoms in both glasses are four-coordinate with the average $Ge-O$ bond order of 4.17. Three-coordinate and five-coordinate atoms constitute of 1.5% and 2.5% of $Ge$ atoms in the glass. In addition, only two $Ge-Ge$ radicals were observed in the glass. All these structural characterizations belonging to the glass proves that $ReaxFF_{present}$ successfully generates a glass from its crystalline form in good overall agreement with experiments. Table 4.4 summarizes our findings regarding the structural properties of the glass, together experimental and molecular dynamics simulations results from the

literature.

## 4.3 ReaxFF development for $Si/SiO_2$ system

Herein, the reparametrization of the Si/O related force field parameters developed by Fogarty et al. ($ReaxFF_{SiOH(2010)}$) [177] is reported as another force field developed in this thesis. In a manner conforming to DFT works [178, 179], we expanded the training set taken from Ref. [177] by including the formation energies of $O$-related point defects in $a-SiO_2/Si$ system and minimum energy migration pathway of $O$ in bulk $Si$. To assess and validate the advanced version of the force field, the melting temperature of $Si$ was determined by applying two-phase approach, then the structural characterization of liquid and solid phases of $Si$ and amorphous silica were performed by using RDF, BAD, coordination number distribution and mass density. At different temperatures below melting point of Si, $O$-diffusion mechanism in bulk $Si$ was investigated, and temperature dependence of diffusion coefficient derived from fitted MSD curves was established. Finally, $a-SiO_2/Si$ system was studied at the temperatures ranging between the room temperature and the melting point of $Si$.

### 4.3.1 Computational Methods

#### 4.3.1.1 Force Field Parametrization Process

$ReaxFF_{SiOH(2010)}$ is capable of describing proton-transfer reactions at the water/silica interface. However, it is unable to describe $Si/SiO_2$ interface at high temperatures. We therefore extended $ReaxFF_{SiOH(2010)}$ description to ensure the MD application of the $Si/SiO_2$ interface even at higher temperatures below the computed melting temperature of bulk $Si$. The original extensive training set taken from Ref. [177] initially contains the QM-based equations of state for condensed phases of $Si$ and $SiO_2$, and structures and energy barriers for $SiO_2$ clusters. We also included the formation energies of $O$-related point defects in $a-SiO_2/Si$ system, and $O$-migration pathway in bulk $Si$. By using the augmented training set, we thoroughly refitted the $ReaxFF_{SiOH2010}$ force field parameters pertaining to $Si-Si$ bond, $Si-O$ bond and

off-diagonal, and $Si-O$ related valence angle parameters. During the training, we minimized the sum of the squared error between ReaxFF values and QM data until Reaxff values and the QM data reached a compromise during the training. The following sections present the details of QM data included in the training set from DFT works [147, 148, 180, 181] and the results of our force field parametrization.

#### 4.3.1.2 Point Defects

The following reaction explains the mechanism underlying the O-diffusion of $O$ observed in the vicinity of $SiO_2$/Si interface.

$$Si + SiO_2 \rightarrow SiO_x + SiO_{2-x} + V_O$$

According to the reaction, $O$ atom coming from $a-SiO_2$ leaves behind a vacancy ($V_O$) in $a-SiO_2$ and leads to an interstitial defect formation in $Si$ network by binding to a host $Si$ atom. In the training set, we, first, described the key elements of the $O$-diffusion through $a-SiO_2/Si$ interface in the force field training set, which are $O$-vacancy in $a-SiO_2$ from Ref. [180] and $O$-interstitial types in bulk $Si$ from Ref. [147], then we included the minimum energy migration pathway of the $O$ in bulk $Si$.

**O-vacancy in** $a-SiO_2$

$O$-vacancies were created in $a-SiO_2$ containing 216 atoms by randomly removing 18 $O$ atoms from the structure. Note that the cartesian coordinates of the supercell $a-SiO_2$ were taken from Ref. [182]. The following formula was defined in the training set for the description of the vacancy formation energy:

$$E_{form,vac} = 1/n[E_{(silica-nO)} - (E_{silica} - n/2E_{O_2})]$$

where n is the number of vacancies in the supercell, 18, $E_{silica-nO}$ is the total system energy of the supercell including 18 vacancies, and $E_{silica}$ and $E_{O_2}$ are the reference energies of bulk amorphous silica containing 216 atoms and $O_2$ molecule. Table 4.5 presents the formation energy of an $O$-vacancy predicted by $ReaxFF_{present}$ and

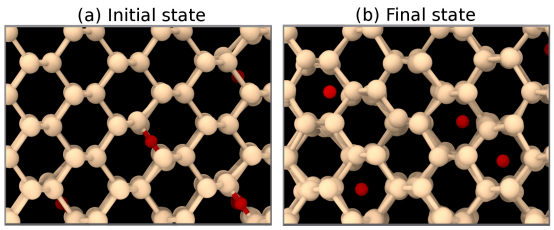


Figure 4.19: Snapshots taken from the MD simulation performed by $ReaxFF_{Fogarty}$ at 1000 K. (a) The initial configuration of the supercell where O atoms are initially positioned at BC sites and (b) the annealed supercell at 1000 K for 2.5 ns where O atoms are positioned at H and T sites inside the units of honeycomb in the lattice (OVITO).

DFT [180]. $ReaxFF_{present}$ excellently predicts the vacancy formation energy with a slight difference from DFT by about 4.5 kcal/mol.

Table 4.5: Formation energy (in kcal/mol) of $O$-vacancy in $a-SiO_2$ computed by DFT [180] and $ReaxFF_{present}$. $E_{form,vac}$ is formation energy of $O$-vacancy in $a-SiO_2$.

| Defect Type | $ReaxFF_{present}$ | DFT |
|---|---|---|
| $E_{form,vac}$ | 134.5 | 139.0 |

**O-interstitial in Diamond Si**

As in diamond Ge mentioned in Sec. 4.3.1.3, BC interstitial configuration is the most stable site followed by S, T and H sites [147, 148, 181] in diamond Si, as indicated in Table 4.6 where the formation energy of $O$ atom at the BC position is taken as a reference. However, $ReaxFF_{SiOH(2010)}$ is unable to reproduce the relative stability of the $O$-interstitial defects - so that it leads to an undesirable $O$-diffusion in bulk Si even at low temperatures as seen in Figure 4.19 where $O$ atoms, though being initially positioned at the BC sites in the matrix containing 512 $Si$ and 15 $O$ atoms (Figure 4.19-a), diffuse through a jump sequence of H→T→H sites (Figure 4.19-b) instead of the BC→S→BC sequence under the heat treatment at 1000 K.

In the present study, four supercells were constructed from the diamond $Si$ unit cell with a lattice constant of 5.463 Å to obtain a force field reproducing a correct order of the relative stability and thus, to fix the $O$-diffusion problem observed in the $Si$ matrix by $ReaxFF_{SiOH(2010)}$. Each supercell with a dimension of 16.4 Å contains

216 $Si$ atoms and an additional $O$ atom individually positioned at the BC, H, T, and S sites.

After refitting the force field parameters of interest, $ReaxFF_{present}$ predicts the relative stability of interstitial configurations in the same order with DFT [147] as evident from Table 4.6. The BC site was successfully determined to be most stable, and $O$ atom is allowed to diffuse by a correct jump sequence of BC→S→BC [147–150,181]. Furthermore, the relative formation energies of the H and T sites with respect to the BC site are estimated to be very close to the DFT values with slight shifts of 2.5 and 1.4 kcal/mol, respectively. $ReaxFF_{present}$ reaches a good agreement with DFT/experiment by predicting the relative energy of S site, called energy barrier, to be 64.8 kcal/mol.

Table 4.6: Relative total energies for four different $O$-interstitial configurations in bulk $Si$ computed by $ReaxFF_{SiOH(2010)}$, $ReaxFF_{present}$, DFT [147] and experiments [178, 179].

| Interstitial Type | BC (kcal/mol) | H (kcal/mol) | T (kcal/mol) | S (kcal/mol) |
|---|---|---|---|---|
| $ReaxFF_{present}$ | 0 | 85.4 | 84.4 | 64.8 |
| DFT | 0 | 87.9 | 85.8 | 57.3 |
| Exp. | - | - | - | 58.8 |

**Migration of O-interstitial in Diamond Si**

As discussed in detail for the Ge case in Sec. 4.3.1.3, the recent DFT studies [148, 181] also demonstrate that the transition pathway of $O$ atom in diamond $Si$ exhibiting the asymmetric geometry (Figure 4.5-b) yields the more accurate result than the other DFT studies [152–154] considering the symmetric transition state (Figure 4.5-d in Sec. 4.3.1.3).

In this study, the migration path of $O$ atom involving BC and S sites and the (110) plane was derived by taking into account the asymmetric transition concept (Figure 4.21). Eight supercells were built from diamond $Si$ unit cell. An additional $O$ atom was individually defined in each supercell containing 216 $Si$ atoms, as illustrated in Figure 4.21. In the same way with Ge, the calculations were carried out by applying bond restraint only to the $Si-O$ bond distances and keeping relaxed the remaining internal coordinates for the intermediate points. For only the BC (Figure 4.20-a and 4.20-h) and S (Figure 4.20-e) configurations, bond restraint was also applied to the $Si-Si$ bond distances between the center and right, and the center and left $Si$ atoms.

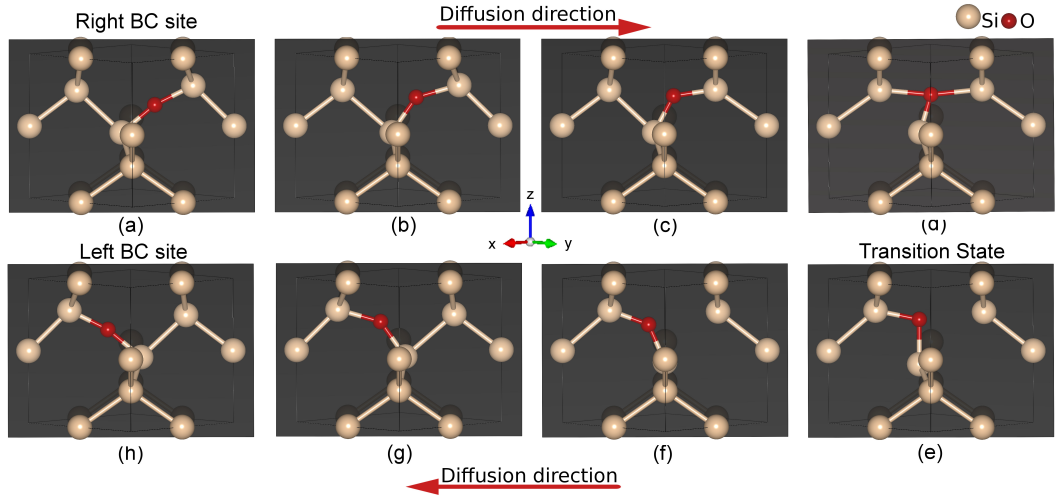


Figure 4.20: Ball-stick representation of minimum energy migration path of $O$-interstitial in the $Si$ unit cell, derived from Refs. [148, 181] as an input data for the force field training set where gray background represents (110) plane in [100] direction. $O$ diffuses by jumping from (a) the right BC site to (h) the left BC site or vice versa. During the diffusion, (e) $O$ atom goes through the asymmetric transition state (ATS) at the S site (VESTA).

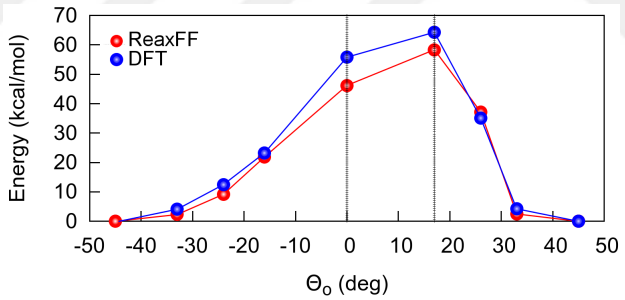


Figure 4.21: Energy of $O$-interstitial diffusing between two neighboring BC sites in the (110) plane in the $Si$ matrix, estimated by QM [181] and $ReaxFF_{present}$. $\Theta_0$ is the angle of $O$ atom with respect to [100] axis shown in Figure 4.5. $ReaxFF_{present}$ produces an asymmetric transition state at $\Theta_0$=17$^o$ with an energy barrier of 64.8 kcal/mol, showing good agreement with DFT [148].

The diffusion barrier that needs to be overcome by $O$ atom to achieve the transition state at the S site was calculated as 64.8 kcal/mol by $ReaxFF_{present}$ which is in qualitative agreement with theory and experiments with a slight shift of 6 and 7.5 kcal/mol, respectively, as shown in Table 4.6 where the barrier is a simply energy

difference between the S and BC sites. Also, the graph displayed in Figure 4.21 shows that $ReaxFF_{present}$ successfully resulted in the asymmetric migration path for $O$ atom, in line with DFT reports [148, 181].

Further $O$-diffusion analysis in bulk $Si$ is presented in Sec. 4.4.1.3. Comparison between ReaxFF and QM for the equations of state for different polymorphs of $Si$ and $SiO_2$ condensed phases that were included in the training set, and $ReaxFF_{present}$ force field parameters developed in this work are supplied in Appendix B.

#### 4.3.1.3 ReaxFF MD simulations

We performed following MD simulations with ADF/ReaxFF [40, 160, 162] for the further validation of $ReaxFF_{present}$ force field parameters: (i) the melting point calculation of bulk Si and the structural characterization of the liquid and solid Si, (ii) the investigation of O-diffusion in bulk Si at different target temperatures until below the computed melting point of Si and constructing a relationship between the temperature and diffusion coefficient, (iii) the structural analysis of a-Si$O_2$ glass and (iv) the evolution of the a-$SiO_2$/Si interface in terms of O-diffusion at high temperatures.

**Two-phase approach**

A supercell including 5488 $Si$ atoms was constructed from the diamond unit cell, established in a periodic 38.3x38.3x76.5 Å$^3$ computational box. Half of the supercell in the z-direction was frozen, and the other part was annealed in an NVT ensemble by setting their initial temperatures at 300 and 5000 K, respectively, in order to comprise two phases in coexistence (Figure 4.22-a). Each of solid and liquid parts has the same density and contains 2744 atoms. As a next step, the system was further equilibrated at target temperatures in an NPT ensemble to determine which of two phases grows during the simulation. When the temperature was above the melting point of $Si$, the solid-liquid interface moved towards to the crystal phase (Figure 4.22-b) or vice versa (Figure 4.22-c) and, the most stable phase eventually filled the entire volume of the computational box (Figure 4.22-d and 4.22-e). This process was repeated at different temperatures by applying both versions of the force field, $ReaxFF_{SiOH(2010)}$ and $ReaxFF_{present}$, until reaching the melting temperature of bulk $Si$.

**Results and Discussion:** Figure 4.22 shows the solid and liquid phases of $Si$ generated by $ReaxFF_{present}$. Our current force field parametrization resulted that the crystal phase completely overtakes the liquid phase at 2421 K (Figure 4.22-d) while the liquid phase filled the volume of the box at 2425 K (Figure 4.22-e). The melting point of bulk $Si$ was determined to be a temperature being between 2421 and 2425 K. $ReaxFF_{SiOH(2010)}$ yields the melting temperature between 2689-2690 K. Note that both ReaxFF versions significantly overestimate the melting temperature of $Si$, compared to the experimental value of 1683 K [183].

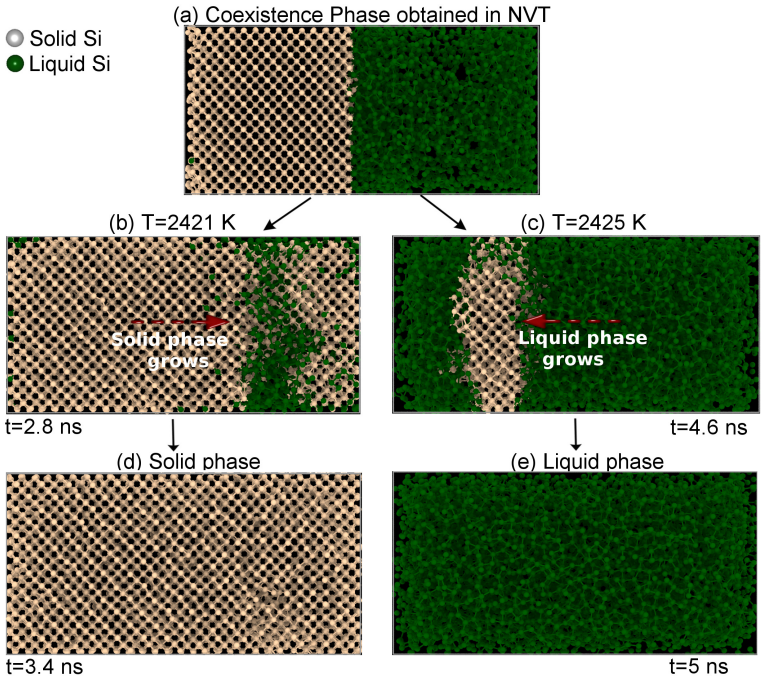


Figure 4.22: Snapshots taken from the two-phase MD simulations. (a) Coexistence phase including liquid and solid of $Si$ obtained in the NVT (b) solid/liquid interface moving towards to liquid phase (c) solid/liquid interface moving towards to crystal phase (d) crystal phase completely overtaking liquid phase at 2420 K for 3.4 ns (e) liquid phase filling the box at 2421 K for 5 ns (OVITO).

Table 4.7 presents the data belonging to the structural properties of liquid phases of $Si$ at 2425 and 2690 K, by $ReaxFF_{present}$ and $ReaxFF_{SiOH(2010)}$, respectively, and solid phase of $Si$ at 300 K by, again, both versions of ReaxFF. The density of the solid phase is still overestimated by $ReaxFF_{present}$, but the density of the liquid phase falls within the reported values in literature. $d_{SiSi}$, $Si$–$Si$ bond length, being an average distance between two bonded $Si$ atoms predicted by $ReaxFF_{present}$ was found closer

H[]
Table 4.7: Structural properties of the solid and the liquid phases of $Si$ generated by $ReaxFF_{SiOH(2010)}$ and $ReaxFF_{present}$.

| Property | | $ReaxFF_{SiOH(2010)}$ $(gr/cm^3)$ | $ReaxFF_{present}$ $(gr/cm^3)$ | Experiment $(gr/cm^3)$ |
|---|---|---|---|---|
| Melting Point (K) | | [2689-2690] | [2421-2425] | [a]1683 |
| Density $(gr/cm^3)$ | $\alpha - Si$ | 2.48 | 2.47 | [b]2.33 |
| | Liquid $Si$ | 2.52 | 2.61 | [c]2.56, [d]2.58 [e]2.61, [f]2.65 |
| $d_{SiSi}$ $(\AA)$ | $\alpha - Si$ | 2.296 | 2.312 | [g]2.368 |
| | Liquid $Si$ | 2.392 | 2.376 | - |

[a]Reference [183], [b]Reference [184], [c]Reference [185], [d]Reference [186], [e]Reference [187], [f]Reference [188], [g]Reference [189], [h]Reference [190], [i]Reference [190]

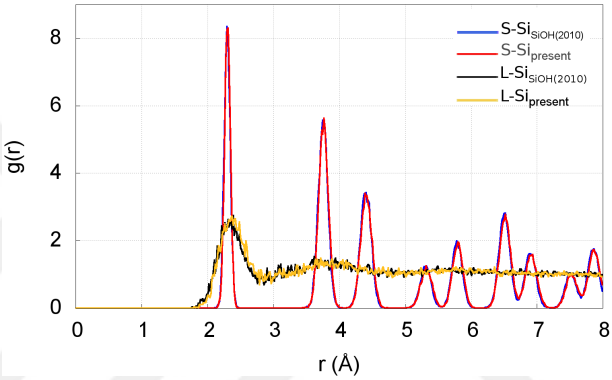


Figure 4.23: Partial RDFs belonging to the liquid and solid phases of $Si$ . $L - Si_{SiOH(2010)}$ and $S - Si_{SiOH(2010)}$ stand for liquid and solid phases, respectively, generated by $ReaxFF_{SiOH(2010)}$. In the same manner, $L - Si_{present}$ and $S - Si_{present}$ are the labels for $ReaxFF_{present}$.

to the literature value of alpha $Si$ ($\alpha - Si$ ) than that of $ReaxFF_{SiOH(2010)}$.

From the graph in Figure 4.23, partial RDFs of liquid and solid phases generated by both versions of the force field perfectly match with each other.

**Validation of Oxygen Diffusion in Silicon**

Besides the results presented in Sec. 4.4.1.2 that provides a clear indication of $O$-interstitial migration mechanism in bulk $Si$ reproduced by $ReaxFF_{present}$, the diffusion process was also addressed at different target temperatures within the range of [800-2400 K] by applying $ReaxFF_{SiOH(2010)}$ and $ReaxFF_{present}$. For this aim, a supercell containing 512 $Si$ atoms was generated from the diamond $Si$ unit cell with a

dimension of 5.463 $\mathring{A}$, and 15 $O$ atoms were randomly located at the bond-centers of two nearest-neighbor host atoms in the crystal. The unfolding trajectories of $O$ atoms in the bulk $Si$ were achieved at different temperatures in two consecutive steps: (i) In the first step, the system was gradually annealed at target temperature in an NVT ensemble using a Berendsen thermostat with a strong coupling constant of 100 fs for 1 ns. (ii) After reaching equilibrium at target temperature, the system was maintained for 3.5 ns with a weak coupling constant of 1000 fs by approaching NVE ensemble to achieve a fairly linear MSD plot. The diffusion trajectories were collected every 50 fs for 3.5 ns. Time step was set to 0.5 fs. The diffusion coefficient describing the diffusion behavior of the particle, D(t), was computed using Einstein diffusion relation [159] (Eq. 4.2). In addition, the relationship between temperature and diffusion coefficient averaged over all $O$ atoms in $Si$ was established.

**Results and Discussion:** Figure 4.24 shows the diffusion trajectories of $O$ atom generated by $ReaxFF_{present}$ at different temperatures such 1400, 1425, 1800 and 2400 K, where white and red balls are $Si$ and $O$ atoms, respectively, and green lines around the $O$ atoms represent the trajectory of $O$ atom in the bulk over the total elapsed time. As evident from Figure 4.24, every $O$ atom occupies the BC sites at each target temperature as in the experiments [147, 148, 181]. In Figure 4.24-a, $O$ atoms are confined to vibrate around themselves and can not hop the other BC sites during the simulation until above 1400 K because they do not have energy required for overcoming the barrier. They reach the transition state and jump to the next BC site at the temperatures over 1400 K (Figure 4.24-b), showing good agreement with the experiment [191] where $O$-diffusion initiates at 1423.15 K (1150 $^oC$). At further heat treatment, $ReaxFF_{present}$ successfully allows $O$ atoms to still hop between only two nearest BC sites even at higher temperatures below the computed melting point of bulk $Si$ (Figure 4.24-c and 4.24-d).

Figure 4.25 shows the comparison of $ReaxFF_{present}$ and the experiment [191] in terms of the temperature dependence of the diffusion coefficient. The new model of force field predicts the diffusion coefficient in overall good agreement with the experiment. Note that the experimental values of the diffusion coefficient was obtained by using a normalized diffusion coefficient equation provided by Ref. [191].

We also examined the diffusion behavior of $O$ atom based on $ReaxFF_{present}$ within the range of [800-2400 K]. As illustrated in Fig.4.25-a, the plot belonging $ReaxFF_{present}$ reveals four different regions depending on the temperature. The distinct character of the each region is illustrated by the MSD plots labeled with the region numbers in Figure 4.25-b and 4.25-c, and the representative diffusion trajectories in Figure 4.25-$a_1$, $b_1$, $c_1$, $d_1$ and $e_1$.

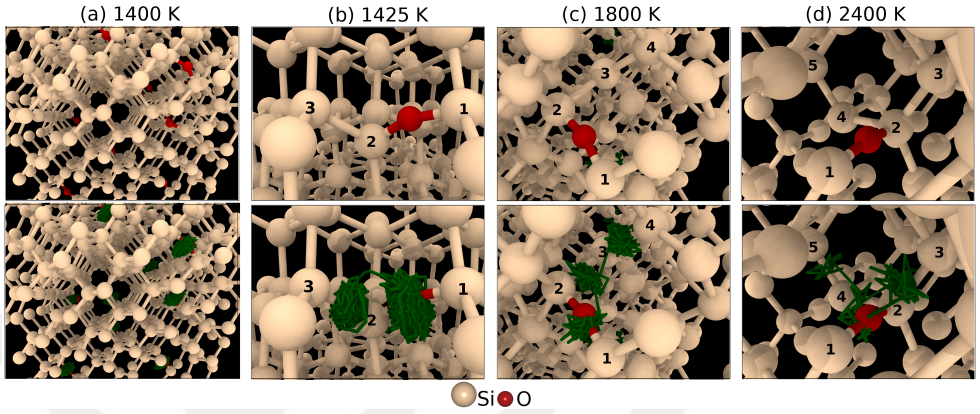


Figure 4.24: Snapshots taken from the final MD steps of the simulations by $ReaxFF_{present}$ at different target temperatures. The top four snapshots represent the initial configuration of the system from different views, and the bottom four images show the diffusion trajectory of O atom for 3.5 ns with a green line. (a) No diffusion was observed at 1400 K, and O atoms at BC sites vibrate around themselves. (b) At 1425 K, O atom residing in the BC site neighboring 1. and 2. Si atoms hops to the next BC site between 2. and 3. Si atoms, and, during the jumping, O atom goes through the transition state at the S site located above 2. Si atom. (c) At 1800 K, O atom initially being at BC site neighboring 1. and 2. atoms, first, jumps to the BC site between 2. and 3. Si atoms, and then hops the next BC site between 3. and 4. Si atoms. (d) At 2400 K, O diffuses by hoping, first, the BC site between 1. and 2. Si atoms following by the BC sites between 2. and 3. Si atoms, and 3. and 4. Si atoms. Finally, it occupies the BC site between 4. and 5. Si atoms (OVITO).

In the I. region between 800 and 1400 K, the diffusion does not occur where $O$ atoms are confined to vibrate around themselves (Figure 4.25-$a_1$ and MSD plot labeled with I in Figure 4.25-b). In the other regions, $O$ atom exhibits the anomalous diffusion behavior in different combinations of confined (Figure 4.25-$a_1$), free (Figure 4.25-$b_1$) and directed (Figure 4.25-$c_1$) diffusion types [192]. In the II. region, the slopes of

MSD curves labeled with II in Figure 4.25-b decrease and finally, the MSD profiles reach a plateau. It means that $O$ atoms, first, begin to freely diffuse through jumping their neighboring BC sites at the temperatures over 1400 K, then, they are likely blocked by their neighbors so that begin to exhibit a confinement trajectory (Figure 4.25-$a_1$) around themselves. In the III. region, $O$ atoms are energetically free to further diffuse between the BC sites.

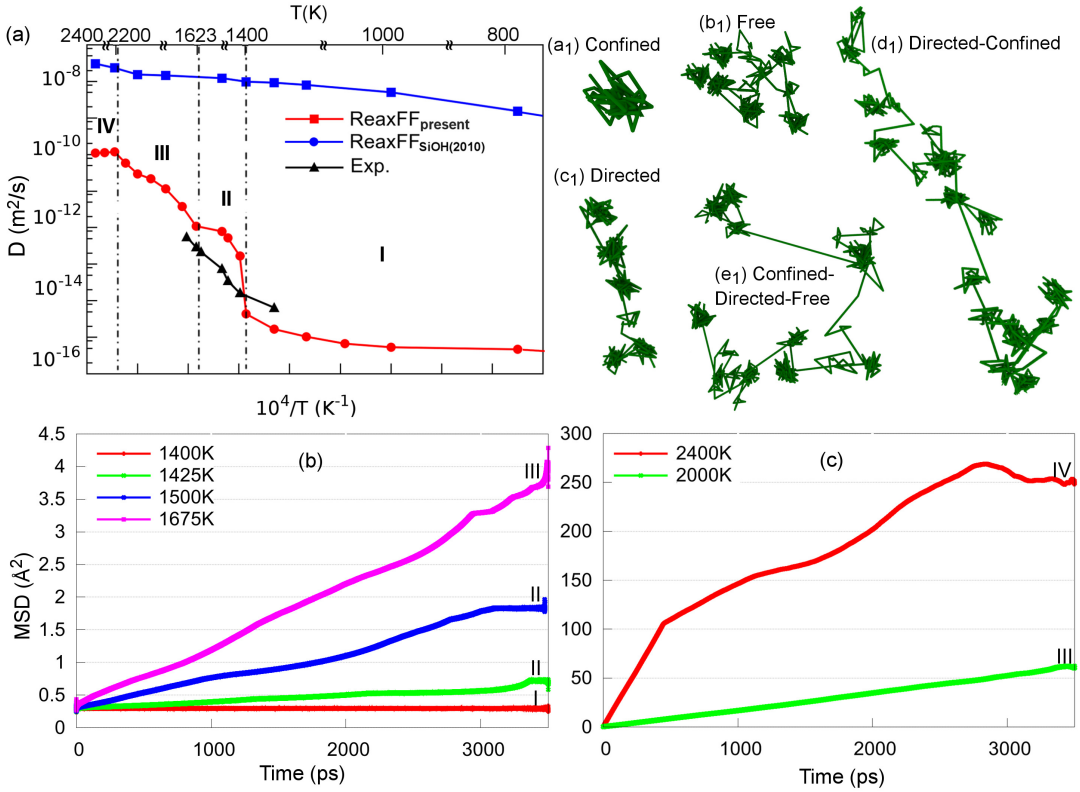


Figure 4.25: (a) Temperature dependence of the diffusion coefficient computed by both versions of the ReaxFF force field and experiment [191], (b) and (c) MSD profiles at given temperatures where the enumeration with roman numbers refers to indicated regions in (a). The observed trajectory types of $O$ atom during diffusion are as following: ($a_1$) confined, ($b_1$) free, ($c_1$) directed and anomalous diffusion types combined of ($d_1$) directed-confined and ($e_1$) directed-free-confined. The main difference between the trajectories in ($d_1$) and ($e_1$) is that $O$ atoms intermittently moves away from their initial locations in ($d_1$) contrary to $O$ atoms moving back towards their initial positions in ($e_1$).

The MSD plot representing III. region in Figure 4.25-b exhibits a combination of likely directed and confined as illustrated in Figure 4.25-$d_1$ where $O$ atoms intermit-

tently move away from their initial points in an accelerated manner. The MSD plot, again, labeled with III in Figure 4.25-c shows a predominantly free (normal) diffusion. In the IV. region, MSD plots generally exhibit downward trend in some places towards to the end as shown in Figure 4.25-c which is likely caused by the accelerated $O$ atoms hitting the other atoms with rising temperature and being directed towards to their initial frames by changing their direction (Figure 4.25-e$_1$).

**Silica glass by Melt-quenching Method**

In this work, with a particular focus on $a-SiO_2/Si$ system at the high temperatures, the $a-SiO_2$ was prepared by applying the melt-quenching method with the application of $ReaxFF_{SiOH(2010)}$ and $ReaxFF_{present}$, separately. The initial configuration of bulk crystal $SiO_2$ ($c-SiO_2$ ) including 1000 $Si$ and 2000 $O$ atoms was built from the $\beta-cristobalite$ unit cell with a lattice constant of 7.13 Å [193], and established in a cubic simulation box of a dimension 35.650 Å with periodic boundary conditions. The space group and space group number of the $\beta$-$cristobalite$ $SiO_2$ is $Fd\overline{3}m$ and 227, respectively. The MD energy minimization was performed to avoid the overlapped atoms which lead to excessive forces and energy differences between consecutive steps in MD. The relaxed system was annealed twice from 7000 to 300K in an NVT and NPT ensembles, separately, at zero pressure in order to achieve a glass having correct structural properties. (ii) In the first annealing process, the initial temperature of the bulk $c-SiO_2$ was set at 7000 K, and the bulk was equilibrated at such high temperature for 50 ps in the NVT ensemble until achieving a completely liquid phase, (iii) whereupon obtaining the liquid phase, the system was cooled down to 300 K in 100 ps, and relaxed at 300 K for 500 ps to reduce the density of intrinsic point defects located in the structure. (v) In the second annealing process, the system was again heated at 7000 K for 100 ps and cooled down to 300K for 200 ps, in this case, in the NPT ensemble. Finally, the amorphous structure was relaxed still in the NPT ensemble for 100 ps. The relaxation resulted in a 39.7508x39.0886x36.7919 Å$^3$ glass. In the simulation, a velocity-Verlet algorithm was employed to solve Newton's equation of motion, and the time step is 0.5 fs. The temperature-damping and the pressure-damping constants were set at 100 and 5000 fs, respectively. The validation of the glasses prepared by the $ReaxFF_{SiOH(2010)}$ and $ReaxFF_{present}$ were performed against to DFT/experiments using their computed structural properties including mass

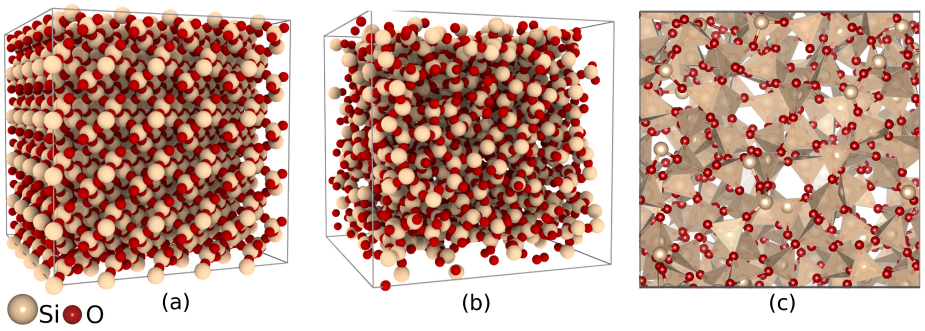


Figure 4.26: (a) The initial bulk configuration of crystalline $\beta - SiO_2$, (b) $a - SiO_2$ quenched from the liquid state to 300 K and (c) the polyhedral model of $a - SiO_2$ (VESTA).

density, partial RDFs, coordination number distribution and BADs.

**Results and Discussion:** Figure 4.26 shows the initial configuration of bulk $c - SiO_2$ and its amorphous form obtained by applying the new model of ReaxFF. The mass density of the glass ($glass_{present}$) was excellently predicted by $ReaxFF_{present}$ to be 2.21 $gr/cm^3$ while the reported density of the glass ($glass_{SiOH(2010)}$) prepared by $ReaxFF_{SiOH(2010)}$ [177] is higher than the experimental density of 2.20 $gr/cm^3$ [194, 195] (Table 4.8).

Figure 4.27-a and Table 4.8 show that the average $Si-O$ bond distances ($d_{SiO}$) computed by $ReaxFF_{SiOH(2010)}$ and $ReaxFF_{present}$ are in good agreement with each other and the experiments. The $Si - Si$ bond-distance, 3.1 Å, predicted by the $ReaxFF_{SiOH(2010)}$, is nearly same with experiment [195], and the new force field model yields a slight narrowing in the $Si - Si$ bond distance. As for $O - O$ bond distance, $ReaxFF_{present}$ gives a much closer result to the experiments [195, 196] than $ReaxFF_{SiOH(2010)}$. From the data presented in Table 4.8 and the graph in Figure 4.27-b, the new force field framework correctly generates $Si - O - Si$ and $O - Si - O$ angle distributions having peaks at $152^\circ$ and $108^\circ$, respectively, being consistent with the experiments. However, $ReaxFF_{SiOH(2010)}$ predicts that most of the $Si - O - Si$ angles are centered around 154 where there is a slight discrepancy between $ReaxFF_{SiOH(2010)}$ and the experiments [197–199], by about $3^\circ$ . Also, most of the $O - Si - O$ angles calculated by $ReaxFF_{SiOH(2010)}$ gather around the $105^\circ$, and the analysis gives a peak at $107^\circ$ with a shift of $2^\circ$ from the experiment.

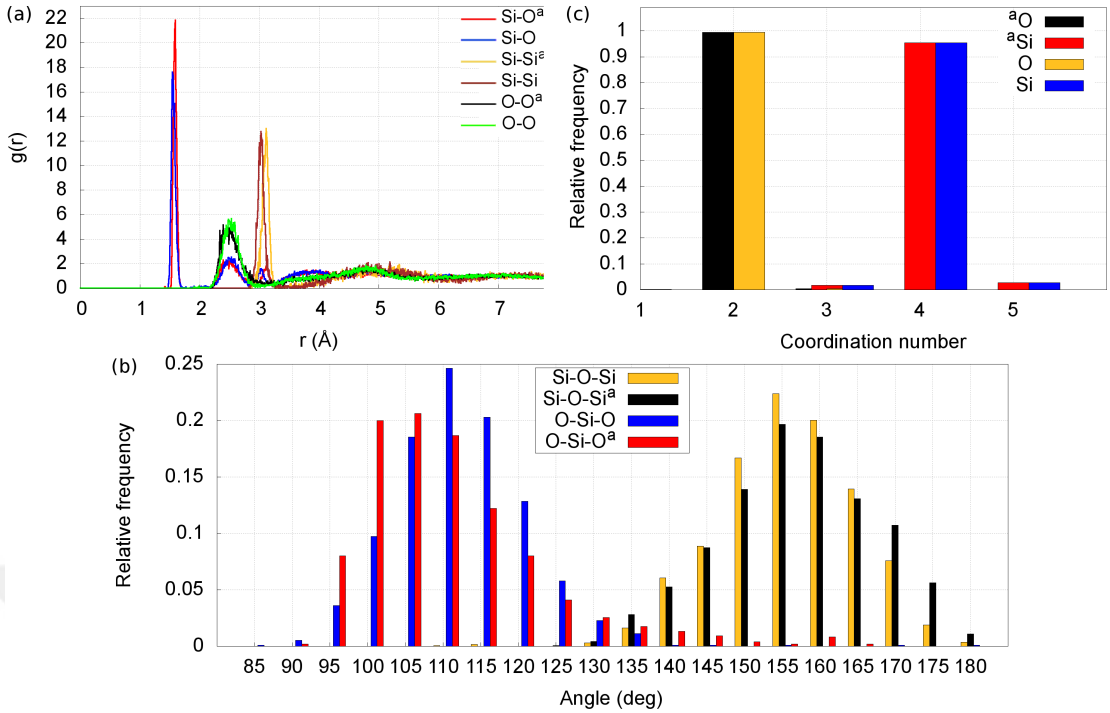


Figure 4.27: Structural characterizations of $glass_{present}$ and $glass_{SiOH(2010)}$ with superscript $a$. (a) $Si-O$, $Si-Si$, and $O-O$ partial radial distribution functions (b) $O-Si-O$ and $Si-O-Si$ BADs and (c) analysis for coordination number distribution of both glasses quenched from the liquid state to 300 K.

Table 4.8: Structural properties of the silica prepared by $ReaxFF_{SiOH(2010)}$ and $ReaxFF_{present}$.

| Property | $ReaxFF_{SiOH(2010)}$ | $ReaxFF_{present}$ | Experiment |
|---|---|---|---|
| Density (gr/cm$^3$) | 2.25 | 2.21 | 2.20[a,b] |
| $d_{SiO}$ (Å) | 1.59±0.08 | 1.58±0.09 | 1.608±004[c] |
| $Si-Si$ bond dist. (Å) | 3.07±0.14 | 3.02±0.13 | - |
| $O-O$ dist. (Å) | 2.56±0.32 | 2.58±0.27 | 2.65[a] |
| $Si-O$ RDF first max. (Å) | 1.58 | 1.56 | 1.608[c], 1.620[a] |
| $Si-Si$ RDF first max. (Å) | 3.11 | 3.03 | 3.077, 3.12[a] |
| $O-O$ RDF first max. (Å) | 2.39 | 2.52 | 2.626[c], 2.65[a] |
| $Si-O-Si$ (deg) | 154.0 | 152.0 | 151.0[d,e,f] |
| $O-Si-O$ (deg) | 107.0 | 108.0 | 109.4[g], 109.5[a] |
| $Si$ coordination | 4.010 | 4.010 | - |
| $O$ coordination | 2.005 | 2.005 | - |

[a]Reference [195], [b]Reference [194], [c]Reference [196], [d]Reference [197], [e]Reference [198], [f]Reference [199], [g]Reference [200]

Further analysis of the glasses performed in terms of the coordination number distribution is illustrated in Figure 4.27-c. It shows that both glasses have similar coordination characteristics. Each glass contains mostly four-coordinate $Si$ and two-coordinate $O$ atoms. Only 2 $O$ and 9 $O$ atoms have one and three $Si$ neighbors, respectively, in the $glass_{present}$, and 4 $O$ and 5 $O$ atoms have one and three $Si$ neighbors, respectively, in the $glass_{SiOH(2010)}$, even though their total bond order of 2. Moreover, as evident from the graph displayed in Figure 4.27-c, there is no $O-O$ radical remained in the glasses. Around 96% of $Si$ atoms in both glasses are four-coordinate with the average $Si-O$ bond order of 3.8. Figure 4.26-c shows four-coordinate $Si$ atoms in the polyhedral model of the $glass_{present}$ where the centers of four nearest neighbor $O$ atoms around $Si$ are joined by the lines. Three-coordinate and five-coordinate atoms constitute of 1.5% and 2.5% of $Si$ atoms in the $glass_{present}$ with the bond orders of 2.81 and 3.84, respectively, and 1.2% and 2.1% of $Si$ atoms in the $glass_{SiOH(2010)}$ with the bond orders of 2.88 and 3.88, respectively. In addition, only one and two $Si-Si$ radicals were observed in the $glass_{present}$ and the $glass_{SiOH(2010)}$, respectively. All these structural characterizations belonging the $glass_{present}$ and the $glass_{SiOH(2010)}$ prove that $ReaxFF_{present}$ successfully generates a glass from its crystalline form in good overall agreement with $ReaxFF_{SiOH(2010)}$, DFT and experiments.

### $a-SiO_2/Si$ system at high temperatures

To address $O$-diffusion directly in $a-SiO_2/Si$ system, the lattice model of the system with dimensions of $65x65x80$ Å$^3$ was constructed by using the glass mentioned above and the bulk crystal $Si$. To create a relatively larger glass, the coordinates of $a-SiO_2$ were replicated and translated in the y-direction and adjacent to the original ones. $a-SiO_2$ glass containing 5802 atoms in dimensions of $65x65x22$ $\mathring{A}^3$ was cut from the generated larger glass. After that, the energy minimization was individually performed to the cut $a-SiO_2$ glass in order to prevent the overlapping atoms and bad contacts. The relaxed $a-SiO_2$ was deposited on the diamond $Si$ matrix normal to the z-axis by leaving a gap of 2 $\mathring{A}$ between two layers, and finally, $a-SiO_2/Si$ system comprising 14754 atoms in the dimensions of $65x65x100$ Å$^3$ was constructed by inserting a vacuum region with a height of 20 Å at the top of the silica. With the application of $ReaxFF_{SiOH(2010)}$ and $ReaxFF_{present}$, separately, the total system

was annealed at temperatures ranging between [300-2400 K] for 500 ps.

Figure 4.28 illustrates the diffusion results regarding the $a-SiO_2/Si$ system annealed by applying $ReaxFF_{SiOH(2010)}$ and $ReaxFF_{present}$.

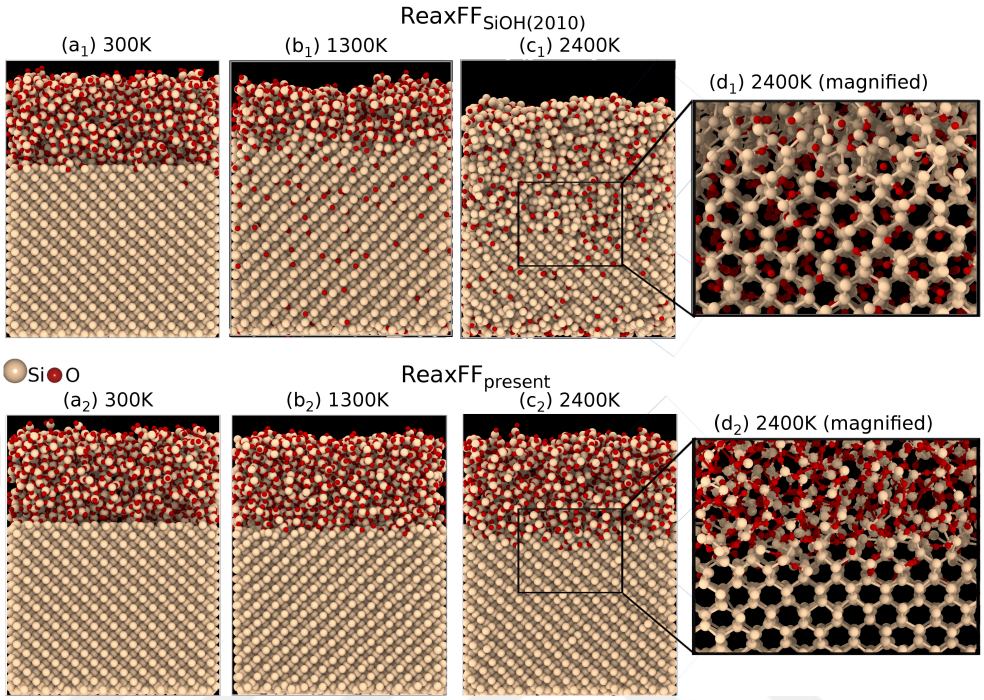


Figure 4.28: $a - SiO_2/Si$ system annealed at temperatures ranging between [300-2400 K] for 500 ps by applying $ReaxFF_{present}$ and $ReaxFF_{SiOH(2010)}$. Snapshots shown in ($a_1$), ($b_1$), ($c_1$), ($d_1$) belongs to the results generated by $ReaxFF_{SiOH(2010)}$. ($a_2$), ($b_2$), ($c_2$), ($d_2$) represents the results reproduced by $ReaxFF_{present}$. Also, ($d_1$) and ($d_2$) illustrate the magnified views of the framed regions with black enclosures at 2400 K (OVITO).

The plot displayed in Figure 4.29 also shows the $O$ solubility being the $O$ content of the $Si$ substrate and depth distribution of the $O$ atoms in the substrate reproduced by both versions of the ReaxFF force field depending on the annealing temperature. Note that the depth profiling based on $ReaxFF_{SiOH(2010)}$ is not shown in the graph since $O$ atoms diffused from the silica layer were determined throughout the $Si$ substrate within the range of [1300-2400 K]. Contrary to $ReaxFF_{present}$ and the experiments [178,179,191], $ReaxFF_{SiOH(2010)}$ resulted that $O$ begins to diffuse even at low temperature such as 300 K (Figure 4.28-$a_1$). With the application of $ReaxFF_{present}$ to the system, the graph in Figure 4.29 show that the $O$ atoms react with only the

bonds between the $Si$ atoms in the first and second layer of the $Si$ substrate in the vicinity of the interface where $O$-depth in the $Si$ matrix is about 2 Å, until 1400 K. At the temperatures over 1400 K, $O$ atoms begin to jump the sites neighboring the $Si$ atoms located in the third layer of the $Si$ substrate. The most striking difference between both versions of the ReaxFF force fields can be explicitly seen from Figure 4.28-$d_1$ and 4.28-$d_2$. In Figure 4.28-$d_2$, $ReaxFF_{present}$ successfully directs the $O$ atoms to occupy the BC sites in the $Si$ matrix even at 2400 K, being consistent with DFT/experiments [147, 148, 150, 181, 201], while $ReaxFF_{SiOH(2010)}$ results that the $O$ atoms are positioned at the H and T sites inside of honeycomb units through the $Si$ substrate instead of the BC sites as can be seen in Figure 4.28-$d_1$.

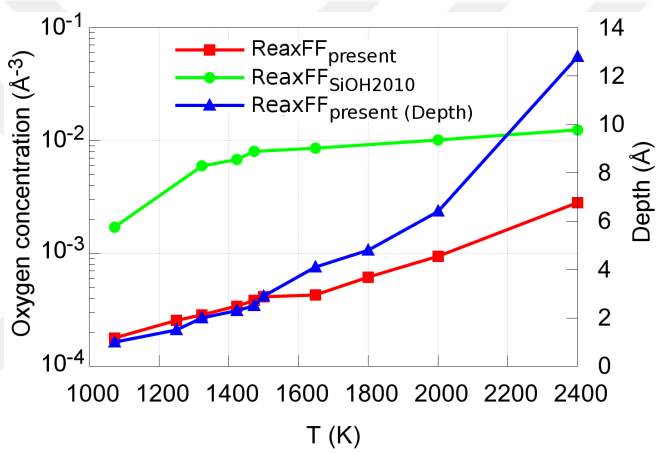


Figure 4.29: Temperature dependence of $O$ solubility and depth profiles in the $Si$ substrate based on $ReaxFF_{present}$ and $ReaxFF_{SiOH(2010)}$ under heat treatment where the label of $ReaxFF_{present(Depth)}$ represents the depth profiling of $O$ generated by the new force field, and the labels of $ReaxFF_{present}$ and $ReaxFF_{SiOH(2010)}$ belong to the $O-$concentration plots.

By improving the force field with a particular emphasis on the formation energies of the $O$-interstitial sites and the diffusion path of $O$ atom in the bulk $Si$, the best agreement between the force field and experiment was successfully achieved as proved throughout this subsection. In $a - SiO_2/Si$ system, we were also able to fix the diffusion problem observed at high temperatures by $ReaxFF_{SiOH(2010)}$, and to reproduce experimentally/theoretically defined diffusion mechanism in the system.

## 4.4 Concluding Remarks

In this chapter, we aimed to develope the ReaxFF force field to provide overall description of the L-LPE system comprised of complex Si/Ge, Si/$SiO_2$ and Ge/$SiO_2$ interfaces. The force field parameters for Si/Ge alloys has been already developed by Psofogiannakis et al. [145]. We also improved the reactive force field considering the Si/$SiO_2$ interface and Ge/O interactions in the L-LPE system. On the basis of our force field parametrization results regarding the Ge/O and Si/O interactions, we can draw the following conclusions: to give the force field the ability to simulate the diffusion mechanism mediated by interstitial atom in the condensed phase, it is a critical to describe correctly the relative stability of different interstitial centers besides their structures and energies in the force field training set. In addition, introducing the minimum energy migration pathway with an experimental/theoretical value of energy barrier in the training set by taking into account the stability ordering of the interstitials lead us to inevitably obtain a force field being capable of enabling to simulate the experimental/theoretical diffusion mechanism. After re-optimization of the Ge/O related force field parameters developed by Zheng et al. [146] with those key points in mind, our results show that ReaxFF successfully generates the energies of the BC, S, T and H interstitial sites within a correct stability order [147] and the asymmetric migration pathway lying between adjacent two BC sites [148]. MD simulations performed based on the ReaxFF and Tersoff show that advanced model of ReaxFF is more capable of simulating the diffusion process of the O in Ge under different temperatures ranging between 800-2000 K than Tersoff. In addition, the Arrhenius plot illustrates that ReaxFF yields an activation energy value of 50.02 kcal/mol within the temperature range of [800-2000 K] showing good agreement with the experiment with a slight shift of 2.8 kcal/mol [155–157]. Moreover, ReaxFF simulations show that, irrespective of the temperature, O atoms diffuse along the pathway between BC centers, which is also observed in in DFT studies, whereas the Tersoff potential exhibit incorrect diffusion behavior at temperatures over 1400K, showing jumps between BC and H sites which contradicts earlier theoretical work [147, 148]. We can attribute the inability of Tersoff to reproduce the diffusion mechanism in line with DFT at high temperatures (>1400 K) to its incorrect prediction of the relative stability ordering of the interstitial centers. We further validated the re-developed ReaxFF

Ge/O description with MD simulations on the $GeO_2$/Ge interface. ReaxFF showed that the oxidation of Ge substrate with the $GeO_2$ slabs triggers the $GeO_2$ formation in the vicinity of the interface during the simulations, showing excellent agreement with the experiments [166, 167]. However, when we applied Tersoff potential to the same simulations, we observed that experimentally reported $GeO_2$ formation does not occurs at the interface, and the reaction occurring at the interface shows similarity with that of the Si/$SiO_2$ interface. Furthermore, we compared an amorphous $GeO_2$ structure, as generated using the re-developed ReaxFF parameters, with experiment, finding good structural agreement. As such, we believe that these new ReaxFF Ge/O parameters provide an important computational tool for studying germanium/germanium oxide interfaces.

As for the ReaxFF force field development for $SiO_2$/Si system, the major driving force behind the improvement of $ReaxFF_{SiOH(2010)}$ [177] is to ensure the MD simulations of $a-SiO_2/Si$ interface event at high temperatures the below computed melting point of bulk $Si$. For this purpose, we refitted of $ReaxFF_{SiOH(2010)}$ force field parameters by putting a special emphasis on $O$-diffusion in bulk $Si$ and $O$-related point defect formations in the vicinity of $a-SiO_2/Si$ interface. After a thorough optimization, we found that our force field parametrization successfully predicts the order of relative stability of $O$-interstitial sites from most stable to least stable to be $BC \rightarrow S \rightarrow T \rightarrow H$, showing good agreement with Ref. [147], and $O$-vacancy formation energy in the silica agrees with DFT [180]. In addition, $ReaxFF_{present}$ correctly describes the asymmetric diffusion mechanism of $O$ in $Si$ network which occurs through the jumps between the neighboring BC sites by going through the transition state at the split site [147, 148, 150, 181], which is the most remarkable conclusion of this work. The diffusion barrier is predicted to be 64.8 kcal/mol, being reasonably close to the experimental reported value of 58.3 kcal/mol [178, 179]. We further validated $ReaxFF_{present}$ force field parameters by performing the MD simulations in many aspects: (i) the melting point of bulk $Si$ was determined by applying two-phase approach and the structural properties of the liquid and solid phases of $Si$ were analyzed based on the mass density and the pair correlation function. (ii) the $O$-diffusion behavior in $Si$ matrix was investigated at different target temperatures until below the computed melting point of $Si$ by applying $ReaxFF_{present}$ and the

temperature dependence of diffusion coefficient was established. Our results demonstrate that $ReaxFF_{present}$ allows $O$ atoms to diffuse through the $Si$ matrix at the temperatures over 1400 K as in the experiment [191]. The relationship between the temperature and diffusion coefficient produced by $ReaxFF_{present}$ fits in well with the experiment [191]. We also reported that $O$ atoms exhibits the anomalous diffusion behavior in different combinations of free, directed and confined diffusion. (iii) As a next step of the validation process of $ReaxFF_{present}$, $a-SiO_2/Si$ system was modeled by using the glass with a mass density of 2.21 $gr/cm^3$, showing excellently agreement with the experimental value of 2.20 $gr/cm^3$ [195], and simulated at the temperatures within the range of [300-2400 K] to demonstrate the ability of the force field to reflect experimentally/theoretically defined diffusion. Based on all these results, we confidently state that the MD applications prove the concept that the new force field gives more accurate and realistic results with experiments and DFT works for a detailed mechanism of $a-SiO_2/Si$ system.

# CHAPTER 5

# CONCLUSIONS AND OUTLOOK

## 5.1 Conclusions

In this thesis, we presented the theoretical studies regarding the InP and Si/O/Ge systems. The structural behaviors of the InP nanostructures were reported in detail under different conditions by using MD simulations [108, 109] (Chapter 3). We improved the ReaxFF force fields for Si/O [144] and Ge/O [143] interactions in the L-LPE system (Chapter 4).

On the basis of our results presented throughout the thesis, we can specify the main contributions of this thesis as follows:

- We successfully developed the ReaxFF force field for Si/$SiO_2$ interface in the L-LPE.

- For Ge/$SiO_2$ interface in the L-LPE, we developed the force field for Ge/O interactions with a particular focus on O related point defects in bulk Ge. Based on our MD results, we further verified that Ge/O related Tersoff potential parameters are unable to describe the theoretical O-interstitial diffusion mechanism in Ge at higher temperatures than 1400 K. They are also not capable of simulating the Ge/$GeO_2$ interface, it produces the results contradicting the experiments. The ReaxFF developed in this thesis produces more realistic results showing excellent agreement with experiments than Tersoff as demonstrated in Chapter 4. The advanced versions of the ReaxFF force field parameters for Ge/O [143] and Si/O [144] supplied in Appendix B are the most remarkable contribution of this thesis to the literature.

## 5.2 Outlook

The works for the InP and Si/Ge/O systems in this thesis contributes to the continuing trend in the semiconductor technology. Providing the atomic insight into the mechanical behaviors of the InP nanostructures under different conditions such as heating, cooling, strain, compression etc. gives the freedom of designing and manipulating them for the use of in the technology. Additionally, the ReaxFF force fields developed for Si/$SiO_2$ and Ge/O interactions in this thesis will bring very pragmatic opportunity for experimentalists with more realistic and accurate results on the atomistic level.

In addition to all these, for the sake of accuracy and curiosity, to achieve a powerful ReaxFF force field accurately describing the L-LPE system as in experiments, the following cases should be explored in the future.

- The force field should be tested for Si/Ge interface in the L-LPE system, and if the need arises, it was further optimized in the same manner with the Si/$SiO_2$ interface and Ge/O interactions.
- The ReaxFF force field should be extended to Si/O/Ge interactions by including more crystal data to the training set such as the Ge-related point defect and diffusion pathway inside $SiO_2$, the interfacial excess energy associated with Ge/$SiO_2$ interface, adsorption/desorption energies of Ge on $SiO_2$, equations of state and heats of formation for Si/O/Ge condensed phases etc.
- After obtaining the force field describing all interactions in the L-LPE system coated with $SiO_2$ insulator, the research may be gone even further with the new insulator such as $TiO_2$, $HfO_2$, $La_2O_3$ etc.

For many years, silicon has been the dominant semiconductor in the CMOS tehcnology. However, recently, the need has arisen to replace Si with new material because Si-based CMOS technology reached its geometrical scaling limits. Thanks to the key development in high-k dielectric technology in Ge, single crystal Ge has reemerged as a promising candidate for CMOS technology. On the other hand, there is some manufacturing problems encountered in the fabrication of single crystal Ge such as agglomeration, polycrystallization due to the random nucleation of Ge in the stripes

etc. But, ultimately, curiosity-driven research will continue to unravel experimental manufacturing problems regarding the single crystal Ge on the atomistic level so that will contribute to keep pace with the technological advancement in Ge.

## REFERENCES


[1] E. Polak. In *Computational Methods in Optimization*. Academic Press, 1971.

[2] P. Debye. Näherungsformeln für die zylinderfunktionen für große werte des arguments und unbeschränkt veränderliche werte des index. *Mathematische Annalen*, 67(4):535–558, Dec 1909.

[3] Jonathan R Shewchuk. An introduction to the conjugate gradient method without the agonizing pain. Technical report, Pittsburgh, PA, USA, 1994.

[4] Runar Heggelien Refsnaes. A brief introduction to conjugate gradient method. Technical report, Pittsburgh, PA, USA, 1994.

[5] Runar Heggelien Refsnaes. A brief introduction to conjugate gradient method. `http://www.idi.ntnu.no/~elster/tdt24/tdt24-f09/cg.pdf`. Accessed: 2018-06-05.

[6] B. J. Alder and T. E. Wainwright. Phase transition for a hard sphere system. *The Journal of Chemical Physics*, 27(5):1208–1209, 1957.

[7] Loup Verlet. Computer "experiments" on classical fluids. i. thermodynamical properties of lennard-jones molecules. *Phys. Rev.*, 159:98–103, Jul 1967.

[8] LOUP VERLET. Computer "experiments" on classical fluids. ii. equilibrium correlation functions. *Phys. Rev.*, 165:201–214, Jan 1968.

[9] D. Beeman. Some multistep methods for use in molecular dynamics calculations. *Journal of Computational Physics*, 20(2):130 – 139, 1976.

[10] Predictor-corrector method. `https://www.saylor.org/site/wp-content/uploads/2011/06/MA221-6.2.pdf`. Accessed: 2018-06-05.

[11] Furio Ercolessi. A molecular dynamics premier. `http://cms.sjtu.edu.cn/doc/reading/md/A_Molecular_Dynamics_Primer_(Ercolessi).pdf`. Accessed: 2018-06-05.

[12] Peter Young. The leapfrog method and other “symplectic” algorithms for integrating newton’s laws of motion. `http://young.physics.ucsc.edu/115/leapfrog.pdf`. Accessed: 2018-06-05.

[13] J. Willard Gibbs. In *Elementary Principles in Statistical Mechanics*. Charles Scribner’s Sons, 1902.

[14] H. J. C. Berendsen, J. P. M. Postma, W. F. van Gunsteren, A. DiNola, and J. R. Haak. Molecular dynamics with coupling to an external bath. *The Journal of Chemical Physics*, 81(8):3684–3690, 1984.

[15] Shichi Nosé. A molecular dynamics method for simulations in the canonical ensemble. *Molecular Physics*, 52(2):255–268, 1984.

[16] Shuichi Nosé. A unified formulation of the constant temperature molecular dynamics methods. *The Journal of Chemical Physics*, 81(1):511–519, 1984.

[17] William G. Hoover. Canonical dynamics: Equilibrium phase-space distributions. *Phys. Rev. A*, 31:1695–1697, Mar 1985.

[18] P. Vashishta, Rajiv K. Kalia, José P. Rino, and Ingvar Ebbsjö. Interaction potential for Si$O_2$: A molecular-dynamics study of structural correlations. *Phys. Rev. B*, 41:12197–12209, Jun 1990.

[19] Paulo Sergio Branicio, José Pedro Rino, Chee Kwan Gan, and Hélio Tsuzuki. Interaction potential for indium phosphide: a molecular dynamics and first-principles study of the elastic constants, generalized stacking fault and surface energies. *Journal of Physics: Condensed Matter*, 21(9):095002, 2009.

[20] Glenn J. Martyna, Mark E. Tuckerman, Douglas J. Tobias, and Michael L. Klein. Explicit reversible integrators for extended systems dynamics. *Molecular Physics*, 87(5):1117–1157, 1996.

[21] Claire Y. Chuang, Qiming Li, Darin Leonhardt, Sang M. Han, and Talid Sinno. Atomistic analysis of Ge on amorphous $SiO_2$ using an empirical interatomic potential. *Surface Science*, 609:221 – 229, 2013.

[22] K. Shintani, Y. Yano, and M. Abe. Molecular-dynamics study of SiGe epitaxy on a Si substrate. *physica status solidi (c)*, 3(3):701–704, 2006.

[23] J. Wei, H. J. Liu, X. J. Tan, L. Cheng, J. Zhang, D. D. Fan, J. Shi, and X. F. Tang. Theoretical study of the thermoelectric properties of SiGe nanotubes. *RSC Adv.*, 4:53037–53043, 2014.

[24] Tatsuya Ohira, Takaji Inamuro, and Takeshi Adachi. Molecular dynamics simulation of amorphous silicon with tersoff potential. *Solar Energy Materials and Solar Cells*, 34(1):565 – 570, 1994.

[25] Keya Dharamvir, V.K. Jindal, and Veena Verma. Structure and elastic modulii of silicon nanotubes. *Journal of Nano Research*, 2:85–90, 6 2008.

[26] Daniele Scopece, Francesco Montalenti, and Matthew J. Beck. Stability of Ge on Si (1 1 10) surfaces and the role of dimer tilting. *Phys. Rev. B*, 85:085312, Feb 2012.

[27] P. Z. Zhu and F. Z. Fang. Molecular dynamics simulations of nanoindentation of monocrystalline germanium. *Applied Physics A*, 108(2):415–421, 2012.

[28] Hong Yan, Xiao Hu, and Hannes Jonsson. Atomic structure of $\beta$-sic(100) surfaces: a study using the tersoff potential. *Surface Science*, 316(1):181 – 188, 1994.

[29] J. Tersoff. Empirical interatomic potential for silicon with improved elastic properties. *Phys. Rev. B*, 38:9902–9905, Nov 1988.

[30] J. Tersoff. Modeling solid-state chemistry: Interatomic potentials for multicomponent systems. *Phys. Rev. B*, 39:5566–5568, Mar 1989.

[31] Lammps-Tersoff potential parameters; http://lammps.sandia.gov.

[32] Adri C. T. van Duin, Siddharth Dasgupta, Francois Lorant, and William A. Goddard. Reaxff: A reactive force field for hydrocarbons. *The Journal of Physical Chemistry A*, 105(41):9396–9409, 2001.

[33] Adri C. T. van Duin, Alejandro Strachan, Shannon Stewman, Qingsong Zhang, Xin Xu, and William A. Goddard. Reaxffsio reactive force field for silicon and silicon oxide systems. *The Journal of Physical Chemistry A*, 107(19):3803–3811, 2003.

[34] G. C. Abell. Empirical chemical pseudopotential theory of molecular and metallic bonding. *Phys. Rev. B*, 31:6184–6196, May 1985.

[35] J. Tersoff. New empirical approach for the structure and energy of covalent systems. *Phys. Rev. B*, 37:6991–7000, Apr 1988.

[36] J. Tersoff. Empirical interatomic potential for carbon, with applications to amorphous carbon. *Phys. Rev. Lett.*, 61:2879–2882, Dec 1988.

[37] Donald W. Brenner. Empirical potential for hydrocarbons for use in simulating the chemical vapor deposition of diamond films. *Phys. Rev. B*, 42:9458–9471, Nov 1990.

[38] Wilfried J. Mortier, Swapan K. Ghosh, and S. Shankar. Electronegativity-equalization method for the calculation of atomic charges in molecules. *Journal of the American Chemical Society*, 108(15):4315–4320, 1986.

[39] Michael R. Weismiller, Adri C. T. van Duin, Jongguen Lee, and Richard A. Yetter. Reaxff reactive force field development and applications for molecular dynamics simulations of ammonia borane dehydrogenation and combustion. *The Journal of Physical Chemistry A*, 114(17):5485–5492, 2010. PMID: 20384351.

[40] Kimberly Chenoweth, Adri C. T. van Duin, and William A. Goddard. Reaxff reactive force field for molecular dynamics simulations of hydrocarbon oxidation. *The Journal of Physical Chemistry A*, 112(5):1040–1053, 2008. PMID: 18197648.

[41] C.J. Keavney, V.E. Haven, and S.M. Vernon. In *Photovoltaic Specialists Conference, 1990., Conference Record of the Twenty First IEEE*, volume 1, pages 141–144, 1990.

[42] Martin A. Green, Keith Emery, Yoshihiro Hishikawa, Wilhelm Warta, and Ewan D. Dunlop. *Progress in Photovoltaics: Research and Applications*, 20:12–20, 2012.

[43] Jesper Wallentin, Nicklass Anttu, Damir Asoli, Maria Huffman, Ingvar Aberg, H. Magnusson, Martin, Gerald Siefer, Peter Fuss-Kailuweit, Frank Dimroth, Bernd Witzigmann, H.Q. XU, Lars Samuelsen, Knut Deppeet, and T. Borgström, Magnus. *Science*, 339:1057–1060, 2013.

[44] N. Anttu and H. Q. Xu. *Journal of Nanoscience and Nanotechnology*, 10:7183–7187, 2010.

[45] M.T. Borgström, Jesper Wallentin, and Heurlin. *Selected Topics in Quantum Electronics, IEEE Journal of*, 17:1050–1061, 2011.

[46] Robert F. Service. *Science*, 339:263, 2013.

[47] `http://www.aerostudents.com/files/solarCells/solarCellsTheoryFullVersion.pdf. (Retrievedon2January2014).`

[48] L. J. Lauhon, Mark S. Gudiksen, and Charles M. Lieber. *Philosophical Transactions of the Royal Society of London. Series A: Mathematical, Physical and Engineering Sciences*, 362:1247–1260, 2004.

[49] William R Frensley. chapter 1. 1994.

[50] Ethan D Minot, Freek Kelkensberg, Maarten Van Kouwen, Jorden A Van Dam, Leo P Kouwenhoven, Valery Zwiller, Magnus T Borgström, Olaf Wunnicke, Marcel A Verheijen, and Erik PAM Bakkers. *Nano letters*, 7:367–371, 2007.

[51] Andreas Fuhrer, Linus E. Fröberg, Jonas Nyvold Pedersen, Magnus W. Larsson, Andreas Wacker, Mats-Erik Pistol, and Lars Samuelson. *Nano Letters*, 7:243–246, 2007.

[52] V Zwiller, N Akopian, M van Weert, M van Kouwen, U Perinetti, L Kouwenhoven, R Algra, J Gómez Rivas, E Bakkers, G Patriarche, L Liu, J-C Harmand, Y Kobayashi, and J Motohisa. *Comptes Rendus Physique*, 9:804 – 815, 2008.

[53] Premila Mohan, Junichi Motohisa, and Takashi Fukui. *Applied Physics Letters*, 88, 2006.

[54] Keitaro Ikejiri, Yusuke Kitauchi, Katsuhiro Tomioka, Junichi Motohisa, and Takashi Fukui. *Nano Letters*, 11:4314–4318, 2011.

[55] Xiangfeng Duan, Yu Huang, Yi Cui, Jianfang Wang, and Charles M Lieber. *Nature*, 409:66–69, 2001.

[56] Jianfang Wang, Mark S. Gudiksen, Xiangfeng Duan, Yi Cui, and Charles M. Lieber. *Science*, 293:1455–1457, 2001.

[57] Ying Ding, Junichi Motohisa, Bin Hua, Shinjiroh Hara, and Takashi Fukui. *Nano Letters*, 7:3598–3602, 2007.

[58] M. T. Björk, B. J. Ohlsson, T. Sass, A. I. Persson, C. Thelander, M. H. Magnusson, K. Deppert, L. R. Wallenberg, and L. Samuelson. *Nano Letters*, 2:87–89, 2002.

[59] M. T. Björk, A. Fuhrer, A. E. Hansen, M. W. Larsson, L. E. Fröberg, and L. Samuelson. *Phys. Rev. B*, 72:201307, 2005.

[60] Hajime Goto, Katsutoshi Nosaki, Katsuhiro Tomioka, Shinjiro Hara, Kenji Hiruma, Junichi Motohisa, and Takashi Fukui. *Applied Physics Express*, 2(3):035004, 2009.

[61] Magnus W Larsson, Jakob B Wagner, Mathias Wallin, Paul Hakansson, Linus E Froberg, Lars Samuelson, and L Reine Wallenberg. *Nanotechnology*, 18:015504, 2007.

[62] X. Duan and C. M. Lieber. *Advanced Materials*, 12:298–302, 2000.

[63] Toru Akiyama, Kohji Nakamura, and Tomonori Ito. *Phys. Rev. B*, 73:235308, 2006.

[64] N. Akopian, G. Patriarche, L. Liu, J.-C. Harmand, and V. Zwiller. *Nano Letters*, 10:1198–1201, 2010.

[65] Kurananda Pemasiri, Mohammad Montazeri, Richard Gass, Leigh M. Smith, Howard E. Jackson, Jan Yarrison-Rice, Suriati Paiman, Qiang Gao, H. Hoe Tan, Chennupati Jagadish, Xin Zhang, and Jin Zou. *Nano Letters*, 9:648–654, 2009.

[66] Rienk E Algra, Marcel A Verheijen, Magnus T Borgström, Lou-Fe Feiner, George Immink, Willem J P van Enckevort, Elias Vlieg, and Erik P A M Bakkers. *Nature*, 456:369–372, 2008.

[67] Robert A. Taylor, Patrick E. Phelan, Todd P. Otanicar, Chad A. Walker, Monica Nguyen, Steven Trimble, and Ravi Prasher. Applicability of nanofluids in high flux solar collectors. *Journal of Renewable and Sustainable Energy*, 3(2), 2011.

[68] Baoquan Sun, Eike Marx, and Neil C. Greenham. Photovoltaic devices using blends of branched CdSe nanoparticles and conjugated polymers. *Nano Letters*, 3(7):961–963, 2003.

[69] Christoph Rier, Gabi Schierning, Hartmut Wiggers, Roland Schmechel, and Dieter Jäger. Photovoltaic devices from silicon nanoparticles. *MRS Proceedings*, 1260, 1 2010.

[70] Wanli Ma, Joseph M. Luther, Haimei Zheng, Yue Wu, and A. Paul Alivisatos. Photovoltaic devices employing ternary PbSxSe1-x nanocrystals. *Nano Letters*, 9(4):1699–1703, 2009.

[71] Nguyen TK Thanh and Luke AW Green. Functionalisation of nanoparticles for biomedical applications. *Nano Today*, 5(3):213 – 230, 2010.

[72] G.L. Prasad. Biomedical applications of nanoparticles. In Thomas J. Webster, editor, *Safety of Nanoparticles*, Nanostructure Science and Technology, pages 89–109. Springer New York, 2009.

[73] Po C Chen, Sandra C Mwakwari, Adegboyega K Oyelere, Correspondence Adegboyega, and K Oyelere. Review gold nanoparticles: From nanomedicine to nanosensing.

[74] Elodie Boisselier and Didier Astruc. Gold nanoparticles in nanomedicine: preparations, imaging, diagnostics, therapies and toxicity. *Chem. Soc. Rev.*, 38:1759–1782, 2009.

[75] Marcel Bruchez, Mario Moronne, Peter Gin, Shimon Weiss, and A. Paul Alivisatos. Semiconductor nanocrystals as fluorescent biological labels. *Science*, 281(5385):2013–2016, 1998.

[76] Faramarz Farahi, Pedro Jorge, Mona Mayeh, Ramazan Benrashid, Paulo Caldas, and Jose Santos. Applications of nanoparticles in optical chemical and biological sensors. *Proc. SPIE*, 5590:66–76, 2004.

[77] Nir Tessler, Vlad Medvedev, Miri Kazes, ShiHai Kan, and Uri Banin. Efficient near-infrared polymer nanocrystal light-emitting diodes. 295(5559):1506–1508, 2002.

[78] Brian FG Johnson. From clusters to nanoparticles and catalysis. *Coordination Chemistry Reviews*, 190-192(0):1269–1285, 1999.

[79] Yoshikazu Homma, Takayuki Yamashita, Paul Finnie, Masato Tomita, and Toshio Ogino. Single-walled carbon nanotube growth on silicon substrates using nanoparticle catalysts. *Japanese Journal of Applied Physics*, 41(1A):L89, 2002.

[80] Thomas Nann, Saad K. Ibrahim, Pei-Meng Woi, Shu Xu, Jan Ziegler, and Christopher J. Pickett. Water splitting by visible light: A nanophotocathode for hydrogen production. *Angewandte Chemie International Edition*, 49(9):1574–1577, 2010.

[81] K. Kamimura, T. Suzuki, and A. Kunioka. Metal insulator semiconductor Schottky barrier solar cells fabricated on InP. *Applied Physics Letters*, 38(4):259–261, 1981.

[82] B. K. Ridley. Anatomy of the transferred electron effect in III-V semiconductors. *Journal of Applied Physics*, 48(2):754–764, 1977.

[83] Maojun Zheng, Lide Zhang, Guanghai Li, and Zhi Jiang. Preparation and optical properties of composite thin films with embedded InP nanoparticles. *Chinese Science Bulletin*, 46(6):461–465, 2001.

[84] Stuart K. Stubbs, Samantha J. O. Hardman, Darren M. Graham, Ben F. Spencer, Wendy R. Flavell, Paul Glarvey, Ombretta Masala, Nigel L. Pickett, and David J. Binks. Efficient carrier multiplication in InP nanoparticles. *Phys. Rev. B*, 81:081303, Feb 2010.

[85] B. F. Spencer, D. M. Graham, C. Lange, S. Chattopadhyay, and W. R. Flavell. Developing InP-based solar cells: Time-resolved terahertz measurements of photoconductivity and carrier multiplication efficiencies. In *Infrared Millimeter and Terahertz Waves (IRMMW-THz), 2010 35th International Conference on*, pages 1–3, Sept 2010.

[86] H.J. Schimper, Z. Kollonitsch, K. Moller, U. Seidel, U. Bloeck, K. Schwarzburg, F. Willig, and T. Hannappel. Material studies regarding InP-based high-efficiency solar cells. *Journal of Crystal Growth*, 287(2):642 – 646, 2006. The 16th American Conference on Crystal Growth and Epitaxy {ACCGE} 16 The 12th Biennial Workshop on {OMVPE} {OMVPE} 12.

[87] Shanmin Gao, Jun Lu, Nan Chen, Yan Zhao, and Yi Xie. Aqueous synthesis of III-V semiconductor GaP and InP exhibiting pronounced quantum confinement. *Chem. Commun.*, pages 3064–3065, 2002.

[88] L. E. Brus. A simple model for the ionization potential, electron affinity, and aqueous redox potentials of small semiconductor crystallites. *The Journal of Chemical Physics*, 79(11):5566–5571, 1983.

[89] D.A. Vinokurov, V.A. Kapitonov, O.V. Kovalenkov, D.A. Livshits, and I.S. Tarasov. Self-organized nanosize InP and InAsP clusters obtained by metalorganic compound hydride epitaxy. *Technical Physics Letters*, 24(8):623–625, 1998.

[90] J Jasinski, VJ Leppert, Si-Ty Lam, GA Gibson, K Nauka, CC Yang, and Zhang-Lin Zhou. Rapid oxidation of InP nanoparticles in air. *Solid State Communications*, 141(11):624 – 627, 2007.

[91] Sandeep Kumar, Ralf Thomann, and Thomas Nann. Synthesis and electrochemical properties of InP nanocrystals. *Journal of Materials Research*, 21:543–546, 3 2006.

[92] Kuan-Chuan Fang, Cheng-I Weng, and Shin-Pon Ju. An investigation into the structural features and thermal conductivity of silicon nanoparticles using molecular dynamics simulations. *Nanotechnology*, 17(15):3909, 2006.

[93] R. Pekoz, H. Oymak, and Ş. Erkoç. *Rev. Theor. Sci.*, 2, 301-319, (2014).

[94] H. Ustunel and Ş. Erkoç. *J. Comput. Theor. Nanosci.*, 4, 928-956, (2007).

[95] Pu Tian. Molecular dynamics simulations of nanoparticles. *Annu. Rep. Prog. Chem., Sect. C: Phys. Chem.*, 104:142–164, 2008.

[96] P. S. Yadav, D. K. Pandey, S. Agrawal, and B. K. Agrawal. *Quantum Matter*, 3, 39-46, (2014).

[97] J. Y. Guo, C. X. Xu, F. Y. Sheng, Z. L. Jin, Z. L. Shi, J. Dai, and Z. H. Li. *Quantum Matter*, 2, 181-186, (2013).

[98] S. Xu, H. Xing, Z. Ding, Y. Huang, X. Chen, and Y. Shi. *J. Comput. Theor. Nanosci.*, 6, 374-378, (2009).

[99] S. Muruganandam, G. Anbalagan, and G. Murugadoss. Synthesis and structural, optical and thermal properties of CdS:Zn2+ nanoparticles. *Applied Nanoscience*, pages 1–7, 2013.

[100] V. Salles, S. Bernard, R. Chiriac, and P. Miele. Structural and thermal properties of boron nitride nanoparticles. *Journal of the European Ceramic Society*, 32(9):1867 – 1871, 2012. Engineering Ceramics 2011 - from Materials to Components.

[101] MohdAbdul Majeed Khan, Sushil Kumar, Maqusood Ahamed, SalmanA Alrokayan, and MohammadSaleh AlSalhi. Structural and thermal studies of silver nanoparticles and electrical transport study of their thin films. *Nanoscale Research Letters*, 6(1):1–8, 2011.

[102] S. Naderi, A. Ghaderi, S. Solaymani, and M. M. Golzan. Structural, optical and thermal properties of silver colloidal nanoparticles. *The European Physical Journal - Applied Physics*, 58, 5 2012.

[103] V.V. Vodnik, N.D. Abazovic, Z.A. Stojanovic, M. Marinovic-Cincovic, M. Mitric, and M.I. Comor. Optical, structural and thermal characterization of gold nanoparticles - poly(vinylalcohol) composite films. *Journal of Composite Materials*, 46:987–995, apr 2012.

[104] A. A. Guzelian, J. E. B. Katari, A. V. Kadavanich, U. Banin, K. Hamad, E. Juban, A. P. Alivisatos, R. H. Wolters, C. C. Arnold, and J. R. Heath. Synthesis of size-selected, surface-passivated InP nanocrystals. *The Journal of Physical Chemistry*, 100(17):7212–7219, 1996.

[105] O. I. Micic, J. R. Sprague, C. J. Curtis, K. M. Jones, J. L Machol, A. J. Nozik, H. Giessen, B. Fluegel, G. Mohs, and N. Peyghambarian. Synthesis and characterization of InP, GaP, and GaInP2 quantum dots. *The Journal of Physical Chemistry*, 99(19):7754–7759, 1995.

[106] David Battaglia and Xiaogang Peng. Formation of high quality InP and InAs nanocrystals in a noncoordinating solvent. *Nano Letters*, 2(9):1027–1030, 2002.

[107] Stephan Haubold, Markus Haase, Andreas Kornowski, and Horst Weller. Strongly luminescent InP/ZnS core-shell nanoparticles. *ChemPhysChem*, 2(5):331–334, 2001.

[108] Nadire Nayir, Emre S. Tasci, and Sakir Erkoc. Structural properties of indium phosphide nanorods: molecular dynamics simulations.

[109] Nadire Nayir, Emre S. Tasci, and Sakir Erkoc. Structural and thermal properties of indium phosphide nanoparticles: Molecular dynamics simulations.

[110] Koichi Momma and Fujio Izumi. *VESTA3* for three-dimensional visualization of crystal, volumetric and morphology data. *Journal of Applied Crystallography*, 44(6):1272–1276, Dec 2011.

[111] Koichi Momma and Fujio Izumi. *VESTA*: a three-dimensional visualization system for electronic and structural analysis. *Journal of Applied Crystallography*, 41(3):653–658, Jun 2008.

[112] E. Simoen C. Claeys. Germanium-based technologies: From materials to devices. *Elsevier, Amsterdam, 2007*.

[113] Mo Wu, Y. I. Alivov, and Hadis Morkoç. High-$\kappa$ dielectrics and advanced channel concepts for si mosfet. *Journal of Materials Science: Materials in Electronics*, 19(10):915–951, Oct 2008.

[114] H. Tahini, A. Chroneos, R. W. Grimes, U. Schwingenschlögl, and H. Bracht. Diffusion of e centers in germanium predicted using gga+u approach. *Applied Physics Letters*, 99(7):072112, 2011.

[115] A. Chroneos, U. Schwingenschlögl, and A. Dimoulas. Impurity diffusion, point defect engineering, and surface interface passivation in germanium. *Annalen der Physik*, 524(3-4):123–132.

[116] H Tahini, A Chroneos, R W Grimes, U Schwingenschlögl, and A Dimoulas. Strain-induced changes to the electronic structure of germanium. *Journal of Physics: Condensed Matter*, 24(19):195802, 2012.

[117] Chi On Chui, Hyoungsub Kim, D. Chi, B.B. Triplett, P.C. McIntyre, and K.C. Saraswat. A sub-400/spl deg/C germanium MOSFET technology with high-/spl kappa/ dielectric and metal gate. In *Electron Devices Meeting, 2002. IEDM '02. International*, pages 437–440, Dec 2002.

[118] C.H. Lee, T. Nishimura, T. Tabata, S.K. Wang, K. Nagashio, K. Kita, and A. Toriumi. Ge MOSFETs performance: Impact of Ge interface passivation. In *Electron Devices Meeting (IEDM), 2010 IEEE International*, pages 18.1.1–18.1.4, Dec 2010.

[119] H. Shang, H. Okorn-Schimdt, J. Ott, P. Kozlowski, S. Steen, E.C. Jones, H.-S.P. Wong, and W. Hanesch. Electrical characterization of germanium p-channel MOSFETs. *Electron Device Letters, IEEE*, 24(4):242–244, April 2003.

[120] S. Takagi, R. Zhang, S.-H. Kim, N. Taoka, M. Yokoyama, J.-K. Suh, R. Suzuki, and M. Takenaka. MOS interface and channel engineering for high-mobility Ge/III-V CMOS. In *Electron Devices Meeting (IEDM), 2012 IEEE International*, pages 23.1.1–23.1.4, Dec 2012.

[121] Rodolfo E. Camacho-Aguilera, Yan Cai, Neil Patel, Jonathan T. Bessette, Marco Romagnoli, Lionel C. Kimerling, and Jurgen Michel. An electrically pumped germanium laser. *Opt. Express*, 20(10):11316–11320, May 2012.

[122] Jifeng Liu, Xiaochen Sun, Dong Pan, Xiaoxin Wang, Lionel C. Kimerling, Thomas L. Koch, and Jurgen Michel. Tensile-strained, n-type Ge as a gain medium formonolithic laser integration on Si. *Opt. Express*, 15(18):11272–11277, Sep 2007.

[123] Solomon Assefa, Fengnian Xia, and Yurii A. Vlasov. Reinventing germanium avalanche photodetector for nanophotonic on-chip optical interconnects. *Nature*, 464:80–84, 2010.

[124] Yasuhiko Ishikawa, Kazumi Wada, Douglas D. Cannon, Jifeng Liu, Hsin-Chiao Luan, and Lionel C. Kimerling. Strain-induced band gap shrinkage in Ge grown on Si substrate. *Applied Physics Letters*, 82(13):2044–2046, 2003.

[125] S. M. Ting and E. A. Fitzgerald. Metal-organic chemical vapor deposition of single domain GaAs on ge/$Ge_xSi_{1-x}/Si$ and Ge substrates. *Journal of Applied Physics*, 87(5):2618–2628, 2000.

[126] A. G. Taboada, T. Kreiliger, C. V. Falub, F. Isa, M. Salvalaglio, L. Wewior, D. Fuster, M. Richter, E. Uccelli, P. Niedermann, A. Neels, F. Mancarella, B. Alén, L. Miglio, A. Dommann, G. Isella, and H. von Känel. Strain relaxation of gaas/ge crystals on patterned si substrates. *Applied Physics Letters*, 104(2):–, 2014.

[127] V. Reboud, A. Gassenq, J.M. Hartmann, J. Widiez, L. Virot, J. Aubin, K. Guilloy, S. Tardif, J.M. Fédéli, N. Pauc, A. Chelnokov, and V. Calvo. Germanium based photonic components toward a full silicon/germanium photonic platform. *Progress in Crystal Growth and Characterization of Materials*, 63(2):1 – 24, 2017.

[128] Shu Nakaharai, Tsutomu Tezuka, Naoharu Sugiyama, Yoshihiko Moriyama, and Shin ichi Takagi. Characterization of 7-nm-thick strained ge-on-insulator layer fabricated by ge-condensation technique. *Applied Physics Letters*, 83(17):3516–3518, 2003.

[129] Gianni Taraschi, Arthur J. Pitera, and Eugene A. Fitzgerald. Strained si, sige, and ge on-insulator: review of wafer bonding fabrication techniques. *Solid-State Electronics*, 48(8):1297 – 1305, 2004. Strained-Si Heterostructures and Devices.

[130] R. R. Lieten, S. Degroote, M. Leys, N. E. Posthuma, and G. Borghs. Solid phase epitaxy of amorphous Ge on Si in N2 atmosphere. *Applied Physics Letters*, 94(11):112113, 2009.

[131] J. J. Wen, Z. Liu D. L. Zhang, T. W. Zhou, C. L. Xue, Y. H. Zuo, C. B. Li, Q. M. Wang, and B. W. Cheng. Effects of rapid thermal process temperatures on strain and si concentration distributions in ge-on-insulator structures formed by rapid melt growth. *ECS Solid State Lett.*, 3:Q33–Q35, 2014.

[132] Zhi Liu, Juanjuan Wen, Tianwei Zhou, Chunlai Xue, Yuhua Zuo, Chuanbo Li, Buwen Cheng, and Qiming Wang. Lateral growth of single-crystal ge on insulating substrate using amorphous si seed by rapid melting growth. *Thin Solid Films*, 597(Supplement C):39 – 43, 2015.

[133] Tatsuya Hashimoto, Chiaki Yoshimoto, Takuji Hosoi, Takayoshi Shimura, and Heiji Watanabe. Fabrication of local Ge-on-insulator structures by lateral liquid-phase epitaxy: Effect of controlling interface energy between ge and insulators on lateral epitaxial growth. *Applied Physics Express*, 2(6):066502, 2009.

[134] H. Chikita, R. Matsumura, Y. Tojo, H. Yokoyama, T. Sadoh, and M. Miyao. In-depth analysis of high-quality Ge-on-insulator structure formed by rapid-melting growth. *Thin Solid Films*, 557:139 – 142, 2014. The 8th International Conference on Silicon Epitaxy and Heterostructures (ICSI-8) and the 6th International Symposium on Control of Semiconductor Interfaces (ISCSI-VI).

[135] Chih-Kuo Tseng, Wei-Ting Chen, Ku-Hung Chen, Han-Din Liu, Yimin Kang, Neil Na, and Ming-Chang M. Lee. A self-assembled microbonded germanium/silicon heterojunction photodiode for 25 Gb/s high-speed optical interconnects. *Scientific Reports*, 3:3225, 2013.

[136] Ryo Matsumura, Yuki Tojo, Masashi Kurosawa, Taizoh Sadoh, and Masanobu Miyao. Dynamic analysis of rapid-melting growth using SiGe on insulator. *Thin Solid Films*, 557:125 – 128, 2014. The 8th International Conference on Silicon Epitaxy and Heterostructures (ICSI-8) and the 6th International Symposium on Control of Semiconductor Interfaces (ISCSI-VI).

[137] Masanobu Miyao, Takanori Tanaka, Kaoru Toko, and Masanori Tanaka. Giant Ge-on-insulator formation by SiGe mixing-triggered liquid-phase epitaxy. *Applied Physics Express*, 2(4):045503, 2009.

[138] T. Sadoh, M. Kurosawa, K. Toko, and M. Miyao. Coherent lateral-growth of Ge over insulating film by rapid-melting-crystallization. *Thin Solid Films*, 557:135 – 138, 2014. The 8th International Conference on Silicon Epitaxy and Heterostructures (ICSI-8) and the 6th International Symposium on Control of Semiconductor Interfaces (ISCSI-VI).

[139] Hiroyuki Yokoyama, Kaoru Toko, Taizoh Sadoh, and Masanobu Miyao. Nanolithography free formation of high density Ge-on-insulator network for epitaxial template. *Applied Physics Letters*, 100(9):–, 2012.

[140] T. A. Langdo, C. W. Leitz, M. T. Currie, E. A. Fitzgerald, A. Lochtefeld, and D. A. Antoniadis. High quality Ge on Si by epitaxial necking. *Applied Physics Letters*, 76(25):3700–3702, 2000.

[141] R. Hull, J. C. Bean, L. Peticolas, and D. Bahnck. Growth of $Ge_xSi_{1-x}$ alloys on Si(110) surfaces. *Applied Physics Letters*, 59(8):964–966, 1991.

[142] S. Balakumar, M. M. Roya, B. Ramamurthya, C. H. Tunga, Gao Feia, S. Tripathyb, Chi Dongzhib, R. Kumara, N. Balasubramaniana, and D. L. Kwonga. Fabrication aspects of germanium on insulator from sputtered Ge on Si-substrates. *Electrochemical and Solid-State Letters*, 9:G158–G160, 2006.

[143] Nadire Nayir, Adri C. T. van Duin, and Sakir Erkoc. Development of a reaxff reactive force field for interstitial oxygen in germanium and application to $GeO_2$/Ge interfaces. (in prep.).

[144] Nadire Nayir, Adri C. T. van Duin, and Sakir Erkoc. Development of the reaxff reactive force field for inherent point defects in the Si/Silica system. (in prep.).

[145] George Psofogiannakis and Adri C.T. van Duin. Development of a reaxff reactive force field for si/ge/h systems and application to atomic hydrogen bombardment of si, ge, and sige (100) surfaces. *Surface Science*, 646(Supplement C):253 – 260, 2016. Surface science for heterogeneous catalysis, a special issue in Honour of Richard Lambert.

[146] Yuanxia Zheng, Sungwook Hong, George Psofogiannakis, G. Bruce Rayner, Suman Datta, Adri C.T. van Duin, and Roman Engel-Herbert. Modeling and in situ probing of surface reactions in atomic layer deposition. *ACS Applied Materials & Interfaces*, 9(18):15848–15856, 2017. PMID: 28380291.

[147] K. Sueoka and J. Vanhellemont. Ab initio studies of intrinsic point defects, interstitial oxygen and vacancy or oxygen clustering in germanium crystals. *Materials Science in Semiconductor Processing*, 9(4):494 – 497, 2006. Proceedings of Symposium T E-MRS 2006 Spring Meeting on Germanium based semiconductors from materials to devices.

[148] Davide Colleoni and Alfredo Pasquarello. Diffusion of interstitial oxygen in silicon and germanium: a hybrid functional study. *Journal of Physics: Condensed Matter*, 28(49):495801, 2016.

[149] L.H. Li and J.E. Lowther. Plane-wave pseudopotential calculations of intrinsic defects in diamond. *Journal of Physics and Chemistry of Solids*, 58(10):1607 – 1610, 1997.

[150] C. Weigel, D. Peak, J. W. Corbett, G. D. Watkins, and R. P. Messmer. Carbon interstitial in the diamond lattice. *Phys. Rev. B*, 8:2906–2915, Sep 1973.

[151] Peter Pichler. *Intrinsic Point Defects, Impurities, and Their Diffusion in Silicon*. SpringerWienNewYork, 2004.

[152] Peter Deák, Bálint Aradi, Thomas Frauenheim, and Adam Gali. Challenges for ab initio defect modeling. *Materials Science and Engineering: B*, 154-155:187 – 192, 2008. Front-End Junction and Contact Formation in Future Silicon/Germanium Based Devices.

[153] Stefan K. Estreicher, Daniel J. Backlund, Christian Carbogno, and Matthias Scheffler. Activation energies for diffusion of defects in silicon: The role of the exchange-correlation functional. *Angewandte Chemie International Edition*, 50(43):10221–10225, 2011.

[154] J. Coutinho, R. Jones, P. R. Briddon, and S. Öberg. Oxygen and dioxygen centers in si and ge: Density-functional calculations. *Phys. Rev. B*, 62:10824–10840, Oct 2000.

[155] Vasilii Gusakov. Unified model of diffusion of interstitial oxygen in silicon and germanium crystals. *Journal of Physics: Condensed Matter*, 17(22):S2285, 2005.

[156] J.W. Corbett, R.S. McDonald, and G.D. Watkins. The configuration and diffusion of isolated oxygen in silicon and germanium. *Journal of Physics and Chemistry of Solids*, 25(8):873 – 879, 1964.

[157] A. Chroneos and R. V. Vovk. Oxygen diffusion in germanium: interconnecting point defect parameters with bulk properties. *Journal of Materials Science: Materials in Electronics*, 26(10):7378–7380, Oct 2015.

[158] Li-ion diffusion coefficients in cathode materials with adf/reaxff. `https://www.scm.com/wp-content/uploads/ReaxFF-Batteries-DiffusionCoefficients.pdf`. Accessed: 2018-07-07.

[159] A. Einstein. On the movement of small particles suspended in a stationary liquid demanded by the molecular-kinetic theory of heat. *Annln Phys.*, 17(549), 1905.

[160] Adri C. T. van Duin, Siddharth Dasgupta, Francois Lorant, and William A. Goddard. Reaxff a reactive force field for hydrocarbons. *The Journal of Physical Chemistry A*, 105(41):9396–9409, 2001.

[161] Kimberly Chenoweth, Adri C. T. van Duin, and William A. Goddard. Reaxff reactive force field for molecular dynamics simulations of hydrocarbon oxidation. *The Journal of Physical Chemistry A*, 112(5):1040–1053, 2008. PMID: 18197648.

[162] ReaxFF 2017, SCM, Theoretical Chemistry, Vrije Universiteit, Amsterdam, The Netherlands; http://www.scm.com.

[163] Steve Plimpton. Fast parallel algorithms for short-range molecular dynamics. *Journal of Computational Physics*, 117(1):1 – 19, 1995.

[164] Akira Toriumi and Tomonori Nishimura. Germanium cmos potential from material and process perspectives: Be more positive about germanium. *Japanese Journal of Applied Physics*, 57(1):010101, 2018.

[165] K. Hofmann, G.W. Rubloff, M. Liehr, and D.R. Young. High temperature reaction and defect chemistry at the $Si/SiO_2$ interface. *Applied Surface Science*, 30(1):25 – 31, 1987.

[166] Akira Toriumi and Tomonori Nishimura. Germanium cmos potential from material and process perspectives: Be more positive about germanium. *Japanese Journal of Applied Physics*, 57(1):010101, 2018.

[167] Choong Hyun Lee, Toshiyuki Tabata, Tomonori Nishimura, Kosuke Nagashio, Koji Kita, and Akira Toriumi. Ge/geo 2 interface control with high-pressure oxidation for improving electrical characteristics. *Applied Physics Express*, 2(7):071404, 2009.

[168] Kanichi Kamiya, Toshinobu Yoko, Yoshitaka Itoh, and Sumio Sakka. X-ray diffraction study of na2o geo2 melts. *Journal of Non-Crystalline Solids*, 79(3):285 – 294, 1986.

[169] Philip S Salmon, Adrian C Barnes, Richard A Martin, and Gabriel J Cuello. Structure of glassy geo 2. *Journal of Physics: Condensed Matter*, 19(41):415110, 2007.

[170] M Micoulaut, L Cormier, and G S Henderson. The structure of amorphous, crystalline and liquid geo 2. *Journal of Physics: Condensed Matter*, 18(45):R753, 2006.

[171] R. L. Mozzi and B. E. Warren. The structure of vitreous silica. *Journal of Applied Crystallography*, 2(4):164–172, Oct 1969.

[172] M. Micoulaut, Yves Guissani, and Bernard Guillot. Simulated structural and thermal properties of glassy and liquid germania. *Physical review. E, Statistical, nonlinear, and soft matter physics*, 73 3 Pt 1:031504, 2006.

[173] O. B. Tsiok, V. V. Brazhkin, A. G. Lyapin, and L. G. Khvostantsev. Logarithmic kinetics of the amorphous-amorphous transformations in $SiO_2$ and $GeO_2$ glasses under high pressure. *Phys. Rev. Lett.*, 80:999–1002, Feb 1998.

[174] K. H. Smith, E. Shero, A. Chizmeshya, and G. H. Wolf. The equation of state of polyamorphic germania glass: A two domain description of the viscoelastic response. *The Journal of Chemical Physics*, 102(17):6851–6857, 1995.

[175] Joaquín Peralta, Gonzalo Gutiérrez, and José Rogan. Structural and vibrational properties of amorphous $GeO_2$ : a molecular dynamics study. *Journal of Physics: Condensed Matter*, 20(14):145215, 2008.

[176] Luigi Giacomazzi, P. Umari, and Alfredo Pasquarello. Vibrational spectra of vitreous germania from first-principles. *Phys. Rev. B*, 74:155208, Oct 2006.

[177] Joseph C. Fogarty, Hasan Metin Aktulga, Ananth Y. Grama, Adri C. T. van Duin, and Sagar A. Pandit. A reactive molecular dynamics simulation of the silica-water interface. *The Journal of Chemical Physics*, 132(17):174704, 2010.

[178] R C Newman. Oxygen diffusion and precipitation in czochralski silicon. *Journal of Physics: Condensed Matter*, 12(25):R335, 2000.

[179] J. C. Mikkelsen. The diffusivity and solubility of oxygen in silicon. *MRS Proceedings*, 59:19, 1985.

[180] H. Li and J. Robertson. Germanium oxidation occurs by diffusion of oxygen network interstitials. *Applied Physics Letters*, 110(22):222902, 2017.

[181] Jan Felix Binder and Alfredo Pasquarello. Minimum energy path and atomistic mechanism of the elementary step in oxygen diffusion in silicon: A density-functional study. *Phys. Rev. B*, 89:245306, Jun 2014.

[182] Manveer S Munde, David Z Gao, and Alexander L Shluger. Diffusion and aggregation of oxygen vacancies in amorphous silica. *Journal of Physics: Condensed Matter*, 29(24):245701, 2017.

[183] Melting curve of silicon to 15gpa determined by two-dimensional angle-dispersive diffraction using a kawai-type apparatus with x-ray transparent sintered diamond anvils. *Journal of Physics and Chemistry of Solids*, 69(9):2255 – 2260, 2008. Study of Matter Under Extreme Conditions 2007.

[184] Ivars Henins. Precision density measurement of silicon. *Journal of Research of the National Bureau of Standards- A*, 68A(5), 1964.

[185] Y. Sato, T. Nishizuka, K. Hara, T. Yamamura, and Y. Waseda. Density measurement of molten silicon by a pycnometric method. *International Journal of Thermophysics*, 21(6):1463–1471, Nov 2000.

[186] Hitoshi Sasaki, Eiji Tokizaki, Kazutaka Terashima, and Shigeyuki Kimura. Density variations in molten silicon dependent on its thermal history. *Japanese Journal of Applied Physics*, 33(11R):6078, 1994.

[187] Hitoshi Sasaki, Eiji Tokizaki, Kazutaka Terashima, and Shigeyuki Kimura. Density variation of molten silicon measured by an improved archimedian method. *Japanese Journal of Applied Physics*, 33(7R):3803, 1994.

[188] Yu. N. Taran-Zhovnir, N. M. Kochegura, S. P. Kazachkov, V. R. Pilipchuk, E. A. Markovskii, V. Z. Kutsova, and K. V. Uzlov. The volume properties of silicon in the solid, solid-liquid, and liquid states. *Soviet Physics Doklady*, 34, 1989.

[189] Kristin Persson. Materials data on si (sg:227) by materials project, 11 2014. An optional note.

[190] I. Štich, R. Car, and M. Parrinello. Bonding and disorder in liquid silicon. *Phys. Rev. Lett.*, 63:2240–2243, Nov 1989.

[191] Yoshiko Itoh and Tadashi Nozaki. Solubility and diffusion coefficient of oxygen in silicon. *Japanese Journal of Applied Physics*, 24(3R):279, 1985.

[192] Carol B. Johnson, Leung K. Tang, Aaron G. Smith, Akshaya Ravichandran, Zhiping Luo, Stanislav Vitha, and Andreas Holzenburg. Single particle tracking analysis of the chloroplast division protein ftsz anchoring to the inner envelope membrane. *Cambridge University Press*, 19(3):507–512, 2013.

[193] Th Demuth, Y. Jeanvoine, J. Hafner, and J. G. Ángyón. Polymorphism in silica studied in the local density and generalized-gradient approximations. *Journal of Physics: Condensed Matter*, 11(19):3833, 1999.

[194] R. Brückner. Properties and structure of vitreous silica.II. *Journal of Non-Crystalline Solids*, 5(3):177 – 216, 1971.

[195] R. L. Mozzi and B. E. Warren. The structure of vitreous silica. *Journal of Applied Crystallography*, 2(4):164–172, Oct 1969.

[196] David I. Grimley, Adrian C. Wright, and Roger N. Sinclair. Neutron scattering from vitreous silica iv. time-of-flight diffraction. *Journal of Non-Crystalline Solids*, 119(1):49 – 64, 1990.

[197] M G Tucker, D A Keen, M T Dove, and K Trachenko. Refinement of the si-o-si bond angle distribution in vitreous silica. *Journal of Physics: Condensed Matter*, 17(5):S67, 2005.

[198] Francesco Mauri, Alfredo Pasquarello, Bernd G. Pfrommer, Young-Gui Yoon, and Steven G. Louie. Si-o-si bond-angle distribution in vitreous silica from first-principles $^{29}$Si nmr analysis. *Phys. Rev. B*, 62:R4786–R4789, Aug 2000.

[199] Wim J. Malfait, Werner E. Halter, and Rene Verel. 29si nmr spectroscopy of silica glass: T1 relaxation and constraints on the si-o-si bond angle distribution. *Chemical Geology*, 256(3):269 – 277, 2008. 8th Silicate Melt Workshop.

[200] J. R. G. Da Silva, D. G. Pinatti, C. E. Anderson, and M. L. Rudee. A refinement of the structure of vitreous silica. *The Philosophical Magazine: A Journal of Theoretical Experimental and Applied Physics*, 31(3):713–717, 1975.

[201] Mineo Saito and Atsushi Oshiyama. Stable atomic geometries of oxygen microclusters in silicon. *Phys. Rev. B*, 38:10711–10717, Nov 1988.

# APPENDIX A

## STRUCTURAL PROPERTIES OF INDIUM PHOSPHIDE NANORODS:MOLECULAR DYNAMICS SIMULATIONS

## A.1 Zincblende Nanorods

### A.1.1 Gradual Heating

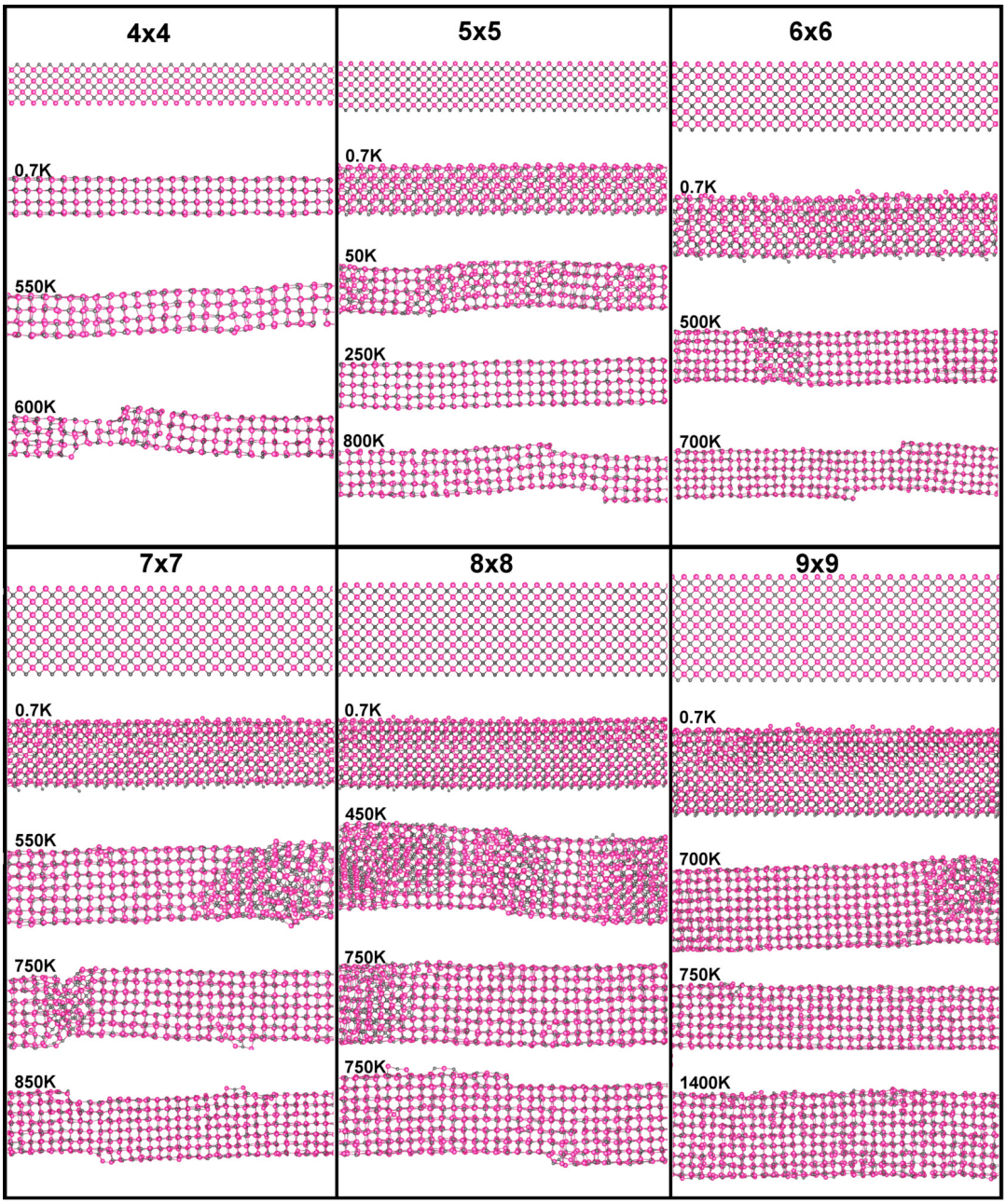


Figure A.1: Gradually heated ZB NRs. When the ZB NRs were subjected to heating, increasing the temperature by 50K, the phase transitions (ZB->RS) and stacking faults were observed except for the 9x9 NR (VESTA).

### A.1.2 Stretching at Constant and Increasing Temperatures (5% and 10% Ratio)

In the stretching figures, the durations for which strain was applied are shown for each nanorod, unit of time being picoseconds (ps). The constant temperature at which the stretching took place is written in all of the stretching figures. For example, 0.7K shown in Figure A.2 refers to the stretching at 0.7K with the temperature having been kept constant all through the simulation. Abbreviation for "stretching at increasing temperatures" is written as "inc.temp." in all of the stretching figures.

#### A.1.2.1 Phase Transitions Under Stretching

When ZB NRs are subjected to stretching, three different phases are observed (ZB, RS and WZ). For all the ZB NRs, the phase sequence was observed to be ZB->RS->WZ in both equilibrium (stretching at constant temperatures) and non-equilibriated (stretching at increasing temperatures) criterias applied simulations under strain for the 5% and 10% stretching ratios. These phases with their occurence times (ps) are shown in the figures below.

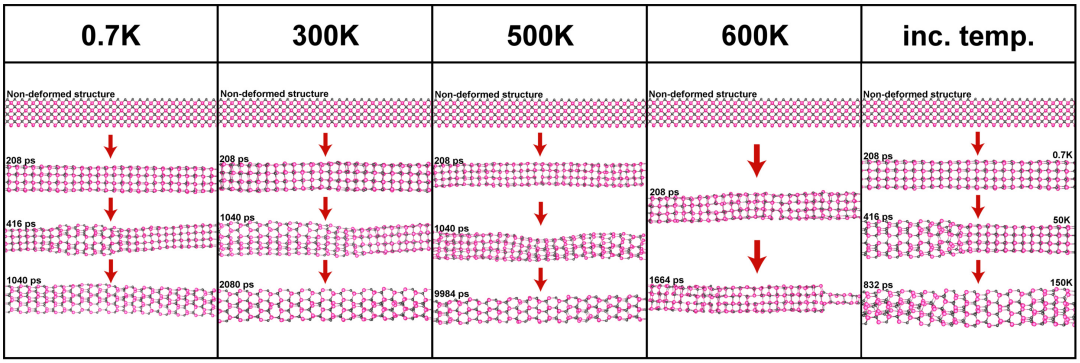


Figure A.2: Phase transitions observed in the 4x4 ZB NR under strain for the 5% S.R. (VESTA)

#### A.1.2.2 Breaking Mechanisms with respect to different phases under strain

Under strain, the breaking mechanisms are seen to depend on the phase of the nanorod. In the RS structured NR, when the NR was elongated, the thinning occurred where

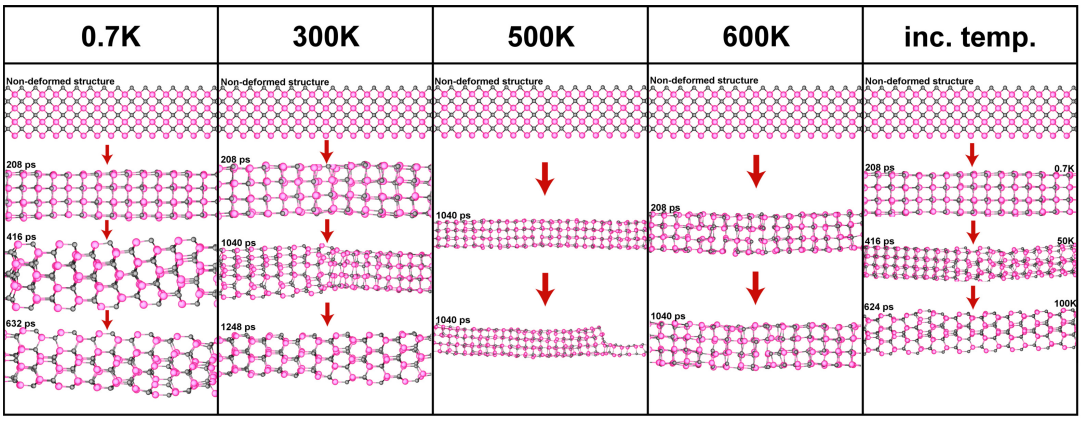


Figure A.3: Phase transitions in the 4x4 ZB NR under strain for the 10% S.R. At this ratio, the WZ phase occurred at a lower temperature (300K) with respect to the the stretching at the 5% S.R. (500K) in Figure A.2 (VESTA).

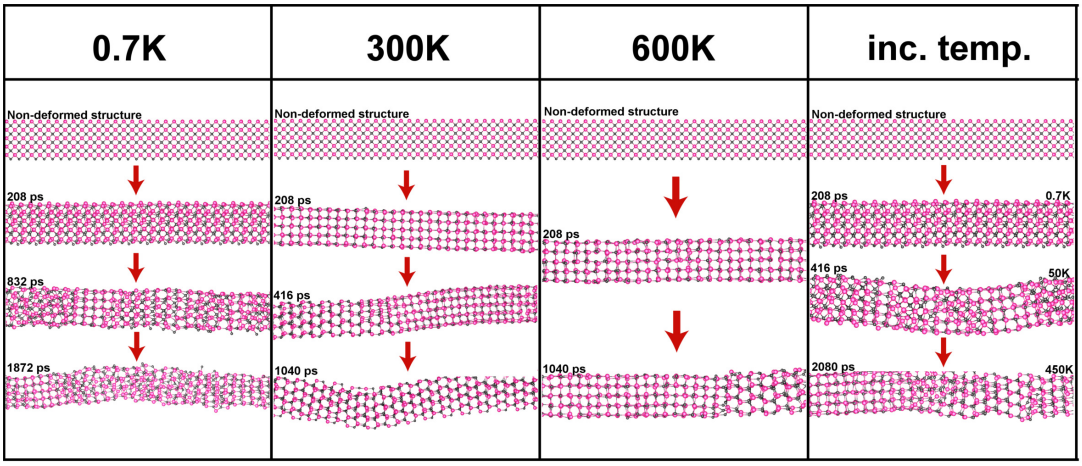


Figure A.4: Phase transitions in the 5x5 ZB NR under strain for the 5% S.R. The WZ phase was observed under strain at 0.7, 300, 600K and increasing temperatures (VESTA).

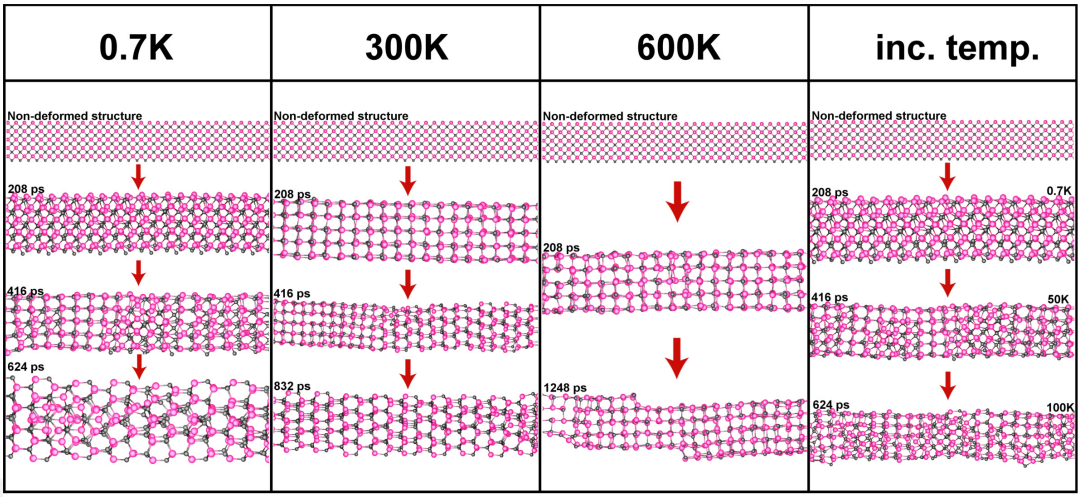


Figure A.5: Phase transitions in the 5x5 ZB NR under strain for the 10% S.R. The WZ phase occurred in the 5x5 ZB NR at lower temperatures (0.7 and 300K) than the stretching for the 5% S.R. in Figure A.4, in addition to increasing temperature (VESTA).

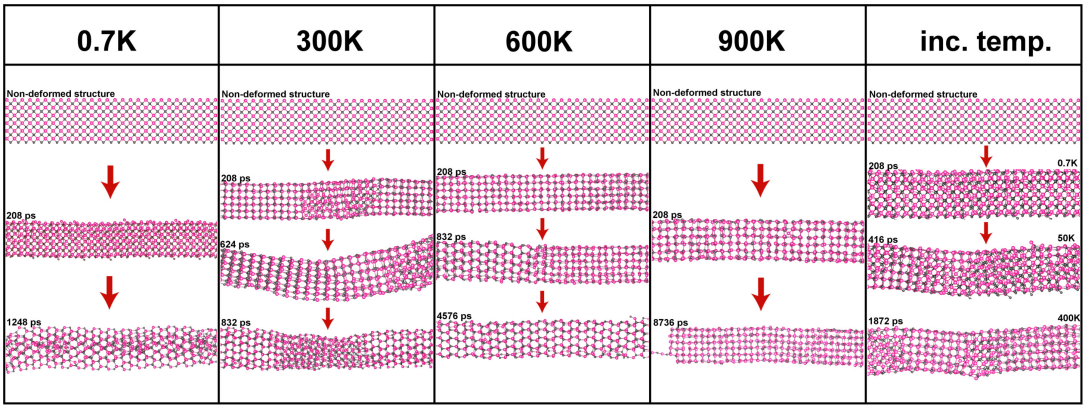


Figure A.6: Phase transitions in the 6x6 ZB NR under strain for the 5% S.R. The WZ phase in the 6x6 ZB NR occurred at 0.7, 300, 600K (VESTA).

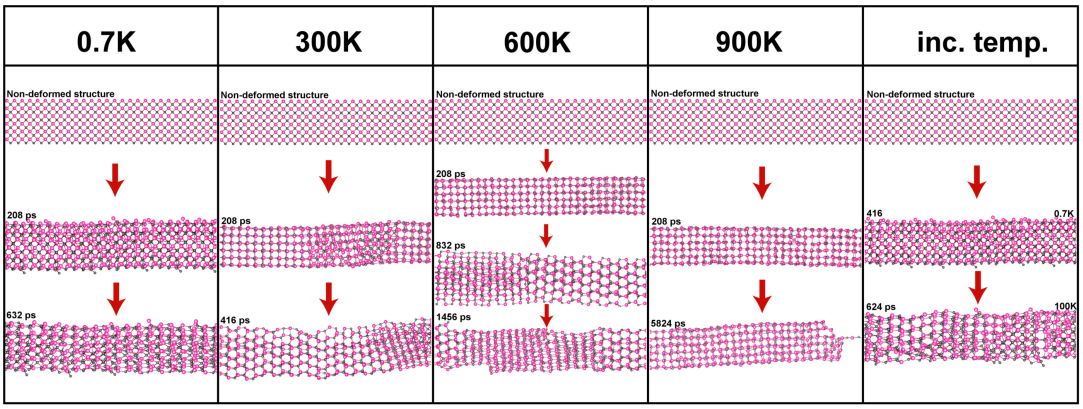


Figure A.7: Phase transitions in the 6x6 ZB NR under strain for the 10% S.R. The WZ phase was observed at the same temperatures (0.7, 300 and 600K) with the stretching for the 5% S.R. in the Figure A.6 but the WZ regions appeared were more dense at 5% than 10% stretching ratio (VESTA).

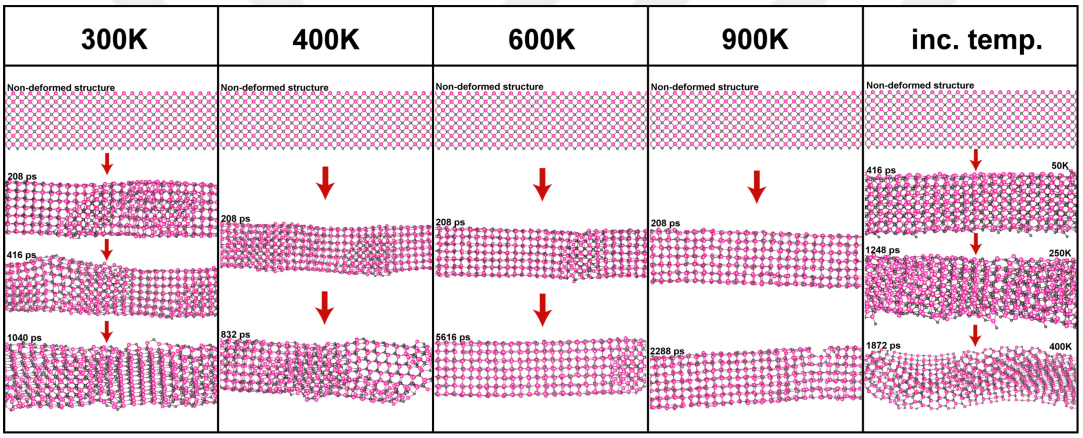


Figure A.8: Phase transitions in the 7x7 ZB NR under strain for the 5% S.R. The WZ regions appeared in the 7x7 ZB NR at 300, 400K and increasing temperature (VESTA).

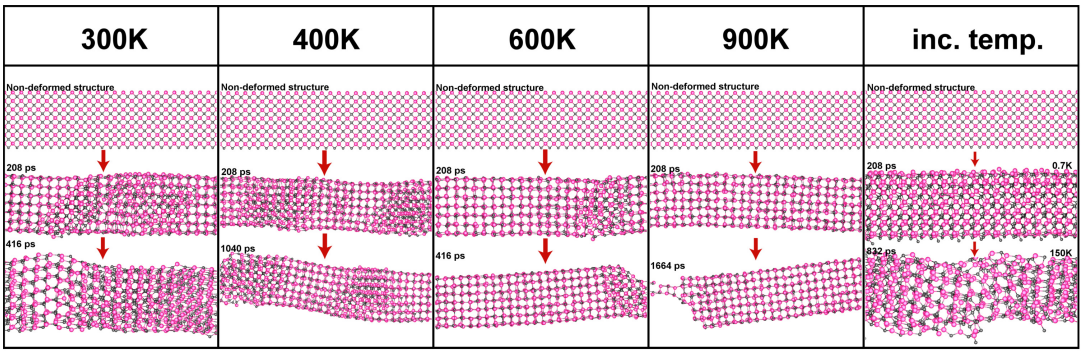


Figure A.9: Phase transitions in the 7x7 ZB NR under strain for the 10% S.R. At this ratio, the WZ phase was not observed at 400K because of higher stretching ratio while appearing at this temperature for the 5% ratio in Figure A.8 (VESTA).

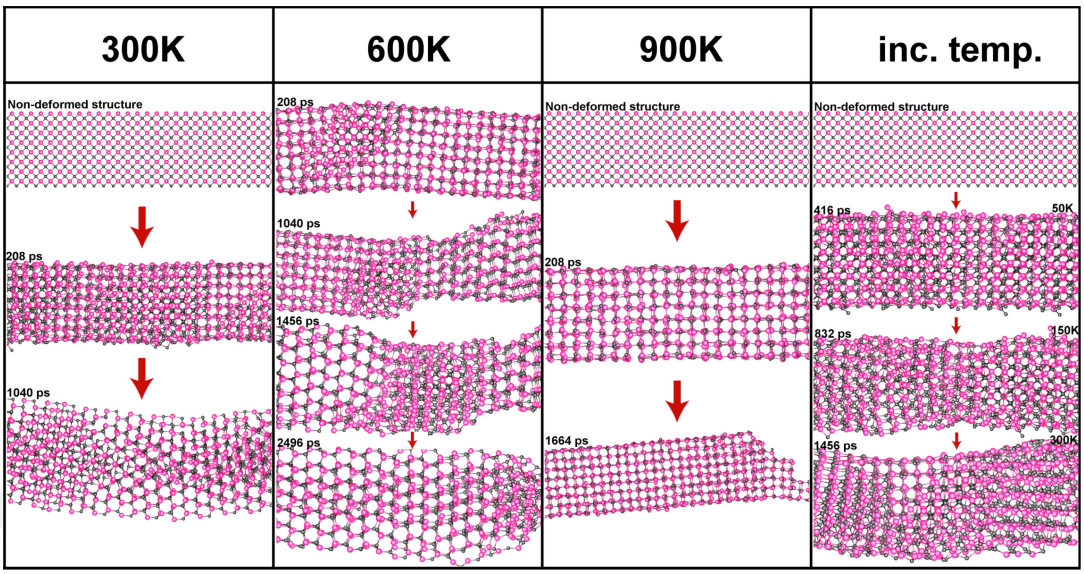


Figure A.10: Phase transitions in the 8x8 ZB NR under strain for the 5% S.R. The WZ phase occurred at 300 and 600K in the 8x8 ZB NR (VESTA).

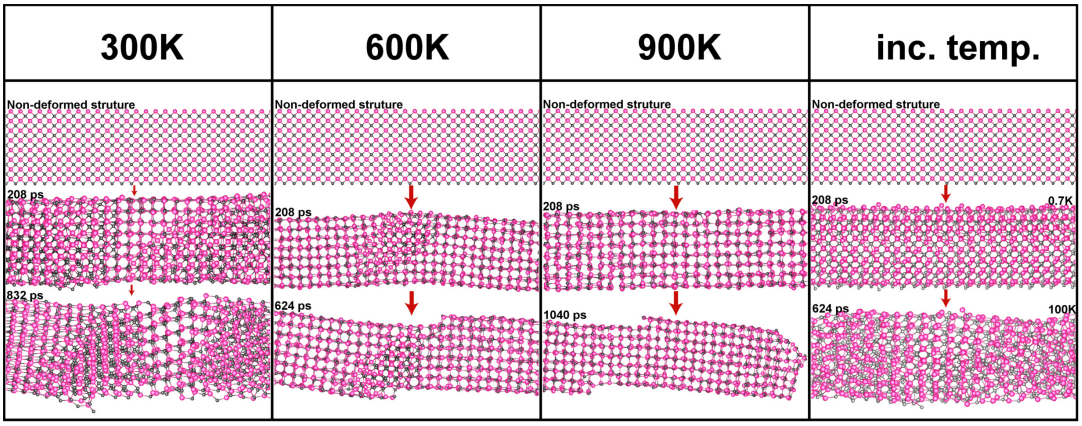


Figure A.11: Phase transitions in the 8x8 ZB NR under strain for the 10% S.R. The WZ region was observed in the 8x8 ZB NR only at 300K while this phase occurred at 300 and 600K for the 5% S.R. in Figure A.10 (VESTA).

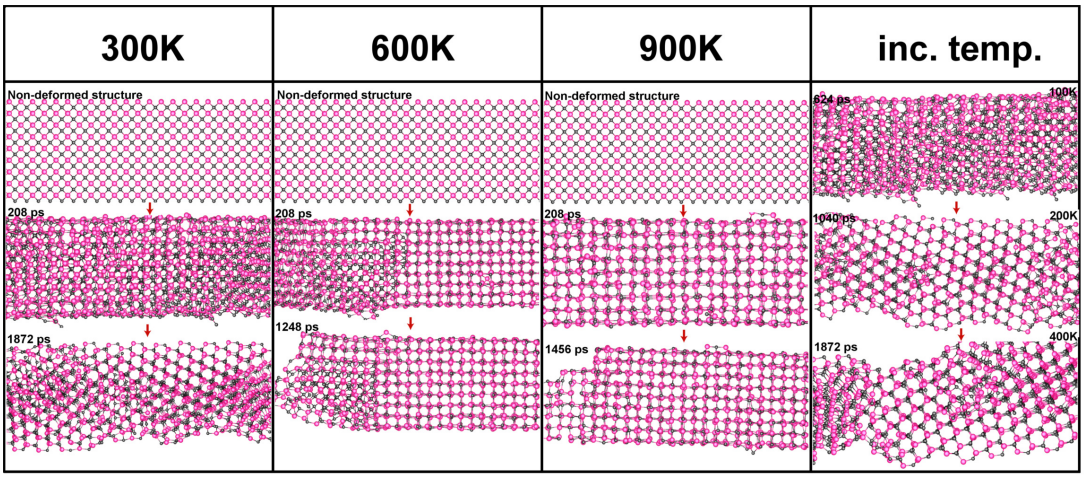


Figure A.12: Phase transitions in the 9x9 ZB NR under strain for the 5% S.R. The WZ phase appeared at 300K (VESTA).

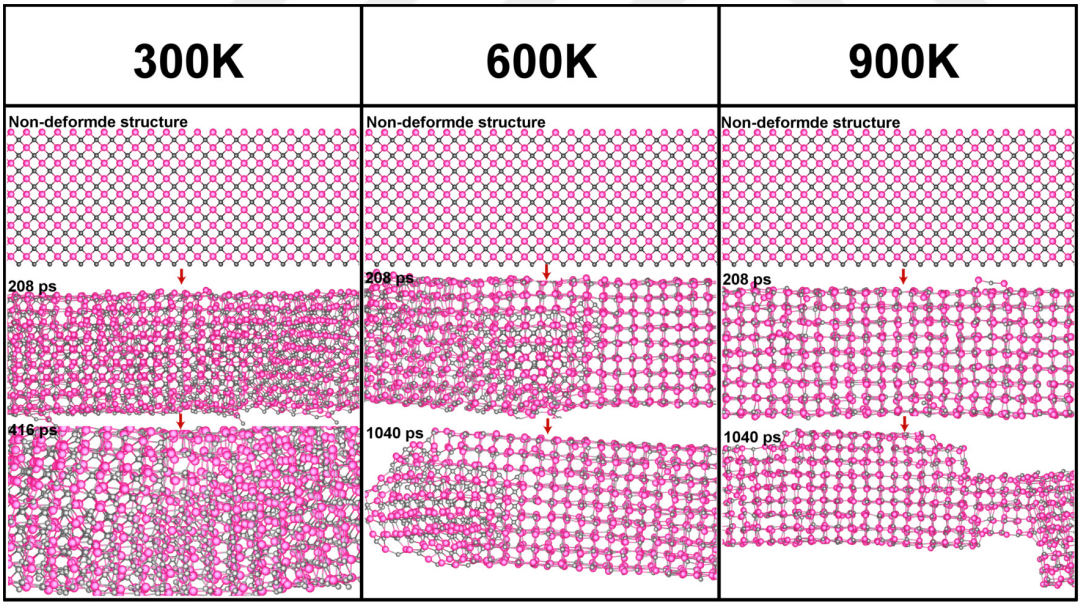


Figure A.13: Phase transitions in the 9x9 ZB NR under strain for the 10% S.R. The WZ phase was not observed in the 9x9 ZB NR for the 10% S.R. because of the thicker NR and higher stretching ratio (VESTA).

the stress was concentrated, without any inclination towards to the breaking points, a single atom chain forming in the thinning region. For those systems in the WZ and ZB phases, an elongation and inclination towards the breaking point were seen. In these figures, the snapshots both before and after the breaking for each nanorod are illustrated together along with their time given in picoseconds.

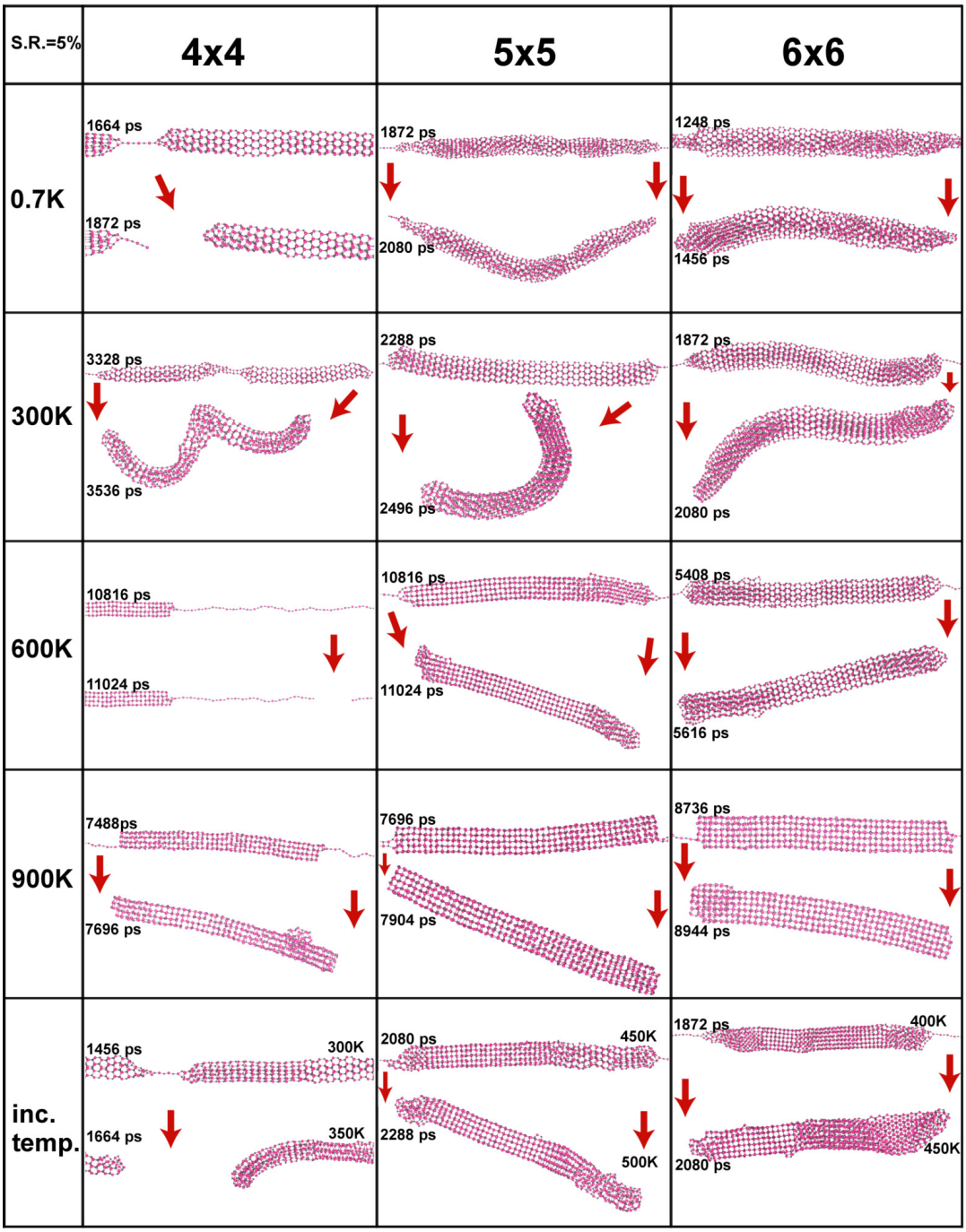


Figure A.14: Breaking mechanism for the 4x4, 5x5 and 6x6 ZB NRs under strain for the 5% S.R. (VESTA).

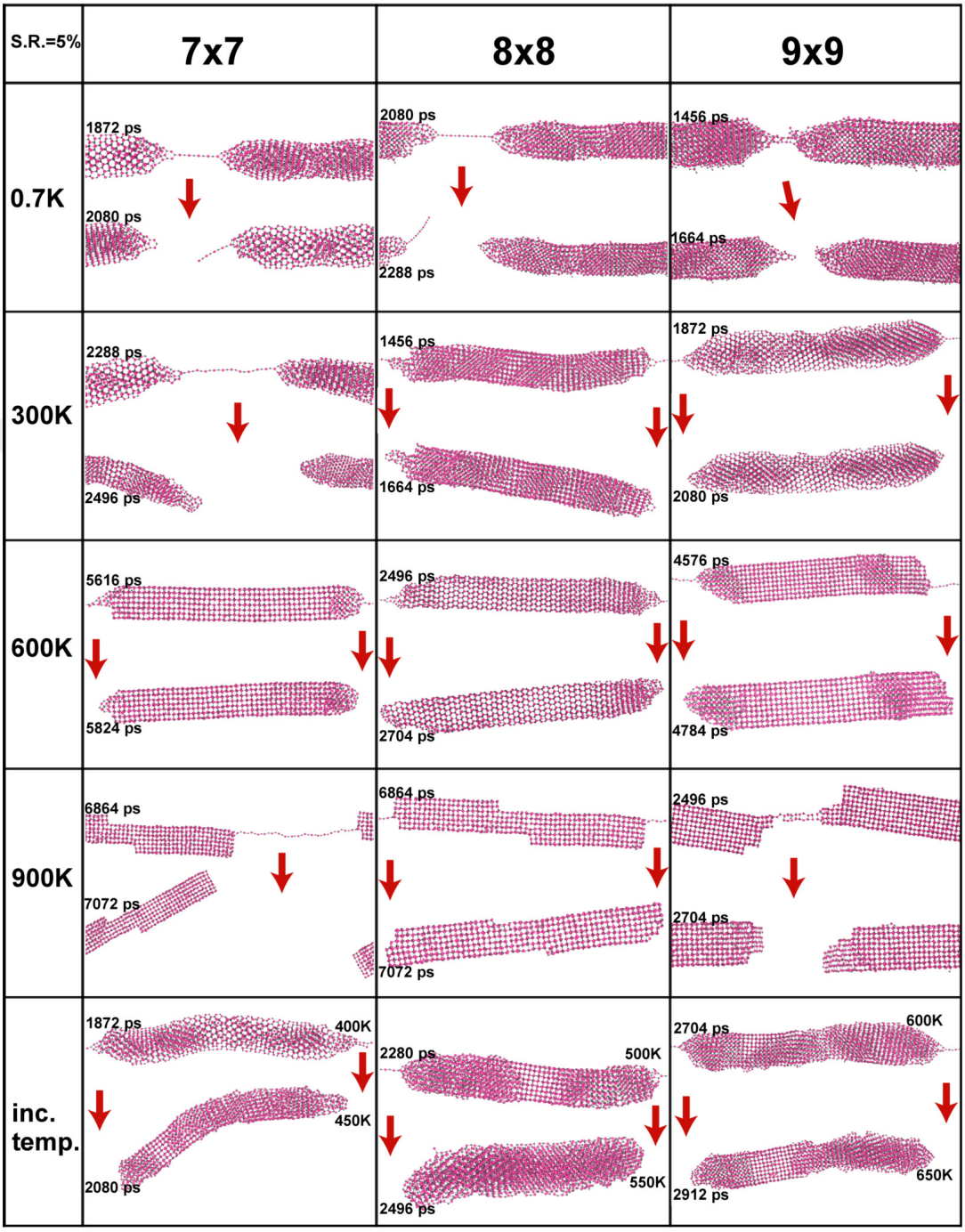


Figure A.15: Breaking mechanism for the 7x7, 8x8 and 9x9 ZB NRs under strain for the 5% S.R. (VESTA).

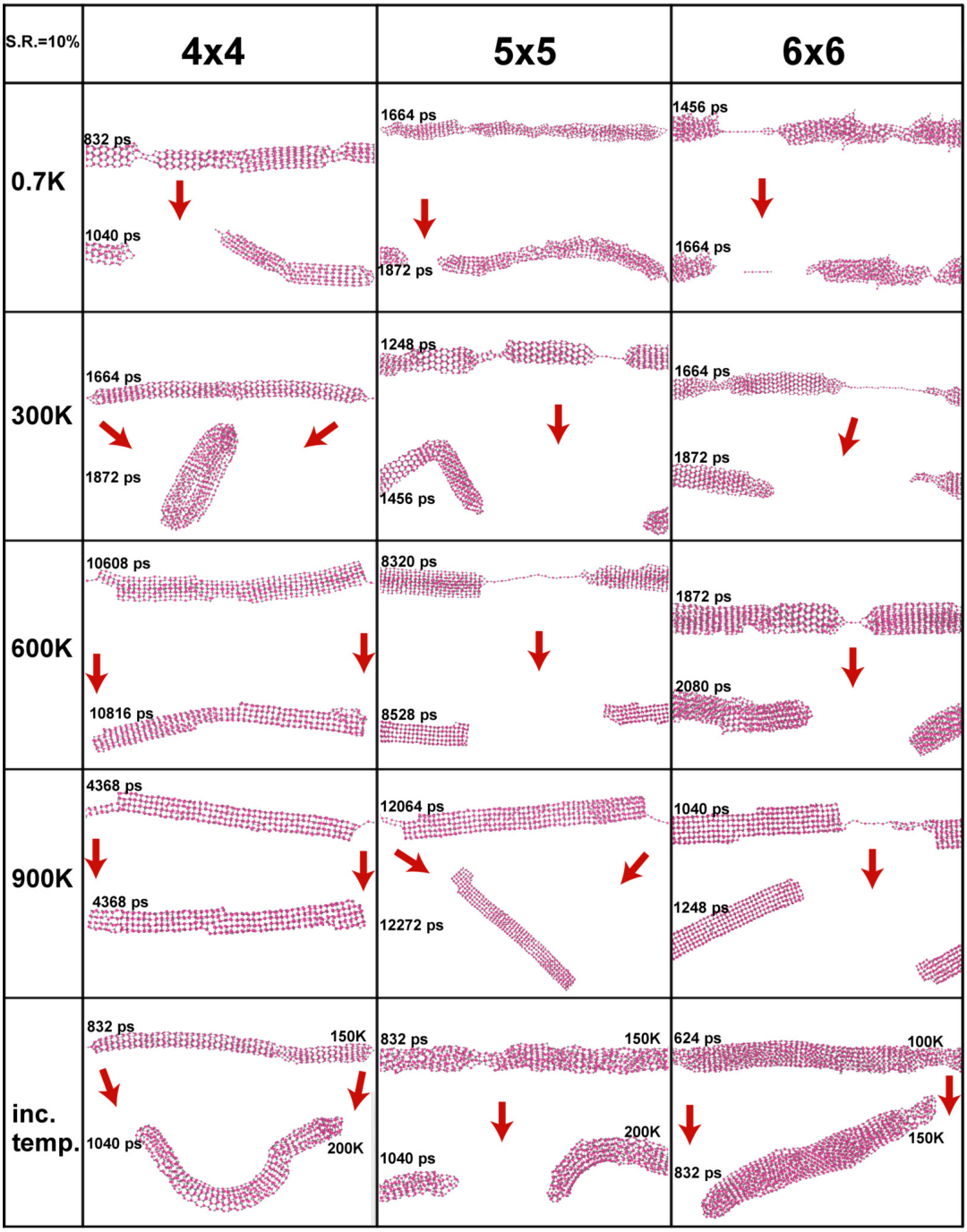


Figure A.16: Breaking mechanism for the 4x4, 5x5 and 6x6 ZB NRs under strain for the 10% S.R. (VESTA).

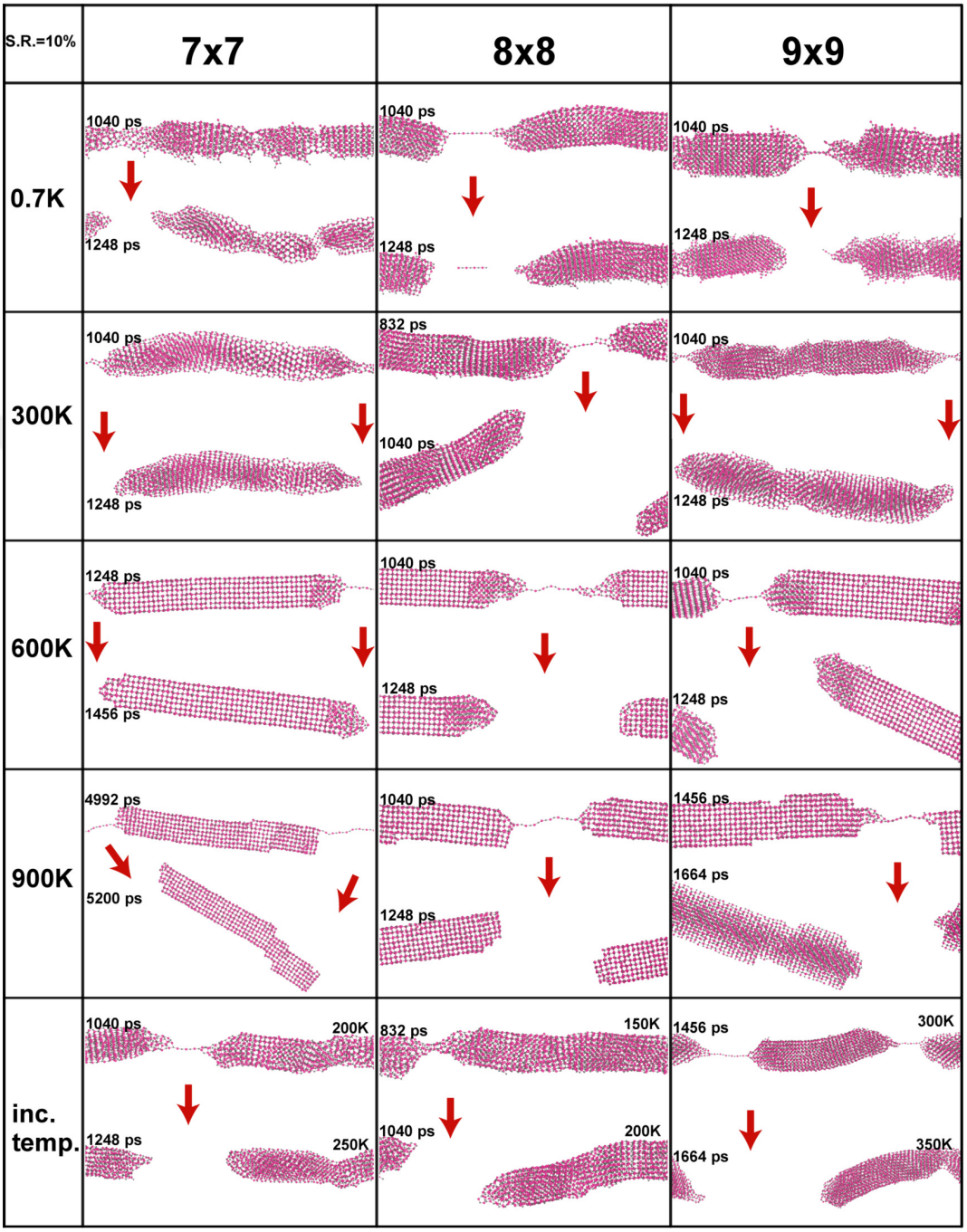


Figure A.17: Breaking mechanism for the 7x7, 8x8 and 9x9 ZB NRs under strain for the 10% S.R. (VESTA).

## A.2 Wurtzite Nanorods

### A.2.1 Gradual Heating and Expansion

#### A.2.1.1 Gradual Heating

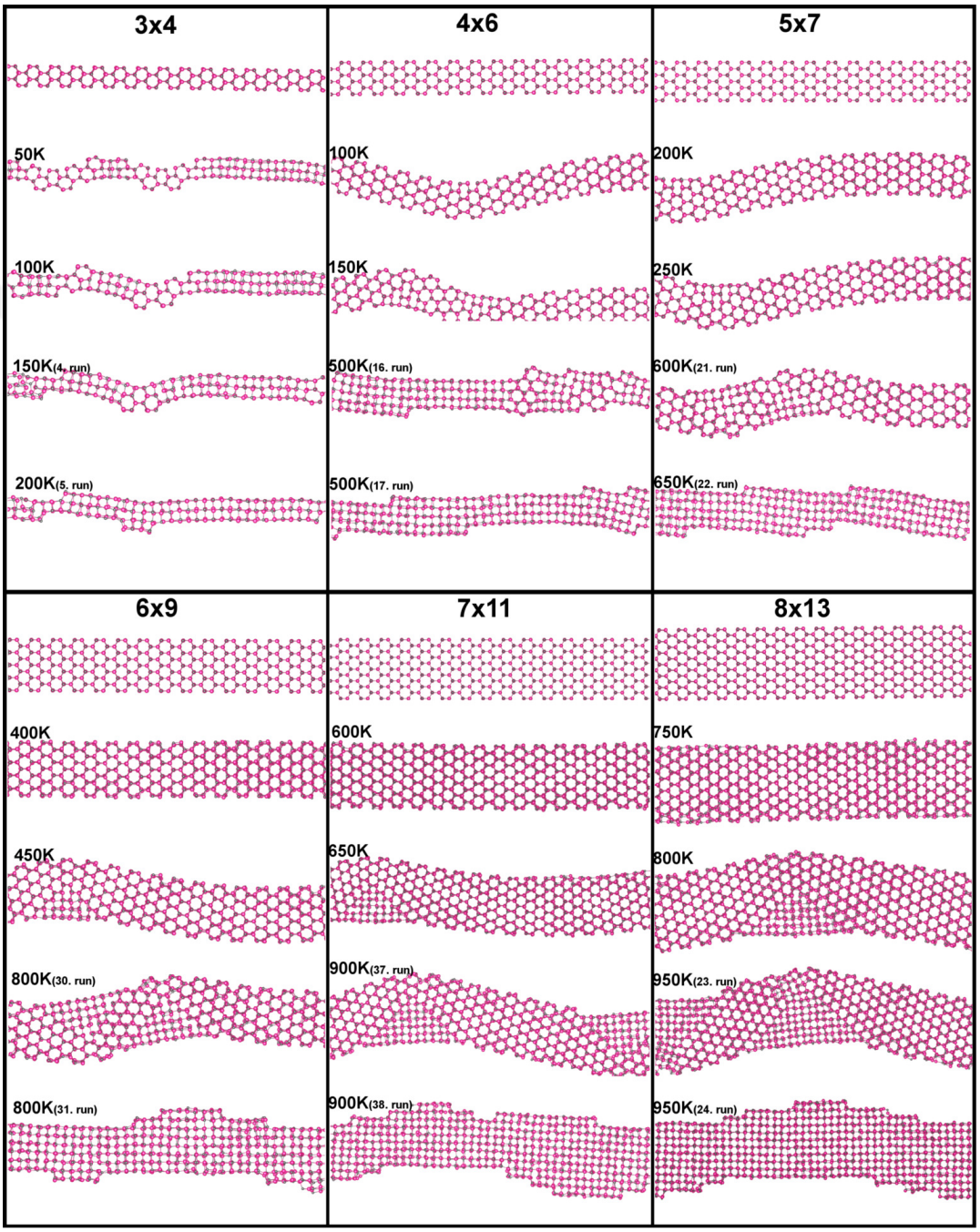


Figure A.18: Gradually heated WZ NRs. When the WZ NRs were subjected to heating via increasing the temperature by 50K, interestingly, stacking faults first occurred at the kinks. Due to these kinks, the completely transformed systems were segmented as a result of the stacking faults (VESTA).137

### A.2.1.2 Expansion

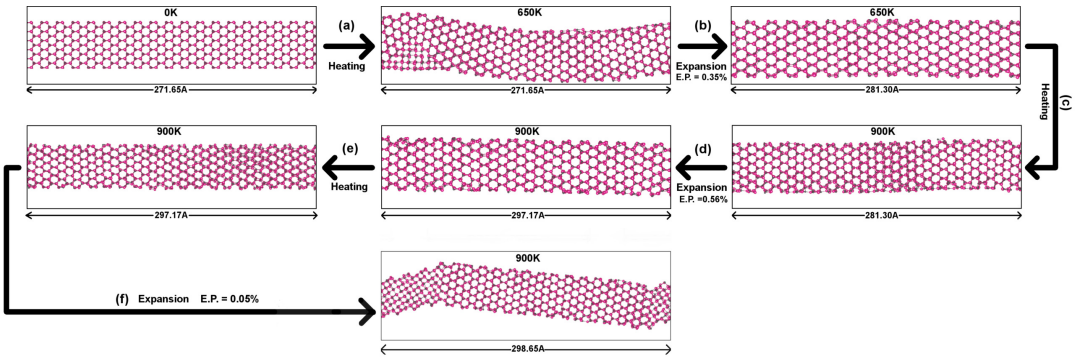


Figure A.19: Expansion and heating procedures were applied to the 7x11 WZ NR in consecutive runs as shown in the figure. Elongation percentages (E.P.) are given for the expanded parts of the NR (VESTA).

## A.2.2 Annealing, Cooling and Stretching

### A.2.2.1 Annealing

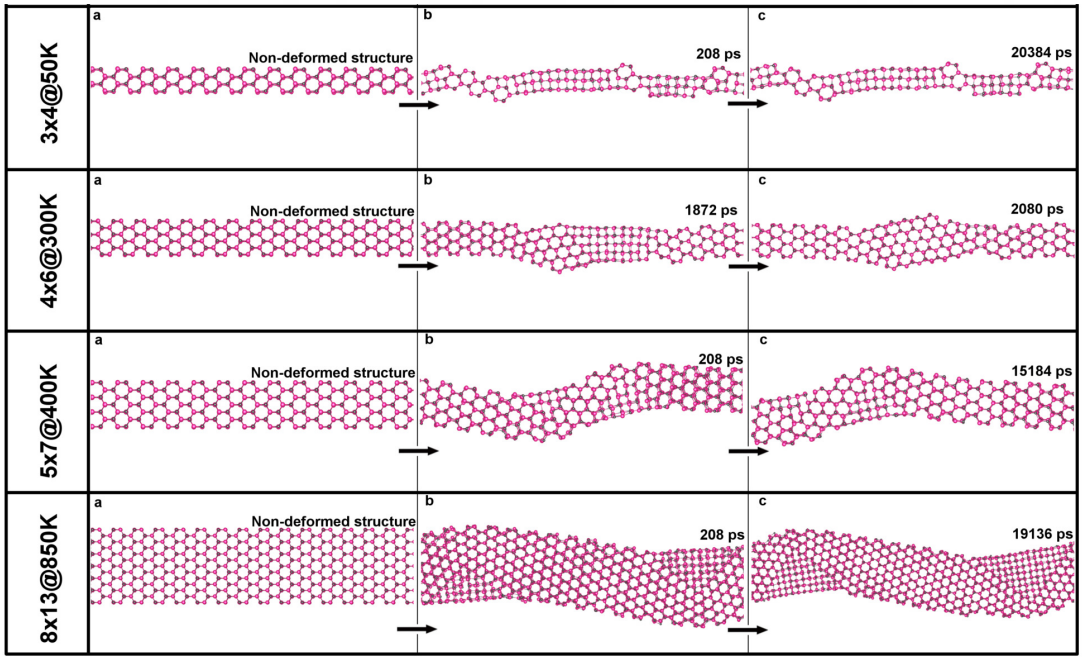


Figure A.20: Heated non-deformed WZ NRs at constant temperatures to investigate the annealing effect. The heating times (ps) are given for each nanorod (VESTA).

### A.2.2.2 Cooling

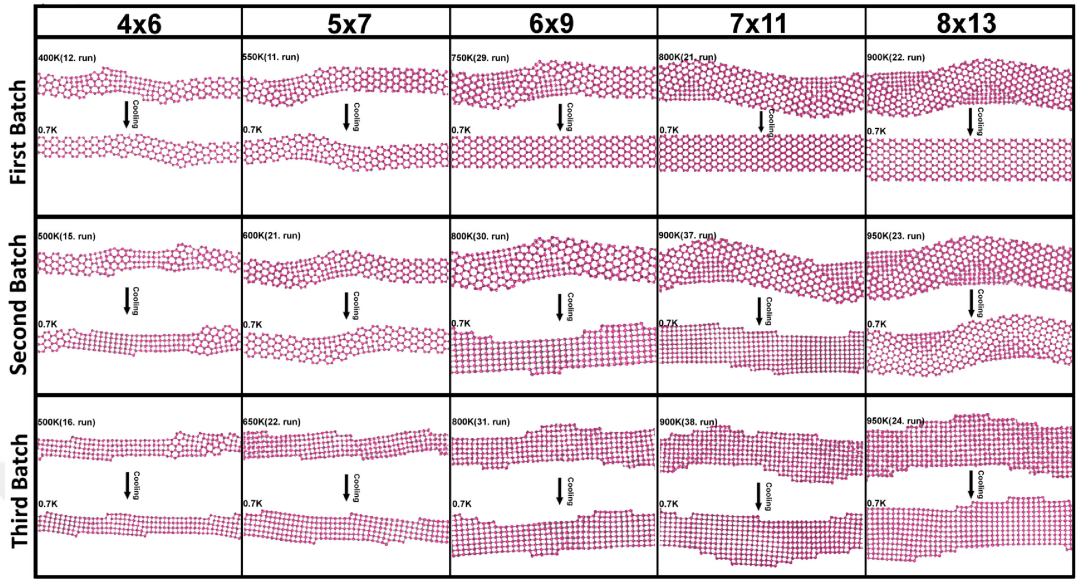


Figure A.21: The cooled WZ NRs to observe if the transition was reversible. It was found that the phase transition temperatures and the ratio of kinks' region to the over all area have effect on the reversibility (VESTA).

### A.2.2.3 Stretching

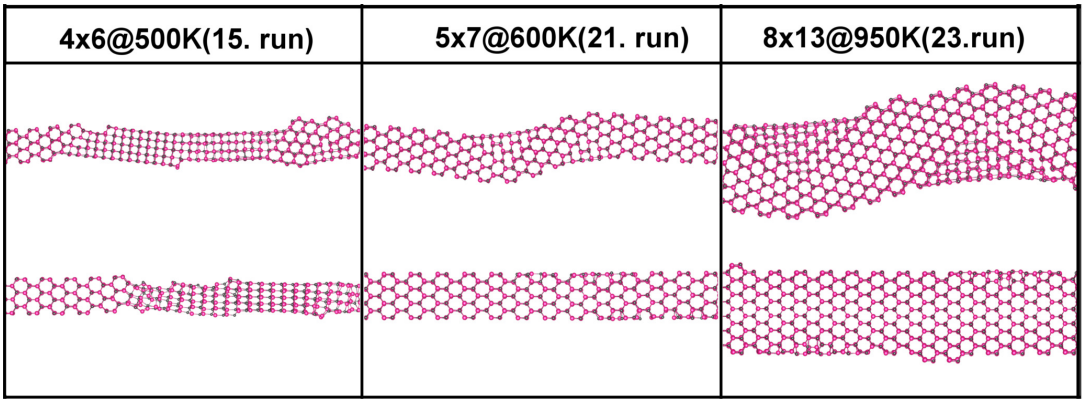


Figure A.22: Cooled WZ NRs were stretched for the 0.5% ratio at 0.7K to see if the cooling process was reversible. The calculations on the thin, average and thick NR specimens showed that the cooled NRs below their phase transition temperatures can completely transform back to the WZ phase under strain (VESTA).

### A.2.3 Stretching (1% and 5% ; 0.5%@600K: 4x6, 6x9, 8x13; 0.5%@900K: 6x9, 8x13)

#### A.2.3.1 Breaking Mechanisms with respect to different phases under streching

In the RS structured NR when the NR was elongated, the thinning occurred where the stress was concentrated, without any inclination towards to the breaking points, a single atom chain forming in the thinning region. For those systems in the WZ phase, an elongation and inclination towards the breaking point were seen. In these figures, the snapshots both before and after the breaking of each nanorod are illustrated together along with their times (ps).

#### A.2.3.2 Phase transition under stretching

When the WZ NRs are subjected to stretching, the NRs undergo irreversible phase transition WZ->RS at increasing temperatures with the nonequilibriated approach. However, both reversible and irreversible phase transitions are observed when the equlibrium criteria is applied with the temperature being kept constant under strain for the 5%, 1% and 0.5% stretching ratios. These phases along with their occurrence times (ps) are shown in the figures below.

### A.2.4 Compression and Stretching

Compression is “stretching with a negative ratio”. So, for all compression runs, the compression parameter is defined as -0.5% S.R. When compression is applied, the NR’s dimension in uniaxial direction is decreased.

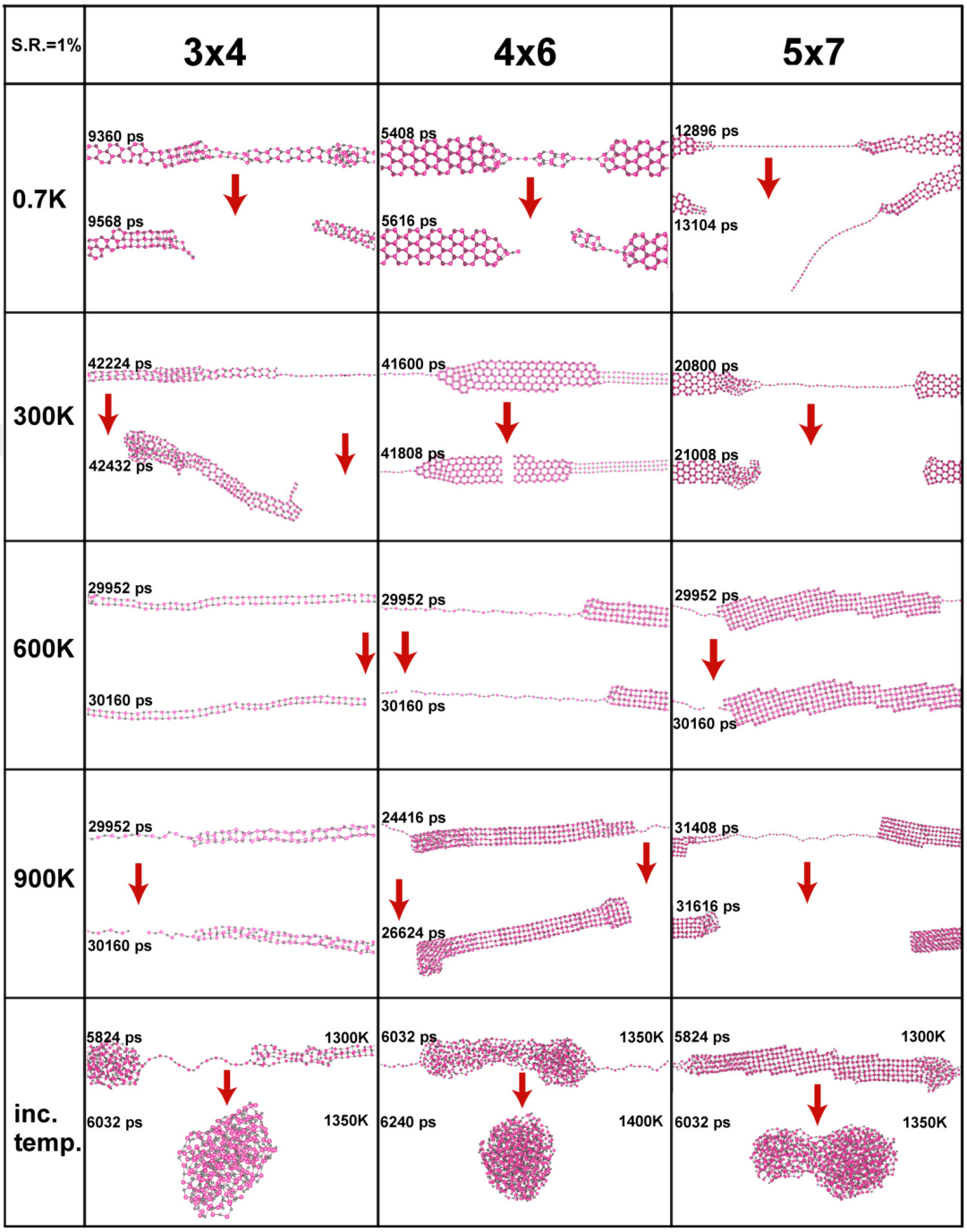


Figure A.23: Breaking mechanism in the stretched 3x4, 4x6 and 5x7 WZ NRs at constant and increasing temperatures (inc.temp.) for the 1% S.R. (VESTA).

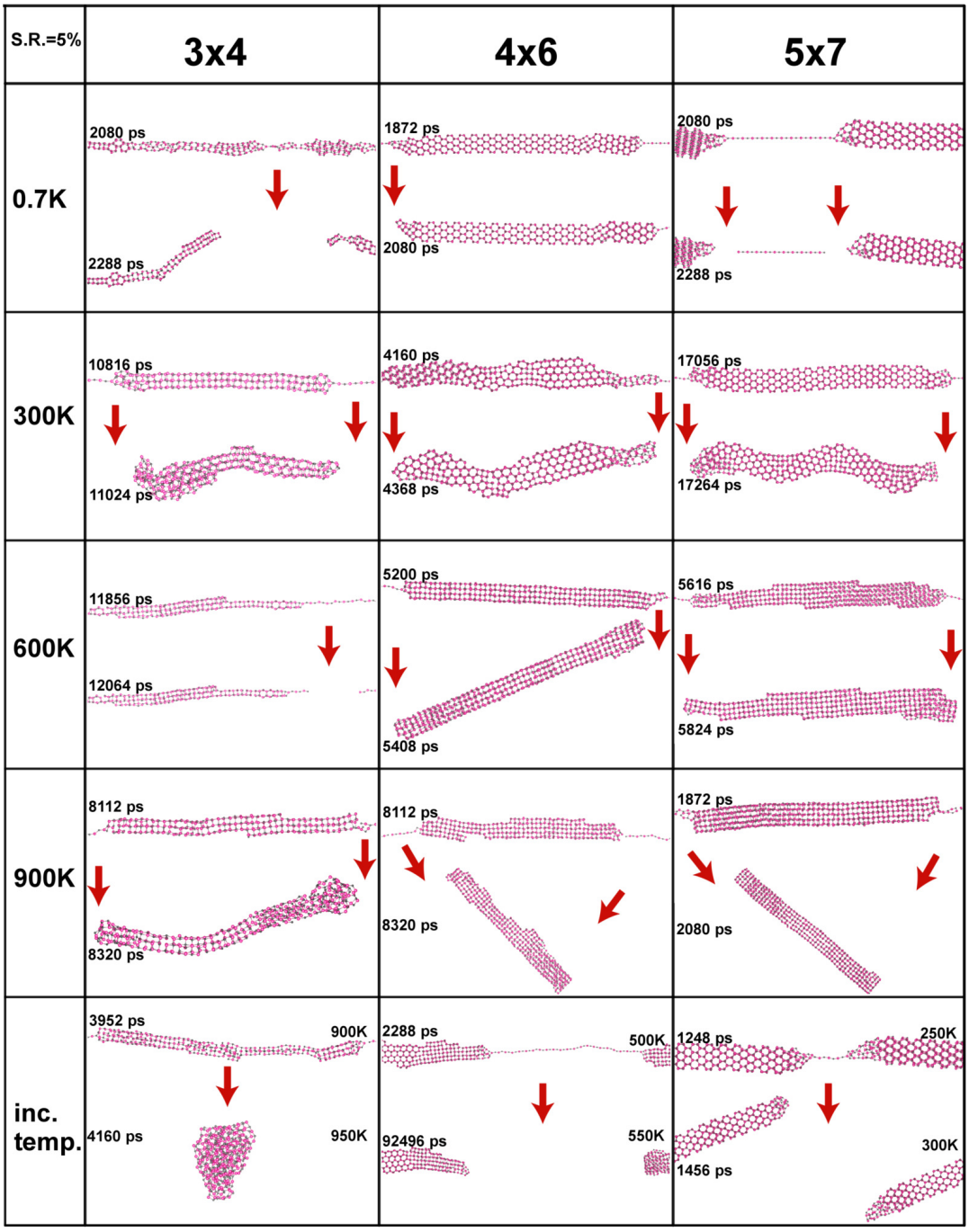


Figure A.24: The 3x4, 4x6 and 5x7 WZ NRs were put under strain for the 5% S.R. at constant and increasing temperatures (inc.temp.) to investigate the breaking mechanism of the NRs (VESTA).

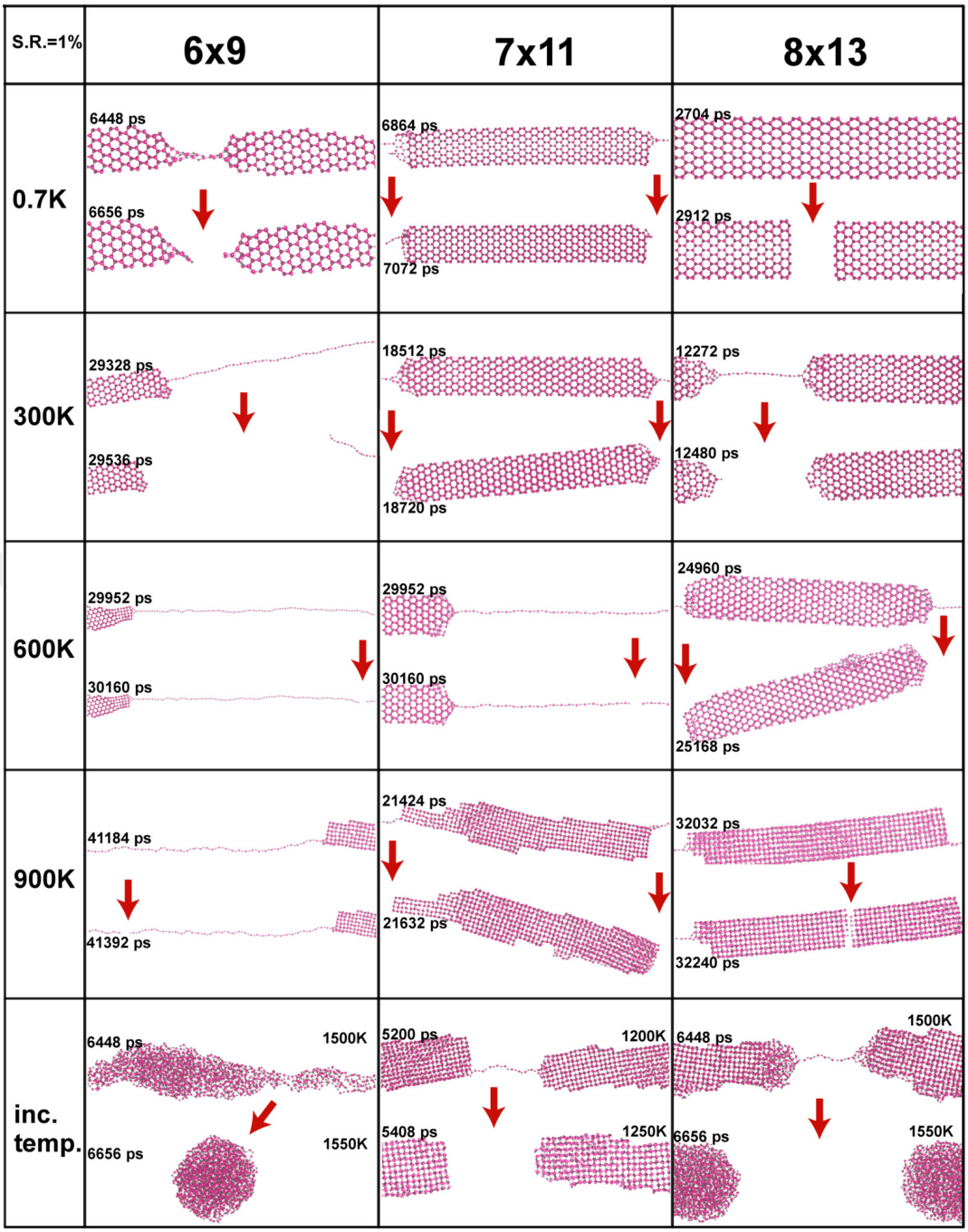


Figure A.25: The 6x9, 7x11 and 8x13 WZ NRs were put under strain for the 1% S.R. at constant and increasing temperatures (inc.temp.) to analyze the breaking mechanism of the NRs (VESTA).

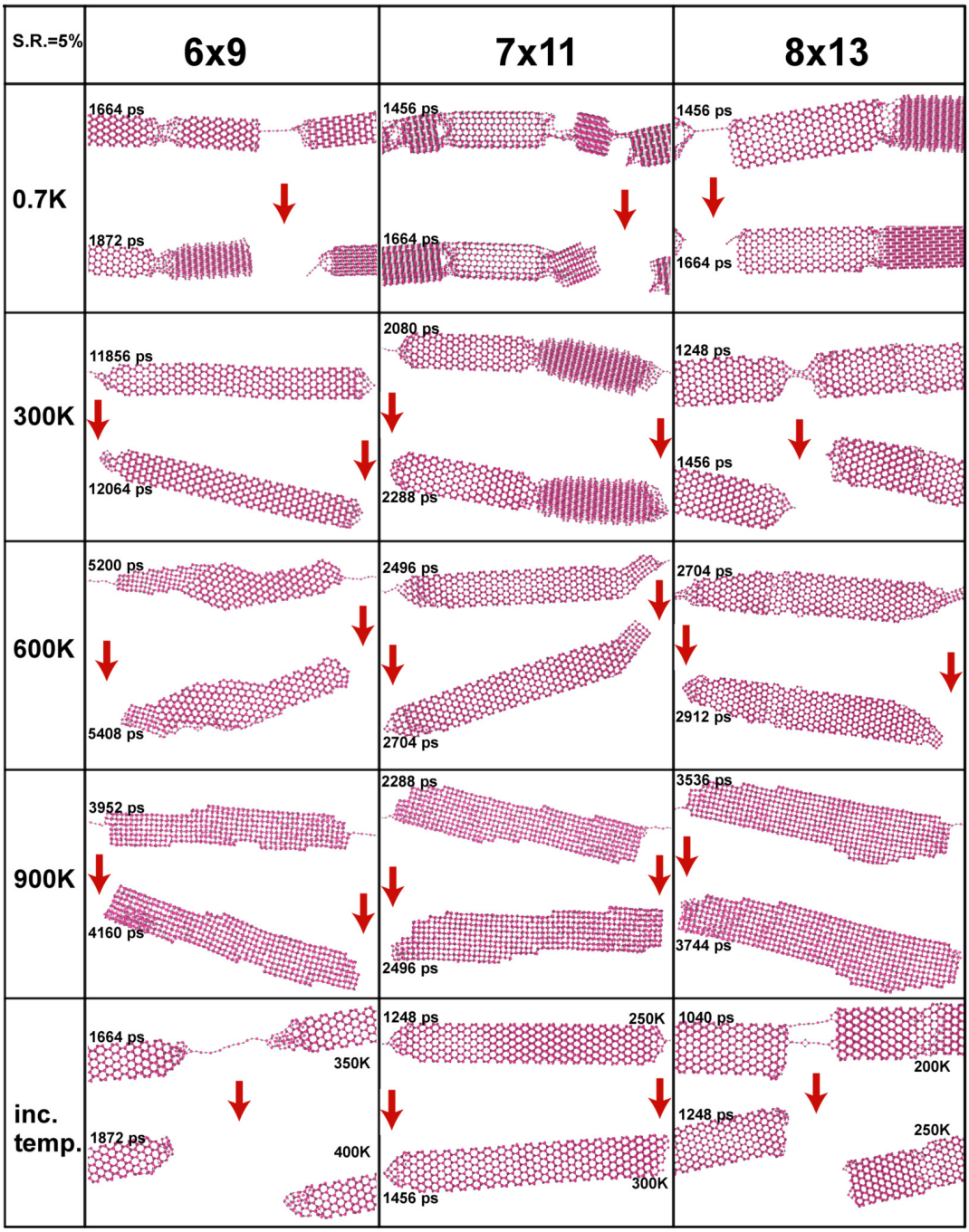


Figure A.26: Breaking mechanisms of the put 6x9, 7x11 and 8x13 WZ NRs under strain for the 5% S.R. at constant and increasing temperatures (inc.temp.) (VESTA).

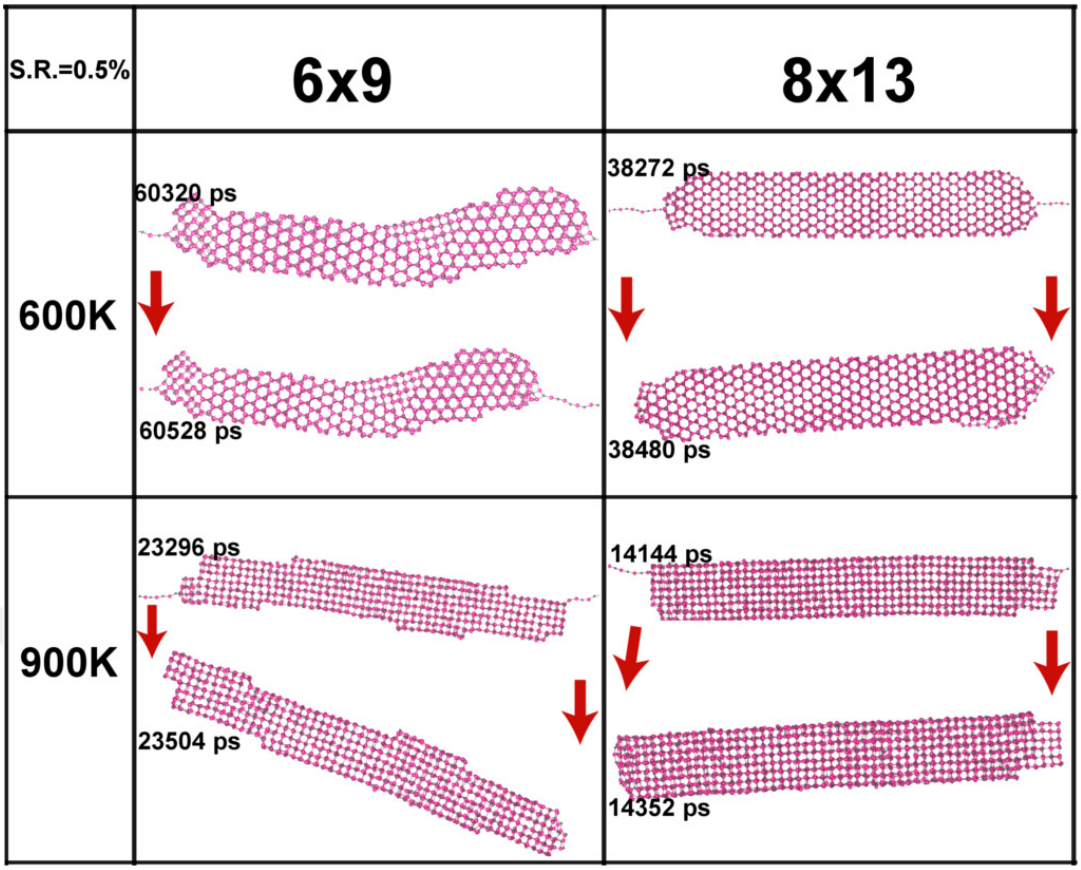


Figure A.27: The 6x9 and 8x13 WZ NRs were put under strain for the 0.5% S.R. at constant temperatures of 600 and 900K (VESTA).

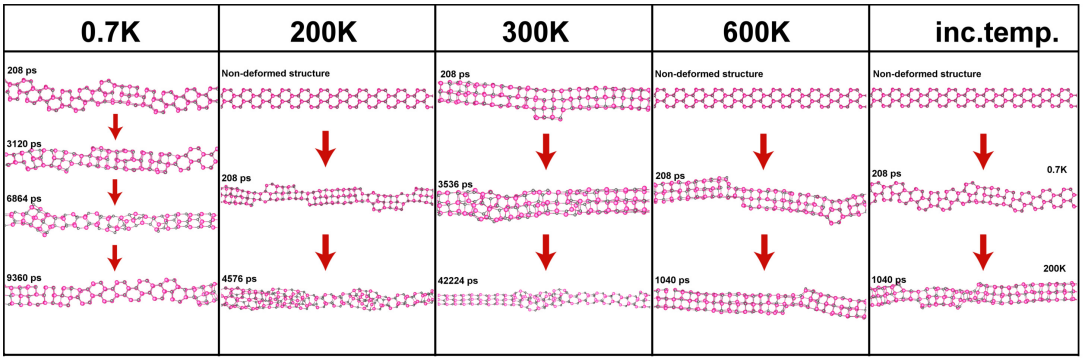


Figure A.28: Observed transitions in the stretched 3x4 WZ NR for the 1% S.R. The WZ phase again appeared at 200 and 300K while the phase transition temperature is 200K for the 3x4 NR. Also, reversible transition occurred at 0.7, 200 and 300K (VESTA).

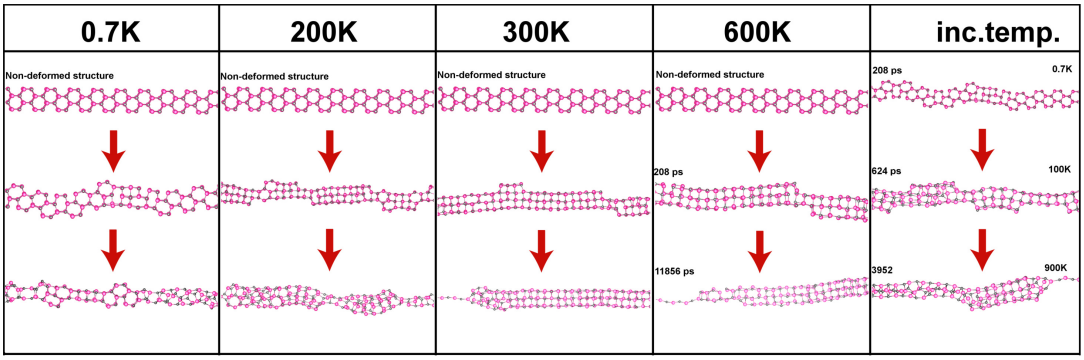


Figure A.29: Observed transitions in the stretched 3x4 WZ NR for the 5% stretching ratio. Due to increasing of the S.R. (from 1% to 5%), the WZ phase occurred at lower temperatures (0.7 and 200K) than 1% stretching ratio (0.7, 200 and 300K) in Figure A.29 (VESTA).

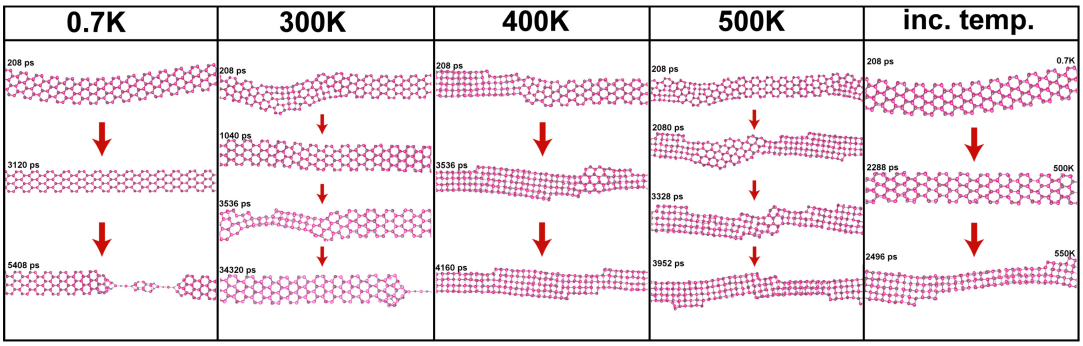


Figure A.30: Observed transitions in the stretched 4x6 WZ NR for the 1% S.R. While the phase transition temperature is 475K for the 4x6 NR, total transition to the RS phase occurred at 400K (lowering effect). Also the reversible transition occurred at 300K (VESTA).

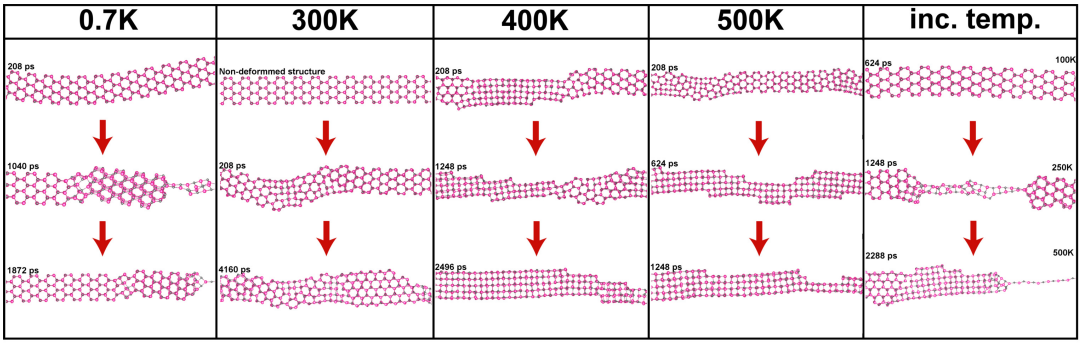


Figure A.31: Observed transitions in the stretched 4x6 WZ NR for the 5% S.R. The WZ phase at lower temperatures (0.7, 300 and 400K) than 5% S.R. (0.7, 300, 400 and 500K as it is shown in Figure A.30) appeared. So it was observed that the occurrence of the WZ phase depends on the stretching ratio (VESTA).

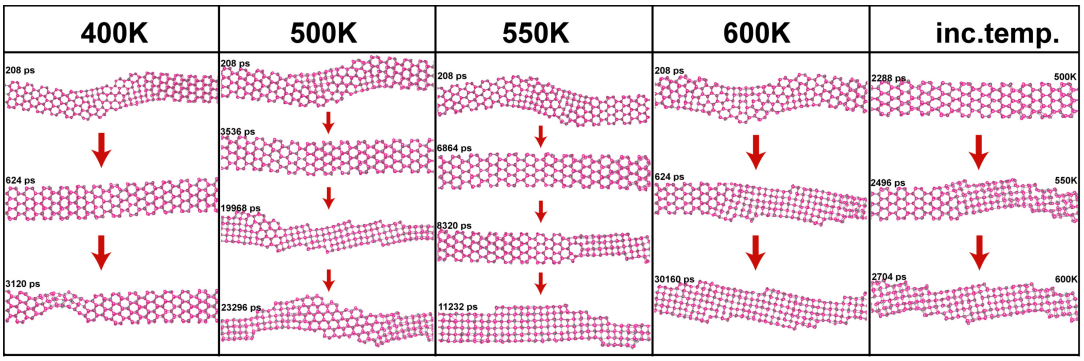


Figure A.32: Observed transitions in the stretched 5x7 WZ NR for the 1% S.R. Complete transition was observed at 550K which is below the phase transition temperature (590K). Also the reversible transition occurred at 400, 500 and 550K (VESTA).

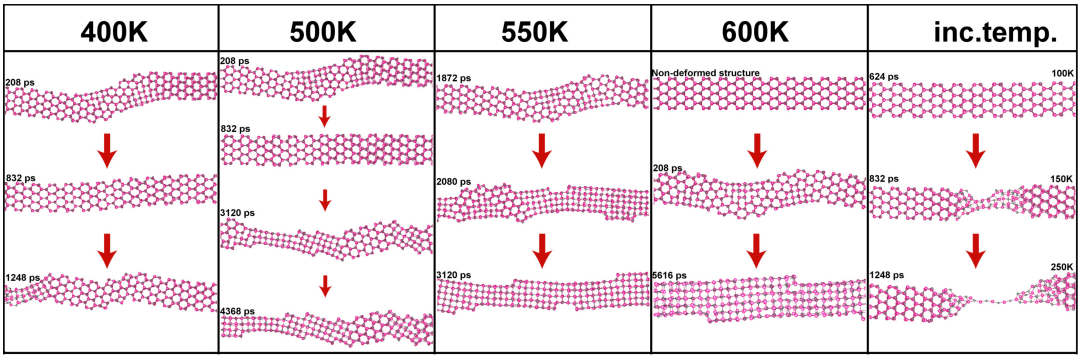


Figure A.33: Observed transitions in the stretched 5x7 WZ NR for the 5% S.R. Comparing the results of the 1% (Figure A.32) and 5% ratios, it was observed that the ratio of the WZ region to the over all area for the 5% ratio is lower while the WZ phase appears at the same temperatures for both ratios. Also, the reversible transition occurred at 400 and 500K (VESTA).

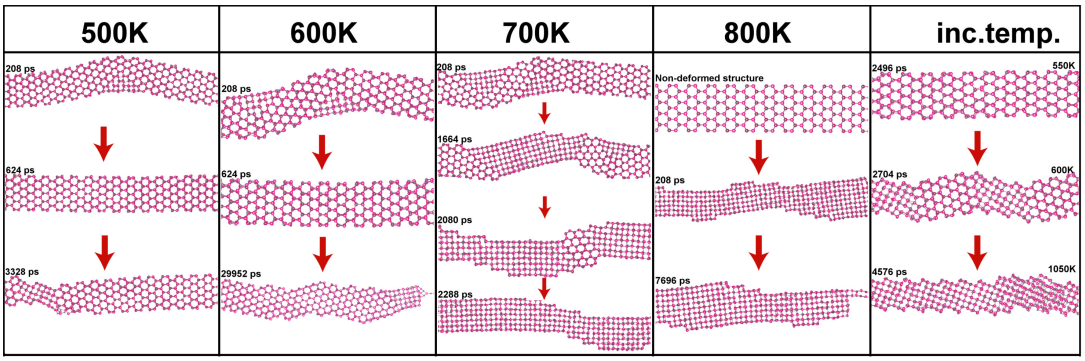


Figure A.34: Observed transitions in the stretched 6x9 WZ NR for the 1% S.R. The complete transition occurred below the phase transition temperature (780K) and reversible transition was observed at 500K (VESTA).

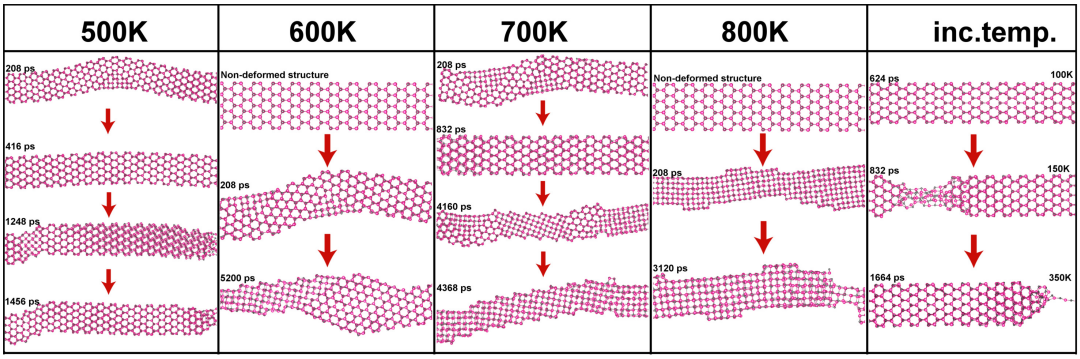


Figure A.35: Observed transitions in the stretched 6x9 WZ NR for the 5% S.R. Reversible phase transition occurred at 500K and the phase transition temperature was reduced from 780K to 700K under strain (VESTA).

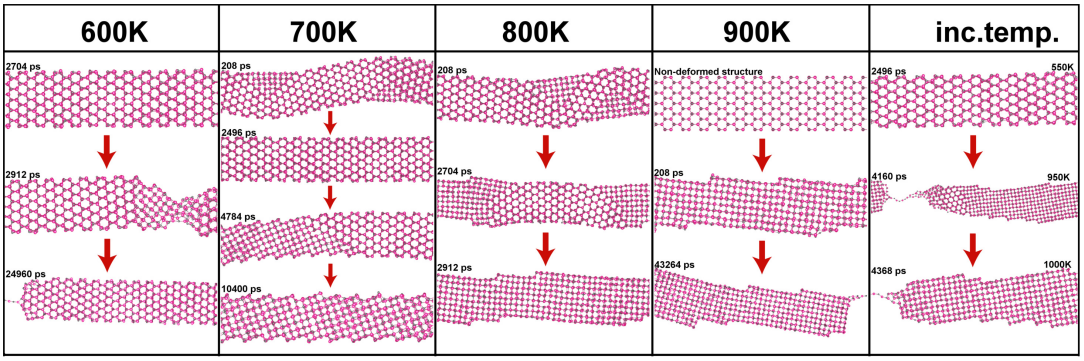


Figure A.36: Observed transitions in the stretched 7x11 WZ NR for the 1% S.R. The RS region was observed where the breaking occured at 600K which is below the first observed transition temperature (650K) and reversible phase transition appeared at 700K. Also, the phase transition temperature reduced to 700K under strain while it was normally 830K (VESTA).

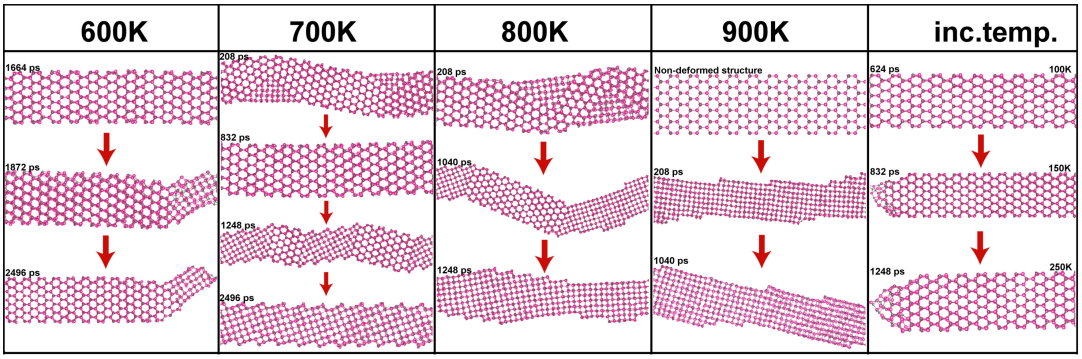


Figure A.37: Observed transitions in the stretched 7x11 WZ NR for 5% S.R. The reversible phase transition was observed at 700K and the RS phase in the breaking region appeared at 600K which is below the 1st observed phase transition temperature. Also, the reducing effect on the phase transition temperature was observed for the 5% ratio (VESTA).

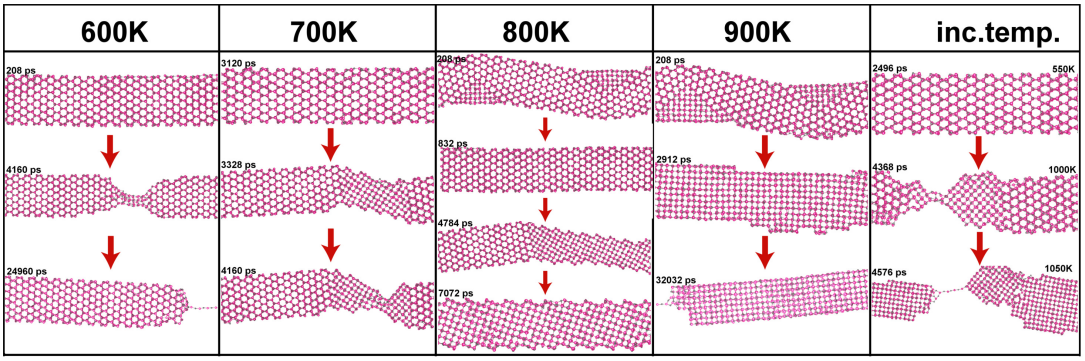


Figure A.38: Observed transitions in the stretched 8x13 WZ NR for the 1% S.R. The RS phase appeared at heavily deformed regions where breaking occurred at 600 and 700K which are below the 1st observed transition temperature and the reversible transition occurred at 800K. Also, the total transition to the RS phase was observed at 800K which is below the phase transition temperature of 895K (VESTA).

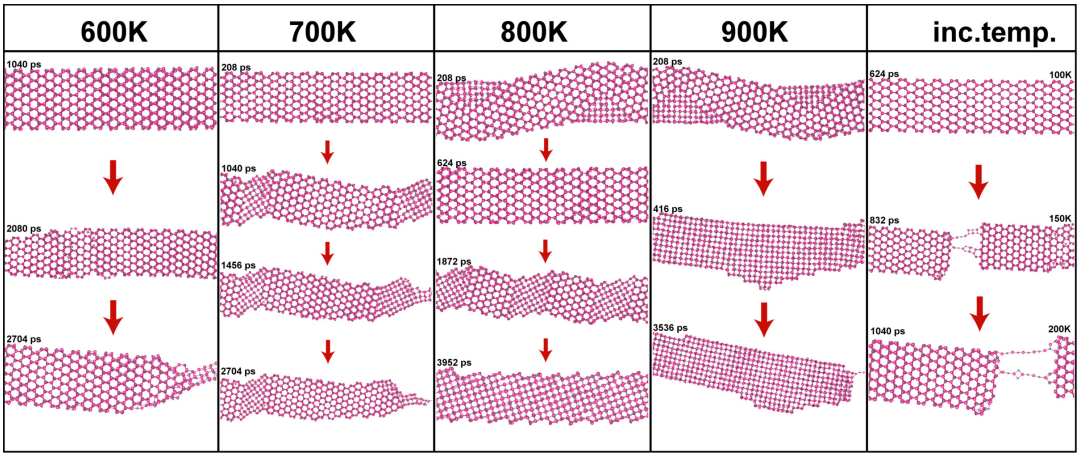


Figure A.39: Observed transitions in the stretched 8x13 WZ NR for the 5% S.R. The RS phase appeared at heavily deformed regions where breaking occurred at 600 and 700K which are below the 1st observed transition temperature and the reversible transition occurred at 800K. Also, the total transition to the RS phase was observed at 800K which is below the phase transition temperature of 895K (VESTA).

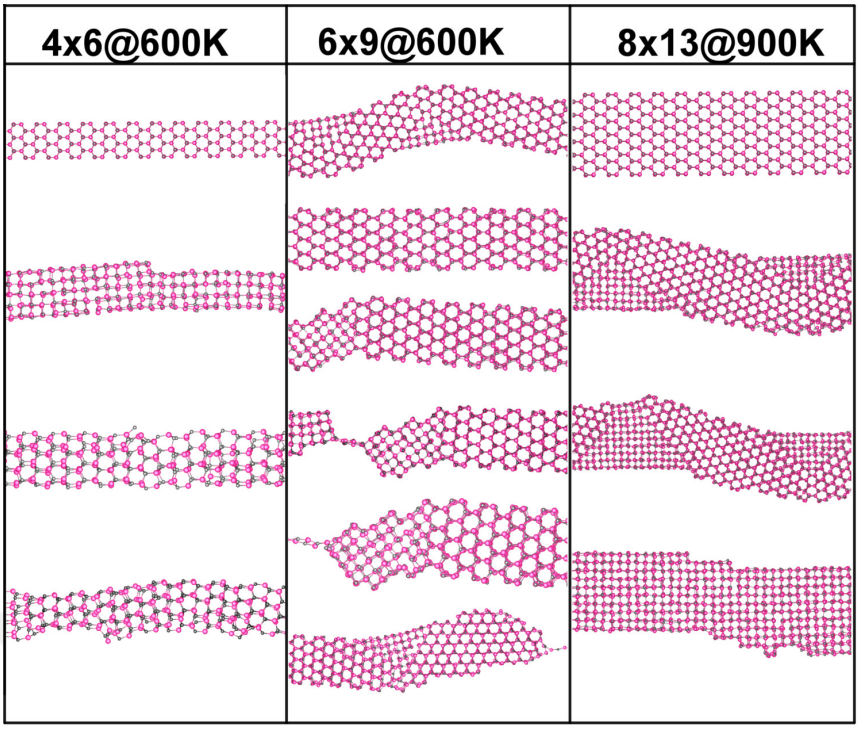


Figure A.40: Observed transitions in the stretched 4x6, 6x9 and 8x13 NRs for the 0.5% S.R. In the 4x6 NR, while the phase transition temperature was 475K, the reversible transition (WZ->RS->WZ) was observed at 600K and the NR in the WZ phase did not evolve back to the RS phase under further stretching. But this effect was not observed for the 8x13 NR at 900K (VESTA).

### A.2.4.1 Stretching after heating

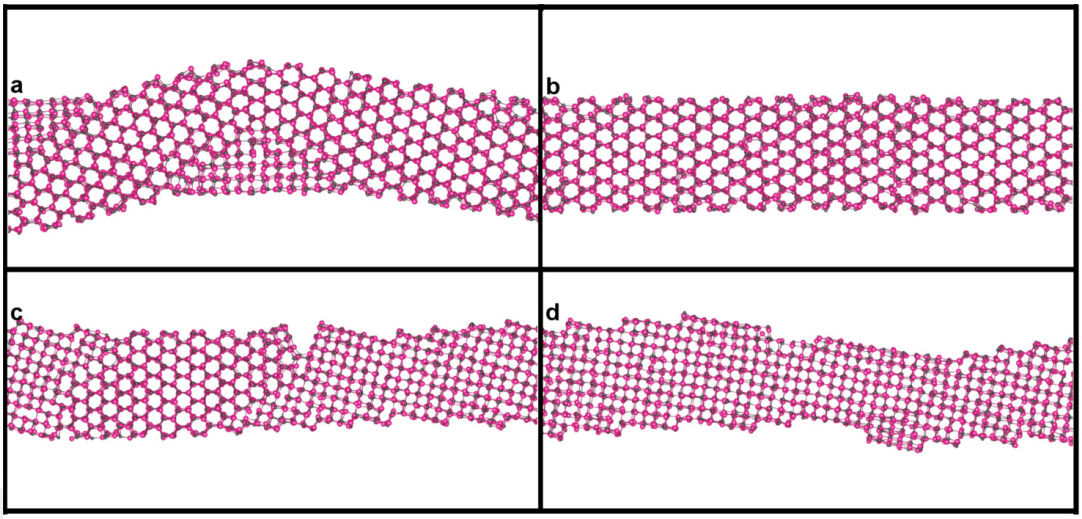


Figure A.41: Gradually heated 8x13 NR until 900K (22. run) was stretched at 900K for the 1% S.R. to investigate if the transition is reversible (VESTA)..

### A.2.4.2 Stretching and Cooling after heating

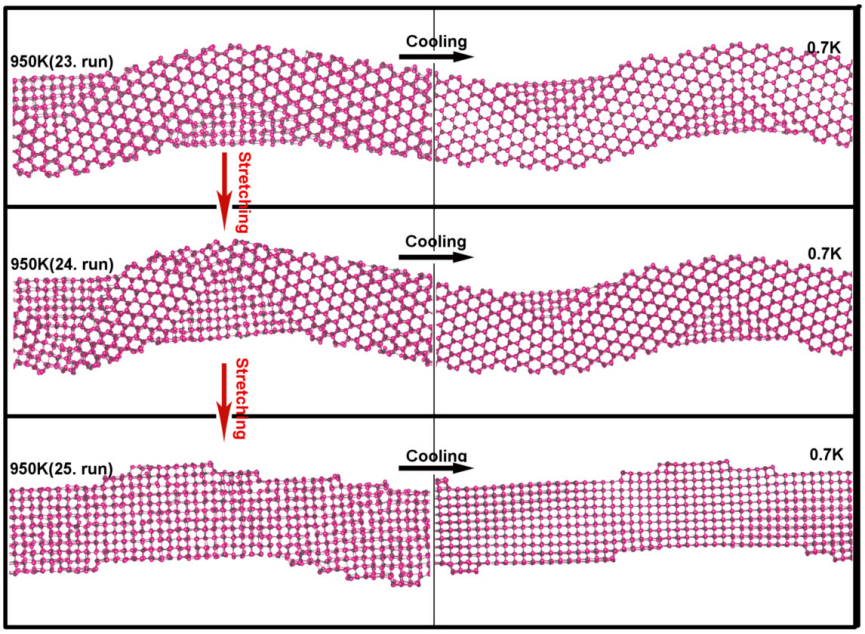


Figure A.42: Gradually heated NR until 950K (23. run) that was first stretched for the 1% S.R. and then 8x13 NRs in 23., newly achieved 24. and 25. runs at 950K were cooled (VESTA).

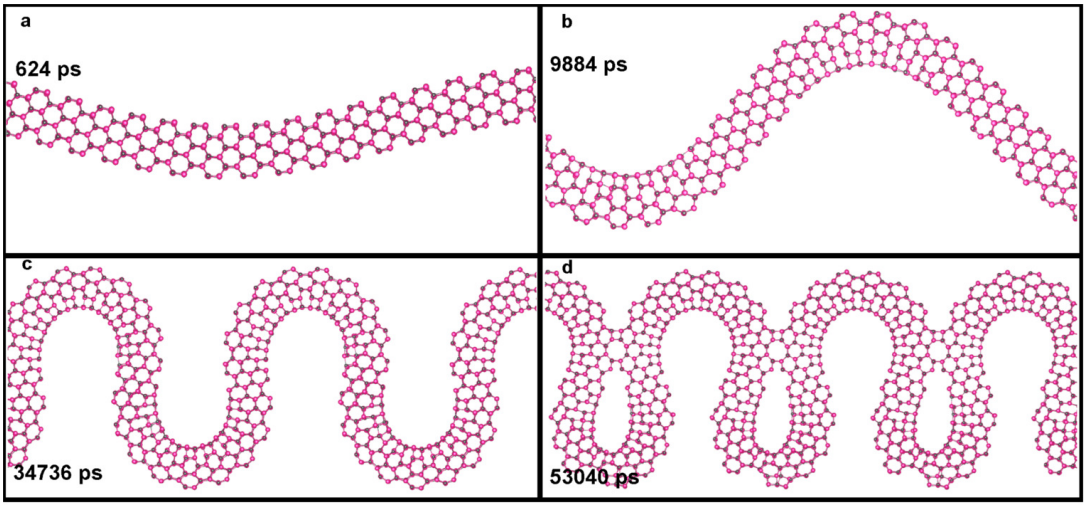


Figure A.43: Compressed 4x6 NR for the -0.5% S.R. at 0.7K (VESTA).

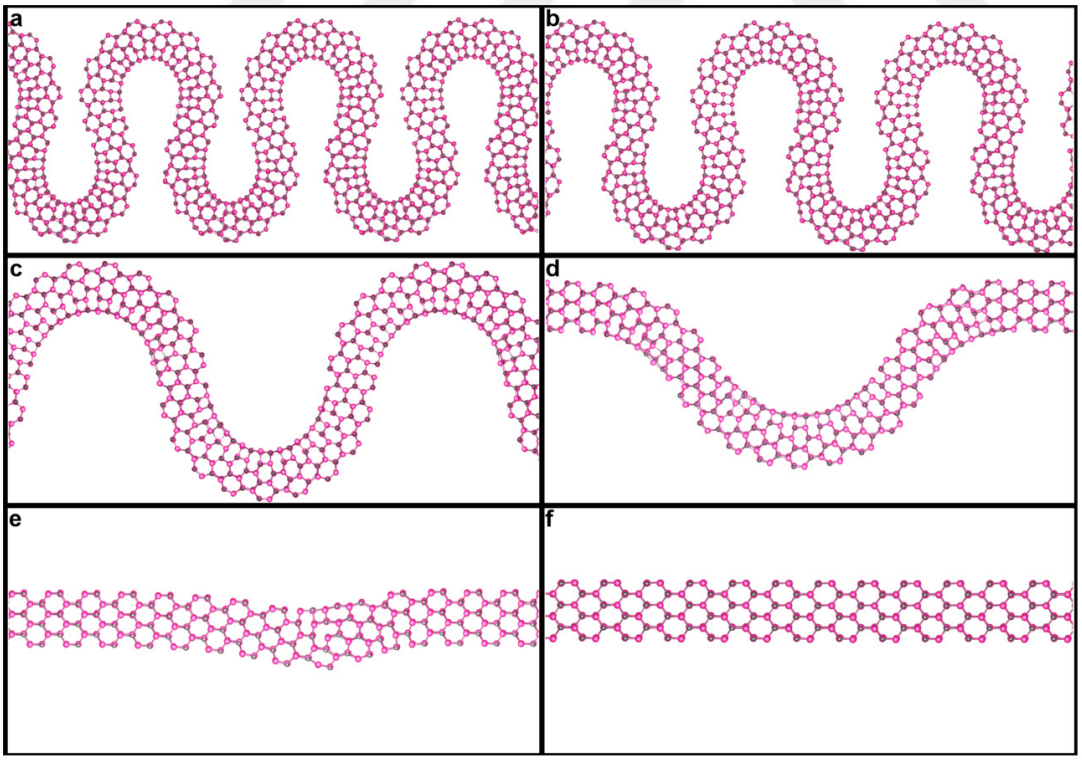


Figure A.44: Compressed 4x6 NR for the -0.5% S.R. was stretched for the 0.5% S.R. at 0.7K (VESTA).

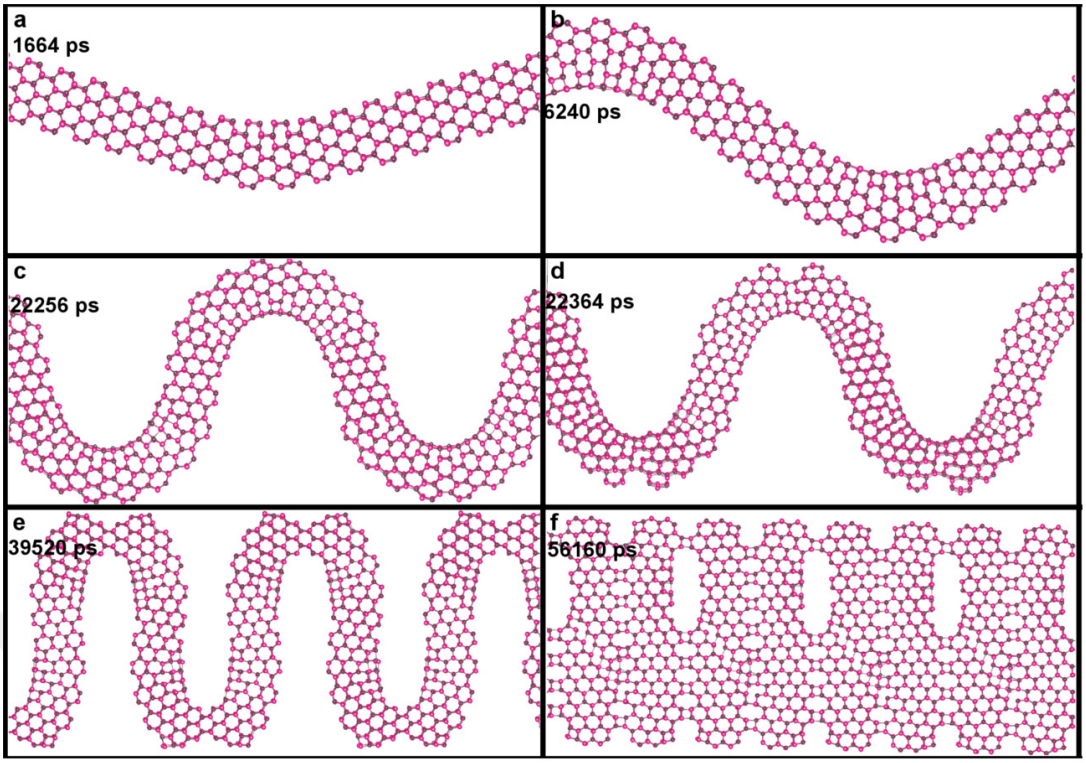


Figure A.45: Compressed 5x7 NR for the -0.5% S.R. at 0.7K (VESTA).

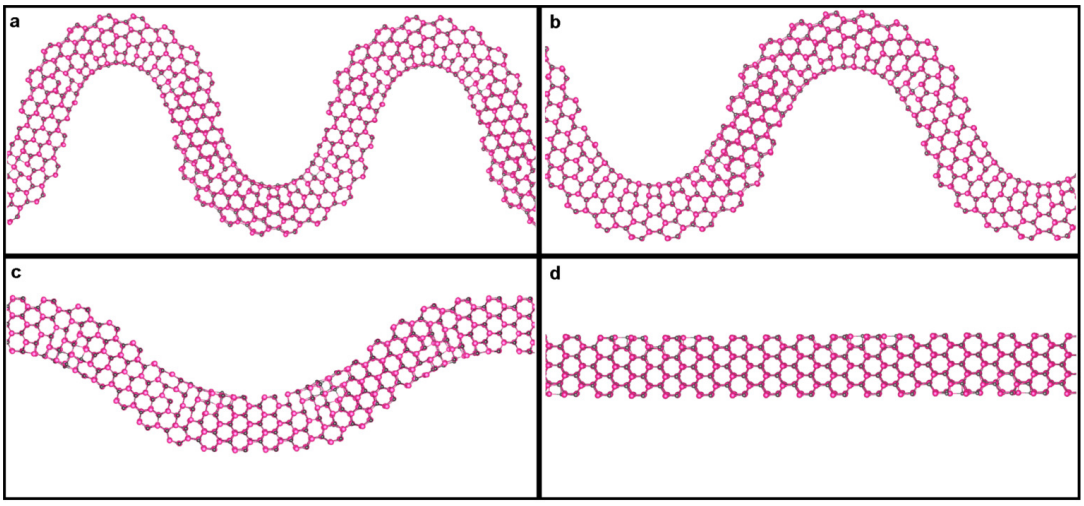


Figure A.46: Compressed 5x7 NR for the -0.5% S.R. was stretched for the 0.5% S.R. at 0.7K (VESTA).

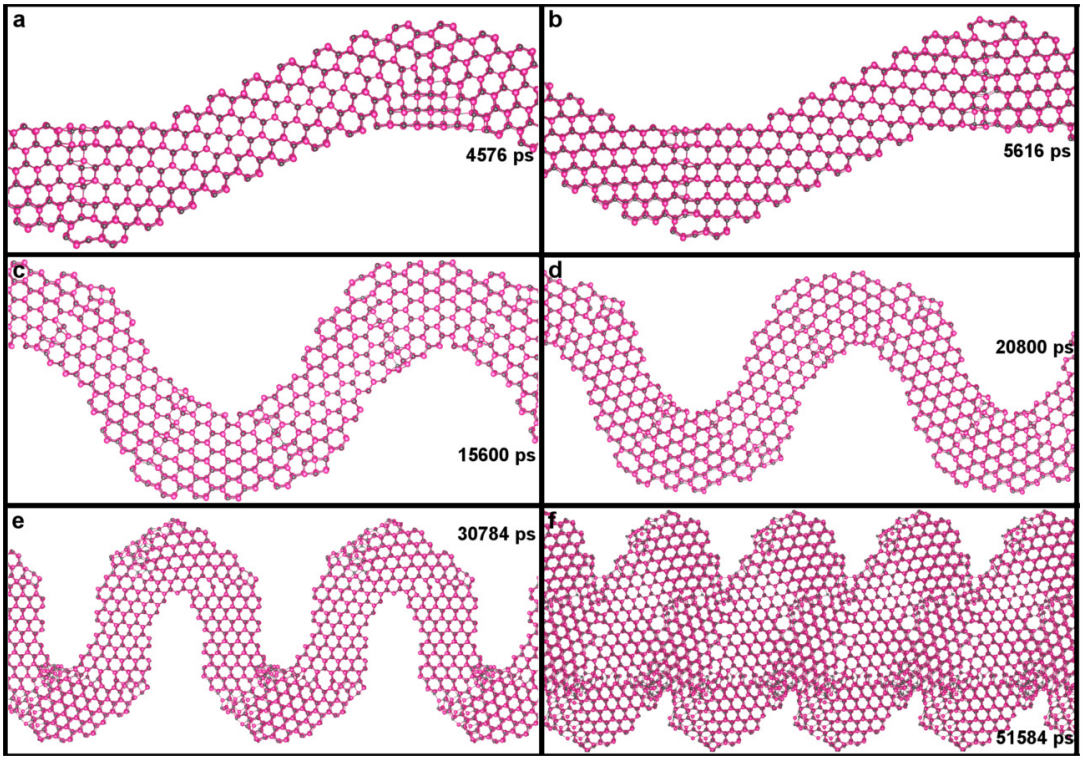


Figure A.47: Compressed 6x9 NR for the -0.5% S.R. at 0.7K (VESTA).

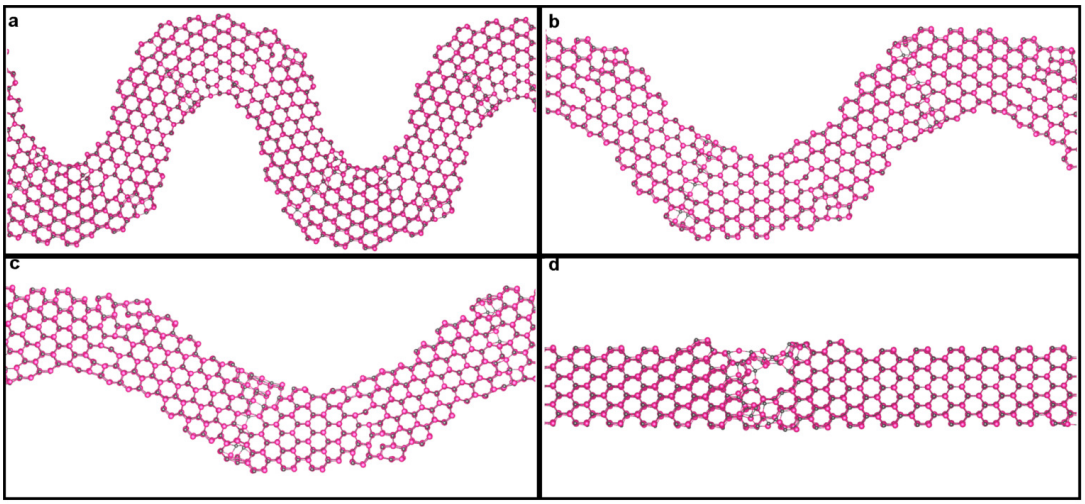


Figure A.48: Compressed 6x9 NR for the -0.5% was stretched for the 0.5% S.R. at 0.7K (VESTA).

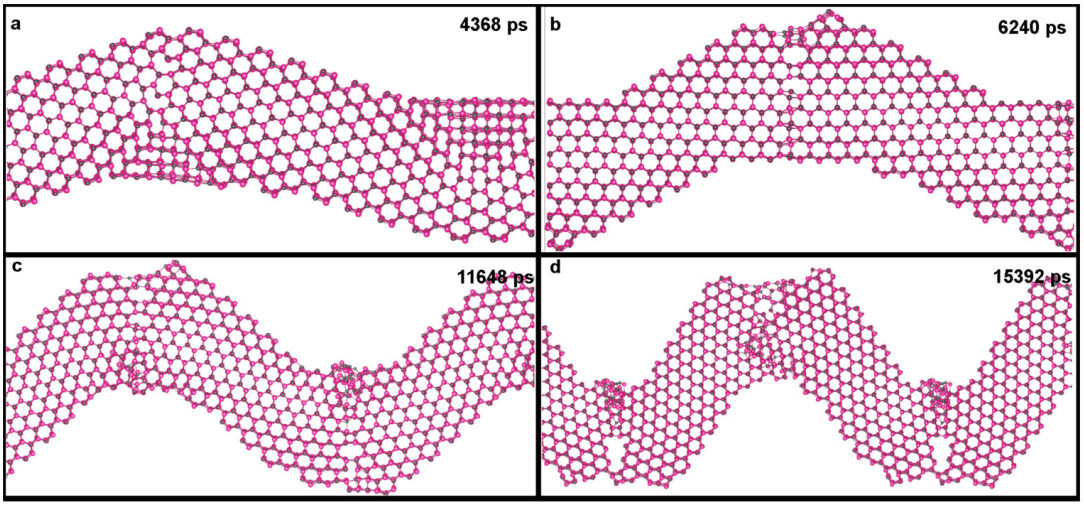


Figure A.49: Compressed 8x13 NR for the -0.5% S.R. at 0.7K (VESTA).

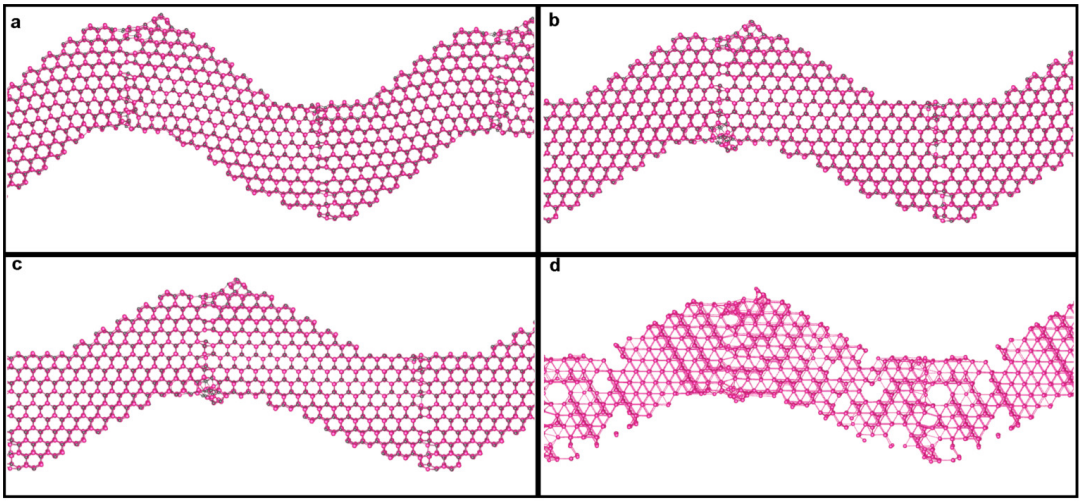


Figure A.50: Compressed 8x13 NR for the -0.5% S.R. was stretched for the 0.5% S.R. at 0.7K (VESTA).

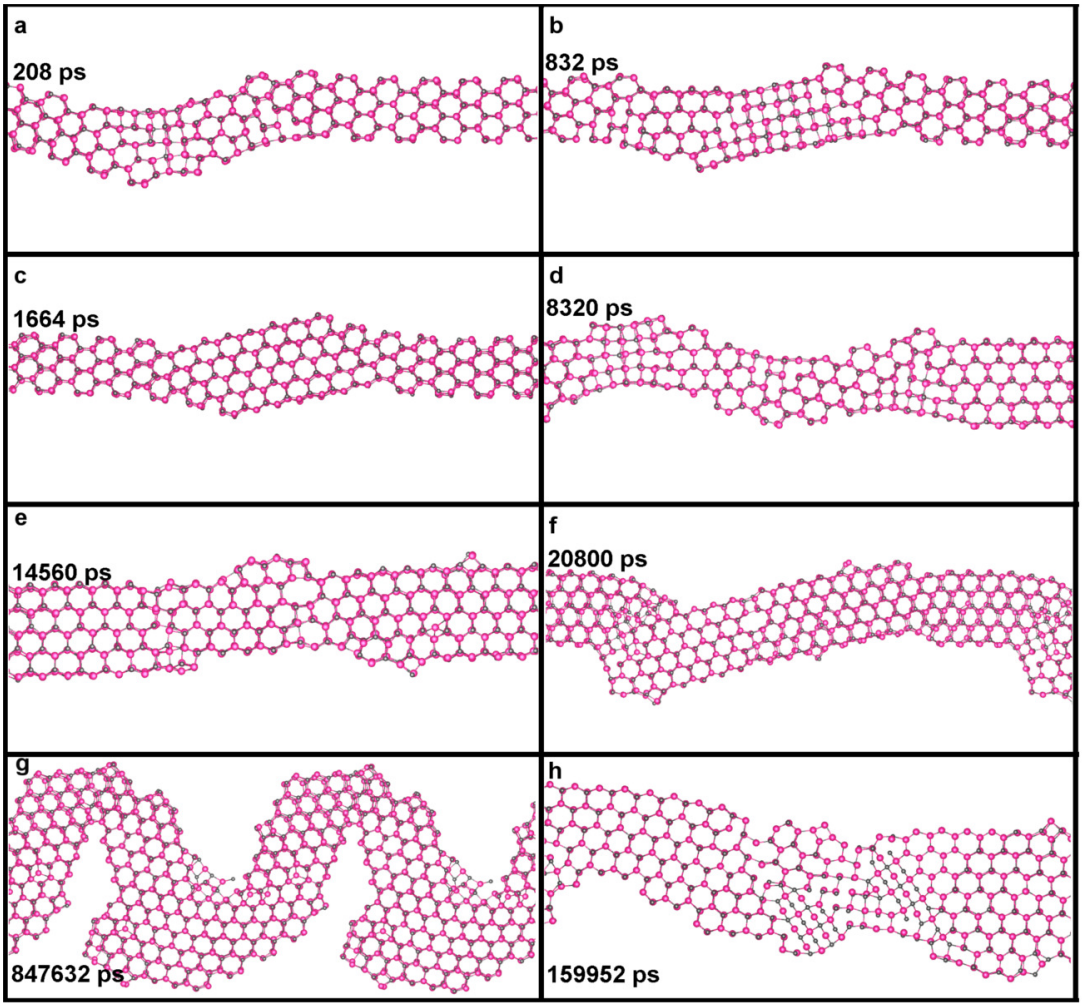


Figure A.51: Compressed 4x6 NR with -0.5% S.R. at 300K (VESTA).

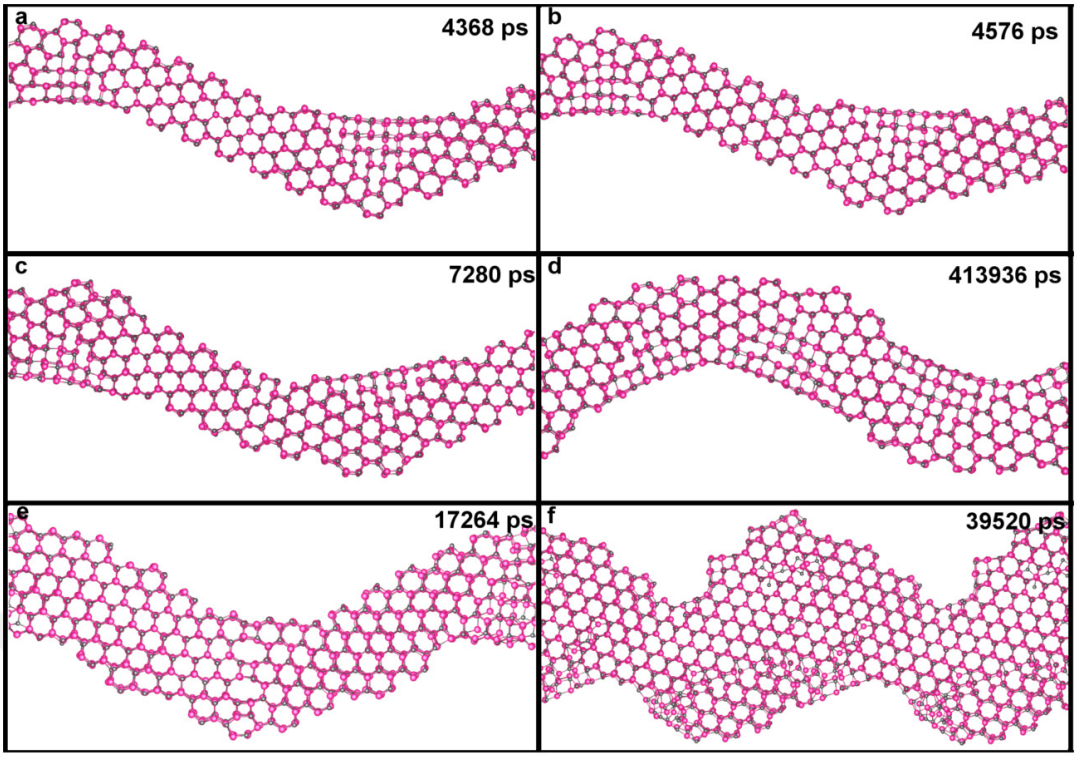


Figure A.52: Compressed 5x7 NR for the -0.5% S.R. at 300K (VESTA).

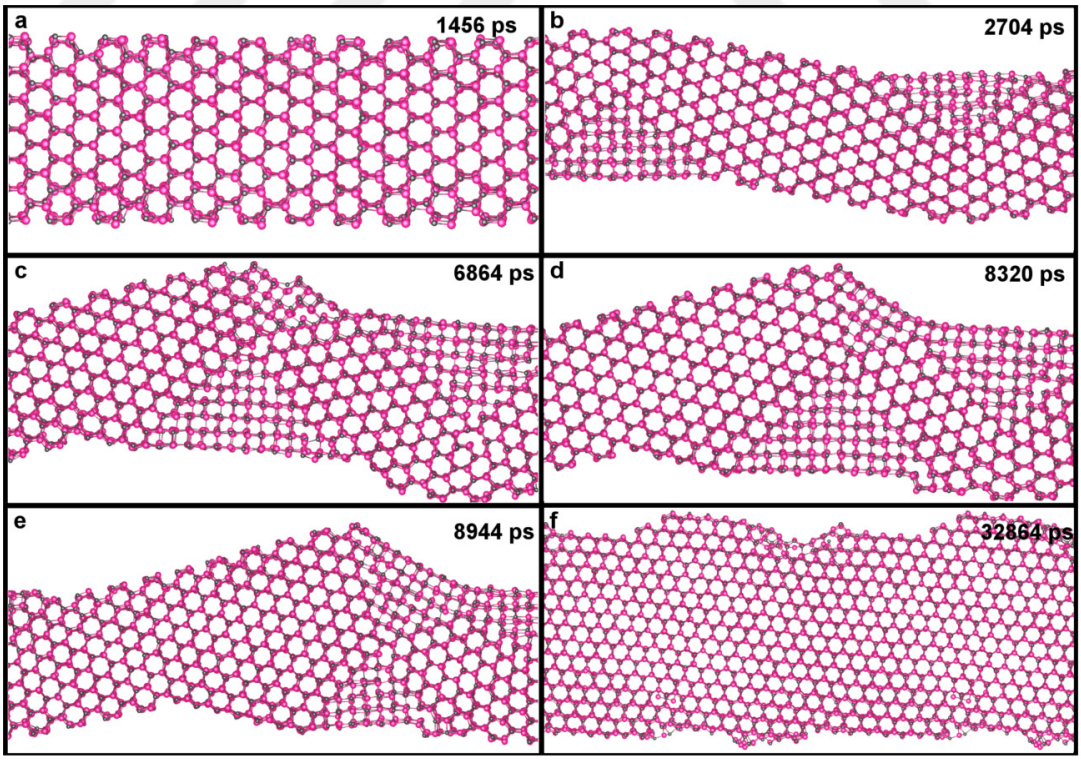


Figure A.53: Compressed 8x13 NR for the -0.5% S.R. at 600K (VESTA).

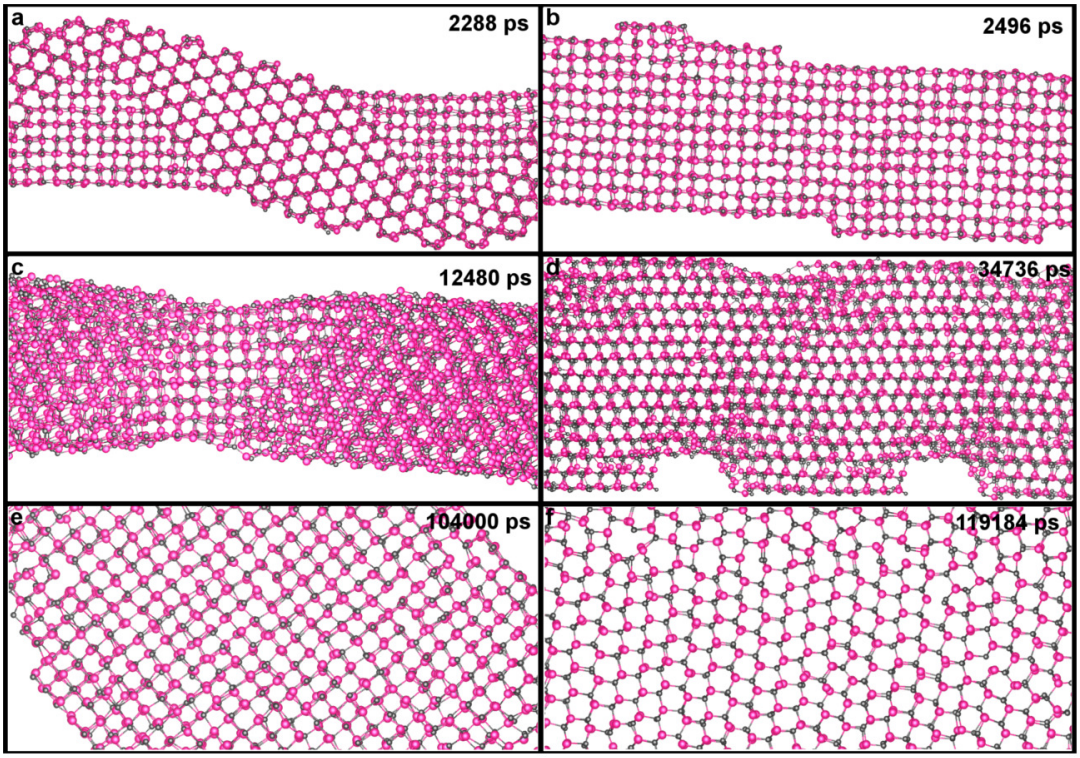


Figure A.54: Compressed 8x13 NR for the -0.5% S.R. at 900K (VESTA).

# APPENDIX B

# THE REAXFF REACTIVE FIELD DEVELOPMENT FOR SI/O AND GE/O SYSTEMS

## B.1 The ReaxFF Reactive force field for Si/O systems

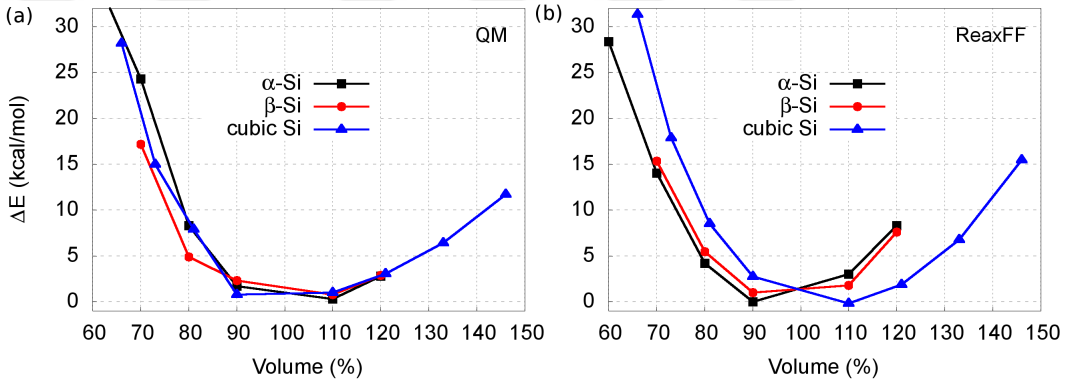


Figure B.1: Energy curves for equations of states of three phases of silicon predicted by (a) QM and (b) ReaxFF.

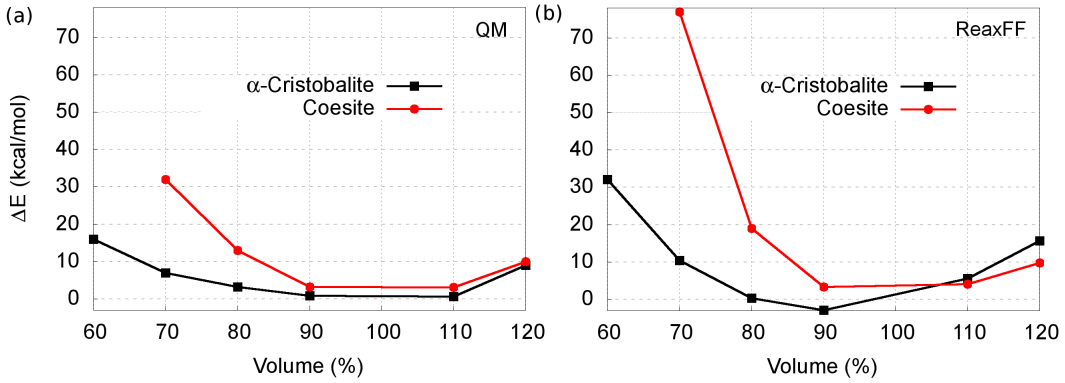


Figure B.2: Energy curves for equations of states of two phases of silica predicted by (a) QM and (b) ReaxFF.

**ReaxFF Reactive Force Field Parameters for Si/O/H**

This force field can be used with the standalone ReaxFF program, as well as with the LAMMPS open-source MD-program and the ADF-program.

```
Reactive MD-force field:  Si/O/H force field 2018
 39        !  Number of general parameters
   50.0000 !Overcoordination parameter
    9.5469 !Overcoordination parameter
   26.5405 !Valency angle conjugation parameter
    1.7224 !Triple bond stabilisation parameter
    6.8702 !Triple bond stabilisation parameter
   12.1176 !Undercoordination parameter
   13.3056 !Undercoordination parameter
  -70.5044 !Triple bond stabilization energy
    0.0000 !Lower Taper-radius
   10.0000 !Upper Taper-radius
    2.8793 !Not used
   33.8667 !Valency undercoordination
    6.0891 !Valency angle/lone pair parameter
    1.0563 !Valency angle
    2.0384 !Valency angle parameter
    6.1431 !Not used
    6.9290 !Double bond/angle parameter
    0.3989 !Double bond/angle parameter:  overcoord
    3.9954 !Double bond/angle parameter:  overcoord
   -2.4837 !Not used
    5.7796 !Torsion/BO parameter
   10.0000 !Torsion overcoordination
    1.9487 !Torsion overcoordination
   -1.2327 !Conjugation 0 (not used)
    2.1645 !Conjugation 1.5591 !vdWaals shielding
    0.1000 !Cutoff for bond order (*100)
    2.1365 !Valency angle conjugation parameter
    0.6991 !Overcoordination parameter
   50.0000 !Overcoordination parameter
    1.8512 !Valency/lone pair parameter
    0.5000 !Not used 20.0000 !Not used
    5.0000 !Molecular energy (not used)
    0.0000 !Molecular energy (not used)
```

```
   2.6962 !Valency angle conjugation parameter
5        !  Nr of atoms; cov.r; valency;a.m;Rvdw;Evdw;gammaEEM;cov.r2;#
           alfa;gammavdW;valency;Eunder;Eover;chiEEM;etaEEM;n.u.
           cov r3;Elp;Heat inc.;n.u.;n.u.;n.u.;n.u.  ov/un;val1;n.u.;val3,vval4
C    1.3817   4.0000  12.0000   1.8903   0.1838   0.9000   1.1341   4.0000
     9.7559   2.1346   4.0000  34.9350  79.5548   5.9666   7.0000   0.0000
     1.2114   0.0000 202.5551   8.9539  34.9289  13.5366   0.8563   0.0000
    -2.8983   2.5000   1.0564   4.0000   2.9663   0.0000   0.0000   0.0000
H    0.8930   1.0000   1.0080   1.3550   0.0930   0.8203  -0.1000   1.0000
     8.2230  33.2894   1.0000   0.0000 121.1250   3.7248   9.6093   1.0000
    -0.1000   0.0000  61.6606   3.0408   2.4197   0.0003   1.0698   0.0000
   -19.4571   4.2733   1.0338   1.0000   2.8793   0.0000   0.0000   0.0000
O    1.2450   2.0000  15.9990   2.3890   0.1000   1.0898   1.0548   6.0000
     9.7300  13.8449   4.0000  37.5000 116.0768   8.5000   8.3122   2.0000
     0.9049   0.4056  59.0626   3.5027   0.7640   0.0021   0.9745   0.0000
    -3.5500   2.9000   1.0493   4.0000   2.9225   0.0000   0.0000   0.0000
Si   2.0175   4.0000  28.0600   2.0473   0.1835   0.8925   1.2962   4.0000
    12.3588   1.2523   4.0000  21.7115 139.9309   4.6988   6.0000   0.0000
    -1.0000   0.0000 128.2031   8.7895  23.9298   0.8381   0.8563   0.0000
    -4.7525   2.1607   1.0338   4.0000   2.5791   0.0000   0.0000   0.0000
X   -0.1000   2.0000   1.0080   2.0000   0.0000   0.0100  -0.1000   6.0000
    10.0000   2.5000   4.0000   0.0000   0.0000   5.00009999.9999   0.0000
    -0.1000   0.0000  -2.3700   8.7410  13.3640   0.6690   0.9745   0.0000
   -11.0000   2.7466   1.0338   2.0000   2.8793   0.0000   0.0000   0.0000
4    !  Nr of bonds; Edis1;LPpen;n.u.;pbe1;pbo5;13corr;pbo6
                     pbe2;pbo3;pbo4;n.u.;pbo1;pbo2;ovcorr
 1  1 158.2004  99.1897  78.0000  -0.7738  -0.4550   1.0000  37.6117   0.4147
       0.4590  -0.1000   9.1628   1.0000  -0.0777   6.7268   1.0000   0.0000
 1  2 169.4760   0.0000   0.0000  -0.6083   0.0000   1.0000   6.0000   0.7652
       5.2290   1.0000   0.0000   1.0000  -0.0500   6.9136   0.0000   0.0000
 2  2 153.3934   0.0000   0.0000  -0.4600   0.0000   1.0000   6.0000   0.7300
       6.2500   1.0000   0.0000   1.0000  -0.0790   6.0552   0.0000   0.0000
 1  3 158.6946 107.4583  23.3136  -0.4240  -0.1743   1.0000  10.8209   1.0000
       0.5322  -0.3113   7.0000   1.0000  -0.1447   5.2450   0.0000   0.0000
 2  3 160.0000   0.0000   0.0000  -0.5725   0.0000   1.0000   6.0000   0.5626
       1.1150   1.0000   0.0000   0.0000  -0.0920   4.2790   0.0000   0.0000
 3  3 142.2858 145.0000  50.8293   0.2506  -0.1000   1.0000  29.7503   0.6051
       0.3451  -0.1055   9.0000   1.0000  -0.1225   5.5000   1.0000   0.0000
 1  4 108.3910  95.0233   0.0000   0.1129  -0.5558   1.0000  17.2117   0.4568
       0.2424  -0.2378  10.1163   1.0000  -0.1020   5.7156   1.0000   0.0000
 2  4 250.0000   0.0000   0.0000  -0.7128   0.0000   1.0000   6.0000   0.1186
```

```
       18.5790   1.0000   0.0000   1.0000  -0.0731   7.4983   0.0000   0.0000
 3  4 291.4687  16.2724   0.0000  -0.6232  -0.3000   1.0000  36.0000   0.6762
       9.6502  -0.4634  29.9983   1.0000  -0.1500   7.6885   1.0000   0.0000
 4  4  78.6948  12.3833  30.0000   0.2706  -0.3000   1.0000  16.0000   0.0100
       0.7257  -0.9788   7.8412   1.0000  -0.0824   8.5016   0.0000   0.0000
6     !  Nr of off-diagonal terms; Ediss;Ro;gamma;rsigma;rpi;rpi2
 1  2   0.1239   1.4004   9.8467   1.1210  -1.0000  -1.0000
 1  3   0.1156   1.8520   9.8317   1.2854   1.1352   1.0706
 2  3   0.0283   1.2885  10.9190   0.9215  -1.0000  -1.0000
 1  4   0.0541   2.0811  13.5179   1.7778   1.5840  -1.0000
 2  4   0.1659   1.4000  11.7054   1.3437  -1.0000  -1.0000
 3  4   0.1556   2.1618  10.4851   1.7448   1.3513  -1.0000
40    !  Nr of angles;at1;at2;at3;Thetao,o;ka;kb;pv1;pv2
 1  1  1  59.0573  30.7029   0.7606   0.0000   0.7180   6.2933   1.1244
 1  1  2  65.7758  14.5234   6.2481   0.0000   0.5665   0.0000   1.6255
 2  1  2  70.2607  25.2202   3.7312   0.0000   0.0050   0.0000   2.7500
 1  1  3  49.6811   7.1713   4.3889   0.0000   0.7171  10.2661   1.0463
 2  1  3  65.0000  13.8815   5.0583   0.0000   0.4985   0.0000   1.4900
 3  1  3  77.7473  40.1718   2.9802 -25.3063   1.6170 -46.1315   2.2503
 1  2  1   0.0000   3.4110   7.7350   0.0000   0.0000   0.0000   1.0400
 1  2  2   0.0000   0.0000   6.0000   0.0000   0.0000   0.0000   1.0400
 1  2  3   0.0000  25.0000   3.0000   0.0000   1.0000   0.0000   1.0400
 2  2  2   0.0000  27.9213   5.863   0.0000   0.0000   0.0000   1.0400
 2  2  3   0.0000   8.5744   3.0000   0.0000   0.0000   0.0000   1.0421
 3  2  3   0.0000  15.0000   2.8900   0.0000   0.0000   0.0000   2.8774
 1  3  1  73.5312  44.7275   0.7354   0.0000   3.0000   0.0000   1.0684
 1  3  3  79.4761  36.3701   1.8943   0.0000   0.7351  67.6777   3.0000
 1  3  2  70.1880  20.9562   0.3864   0.0000   0.0050   0.0000   1.6924
 2  3  2  85.8000   9.8453   2.2720   0.0000   2.8635   0.0000   1.5800
 2  3  3  75.6935  50.0000   2.0000   0.0000   1.0000   0.0000   1.1680
 3  3  3  80.7324  30.4554   0.9953   0.0000   1.6310  50.0000   1.0783
 4  4  4  71.0490  32.4076   1.2648   0.0000   0.0133   0.0000   1.2899
 2  4  4  79.0296   4.8472   8.0000   0.0000   4.0000   0.0000   1.0400
 2  4  2  76.7122  31.0021   2.4370   0.0000   0.1930   0.0000   1.0400
 3  4  4  97.1370  39.9525   1.0978   0.0000   0.5073   0.0000   1.3154
 2  4  3  77.4530  40.0000   1.1121   0.0000   4.0000   0.0000   1.1201
 3  4  3  95.2092  40.0000   1.1635   0.0000   0.3525   0.0000   3.0000
 4  3  4  47.4477   8.8967   0.5000   0.0000   4.0000   0.0000   1.0400
 2  3  4  80.0391   4.5313   8.0000   0.0000   3.3561   0.0000   1.8653
 3  3  4  20.0000   8.1399   2.7859   0.0000   3.0206   0.0000   1.6650
 2  2  4   0.0000  72.1101   7.6682   0.0000   2.7489   0.0000   1.0400
```

```
  4  2  4   0.0000  59.2363   2.3343   0.0000   1.3778   0.0000   2.3874
  3  2  4   0.0000  15.0000   2.8577   0.0000   4.0000   0.0000   1.1566
  1  1  4  72.5239  22.3583   2.0393   0.0000   1.0031   0.0000   1.0400
  1  4  1  69.1709  18.9268   2.1226   0.0000   1.0031   0.0000   1.0400
  4  1  4  68.6453  18.7377   2.0496   0.0000   1.0031   0.0000   1.0400
  1  4  4  68.9902  19.7021   2.0587   0.0000   1.0031   0.0000   1.0400
  2  1  4  72.6403  13.6964   2.4702   0.0000   1.0000   0.0000   1.0400
  1  4  2  71.8708  14.6864   2.4702   0.0000   1.0000   0.0000   1.0400
  1  3  4  85.8521  12.6881   1.0112   0.0000   1.0000   0.0000   1.3220
  1  4  3  71.7524  35.8987   1.5000   0.0000   1.0000   0.0000   1.0487
  3  1  4  70.0000   5.0250   1.0000   0.0000   1.0000   0.0000   1.2500
  1  2  4   0.0000   2.5000   1.0000   0.0000   1.0000   0.0000   1.2500
29 !  Nr of torsions;at1;at2;at3;at4;;V1;V2;V3;V2(BO);vconj;n.u;n
  1  1  1  1  -0.2500  34.7453   0.0288  -6.3507  -1.6000   0.0000   0.0000
  1  1  1  2  -0.2500  29.2131   0.2945  -4.9581  -2.1802   0.0000   0.0000
  2  1  1  2  -0.2500  31.2081   0.4539  -4.8923  -2.2677   0.0000   0.0000
  1  1  1  3  -0.3495  22.2142  -0.2959  -2.5000  -1.9066   0.0000   0.0000
  2  1  1  3   0.0646  24.3195   0.6259  -3.9603  -1.0000   0.0000   0.0000
  3  1  1  3  -0.5456   5.5756   0.8433  -5.1924  -1.0180   0.0000   0.0000
  1  1  3  1   1.7555  27.9267   0.0072  -2.6533  -1.0000   0.0000   0.0000
  1  1  3  2  -1.4358  36.7830  -1.0000  -8.1821  -1.0000   0.0000   0.0000
  2  1  3  1  -1.3959  34.5053   0.7200  -2.5714  -2.1641   0.0000   0.0000
  2  1  3  2  -2.5000  70.0597   1.0000  -3.5539  -2.9929   0.0000   0.0000
  2  1  3  3   0.1933  80.0000   1.0000  -4.0590  -3.0000   0.0000   0.0000
  3  1  3  1  -1.9889  76.4820  -0.1796  -3.8301  -3.0000   0.0000   0.0000
  3  1  3  2   0.2160  72.7707  -0.7087  -4.2100  -3.0000   0.0000   0.0000
  1  3  3  2  -2.5000  -3.3822   0.7004  -5.4467  -2.9586   0.0000   0.0000
  2  3  3  2   2.5000  -4.0000   0.9000  -2.5000  -1.0000   0.0000   0.0000
  1  3  3  3   1.2329  -4.0000   1.0000  -2.5000  -1.7479   0.0000   0.0000
  2  3  3  3   0.8302  -4.0000  -0.7763  -2.5000  -1.0000   0.0000   0.0000
  3  3  3  3  -2.5000  -4.0000   1.0000  -2.5000  -1.0000   0.0000   0.0000
  0  1  2  0   0.0000   0.0000   0.0000   0.0000   0.0000   0.0000   0.0000
  0  1  2  0   0.0000   0.0000   0.0000   0.0000   0.0000   0.0000   0.0000
  0  2  3  0   0.0000   0.1000   0.0200  -2.5415   0.0000   0.0000   0.0000
  0  1  1  0   0.0000  50.0000   0.3000  -4.0000  -2.0000   0.0000   0.0000
  0  3  3  0   0.5511  25.4150   1.1330  -5.1903  -1.0000   0.0000   0.0000
  2  4  4  2   0.0000   0.0000   0.0640  -2.4426   0.0000   0.0000   0.0000
  2  4  4  4   0.0000   0.0000   0.1587  -2.4426   0.0000   0.0000   0.0000
  0  2  4  0   0.0000   0.0000   0.1200  -2.4847   0.0000   0.0000   0.0000
  1  1  3  3  -2.0000  73.0530   1.5000  -9.0000  -2.0000   0.0000   0.0000
  1  3  3  1   0.0002  80.0000  -1.5000  -2.5000  -2.0000   0.0000   0.0000
```

```
 3  1  3  3  -1.8835  20.0000   1.5000  -9.0000  -2.0000   0.0000   0.0000
1          !  Nr of hydrogen bonds;at1;at2;at3;Rhb;Dehb;vhb1
 3  2  3   2.1200  -3.5800   1.4500  19.5000
```

## B.2 The ReaxFF Reactive force field for Ge/O systems

This force field can be used with the standalone ReaxFF program, as well as with the LAMMPS open-source MD-program and the ADF-program.

```
Reactive MD-force field:  Ge/O/H force field 2018
 39        !  Number of general parameters
   50.0000 !Overcoordination parameter
    9.5469 !Overcoordination parameter
   26.5405 !Valency angle conjugation parameter
    1.7224 !Triple bond stabilisation parameter
    6.8702 !Triple bond stabilisation parameter
   12.1176 !Undercoordination parameter
   13.3056 !Undercoordination parameter
  -70.5044 !Triple bond stabilization energy
    0.0000 !Lower Taper-radius
   10.0000 !Upper Taper-radius
    2.8793 !Not used
   33.8667 !Valency undercoordination
    6.0891 !Valency angle/lone pair parameter
    1.0563 !Valency angle
    2.0384 !Valency angle parameter
    6.1431 !Not used
    6.9290 !Double bond/angle parameter
    0.3989 !Double bond/angle parameter:  overcoord
    3.9954 !Double bond/angle parameter:  overcoord
   -2.4837 !Not used
    5.7796 !Torsion/BO parameter
   10.0000 !Torsion overcoordination
    1.9487 !Torsion overcoordination
   -1.2327 !Conjugation 0 (not used)
    2.1645 !Conjugation 1.5591 !vdWaals shielding
    0.1000 !Cutoff for bond order (*100)
    2.1365 !Valency angle conjugation parameter
    0.6991 !Overcoordination parameter
   50.0000 !Overcoordination parameter
    1.8512 !Valency/lone pair parameter
    0.5000 !Not used 20.0000 !Not used
    5.0000 !Molecular energy (not used)
    0.0000 !Molecular energy (not used)
```

```
   2.6962 !Valency angle conjugation parameter
5        !  Nr of atoms; cov.r; valency;a.m;Rvdw;Evdw;gammaEEM;cov.r2;#
           alfa;gammavdW;valency;Eunder;Eover;chiEEM;etaEEM;n.u.
           cov r3;Elp;Heat inc.;n.u.;n.u.;n.u.;n.u.  ov/un;val1;n.u.;val3,vval4
C    1.3817   4.0000  12.0000   1.8903   0.1838   0.9000   1.1341   4.0000
     9.7559   2.1346   4.0000  34.9350  79.5548   5.9666   7.0000   0.0000
     1.2114   0.0000 202.5551   8.9539  34.9289  13.5366   0.8563   0.0000
    -2.8983   2.5000   1.0564   4.0000   2.9663   0.0000   0.0000   0.0000
H    0.8930   1.0000   1.0080   1.3550   0.0930   0.8203  -0.1000   1.0000
     8.2230  33.2894   1.0000   0.0000 121.1250   3.7248   9.6093   1.0000
    -0.1000   0.0000  61.6606   3.0408   2.4197   0.0003   1.0698   0.0000
   -19.4571   4.2733   1.0338   1.0000   2.8793   0.0000   0.0000   0.0000
O    1.2450   2.0000  15.9990   2.3890   0.1000   1.0898   1.0548   6.0000
     9.7300  13.8449   4.0000  37.5000 116.0768   8.5000   8.3122   2.0000
     0.9049   0.4056  59.0626   3.5027   0.7640   0.0021   0.9745   0.0000
    -3.5500   2.9000   1.0493   4.0000   2.9225   0.0000   0.0000   0.0000
Ge   2.0804   4.0000  72.6100   2.5441   0.1939   0.3000   0.9578   4.0000
    11.9727   1.0000   4.0000  10.5217 131.4200   4.2027   6.0120   0.0000
    -1.0000   0.0000 128.9891   8.7895  23.9298   0.8381   0.8563   0.0000
    -4.0000   3.0365   1.0338   6.2998   2.5791   0.0000   0.0000   0.0000
X   -0.1000   2.0000   1.0080   2.0000   0.0000   0.0100  -0.1000   6.0000
    10.0000   2.5000   4.0000   0.0000   0.0000   5.00009999.9999   0.0000
    -0.1000   0.0000  -2.3700   8.7410  13.3640   0.6690   0.9745   0.0000
   -11.0000   2.7466   1.0338   2.0000   2.8793   0.0000   0.0000   0.0000
10    !  Nr of bonds; Edis1;LPpen;n.u.;pbe1;pbo5;13corr;pbo6
                      pbe2;pbo3;pbo4;n.u.;pbo1;pbo2;ovcorr
 1  1 158.2004  99.1897  78.0000  -0.7738  -0.4550   1.0000  37.6117   0.4147
       0.4590  -0.1000   9.1628   1.0000  -0.0777   6.7268   1.0000   0.0000
 1  2 169.4760   0.0000   0.0000  -0.6083   0.0000   1.0000   6.0000   0.7652
       5.2290   1.0000   0.0000   1.0000  -0.0500   6.9136   0.0000   0.0000
 2  2 153.3934   0.0000   0.0000  -0.4600   0.0000   1.0000   6.0000   0.7300
       6.2500   1.0000   0.0000   1.0000  -0.0790   6.0552   0.0000   0.0000
 1  3 158.6946 107.4583  23.3136  -0.4240  -0.1743   1.0000  10.8209   1.0000
       0.5322  -0.3113   7.0000   1.0000  -0.1447   5.2450   0.0000   0.0000
 2  3 160.0000   0.0000   0.0000  -0.5725   0.0000   1.0000   6.0000   0.5626
       1.1150   1.0000   0.0000   0.0000  -0.0920   4.2790   0.0000   0.0000
 3  3 142.2858 145.0000  50.8293   0.2506  -0.1000   1.0000  29.7503   0.6051
       0.3451  -0.1055   9.0000   1.0000  -0.1225   5.5000   1.0000   0.0000
 1  4 161.4618  47.6708  43.3991  -1.0000  -0.3000   1.0000  36.0000   0.0421
      10.0094  -1.2556  14.0726   1.0000  -0.0661   6.5965   1.0000   0.0000
 2  4 158.9186   0.0000   0.0000  -0.6477   0.0000   1.0000   6.0000   0.5768
```

```
       11.2822   1.0000   0.0000   1.0000  -0.0401   5.0156   0.0000   0.0000
 3  4 177.0245  23.3550  43.3991  -1.1750  -0.3000   1.0000  36.0000   0.1143
       0.8240  -0.7601   5.9431   1.0000  -0.2239   4.7456   1.0000   0.0000
 4  4  95.1003  63.0193  30.0000   0.1000  -0.3000   1.0000  16.0000   0.0755
       0.1062  -0.6420   6.1811   1.0000  -0.0602   8.1721   0.0000   0.0000
6     !  Nr of off-diagonal terms; Ediss;Ro;gamma;rsigma;rpi;rpi2
 1  2   0.1239   1.4004   9.8467   1.1210  -1.0000  -1.0000
 1  3   0.1156   1.8520   9.8317   1.2854   1.1352   1.0706
 2  3   0.0283   1.2885  10.9190   0.9215  -1.0000  -1.0000
 1  4   0.2655   1.9097  11.1886   1.9983   1.3682  -1.0000
 2  4   0.0494   1.4125  12.8538   1.2041  -1.0000  -1.0000
 3  4   0.1328   1.6686  12.6993   1.7068   1.4154  -1.0000
39    !  Nr of angles;at1;at2;at3;Thetao,o;ka;kb;pv1;pv2
 1  1  1  59.0573  30.7029   0.7606   0.0000   0.7180   6.2933   1.1244
 1  1  2  65.7758  14.5234   6.2481   0.0000   0.5665   0.0000   1.6255
 2  1  2  70.2607  25.2202   3.7312   0.0000   0.0050   0.0000   2.7500
 1  1  3  49.6811   7.1713   4.3889   0.0000   0.7171  10.2661   1.0463
 2  1  3  65.0000  13.8815   5.0583   0.0000   0.4985   0.0000   1.4900
 3  1  3  77.7473  40.1718   2.9802 -25.3063   1.6170 -46.1315   2.2503
 1  2  1   0.0000   3.4110   7.7350   0.0000   0.0000   0.0000   1.0400
 1  2  2   0.0000   0.0000   6.0000   0.0000   0.0000   0.0000   1.0400
 1  2  3   0.0000  25.0000   3.0000   0.0000   1.0000   0.0000   1.0400
 2  2  2   0.0000  27.9213   5.863   0.0000   0.0000   0.0000   1.0400
 2  2  3   0.0000   8.5744   3.0000   0.0000   0.0000   0.0000   1.0421
 3  2  3   0.0000  15.0000   2.8900   0.0000   0.0000   0.0000   2.8774
 1  3  1  73.5312  44.7275   0.7354   0.0000   3.0000   0.0000   1.0684
 1  3  3  79.4761  36.3701   1.8943   0.0000   0.7351  67.6777   3.0000
 1  3  2  70.1880  20.9562   0.3864   0.0000   0.0050   0.0000   1.6924
 2  3  2  85.8000   9.8453   2.2720   0.0000   2.8635   0.0000   1.5800
 2  3  3  75.6935  50.0000   2.0000   0.0000   1.0000   0.0000   1.1680
 3  3  3  80.7324  30.4554   0.9953   0.0000   1.6310  50.0000   1.0783
 4  4  4  66.6054  16.3154   1.4405   0.0000   0.0133   0.0000   1.1339
 2  2  4   0.0000  20.0379   4.0587   0.0000   1.6371   0.0000   2.1153
 2  4  4  73.5323  10.0544   5.0000   0.0000   0.0651   0.0000   1.3384
 2  4  2  71.8258  25.0000   4.0000   0.0000   2.8421   0.0000   1.6822
 4  2  4   0.0000  30.0000   5.0000   0.0000   1.6371   0.0000   1.7493
 3  4  4  86.9633  30.8758   4.7277   0.0000   0.0710   0.0000   2.2205
 2  4  3  37.6566  31.0456   0.5000   0.0000   3.6128   0.0000   2.0870
 3  4  3  78.8452  39.9385   0.8288   0.0000   4.0000   0.0000   2.0082
 1  4  4  55.5918  23.6896   2.1318   0.0000   3.6469   0.0000   1.9055
 1  4  2  76.3376  18.8721   4.1229   0.0000   0.9194   0.0000   1.2935
```

```
  1   4   1 100.0000    6.5114    2.5828    0.0000    0.6427    0.0000    1.5529
  4   1   4  44.0075    2.7819    0.6763    0.0000    3.6755    0.0000    1.1903
  2   1   4  88.8773   12.8751    9.3121    0.0000    3.0000    0.0000    1.0000
  1   1   4  96.2951   18.3964    1.7282    0.0000    2.2703    0.0000    1.1962
  4   3   4  15.0000    5.8389    1.0637    0.0000    0.8812    0.0000    1.0498
  2   3   4  57.9780   40.0000    1.1853    0.0000    3.9084    0.0000    1.0000
  3   3   4  81.7192   38.6128    3.7556    0.0000    2.5834    0.0000    2.8370
  1   3   4 110.0000   27.5093    5.4413    0.0000    1.7696    0.0000    1.0000
  1   4   3  65.7436   35.5076    1.3133    0.0000    0.1000    0.0000    2.9900
  3   1   4  65.9044   14.7880    2.1288    0.0000    1.5443    0.0000    1.0000

  1   2   4   0.0000    5.4180    1.3319    0.0000    1.3813    0.0000    1.0000
 26 !  Nr of torsions;at1;at2;at3;at4;;V1;V2;V3;V2(BO);vconj;n.u;n
  1   1   1   1  -0.2500   34.7453    0.0288   -6.3507   -1.6000    0.0000    0.0000
  1   1   1   2  -0.2500   29.2131    0.2945   -4.9581   -2.1802    0.0000    0.0000
  2   1   1   2  -0.2500   31.2081    0.4539   -4.8923   -2.2677    0.0000    0.0000
  1   1   1   3  -0.3495   22.2142   -0.2959   -2.5000   -1.9066    0.0000    0.0000
  2   1   1   3   0.0646   24.3195    0.6259   -3.9603   -1.0000    0.0000    0.0000
  3   1   1   3  -0.5456    5.5756    0.8433   -5.1924   -1.0180    0.0000    0.0000
  1   1   3   1   1.7555   27.9267    0.0072   -2.6533   -1.0000    0.0000    0.0000
  1   1   3   2  -1.4358   36.7830   -1.0000   -8.1821   -1.0000    0.0000    0.0000
  2   1   3   1  -1.3959   34.5053    0.7200   -2.5714   -2.1641    0.0000    0.0000
  2   1   3   2  -2.5000   70.0597    1.0000   -3.5539   -2.9929    0.0000    0.0000
  2   1   3   3   0.1933   80.0000    1.0000   -4.0590   -3.0000    0.0000    0.0000
  3   1   3   1  -1.9889   76.4820   -0.1796   -3.8301   -3.0000    0.0000    0.0000
  3   1   3   2   0.2160   72.7707   -0.7087   -4.2100   -3.0000    0.0000    0.0000
  1   3   3   2  -2.5000   -3.3822    0.7004   -5.4467   -2.9586    0.0000    0.0000
  2   3   3   2   2.5000   -4.0000    0.9000   -2.5000   -1.0000    0.0000    0.0000
  1   3   3   3   1.2329   -4.0000    1.0000   -2.5000   -1.7479    0.0000    0.0000
  2   3   3   3   0.8302   -4.0000   -0.7763   -2.5000   -1.0000    0.0000    0.0000
  3   3   3   3  -2.5000   -4.0000    1.0000   -2.5000   -1.0000    0.0000    0.0000
  0   1   2   0   0.0000    0.0000    0.0000    0.0000    0.0000    0.0000    0.0000
  0   1   2   0   0.0000    0.0000    0.0000    0.0000    0.0000    0.0000    0.0000
  0   2   3   0   0.0000    0.1000    0.0200   -2.5415    0.0000    0.0000    0.0000
  0   1   1   0   0.0000   50.0000    0.3000   -4.0000   -2.0000    0.0000    0.0000
  0   3   3   0   0.5511   25.4150    1.1330   -5.1903   -1.0000    0.0000    0.0000
  1   1   3   3  -2.0000   73.0530    1.5000   -9.0000   -2.0000    0.0000    0.0000
  1   3   3   1   0.0002   80.0000   -1.5000   -2.5000   -2.0000    0.0000    0.0000
  3   1   3   3  -1.8835   20.0000    1.5000   -9.0000   -2.0000    0.0000    0.0000
 1          !  Nr of hydrogen bonds;at1;at2;at3;Rhb;Dehb;vhb1
  3   2   3   2.1200   -3.5800    1.4500   19.5000
```

# CURRICULUM VITAE

**Surname, Name:** Nayir, Nadire
**email adress:** nadire.nayr42@gmail.com, nadire@metu.edu.tr, nzn36@psu.edu

## PROFESSIONAL EXPERIENCE

16/04/2017-14/04/2018: Visiting research Scholar at Department of Mechanical and Nuclear Enginerring, PennState University in US for one year with support from the Scientific and Technological Research Council of Turkey (TUBITAK) 2214-A Program, Grant No. 1059B141600161.

## AREA OF EXPERTISE

- The ReaxFF force field development for Ge/O/Si system which enables to study on crystal growth of Ge on $SiO_2$, Ge MOS interfaces such as Ge/$GeO_2$, Ge/$SiO_2$, impurity diffusion in solids, etc.
- Molecular modelling using MD simulations
- Programming for data mining formulations and challenges
- Developing a program for implementation of numerical analysis to solve the problems in Physics.

## COMPUTER SKILLS

- The ReaxFF force field development
- LAMMPS and ReaxFF/ADF Molecular Dynamics simulations
- Programming with PHP, Perl, MATLAB, GNU-Octave and Bash scripting
- Gaussian-09, Quantum Espresso and VASP (basic level) for DFT calculations
- Advanced level Linux OS

## PUBLICATIONS

### PAPERS PUBLISHED IN INTERNATIONAL REFEREED JOURNALS

- N. Nayir, E. S. Tasci, and S. Erkoc, "Structural and thermal properties of Indium Phosphide nanoparticles: Molecular dynamics simulations", J. Comput. Theoret. Nanosci.12,2134 (2015).
- N. Nayir, E. S. Tasci, S. Erkoc, "Structural properties of indium phosphide nanorods: molecular dynamics simulations", Int. J. nanotechnol. 13, 809(2016).
- N. Nayir, A. C. T. van Duin, S. Erkoc, “Development of a ReaxFF Reactive Force Field for Interstitial Oxygen in Germanium and application to $GeO_2$/Ge interfaces" (in preparation)
- N. Nayir, A. C. T. van Duin, S. Erkoc, “Development of The ReaxFF Reactive Force Field for Inherent Point Defects in the Si/Silica system" (in preparation)

### PROCEEDINGS PRESENTED IN NATIONAL MEETINGS

- N. Nayir, E. S. Tasci, S. Erkoc, "Structural and thermal properties of InP nanostructures: Molecular dynamics simulations", Adv. Mater. World Congress (AMWC13), 16-19 September 2013, Cesme Altin Yunus-Izmir, Abstract Book, p. 254 (Poster).

- N. Nayir, E. S. Tasci, S. Erkoc, "Structural properties of InP nanorods under uniaxial strain: Molecular dynamics simulations", TFD30, 2-5 September 2013, Istanbul. Book of Abstracts, p. 374. (poster)

- N. Nayir, E. S. Tasci, S. Yerci, S. Erkoc, “Investigation of the germanium on insulator using Molecular Dynamics Simulations”, 20 th Condensed Matter Physics Meeting, Hacettepe University, December 26, 2014, Ankara, Abstract Book, p. S04 (Speaker)

- N. Nayir, E. S. Tasci, S. Erkoc, "Structural properties of InP nanorods under uniaxial compression: Molecular dynamics simulations", 11 th Nanoscience and Nanotechnology Conference (NanoTR-11), Book of Abstracts, PS2-P52, 22-25 June 2015, METU, Ankara (poster)

- N. Nayir, E. S. Tasci, Z.I. Ozyurt, S. Yerci, S. Erkoc, "Growth kinetics of germanium on insulators by seed-induced lateral liquid beam epitaxy using molecular dynamics simulations", 11 th Nanoscience and Nanotechnology Conference (NanoTR-11), Book of Abstracts, PS3-P10, 22-25 June 2015, METU, Ankara (poster)

- N. Nayir, E. S. Tasci, Z.I. Ozyurt, S. Yerci, S. Erkoc, “Seed-induced Lateral Liquid Beam Epitaxy Growth of Single Crystal Germanium on insulator using Molecular Dynamics Simulations”, 4 th National High-Performance Computing Conference (Performance 2015), October 1-2, METU, Ankara (Speaker)

**PROCEEDINGS PRESENTED IN INTERNATIONAL MEETINGS**

- N. Nayir, E. S. Tasci, S. Erkoc, "Structural properties of InP nanorods under mechanical effects and heat treatment", Collaborative Conference on 3D and Materials Research (CC3DMR-2015), Abstract Book, p. 249 15-19 June 2015, Busan, Korea

- N. Nayir, E. S. Tasci, Z.I. Ozyurt, S. Yerci, S. Erkoc, “Optimization of seed-induced lateral liquid beam epitaxy growth of germanium on insulator by molecular dynamics”, Collaborative Conference on 3D and Materials Research (CC3DMR-2015), Abstract Book, p. 425 15-19 June 2015, Busan, Korea (poster)

- N. Nayir, A.C.T. van Duin, S. Erkoc, “ReaxFF Development for Growth of Germanium on Amorphous SiO2 by Lateral Liquid Phase Epitaxy”, Chemistry graduate Open house 2018, PennState University, University Park, PA, US, March 16 2018 (Poster)